Universidad
Carlos III de Madrid

Ph.D Thesis

Formability of ultra-fine grained metallic materials

Author:

Eva Cristina Moreno Valle

Supervisor:

Dr. Ilchat Sabirov

TESIS DOCTORAL

Formability of ultra-fine grained metallic materials

Autor**: Eva Cristina Moreno Valle**

Director**: Ilchat Sabirov**

Firma del Tribunal Calificador:

Firma

Presidente:

Vocal:

Secretario:

Calificación:

Leganés, de de

“Un científico en su laboratorio no es sólo un técnico, es también un niño colocado ante fenómenos naturales que le impresionan como un cuento de hadas”

Marie Curie

Con todo mi cariño, a mis abuelos

ACKNOWLEDGEMENTS

I acknowledge gratefully the *Fundacion MADRI+D* (Spain) and the National Centre for Research and Development (Poland) for the financial support of this work (Project LIMEDU/ERA-NET MATERA+ /03/ 2011). I would like to thank the Austrian Agency for International Cooperation in Education and Research for the support trough the *Ernst-Mach Stipendium* financed by the Austrian Federal Ministry of Science and Research.

I sincerely appreciate the collaboration with Prof. W. Pachla, Dr. M. Kulczyk, Dr. B. Savoini, Dr. M.A. Monge, Prof. C. Ballesteros, Dr. J.M. Molina-Aldareguia, Dr. M.A. Monclus, Dr. N. A. Enikeev, Dr. V.U. Kazykhanov, Dr. M. T. Perez-Prado, Dr. M.Yu. Murashkin, Dr. E. V. Bobruk and Prof. R.Z. Valiev for their wide research experience resulted in the appended published papers. I would like to express my gratitude to Prof. R. Pippan and Dr. A. Hohenwarter for their guidance in fracture testing during my stay in Austria.

I would like to thank IMDEA Materials Institute for the opportunity of performing my PhD study in a competitive research institute of excellence. I am deeply grateful to my supervisor, Dr. Ilchat Sabirov for his support, guidance and vast knowledge in materials science.

I also wish to extend my gratitude to all my colleagues and staff from IMDEA Materials Institute for their fruitful advices and for the always enjoyable working atmosphere.

Quisiera extender este agradecimiento a Rocío, Ana, Rafa por tan buenos momentos en el laboratorio y tantas otras experiencias compartidas que le han dado un sabor muy especial a esta etapa. A Jose, Vane, Juan Carlos, Edu y Roberto porque he aprendido, me he reído y he disfrutado mucho a vuestro lado. Desde el primer día, siempre me he sentido entre amigos. A Alicia, Luis, Víctor, Hangbo, Arcadio y Lester, gracias a los *japillos* que han sido el contrapunto perfecto al ritmo frenético del último año, grandes momentos y muchas risas. Y sobre todo a Irene, compartiendo jefe, mesa, chocolates y confidencias. Gracias por vuestro respaldo y por las palabras de ánimo que fácilmente me sacaban una sonrisa hasta en los momentos más difíciles.

No puedo olvidar a mis compañeros de Máster que poco a poco se convirtieron en amigos, a Rubén, Sonia, Edwin, Amaia, María, Carolina, Carol, Emilio, Sandra y Lili y en especial a Javi, Rafa y a Kesman, tan diferentes pero de los que he aprendido muchísimo. Espero que sigamos compartiendo buenos ratos juntos sea donde sea que nos lleven nuestros caminos.

Tampoco puedo dejar en el tintero a mis amigos, consaburenses, yebenosos y mi porteña favorita, se han vuelto imprescindibles en mi vida. Quisiera hacer especial mención a Patricia y a Lourdes. A pesar de que cada una tomó su camino, siempre habéis estado ahí. Y sobre todo a Belén y a Mari, porque además hemos vivido juntas las alegrías y miedos propios de la tesis. Chicas, siempre nos quedará Lisboa.

Por supuesto, a mi familia. A mis padres, Polo y Feli, muchas gracias por vuestro "¿y eso qué es para ti? ¡Eso no es nada!" capaz de infundirme todo el valor necesario. A Rosi, siempre atenta y preocupada por mi tesis, has sido un gran apoyo todos estos años. A mi abuela Regina y a los que me faltan, mi abuelo Gabriel y mi aya Esperanza, de los que tanto he aprendido. A mi hermana Ángela, tan alegre y valiente, a la que he echado tanto de menos en Madrid. Y a Alberto, gracias porque todo es mucho más fácil a tu lado. Gracias por tu comprensión, por tu apoyo incondicional y por ilusionarte con mis metas. Todos mis logros son vuestros.

Gracias.

ABSTRACT

Ultra-fine grained (UFG) metallic materials have been a hot topic in materials science for the last 25 years. There is a significant body of research showing that the UFG materials have very high mechanical strength, but their commercialisation is limited due to their low uni-axial tensile ductility. The main objective of this PhD thesis is to study the bi-axial stretching formability of the UFG metallic materials. It is demonstrated that there is a significant effect of the stress state (stress triaxiality) on mechanisms operating during plastic deformation in the UFG commercially pure (CP) Cu and the deformation mechanisms are determined by the stress state. The microstructure of the UFG CP Cu can be designed in such a way so as to show very high formability, even exceeding that of its coarse-grained counterpart. The effect of metallographic and crystallographic texture on the bi-axial stretching formability of the UFG CP Ti has been analysed. It is shown that the UFG CP Ti can show bi-axial stretching formability sufficient for metalforming operations. Coarse dispersoids and fractured particles in the Al 2024 alloy significantly limit its formability, acting as sites for the formation of cracks leading to sample failure at the early stages of deformation. Based on the analysis of the experimental results, a general recipe to improve formability of the UFG metallic materials is proposed.

RESUMEN

En los últimos 25 años, los materiales metálicos de grano ultra-fino han levantado una gran expectación en el mundo de la ciencia de materiales. A pesar de que ya existe un importante trabajo de investigación que demuestra la alta resistencia mecánica de estos materiales, su comercialización se ha visto restringida por su baja ductilidad cuando están sometidos a tracción uniaxial. El principal objetivo de esta tesis es estudiar lo que se conoce en inglés como “stretching formability” bajo un estado de tensiones bi-axial para distintos materiales metálicos de grano ultra-fino. Se ha demostrado que el estado tensional, “stress triaxiality”, influye considerablemente en los mecanismos que operan durante la deformación plástica en el cobre puro comercial (CP Cu, por sus siglas en inglés) de grano ultra-fino. Asimismo, estos mecanismos de deformación están determinados por el estado tensional. La microestructura del CP Cu de grano ultra-fino podría diseñarse de modo que su “stretching formability” supere incluso a su homólogo de grano grueso. En el presente trabajo se analiza el efecto de la textura metalográfica y cristalográfica del CP Ti de grano ultra-fino. Se ha comprobado que su “stretching formability” se adecúa a las exigencias de los procesos industriales de conformado. Por otro lado, los dispersoides gruesos y las partículas fracturadas en una aleación de aluminio Al 2024 limitan su “formability” al actuar como lugares preferentes para la nucleación de fisuras, promoviendo entonces el fallo de la muestra en las etapas iniciales de deformación. En base al análisis de los resultados experimentales, se realiza una propuesta general para mejorar la habilidad al conformado de materiales metálicos de grano ultra-fino.

PREFACE

This PhD thesis is based on the work carried out at IMDEA Materials Institute (Madrid, Spain) under the supervision of Dr. Ilchat Sabirov. This PhD thesis was performed in co-operation with UNIPRESS, Institute of High Pressure Physics of the Polish Academy of Sciences (Warsaw, Poland) and a research group at the Department of Physics of Carlos III University of Madrid (Madrid, Spain) in frames of the European project LIMEDU (FP7 ERA-NET MATERA+ 2009, Project No. MATERA/ESM-1889) funded by the Fundacion MADRI+D and by the National Centre for Research and Development (Project NCBIR/ERA-NET MATERA+ /03/ 2011).

This work has led to three peer-reviewed manuscripts which have been published, one submitted manuscript and two more under preparation by the moment of submission of this PhD thesis:

E.C. Moreno-Valle, W. Pachla, M. Kulczyk, B. Savoini, M.A. Monge, C. Ballesteros, I. Sabirov. "Anisotropy of uni-axial and bi-axial deformation behaviour of pure Titanium after hydrostatic extrusion*" Material Science and Engineering A* 588 (2013) 7–13.

E.C. Moreno-Valle, M.A. Monclus, J.M. Molina-Aldareguia, N. Enikeev, I. Sabirov, *"*Bi-axial deformation behavior and enhanced formability of ultrafine-grained pure copper" *Metallurgical and Materials Transactions A* 44 (2013) 2399-2408.

E.C. Moreno-Valle, I. Sabirov, M.T. Perez-Prado, M.Yu. Murashkin, E.V. Bobruk, R.Z. Valiev. "Effect of the grain refinement via severe plastic deformation on strength properties and deformation behavior of an Al6061 alloy at room and cryogenic temperatures" *Materials Letters* 65 (2011) 2917–2919.

E.C. Moreno-Valle, M.A. Monclus, J.M. Molina-Aldareguia, I. Sabirov, M.Kulczyk, J. Skiba, W. Pachla. "Effect of annealing treatment and temperature on formability of ultra-fine grained commercially pure Titanium" *Material Science and Engineering A* (2014) Submitted.

TABLE OF CONTENTS

LIST OF ABBREVIATIONS AND SYMBOLS

AFM	Atomic Force Microscopy
AR	As-received
ARB	Accumulative Roll Bonding
CG	Coarse Grained
COA	Crack Opening Angle
CP	Commercially Pure
CR	Cryorolling
CTOD	Crack Tip Opening Displacement
DEM	Digital Elevation Model
ECAE	Equal Channel Angular Extrusion
ECAP	Equal Channel Angular Pressing
FCC	Face-Centered Cubic
HAGB	High Angle Grain Boundary
HCP	Hexagonal Close Packed
HE	Hydrostatic Extrusion
HPT	High Pressure Torsion
L-	Longitudinal
LAGB	Low Angle Grain Boundary
NS	Nanostructured
RS	Rotary Swaging
RT	Room Temperature
SAED	Selected Area Electron Diffraction
SEM	Scanning Electron Microscopy
SPD	Severe Plastic Deformation
T-	Transversal
TEM	Transmission Electron Microscopy
UFG	Ultra-fine Grained
E	Young's Modulus
ϑ	Poison Ratio
σ_y	Yield Stress
$\sigma_{0.2}$	0.2% Proof Strength
σ_{UTS}	Ultimate Tensile Strength
m	Strain rate sensitivity
n	Strain Hardening Coefficient
ε	True Strain
ε_U	Uniform Elongation
ε_f	Elongation To Failure
F_{max}	Maximum Punch Load
h_{max}	Maximum Central Deflection
J_i	J-integral
R_{tot}	Crack Growth Resistance

TABLE OF FIGURES

1 INTRODUCTION

1. INTRODUCTION

Improving mechanical strength of metallic materials without degradation of their ductility and formability properties is a highly topical subject due to their wide application in all engineering sectors [1]. It is well known that manipulating the microstructure via grain refinement down to ultra-fine or nanoscale is an excellent method for enhancing mechanical properties in order to enable more effective exploitation of the metallic materials. Severe plastic deformation is an extensively strengthening method because it involves an effective microstructure refinement in metallic materials down to ultra-fine and nanoscale [2,3,4,5]. Despite significant body of experimental and theoretical research on mechanical properties and deformation behaviour of ultra-fine grained (UFG) and nanostructured (NS) metallic materials exists in literature, their formability has not been studied in details yet.

In this brief introduction, the most effective methods for processing of UFG and NS metallic materials are presented and their effect on the microstructure is considered. The main strengthening strategies in the UFG and NS metallic materials are shortly overviewed, and deformation mechanisms along with the main strategies to improve tensile ductility of these metals are outlined. Current state of the art in fracture behaviour of the UFG and NS metallic materials and their potential for commercialization in various sectors of engineering is presented. Finally, the importance of research on formability of UFG and NS metallic materials is demonstrated.

1.1. Fabrication of UFG metallic materials

There are two main processing routes to obtain bulk UFG or NS metallic materials. They can be synthesized either by consolidation of nanocrystallites (so called 'bottom-up' approach) or by breaking down the coarse-grained microstructure into crystalline cells with ultra-fine or nano size (so-called 'top-down' approach). Both 'bottom-up' and 'top-down' approaches to processing of bulk UFG and NS metallic materials have received considerable attention and development in the last 25 years [6]. Powder milling at cryogenic temperatures with further consolidation of the powders [7] is a nice illustration of the 'bottom-up' approach. A well-known example of the 'top-down' approach is grain refinement by severe plastic deformation (SPD) techniques [2]. By

imposing SPD into samples, coarse microstructure is refined into ultra-fine or nano crystallites. Since the first work in this field [8], SPD techniques have advanced to becoming the most developed grain refinement techniques. The main advantage of SPD techniques is their applicability to nearly all metallic materials. Nowadays, from a practical point of view, SPD of bulk billets appears to be the most promising processing route for manufacturing UFG and NS metallic materials for various industrial applications.

In comparison with the bottom-up approach, SPD processing has also other advantages. The final workpiece is fully dense with lack of the usual porosity and contamination typical for the NS materials processed via bottom-up approach. The most common SPD methods are equal channel angular pressing (ECAP), high pressure torsion (HPT), accumulative roll bonding (ARB), cryorolling and hydrostatic extrusion (HE).

It should be also noted that various SPD processes can be combined for further improvement of mechanical properties: for example, ECAP was combined with cold extrusion [9,10], cold rolling [11] and HE [12]. A change of deformation path implies additional refinement of the microstructure [3,13]. Subsequently, it can significantly affect the mechanical properties. Data on mechanical properties of some high strength UFG and NS light metals and alloys are presented in Table 1.

Table 1. Data on mechanical properties of some light metals and alloys showing high mechanical strength ($\sigma_{0.2}$ is the 0.2% proof strength, σ_{UTS} ultimate tensile strength, ε_U uniform elongation, ε_f elongation to failure).

Material	Processing method	Grain size (nm)	$\sigma_{0.2}$ (MPa)	σ_{UTS} (MPa)	ε_u (%)	ε_f (%)	Ref.
AA7075	HPT	22	978	1010	5.0	9.0	[5]
AA6061	HPT	100	660	690	~2.7	5.5	[14]
AA2024	Cryorolling + aging	800	580	630	13.0	18.0	[15]
Pure Ti (Grade 4), Longitudinal direction	ECAP+swaging+ drawing	200	1220	1280	3.7	10.1	[16]
Pure Ti (Grade 4), Transverse direction	ECAP+swaging+ drawing	200	600	1170	6.6	11.8	
Pure Ti (Grade 2)	HE	47	1245	1320	1.8	7.5	[17]
Ti-6Al-4V	ECAP+extrusion+ annealing	250	1310	1370	4.0	12.0	[18]
ZE41A	ECAP	1500	270	315	-	14	[19]
AZ31B	ECAP	1000-4000	350	500	-	15	[20]
AZ31	ECAP	370	372	445	-	9.7	[21]

1.2. Most widely used SPD methods and their effect on the microstructure

There are numerous techniques developed up to date for SPD processing of metallic materials and the detailed list of all those techniques can be found in [22]. In this section, the most widely used SPD methods are described and microstructure evolution during SPD processing is shortly overviewed.

1.2.1. Equal Channel Angular Pressing

Equal channel angular pressing (ECAP), also known as equal channel angular extrusion (ECAE) imposes large plastic deformation on a billet by simple shear. The billet is pressed through a special die which has two intersecting channels at an angle typically in the range of 90º-120º (Figure 1). Cross section of both channels is the same, thus the billet can be subjected to several ECAP passes in order to increase total

strain induced into the billet. Moreover, this method enables rotation of the billet between passes so different slip systems can be activated during plastic deformation of the billet, thus leading to formation of more homogeneous UFG microstructure.

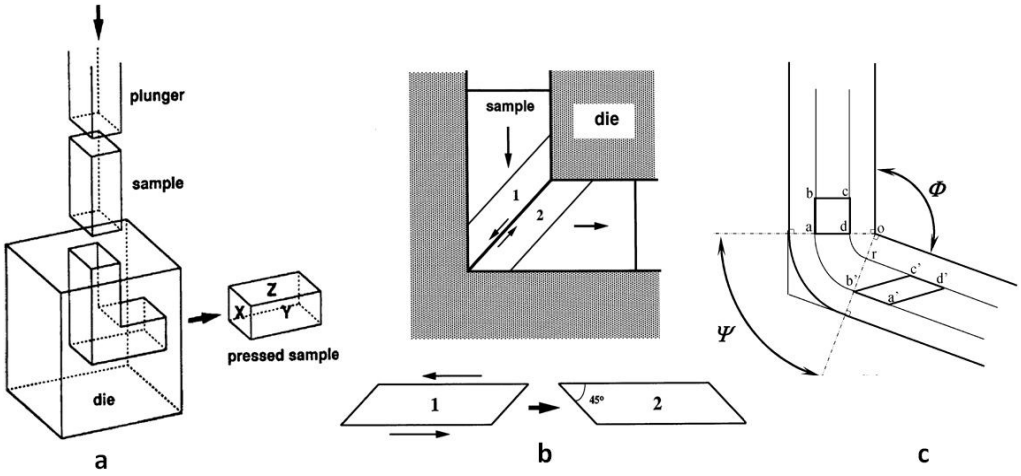

Figure 1. Schematic drawing of ECAP processing: (a) typical ECAP facility (b) shearing plane within the die: the elements numbered 1 and 2 are transposed by shear as indicated in the lower part of the illustration. (c) Principal geometrical parameters of die [3].

The equivalent plastic strain imposed by ECAP can be estimated according to Equation 1 where ***N*** is the number of passes, $\boldsymbol{\varphi}$ the intersection angle of two channels and $\boldsymbol{\psi}$ the angle subtended by the arc of curvature at the intersection point (Figure 1 c) [3].

$$\varepsilon = \frac{N}{\sqrt{3}}\left(2\,cot\left(\frac{\varphi}{2}+\frac{\psi}{2}\right)+\psi\,cosec\left(\frac{\varphi}{2}+\frac{\psi}{2}\right)\right) \qquad \textbf{Equation 1}$$

Various deformation routes so-called A, B_A, B_C and C describe each strain path. The billet is introduced into the die without rotation between passes in A route. B_A route turns the sample 90º in alternate directions. B_C route consists of rotating the sample by 90º always in the same direction between ECAP passes. Billets are rotated by 180º in C route. These processing routes can activate different slip systems by the rotation of the billet in order to refine the microstructure to higher homogeneity degree (Figure 2).

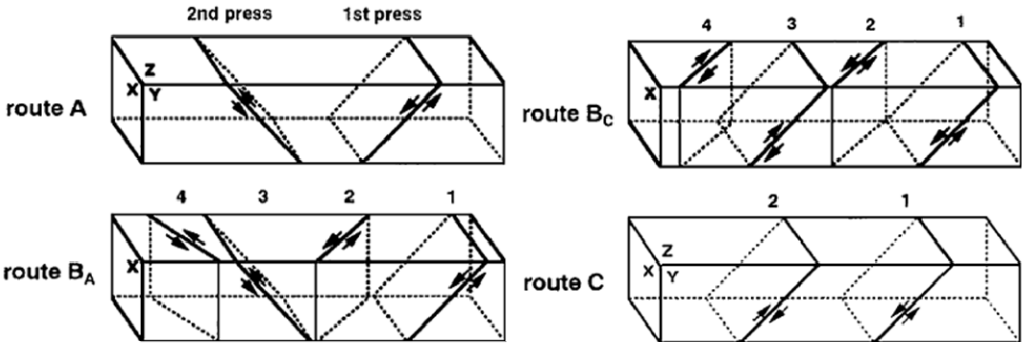

Figure 2. Slip systems view on X,Y,Z planes for consecutive passes using processing routes A, B_A, B_C and C [3].

Preliminary observations at the macroscopic level require to define the orthogonal planes of the ECAP processed billet as X the perpendicular plane to flow direction, Y the flow plane parallel to the side face at the exit point from the die and Z the longitudinal plane parallel to top surface at the exit point from the die (Figure 1 a). After the first ECAP pass, grains on X plane are elongated parallel to Y direction and flattened in Z direction. Grains on Y plane are elongated in an inclined direction, 20-30º with respect to X direction. While an inspection on Z plane reveals that there are no significant changes in microstructure, grains maintain their equiaxed shape with some slip along Y direction. A microscopic observation reveals that mostly low angle grain boundaries (LAGBs) are present in the microstructure as well as bands of subgrains on each plane. However, as number of ECAP passes is increased, the dislocation structure becomes more homogeneous leading the transition from LAGBs to high angle grain boundaries (HAGBs). Consequently, subgrain bands might evolve to equiaxed ultra-fine grains with well-defined grain boundaries with the assistance of dynamic recovery.

It was experimentally demonstrated that B_C is the most effective processing route for producing equiaxed ultra-fine grains in the FCC metals such as pure aluminium [23,24,25,26], aluminium-based alloys [27,28,29] (Figure 3), pure copper and its alloys [30,31] and HCP metals as Ti [32], etc.

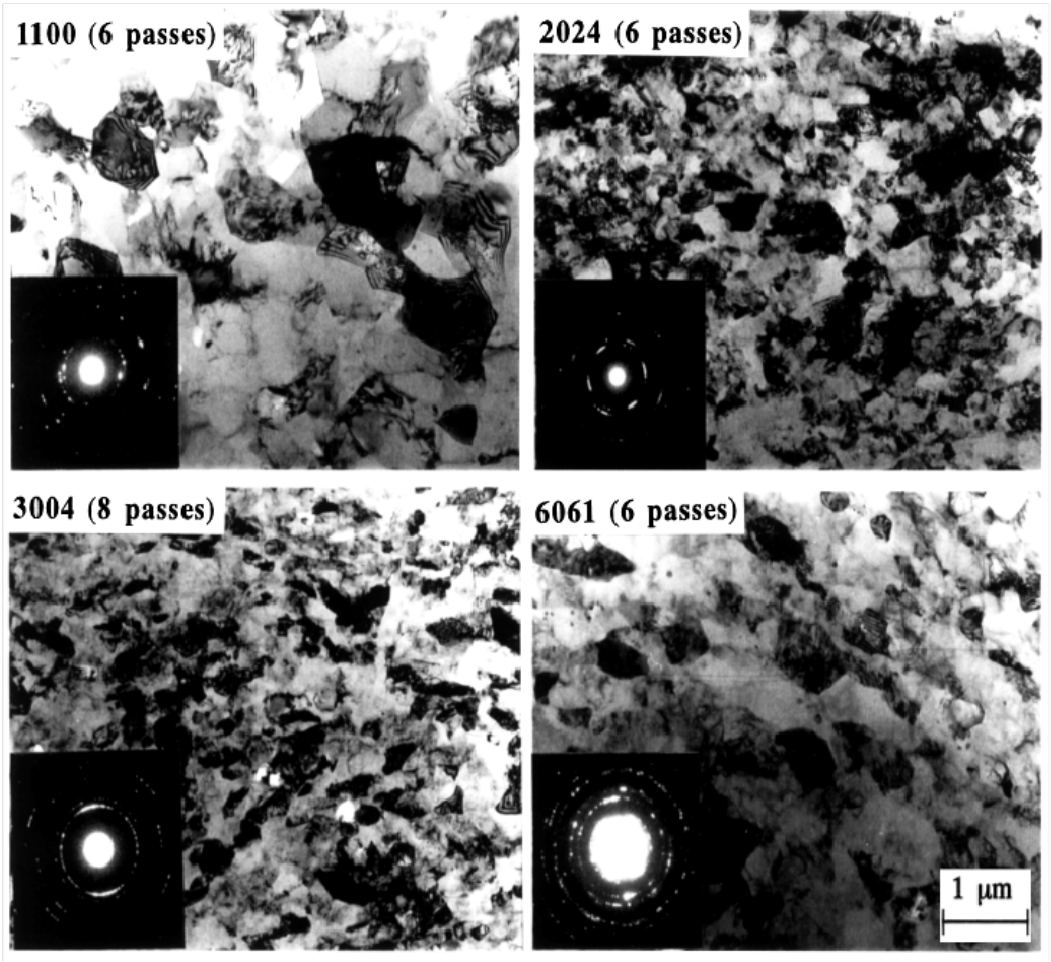

Figure 3. Typical microstructures after ECAP processing via B_C route: Al 1100 alloy after 6 passes, Al2024 alloy after 6 passes, Al3004 after 8 passes and Al 6061 alloy after 6 passes [29].

The ECAP processing technique has been successfully applied even to hard to deform Mg and Mg alloys. A multiple-temperature complex ECAP processing route, consisting of consecutive extrusions at different temperatures and speeds, was developed for a commercial AZ31 Mg alloys [21]. It led to formation of a very homogeneous UFG microstructure with the average grain size of 370 nm (Figure 4) showing very high mechanical strength (0.2% proof strength of 372 MPa) (Table 1).

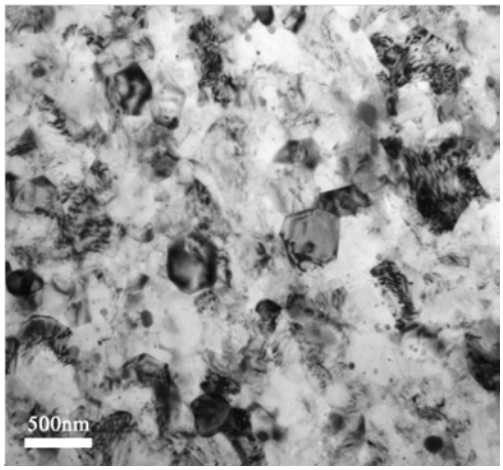

Figure 4. TEM image showing UFG-microstructure of AZ31 Mg alloy after multiple-temperature ECAE processing [21].

1.2.2. High Pressure Torsion

High pressure torsion (HPT) is a potential tool for grain refinement thanks to imposed simultaneously high pressure and torsion deformation. Typically, a disk is placed between two anvils while one of them rotates under pressure of several GPa (Figure 5). Workpieces are deformed by pure shear. HPT processing is very effective in reducing grain size since very high strains can be induced into disks without any crack formation due to very high applied pressure. Two main shortcomings can be noted for the HPT method: (1) Only small disks can be processed using this technique. The dimensions of the HPT disks are usually determined by the maximum pressure that can be applied to the disk during HPT processing. For the maximum pressure of 40 tons, disks usually have a diameter of 8 mm and a thickness of ~1 mm, though larger disks can be processed if higher loads can be applied. Cylindrical bulk samples of an UFG Al-Mg-Sc alloy were also successfully processed with a height of 8.57 mm [33]. However, the inhomogeneity of the microstructure along the height appears as a problem. Thus, processing of bulk samples using HPT technique is still at the early stages of development. (2) The second shortcoming of the HPT method is inhomogeneous strain induced into disk along the disk radius leading to inhomogeneous microstructure and properties along the disk radius. The equivalent true strain imposed by HPT processing is calculated using Equation 2 where N is number of revolutions, r is radius of the disk, h_0 and h are the initial and final thickness, respectively [4].

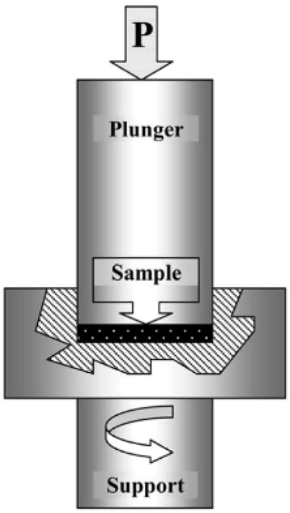

Figure 5. Schematic drawing of HPT facility [4].

$$\varepsilon = ln\left(\frac{2\pi N r h_0}{h^2}\right)$$ **Equation 2**

Non-homogeneous distribution of hardness along disk radius due to inhomogeneous microstructure in the processed disks is demonstrated on Figure 6. Periphery area of disk shows higher values of hardness being theoretically zero just at the centre of the disk, ***r*** = 0 (Equation 2). However, by increasing HPT turns, grain refinement saturates at periphery of the disk while grain refinement continues at the disk centre thus saturating microstructure and hardness along the disk [4].

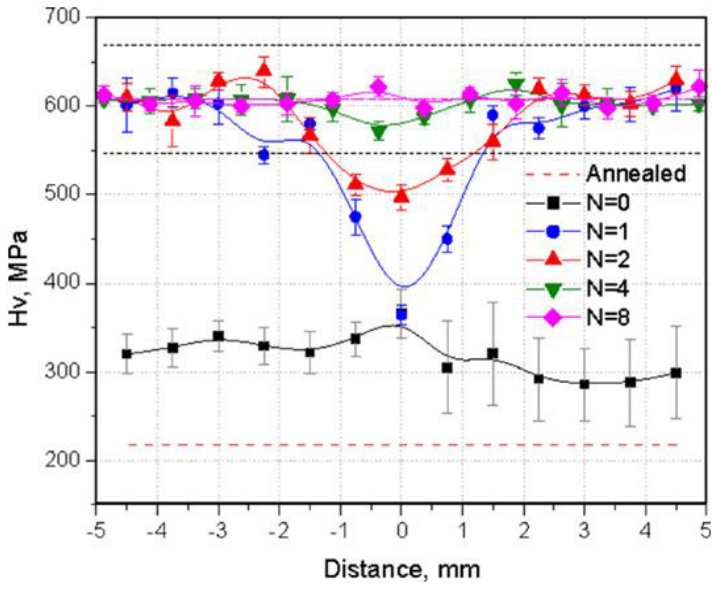

Figure 6. Microhardness distribution across the diameter of pure aluminum disks subjected to pressure of 1GP up to 8 revolutions [4].

Detailed description of the microstructure evolution during HPT processing can be found in [34]. Generally, HPT introduces very high density of crystal defects (dislocation and vacancies). At low strains, subgrain structure with dislocation walls is formed due to dislocation arrangement. Misorientation of these LAGBs increase with increasing strain due to absorption of dislocations by grain boundaries, and thus, LAGBs transform into HAGBs. Finally, a uniform microstructure with ultra-fine or even nano grains containing predominantly HAGBs is formed. For example, microstructure of a solution treated Al7075 after HPT processing at room temperature for 5 turns consists of nanoscale grains (average size of 26 nm) and high dislocation density (marked by "T") appearing in both grain interiors and near grain boundary regions (Figure 7). The FCC solid solution is also observed to be free of precipitates, as revealed by the selected area electron diffraction (SAED) patterns in the lower left panel (Figure 7 a). The final microstructure is determined mainly by the HPT processing temperature and strain. The final grain size is generally in the range of ~100-300 nm for aluminium, copper and its alloys [35,36,37] as well as for pure Ti and Ti-based alloys [38,39,40]. Mg based alloys were also satisfactory processed by HPT achieving significant grain refinement whereas this is not easy by ECAP processing [41].

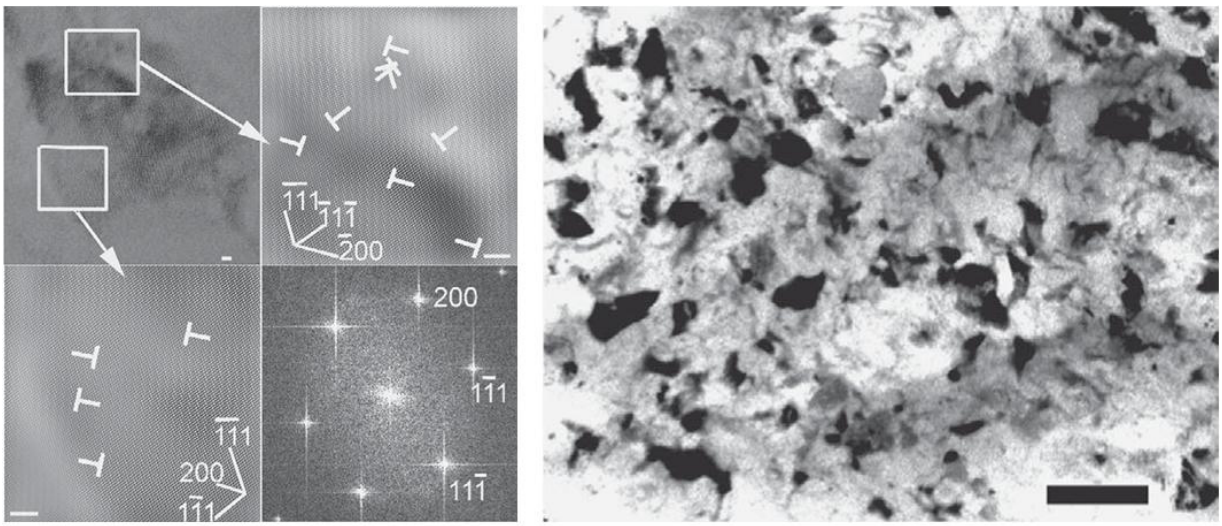

Figure 7. TEM images of microstructure of a solution treated Al7075 after HPT processing: (a) high-resolution TEM. Scale bar is 2 nm; (b) bright-field image. Scale bar is 100 nm [5].

1.2.3. Accumulative Roll Bonding

Accumulative roll bonding (ARB) was proposed in order to fulfil the need in NS materials in form of sheets which could be produced by using conventional rolling facilities (Figure 8). In ARB, sheets are rolled to a certain thickness reduction. Afterwards, they are cut in two halves and both halves are stacked together after a previous degassing stage and surface treatment. Then this process of rolling, cutting and stacking is repeated up to large cumulative strain. Equation 3 describes strain imposed into sheet, where ***N*** is the number of cycles, t_0 and ***t*** the initial and the final thickness of sheet, respectively [22].

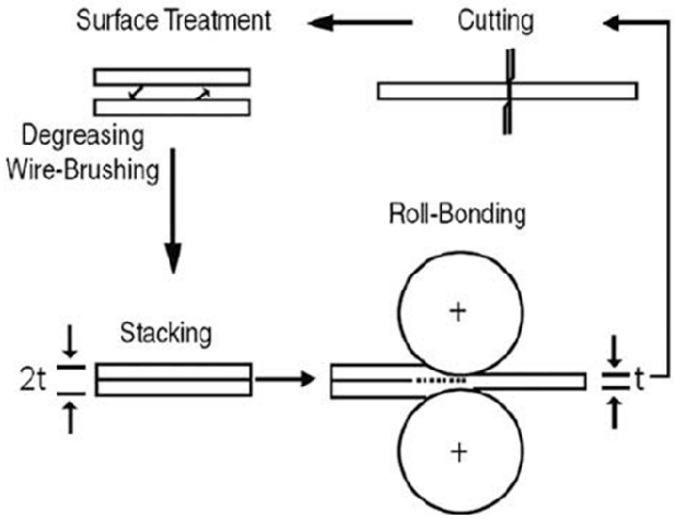

Figure 8. Schematic drawing of ARB process [42].

$$\varepsilon = N\frac{2}{\sqrt{3}} ln\left(\frac{t_0}{t}\right) \qquad \textbf{Equation 3}$$

Examples of effective grain refinement in various metallic materials using ARB can be easily found in literature. After eight ARB cycles, commercially pure (CP) Cu showed a homogeneous UFG microstructure with the average grain size of 180 nm and containing predominantly HAGBs [42]. ARB processing led to formation of homogeneous UFG microstructures with the average grain size of 670 nm in pure Al [43], 280 nm in an Al-Mg alloy and 420 nm in the interstitial-free steel [44]. For instance, the microstructure analysis of an Al7075 alloy during ARB processing to different true strains [45] showed a evolution from a microstructure with cells and high density of dislocations forming tangles after 1 cycle (Figure 9 a) to one composed by equiaxed

grains of an average size of 350 nm, sharp boundaries and low dislocation density after 5 cycles (Figure 9 d). After 3 cycles, cells boundaries were already well defined and dislocation density was lower (Figure 9 b). The saturation of the microstructure after 4 ARB passes was observed, ARB was also found as a successful technique for production of the UFG metal-matrix composites with ceramic nanoparticles [46] and for synthesis of Ti/Al multilayered composite, mainly composed of ultrafine equiaxed grains with a mean size of 200–300 nm [47].

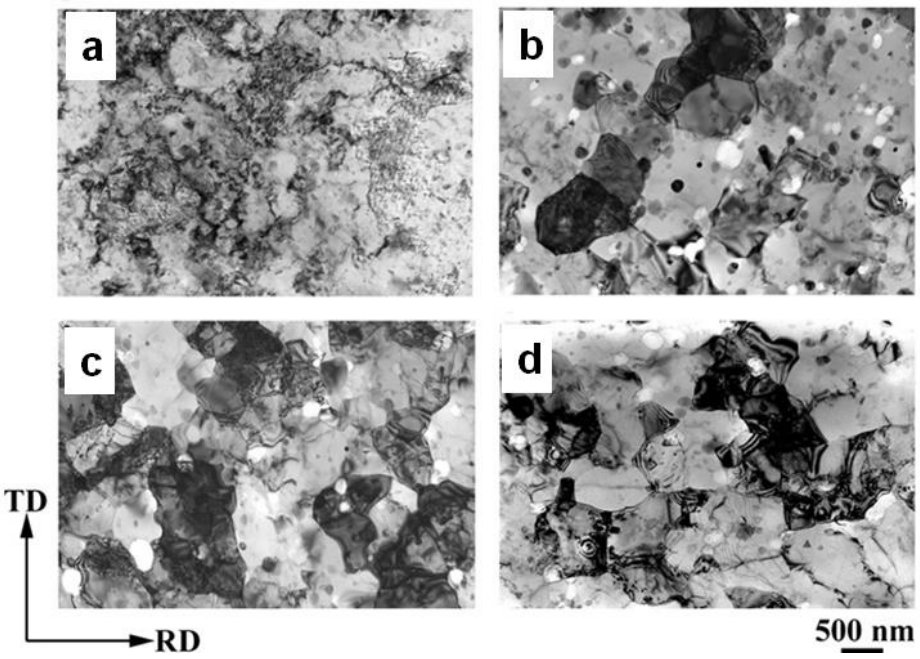

Figure 9. Microstructure evolution of an Al 7075 alloy after ARB processing up to (a) 1 pass; (b) 3 passes; (c) 4 passes and (d) 5 passes [45].

1.2.4. Cryorolling

Cryorolling can be defined as rolling that is carried out at cryogenic temperatures. In cryorolling, the strain hardening is retained up to the extent to which rolling is carried out. This implies that there will be no dislocation annihilation and dynamic recovery, whereas in rolling at room temperature, dynamic recovery is inevitable and softening takes place. During cryorolling, dense dislocation walls are first formed dividing the coarse grains into subgrain structure and containing mainly LAGBs. Observed subgrains are elongated in the rolling direction as parallel bands with poorly defined grain boundaries (Figure 10). Further deformation increases the volume fraction of the non-equilibrium grain boundaries. Equiaxed dislocation-free subgrains (marked by

squares in Figure 10 b) coexist with elongated grains with dislocations inside (marked by a circle in Figure 10 b). Finally, equiaxed UFG microstructure with well defined grain boundaries is formed with a subsequent suitable annealing treatment [48].

The equivalent plastic strain for each pass of rolling can be estimated according to Equation 4, where h_0 and h are the initial and final thickness, respectively [48].

$$\varepsilon = \frac{2}{\sqrt{3}} ln \left(\frac{h_0}{h}\right) \qquad \textbf{Equation 4}$$

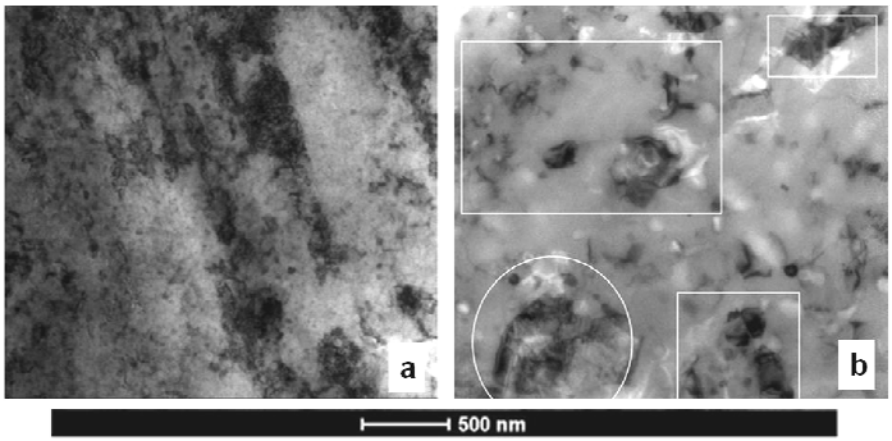

Figure 10. TEM micrograph of a cryorolled Al 7075 alloy at (a) true strain of 2.3; (b) true strain of 3.4 [49].

Cryorolling was successfully employed for grain refinement in a wide range of materials. Solid-solution treated Al2024 alloy after cryorolling exhibited grain size between 400-800 nm and uniformly distributed nano precipitates that enabled a good combination of high strength and ductility [15]. Other UFG aluminium-based alloys were also produced by cryorolling: Al 7075 alloy [49,50] or Al 6063 alloy [51]. Even microstructure of CP Al could be refined down to ultra-fine scale despite of it is quite difficult for other SPD processing due to its high stacking fault energy [52]. CP Ti [53,54] with multimodal grain structure was successfully processed by cryorolling and subsequent annealing.

1.2.5. Hydrostatic Extrusion

Extrusion is a process used to create objects of a fixed, cross-sectional profile. A material is pushed or drawn through a die of the desired cross-section. In the

hydrostatic extrusion (HE) process the billet is completely surrounded by a pressurized liquid, except where the billet contacts the die. This process can be done hot, warm, or cold, however the temperature is limited by the stability of the fluid used. The process must be carried out in a sealed cylinder to contain the hydrostatic medium. The advantages of this process include: 1) No friction between the container and the billet reduces force requirements. This ultimately allows for faster speeds, higher reduction ratios, and lower billet temperatures. 2) Usually the ductility of the material increases when high pressures are applied. 3) An even flow of material. 4) Large billets with large cross-sections can be extruded.

In comparison with other SPD methods, HE usually requires lower total strain for grain refinement due to very high strain rates of the process, generally larger than $10^2 s^{-1}$. HE has high potential to obtain a variety of shapes such as rods, wires or bars with complex shape cross section. However, workpiece temperature might be so elevated that a proper cooling system is required at the die exit. Equation 5 describes true strain imposed into rod where d_0 and d are the initial and final diameter of extruded rods respectively [55].

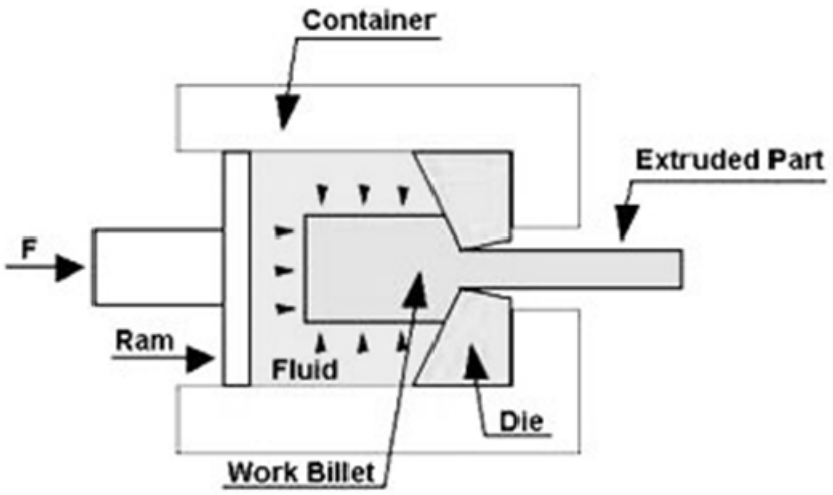

Figure 11. Schematic drawing of HE facility.

$$\varepsilon = 2\, ln\left(\frac{d_0}{d}\right) \qquad \textbf{Equation 5}$$

HE processing often results in formation of lamellae microstructure aligned along extrusion axis, as it was seen on longitudinal section of extruded bars for an Al 2017 alloy [56,57] and CP Ti (grade 2) [58] after HE. This lamellae-type microstructure is

segmented into subgrains with high dislocation density and consequently LAGBs. After deformation to high strain level, the grain boundaries, that separate lamellas with different slip system, are straight and well defined having from medium to high misorientation. Homogeneous microstructure consisting of equiaxed ultrafine grains is observed on transversal section. Consecutive HE passes enables the increase of grain boundaries misorientation due to the easy recovery. Typical microstructures obtained by HE in various metallic materials are shown below (Figure 12). Equiaxed dislocation free grains were found in CP Al while dislocation cell structure was observed in CP Cu (Figure 12 a, c). The presence of alloy elements lead to more efficient grain refinement in aluminium alloys (Figure 12 b). In the case of stainless steel, nanotwins are clearly seen (Figure 12 e, f).

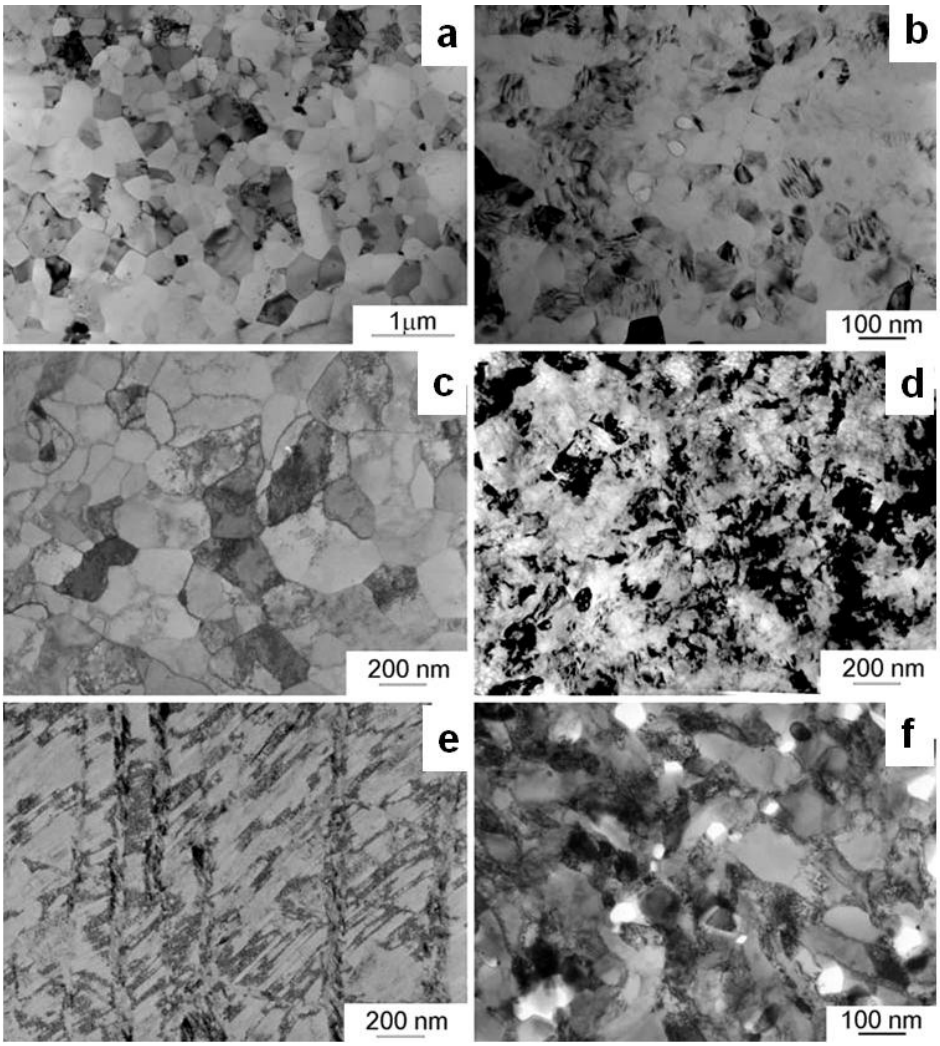

Figure 12. TEM micrographs of hydrostatically extruded with total true strain of 4 (a) aluminum; (b) Al2017; (c) copper; (d) titanium; (e) austenitic stainless steel and (f) Eurofer 97 steel [59].

In the specific case of CP Ti, mostly HAGBs are observed on both longitudinal and transverse sections after 20 HE passes with total strain of 5.47 (Figure 13) [17,58]. Bands of elongated grains are mainly observed on the microstructure on longitudinal section while homogeneous distribution of equiaxed grains of about 50-300 nm are predominant on transverse section. It was reported that further deformation did not imply finer grains. In contrast, there was a slight trend of grain coarsening while strain level was further increased.

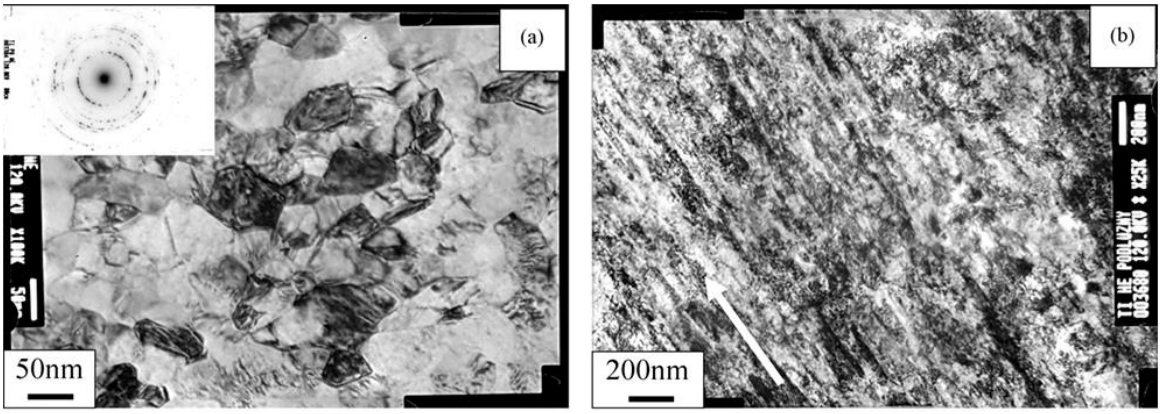

Figure 13. TEM micrographs and SAED pattern of CP Ti after 20 passes of hydrostatic extrusion (a) on transverse section; (b) on longitudinal section. Arrow marks extrusion direction [17].

1.3. Main strengthening mechanisms in metallic materials

Mechanical strength of a conventional polycrystalline metal is controlled by dislocation motion restriction. Generally, pure metals can be strengthened by introduction of obstacles to the glide of dislocations. Any inhomogeneity in the microstructure can act as such an obstacle. Introduction of solute atoms in the metal matrix was the first strengthening route for pure metals [60]. The introduction of solute atoms into solid solution in the solvent-atom lattice produces an alloy which is stronger than the pure metal due to the differences in the radius, modulus and valence between the matrix and solute atoms [61]. The solute must have appreciable solid solubility in the matrix at annealing temperature, remain in the solid solution after a slow cool, and not be removed by reacting with other elements in the alloy. Later it was found that deformation processing of metals and alloys (forging) can also increase metals strength due to strain hardening effect [61]. Thus, dislocation strengthening came up as another

approach to improve strength properties of the Al alloys. The discovery of age hardening effect in Al-Cu alloys nearly century ago gave another efficient strategy to improve strength in age-hardenable alloys via precipitation effect [1]. The size, shape, volume fraction, and coherency of second phase precipitates determine the precipitation hardening of an alloy. These parameters usually depend on the concentration of solute atoms in the matrix, aging temperature and aging time. Hall and Petch in [62] and [63] established a relationship between grain size and yield strength in metallic materials showing an increase of strength with decreasing grain size. So grain size hardening appeared as a new strategy to improve strength of metallic materials. Extensive research on texture and anisotropy of mechanical properties yielded texture strengthening as an effective mechanism in metallic materials with HCP lattice [64]. This section shortly describes the strengthening mechanisms acting in the ultra-fine grained metallic materials as well as their contribution to strength. Superposition of different strengthening mechanisms in the ultra-fine grained metallic materials is also discussed at the end of this section.

1.3.1. Grain size hardening

In metallic materials, grain boundaries act as obstacles to the movement of dislocations which pile up near the grain boundaries. Therefore, the distance travelled by a glissile dislocation before reaching grain boundary decreases with decreasing grain size resulting in higher strength. This effect is referred to as grain size hardening (or strengthening). The yield strength ($\boldsymbol{\sigma_y}$) as a function of grain size ($\boldsymbol{d}$) is described by the well-known Hall-Petch relation [62,63] (Equation 6), where $\boldsymbol{\sigma_o}$ is the Peierls stress and $\boldsymbol{K}$ is the Hall-Petch coefficient. The $\boldsymbol{K}$ coefficient is usually determined experimentally, though it can be also calculated according to Equation 7, where $\boldsymbol{M}$ is the Taylor factor, τ_{CRSS} the critical resolved shear stress, and $\boldsymbol{r}$ the distance from the nearest dislocation piled-up to the dislocation source in the adjacent grain [62,63,65,66].

$$\sigma_y = \sigma_0 + \mathrm{K}\mathrm{d}^{-1/2} \qquad \textbf{Equation 6}$$

$$K = M^2 \tau_{CRSS} r^{1/2} \qquad \textbf{Equation 7}$$

Significant body of experimental research has shown that grain size hardening is the most effective strengthening mechanism in the UFG and NS metallic materials [67]. However, it should be noted that inverse Hall-Petch behavior can be observed in nanocrystalline metals as was reported for nanocrystalline Cu and Pd [68]. Investigations showed that in the NS metals with grain size below ~100 nm, grain boundary mediated mechanisms may start to play an important role in the plastic deformation degrading the grain size strengthening. So, the Hall-Petch slope ***K*** in Equation 7 is generally expected to decrease in metallic materials when grains are smaller than ~100 nm. This effect has been referred to as a negative deviation from the Hall-Petch law [65].

1.3.2. Solid solution hardening

The introduction of solute atoms into a crystal lattice invariably increases the strength of the material. The solid solution hardening is a result of an interaction between the mobile dislocations and the solute atoms. The most relevant mechanisms for substitutional alloying of metal are the elastic interactions due to [61]:

I. The size misfit, where the size of the solute atom differs from the size of the matrix atoms and creates a strain field around the atom

II. The modulus misfit, where the difference in binding force between the solute atoms and the matrix atoms results in a hard or soft “spot” in the matrix.

However, the interaction works, the presence of solute atoms increases the initial yield stress and reduces the dynamic recovery rate of dislocations. This results in a higher dislocation density, a higher work hardening rate and in a different dislocation structure. The solute strengthening, $\Delta\boldsymbol{\sigma_{ss}}$, is defined as function of solute atoms concentration, ***C*** (Equation 8) where ***H*** and ***n*** are constants. The parameter ***n*** can be in the range of 0.5-0.75 (Equation 8) [69].

$$\Delta\sigma_{ss} = HC^n \qquad \textbf{Equation 8}$$

It should be noted that Equation 8 might easily break down in the UFG and NS metals since it has been experimentally demonstrated that solute atoms tend to form segregations and clusters in these materials [70]. These clusters cause even more

distortion in lattice increasing internal energy of alloy. The contribution of the clusters was estimated by Equation 9 where γ_{SRO} is the change in energy per unit area on slip planes, ΔH_{A-B}, the enthalpy of the nearest neighbour bond, y_A, the amount of A atoms in the co-clusters, y_B, the amount of B atoms in the co-clusters, x_A, the amount of A atoms in the Al-rich phase, x_B, the amount of B atoms in the A-rich phase [71].

$$\Delta\tau_{SRO} = \frac{\gamma_{SRO}}{b} = \frac{\Delta H_{A-B}}{b^3} \times \frac{4}{\sqrt{3}}\left[\frac{2}{3}(y_A + y_B) - \left(\frac{2}{3}x_B y_A + \frac{2}{3}x_A y_B + 2x_A x_B\right)\right] \quad \textbf{Equation 9}$$

Segregation of solute atom clusters along grain boundaries of Cu and Al alloys during their SPD processing at low temperatures was experimentally demonstrated using 3D atom probe tomography technique [14,72,73,74]. These clusters of solute atoms might also inhibit dislocation nucleation at grain boundaries being another strengthening factor [75,76].

1.3.3. Precipitation hardening

Precipitation hardening has been widely used for strengthening of various alloys. It is well known that fine precipitates retard dislocation movement since dislocations are not able to overcome precipitates unless there are sharp changes in curvature of dislocation line. Moreover, in the case of dislocation passed precipitate, higher stress level would be required to apply. The residual stresses field - attraction and repulsive interactions between glissile dislocations and semicoherent particles demonstrated by in-situ experiments [77] - contributes effectively to hinder dislocations motion. A homogeneous distribution of nanosized coherent, incoherent and semicoherent precipitates enables dislocation trapping and their accumulation in the grain interior, as well as contributes to thermal stabilization of UFG and NS microstructures [78]. Although precipitation strengthening usually involves loss of ductility, UFG Al and Cu alloys produced via SPD showed improved ductility [15,79,80] due to their increased strain hardening ability. It was demonstrated that a proper annealing treatment to a solutionised Cu-Cr-Zr alloy prior SPD processing enables the precipitation of nanosized Cr particles which are able to trap dislocations leading to a greater microstructure refinement [81].

Aging time and temperature are key parameters for microstructural design in order to obtain optimal precipitation strengthening, since they determine size, shape and volume

fraction of precipitates. Contribution of precipitation strengthening can be calculated according Orowan equation (Equation 10) where ***L*** is the effective interparticle spacing, ϑ Poisson ratio, ***G*** shear modulus, ***D*** the planar diameter of the precipitate particles and ***b*** Burgers vector [82,83].

$$\Delta\sigma_{prec} = \frac{0.4MGb}{\pi L\sqrt{1-\vartheta}} \ln\left(\frac{D}{b}\right) \qquad \textbf{Equation 10}$$

It should be noted that precipitation kinetics of the UFG and NS alloys is different compared to that of their coarse-grained counterparts. For example, complex phase transformations can take place during SPD processing of Al alloys at room temperature and elevated temperatures, such as nucleation of second phase precipitates, their growth, fragmentation, or dissolution [80,84,85,86,87]. Microstructure formed during SPD is usually characterized by increased dislocation and vacancy density and increased volume fraction of grain boundaries leading to increased effective diffusion coefficient. This results in accelerated precipitation kinetic as the latter is controlled by diffusion of solute atoms [88]. Evolution of second phase precipitates during ECAP processing of the Al 7136 alloy at 200ºC was found to be 50 times faster than during conventional aging treatments at the same temperature [88]. The high density of mobile dislocations produced by ECAP promoted the dissolution of small metastable precipitates and the formation of large η precipitates by coalescence. It has been experimentally demonstrated that the precipitation kinetics during post-SPD aging is accelerated, as well [89,90,91]. Again, this effect has been related mainly to high dislocation density (where dislocations act as sites for nucleation of precipitates) and to enhanced diffusion accelerated by the high initial vacancy flux. The contribution of the precipitation hardening into strength of the UFG metallic materials can be significant. For instance, post-processing aging of a solution treated and cryo-rolled Al 2024 alloy at 100ºC for 100 h led to (i) a slight grain growth, (ii) a decrease of dislocation density due to recovery, (iii) formation of high density of nanosized S'-precipitates in the microstructure. Generation of these nanosized S´-precipitates not only compensated for the strength decrease caused by the grain growth and dislocation density decrease, but even further increased the strength by 12.4% [15].

1.3.4. Dislocation strengthening

Presence of a high density of dislocations in the grain/subgrain interior or from dislocation boundaries can also significantly increase strength of metallic materials. This type of strengthening is typical for SPD processed metallic materials with microstructure containing high dislocation density and high volume fraction of LAGBs. Such microstructures can be obtained via SPD processing to low strains, i.e. ECAP processing at room temperature for 1-2 passes [92,93,94], cryorolling [49,95]. For instance, it was demonstrated that ECAP processing by a single pass at room temperature of the solid-solution treated Al-Zn-Mg alloy increases its strength by ~10-40% compared to the strength of the naturally aged non-processed material [92].

Strengthening contribution of dislocations can be estimated by Equation 11, where $\boldsymbol{\rho_{dis}}$ is the dislocation density accumulated in LAGB (i.e. geometrically necessary dislocations), $\boldsymbol{\rho_0}$ the density of dislocations between boundaries (i.e. statistically stored dislocations), $\boldsymbol{b}$ the Burgers vector, $\boldsymbol{G}$ the shear modulus, $\boldsymbol{\alpha}$ a parameter and $\boldsymbol{M}$ the Taylor factor [96]. Likewise, density of geometrically necessary dislocations can be calculated using Equation 12, where $\boldsymbol{S_v}$ is the boundary area per unit volume and $\boldsymbol{\theta}$ the boundary misorientation angle.

$$\sigma_{dis} = M\alpha G b\sqrt{\rho_o + \rho_{dis}} \qquad \textbf{Equation 11}$$

$$\rho_{dis} = \frac{1.5 S_v \theta}{b} \qquad \textbf{Equation 12}$$

1.3.5. Texture strengthening

SPD processing of metallic materials often leads to formation of a strong crystallographic texture since crystallographic planes are prone to orient towards direction of maximum strain during processing. The preferred orientation is strongly related to slip and twinning systems available as well as amount of strain imposed [97].

Wires, rods and bars of a FCC metal develop a double fibre texture with both $\langle 111 \rangle$ and $\langle 100 \rangle$ directions parallel to the working axis. In the case of HCP metals (Ti and Mg) the basal plane mainly turns to be parallel to direction of extrusion. Mechanical, physical and chemical properties of metals depend on crystallographic orientation or in other

words they depend on the orientation of the main slip systems (Figure 14). This was demonstrated for pure Ti subjected to ECAP [32] or to a complex deformation route as ECAP, swaging and drawing [16] where ductility was found to be lower in the extrusion direction (Figure 14). The low yield stress is typically observed if the main slip system is oriented at 45º with respect to the loading axis resulting in the highest Schmid factor, S=0.5 [98]. The yield stress increases with increasing/decreasing angle and can reach maximum when the main slip plane is parallel or perpendicular to the loading axis that results in a very low Schmid factor [98].

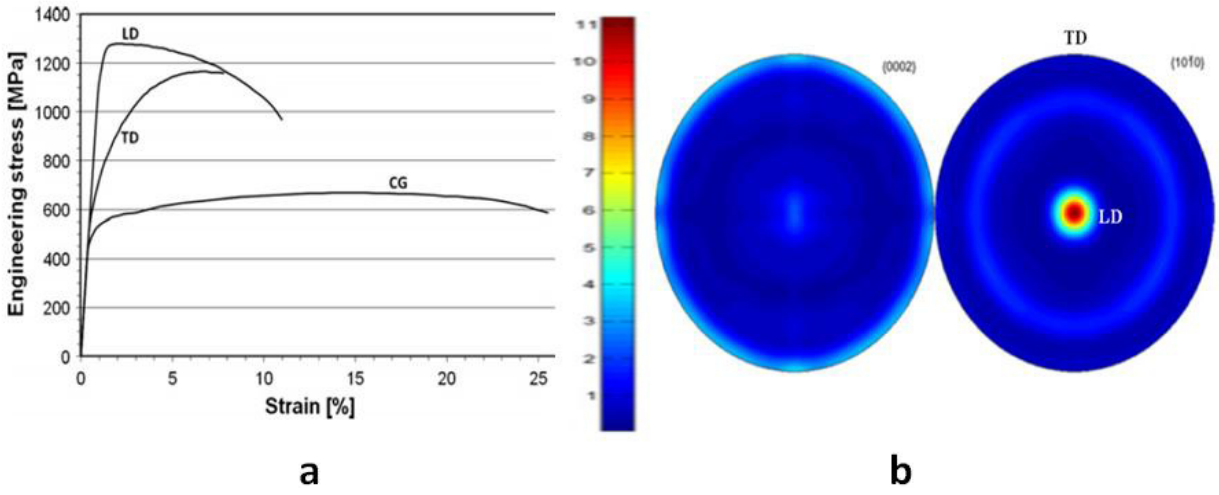

Figure 14. (a) Engineering stress - strain curves from tensile testing of UFG Ti (Grade 4) produced via complex SPD route (ECAP-swaging-drawing); (b) pole figures from texture measurements of the material. LD - longitudinal direction, TD - transverse direction. The images are reproduced from [16].

1.3.6. Superposition of strengthening mechanisms in the UFG metals and alloys

Typically, a few strengthening mechanisms contribute to strength of the UFG metals and alloys. Contributions from different strengthening mechanisms are often taken to be additive assuming that they act independently, and the total strength of the UFG metals, $\boldsymbol{\sigma}$, is estimated as Equation 13 [66,67,91] where $\boldsymbol{\sigma_0}$ is friction stress or, so-called, Peierls-Nabarro stress.

$$\sigma = \sigma_0 + \sigma_{GS} + \sigma_{dis} + \sigma_{TS} + \sigma_{SS} + \sigma_{prec} \qquad \textbf{Equation 13}$$

It might be wrongly assumed that each hardening factor contributes to the total strength separately. They are closely linked with each other and contribution of one of the hardening factors very often can increase only at the expense of contribution of other factors. An example is the aging of solution treated aluminium alloys that results in precipitation hardening whereas the contribution of solid solution hardening to strength decreases due to the migration of solute atoms from matrix into clusters and their further transformation into second phase nanoprecipitatates. The matrix softening is lower compared to the precipitation strengthening though. Maximum strength can be reached by the optimal combination of hardening factors via intelligent microstructural design. The idea is to generate microstructure which provides the maximum contribution from the most efficient hardening mechanisms at minimum/no sacrifice of other hardening mechanisms. A good example is the NS Al 7075 alloy produced via HPT in [5]. This solute solution with a nanosized grains having an average size of 22 nm has a complex hierarchical microstructure which contains high density of dislocations, intragranular solute clusters and two types of intergranular solute segregations. High dislocation density along with contribution of grain boundaries, solute atoms, and their segregations provide 980 MPa yield strength.

Physical understanding of interplay of strengthening mechanisms is essential for the proper microstructural tailoring of NS metallic materials. A body of research into synergetic effects in the superposition of strengthening mechanisms in metallic materials exists in literature [59,99]. The key conclusion of these works is that the different strengthening mechanisms can be additive only if they are fully independent for a given deformation mechanism [59].

1.4. Mechanisms of plastic deformation and their effect on ductility

1.4.1. Overview of mechanisms operating during plastic flow in UFG metallic materials

It is well known that strength and ductility of UFG metallic materials strongly depend on the mechanisms operating during plastic deformation. Conrad [100,101] classified deformation mechanisms in FCC metals (Au, Ag, Cu) into three regimens depending on grain size. For conventional CG metals (d>1μm) dislocation pile-up or twinning are the main deformation mechanism, so-called regime I. Grain boundary shear promoted by

the pile-up of dislocation can be the dominant mechanism in regime II ranged over UFG scale (1μm<d<100nm). Regime III (d<100nm) is defined by the lack of lattice dislocation activity and plastic deformation is mediated by shear of individual grain boundary atoms resulting in break down of the Hall-Petch law and grain softening (Figure 15).

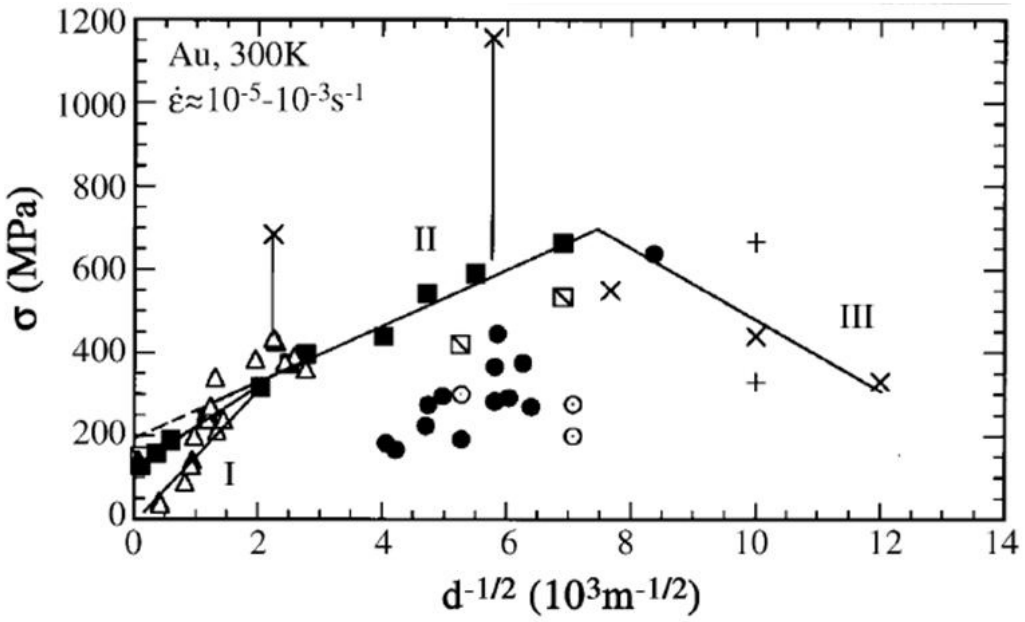

Figure 15. The Hall–Petch plot of the effect of grain size d on the flow stress of Au at 300K and ´ε ≈10^{-5}–10^{-3} s^{-1}. Open symbols are for ε≤0.005, filled are for ε≈0.10–0.20 [102].

In regime I, dislocations glide along slip systems available in crystalline lattice. During plastic deformation, new dislocations are nucleated by whether Frank-Read sources within grains or at grain boundaries. Dislocation tangles are formed by interaction of dislocations on different slip planes. Dislocations also interact with grain boundaries promoting their pile-up on slip plane against grain boundaries as well as against second-phases and sessile dislocations. It should be noted that sessile dislocations only glide by diffusion of atoms or vacancies, and thus they are effective obstacles to mobile dislocations as well (namely, glissile dislocations at low homologue temperatures). This enables the dislocation dissociation into partials, and thus micro-twins and stacking faults are formed. Of course, stacking fault energy has a strong influence on both deformation mechanisms and dislocation storage capacity in the UFG metals [103]. The Orowan model describes dislocation glide (Equation 14 - Equation

16), where $\dot{\varepsilon}$ is strain rate, ρ_m mobile dislocation density, ϑ their velocity, $\Delta\sigma_H$ strength increase given by work hardening, $\Delta\sigma_R$ strength losses due to dislocation annihilation. An increase of dislocation density provides strain hardening (Equation 16).

$$\dot{\varepsilon} = \alpha(M)\rho_m b\vartheta \qquad \textbf{Equation 14}$$

$$\sigma = \sigma_0 + \Delta\sigma_H - \Delta\sigma_R \qquad \textbf{Equation 15}$$

$$\Delta\sigma_H \propto \rho_m b\vartheta \qquad \textbf{Equation 16}$$

Recovery processes can also take place during plastic deformation. Dislocations can annihilate during plastic deformation via climb according to the Weertman model [104]. Dislocations can be also annihilated by their arrangement resulting in formation of dislocation walls in the grain interior. Therefore, the already mentioned substructure of crystalline cells is formed. Further deformation, flux of dislocation along LAGB increases their misorientation resulting in formation of UFG microstructure with well-defined HAGBs. These HAGBs often appear as non-equilibrium grain boundaries and they are characterized by high density of grain boundary dislocations which provide an excess energy. Twinning and dislocation pile-up are restrained for UFG microstructure [101] due to the absence of defects within grains that are able to trap dislocations. In fact, TEM observations often reveal that there are no lattice dislocations in the interior of ultra-fine grains [105] since dislocations move through the grain interior and are dissociated at the opposite grain or subgrain boundary.

This excess of dislocations might promote slip and rotation of grains. This refers to the relative displacement of adjacent grains retaining their original shape and size. Therefore, (micro)-shear bands can be formed during plastic deformation. A (micro)-shear band involves groups of grains that tend to reduce the misalignment through sliding and rotation across the grain boundaries [106]. It was experimentally demonstrated that activation of extensive microshear banding dramatically improves ductility of the UFG Al 6082 alloy [107].

Atomic diffusion processes can significantly contribute to plasticity of UFG and NS metals by grain boundary diffusion or sliding even at low temperatures [108,109]. It is due to the nature of non-equilibrium grain boundaries that favours atomic shuffling and so-called athermal grain boundary diffusion [107,110]. Grain boundary sliding was

observed during plastic deformation of the NS Al 5083 alloy [111] and cryomilled Cu [112]. Study on uni-axial tensile deformation behaviour of nanocrystalline Cu demonstrated a near-perfect elastoplasticity of the material at room temperature when nanocrystalline Cu was deformed to large strains (~15%) without any work hardening and necking that was related to the pre-dominance of grain boundary mediated mechanisms [113]. Generally, for nanocrystalline metals with d<10 nm grain boundary sliding is considered as the main deformation mechanism providing high ductility [105] according to the MD simulations [114].

Mechanisms operating during plastic deformation are usually identified using various experimental techniques such as TEM studies, analysis of surface relief of deformed samples, analysis of stress-strain curves, etc [115]. Another approach to analyze deformation mechanisms are so called transient tests where activation volume $\boldsymbol{v^*}$ of plastic deformation can be estimated. It is generally accepted the activation volume brings considerable insight into the controlling mechanisms of dislocation movement. This parameter can be ascribed to the number of atoms involved in the thermally activated dislocation motion throughout localized obstacles on the slip planes. Consequently, each deformation process can be characterized by the activation volume value and its stress dependence which is described by Equation 17, where $\boldsymbol{M}$ is the Taylor factor, $\boldsymbol{k}$ Boltzmann's constant and $\boldsymbol{T}$ testing temperature. The Seeger model is a geometrical definition of activation volume (Equation 18) where $\boldsymbol{v^*}$ is directly proportional to obstacles spacing $\boldsymbol{l}$, $\boldsymbol{d}$ obstacles diameter and $\boldsymbol{b}$ the Burgers vector.

$$v* = MkT\frac{\partial \ln \dot{\varepsilon}}{\partial \sigma} \qquad \textbf{Equation 17}$$

$$v* = ldb \qquad \textbf{Equation 18}$$

It is suggested that deformation mechanism based on dislocation glide involves high activation volume and this value decreases when dislocation activity is restrained. For a conventional CG FCC metal, activation volume is typically larger than 1000 b^3 at room temperature, whereas for nanocrystalline FCC metal, activation volume can be in the order of ~10 b^3. Atomic diffusion processes entail activation volume in the order of ~1 b^3. It was demonstrated that activation volume for an UFG Cu is almost 10 times lower than for the CG one [116]. These experimental data evidences the effect of

microstructure on plastic deformation where dislocation activity is progressively restricted with reduction of grain size.

1.4.2. Low ductility of UFG metallic materials and main strategies to improve it

Yield stress is defined as the stress required for nucleating dislocations from grain boundaries in an UFG metal [76]. On the other hand, ductility is usually supplied by dislocation glide which is able to accommodate the strain imposed. SPD methods for refining microstructure induce high density of defects promoting strengthening, but ductility is dramatically reduced due to dislocation motion restriction.

In the coarse-grained metals, the uniform strain is usually in good agreement with the well-known Considère criterion [66], which is a geometric criterion stating that when the work hardening rate ($\boldsymbol{d\sigma/d\epsilon}$) decreases to the level of the flow stress, $\boldsymbol{\sigma}$, macro-localization of plastic deformation (necking) should occur resulting in a specimen failure (Equation 19).

$$(\boldsymbol{d\sigma/d\epsilon}) = \boldsymbol{\sigma} \qquad \textbf{Equation 19}$$

The UFG FCC metals are usually characterized by increased strain rate sensitivity even at low temperatures compared to their coarse-grained counterparts [117]. Therefore, the Hart criterion [118] has been employed to predict their uniform elongation. The Hart criterion defines the appearance of localized deformation under tensile load taking into account strain hardening rate ***n*** and strain rate sensitivity ***m*** (Equation 20). Strain hardening rate refers to dislocation accumulation rate into microstructure (Equation 21). High strain hardening ability of the material delays the appearance of plastic instabilities during tensile deformation. Increased strain rate sensitivity delays onset of localization of plastic flow (necking) (Equation 22).

$$\boldsymbol{n + m \geq 1} \qquad \textbf{Equation 20}$$

$$\boldsymbol{n = \frac{1}{\sigma}\frac{\partial \sigma}{\partial \varepsilon}} \qquad \textbf{Equation 21}$$

$$m = \frac{\partial \ln \sigma}{\partial \ln \dot{\varepsilon}}$$ **Equation 22**

Low strain hardening rate is observed in the UFG metals [119]. Although dislocation activity is still operative, this low value might be due to restricted dislocation accumulation, dislocation absorption into grain boundaries and dislocation density saturation. On the other hand, ductility is enhanced while strain level is increased for an UFG CP Cu subjected to up to 16 ECAP passes. It is explained by the higher ability of the UFG microstructure to strain hardening that prevents the premature failure promoting uniform deformation. Therefore, the unique UFG microstructures generated by SPD methods can promote high strength and enhanced ductility. The change of deformation mechanisms in the UFG regime is the predominant cause of this paradox. Otherwise, increasing grain boundary misorientation by lattice rotation or absorption of dislocation into non-equilibrium grain boundaries does not lead a high strain hardening coefficient [108].

When grain is reduced into nanocrystalline regime, grain boundary diffusion can dominate plastic deformation especially at low strain rates. Plasticity mediated by diffusion processes might be the key for achieving enhanced ductility in the NS materials [113].

Ductility enhancement of UFG and nanocrystalline materials keeps on being a scientific challenge. In following section, proposed methods for ductility enhancement will be explained in detail.

1.4.2.1. Strategies to improve ductility

It has been demonstrated that tailoring microstructure can enable a simultaneous increase of strength and ductility [30,108,119,120,121].

Dislocation density is close to saturation in a severe deformed metal due to high imposed stress. Therefore, UFG and NS metals undergo some strain hardening just at the onset of plastic deformation. Unfortunately, this is not extended to the larger strains. Besides there are several dislocation sources, steady state of dislocation density is reached; plastic deformation is localized and the neck is formed. Consequently, a milestone is to increase the strain hardening ability of the UFG or NS metallic materials so it supplies profuse dislocation activity for carrying plasticity.

One of the strategies for promoting uniform tensile deformation is a tailored microstructure composed by homogeneous distribution of micron-sized grains in the ultra-fine grained matrix. This bimodal microstructure can be obtained by short-time annealing of the SPD processed material resulting in partial recrystallization. Such microstructures can be also successfully generated combining cryomilled NS powder with unmilled microstructured powder and their further consolidation [122]. Larger grains provide strain hardening, thus improving ductility, whereas ultrafine grains provide enhanced strength [120].

Another strategy to improve strain hardening ability of the UFG materials and thus their ductility is to introduce nanoprecipitates in the grain interior which act as effective obstacles for dislocations and thus promote accumulation of dislocations in the grain interior. Cheng et al. [15] proposed optimization of both the strength and ductility of the age-hardenable UFG Al2024 alloy by nanoprecipitation after cryo-rolling and subsequent artificial aging. It should be noted that these nanoprecipitates not only increase strain hardening rate but also provide additional precipitation hardening (Figure 16).

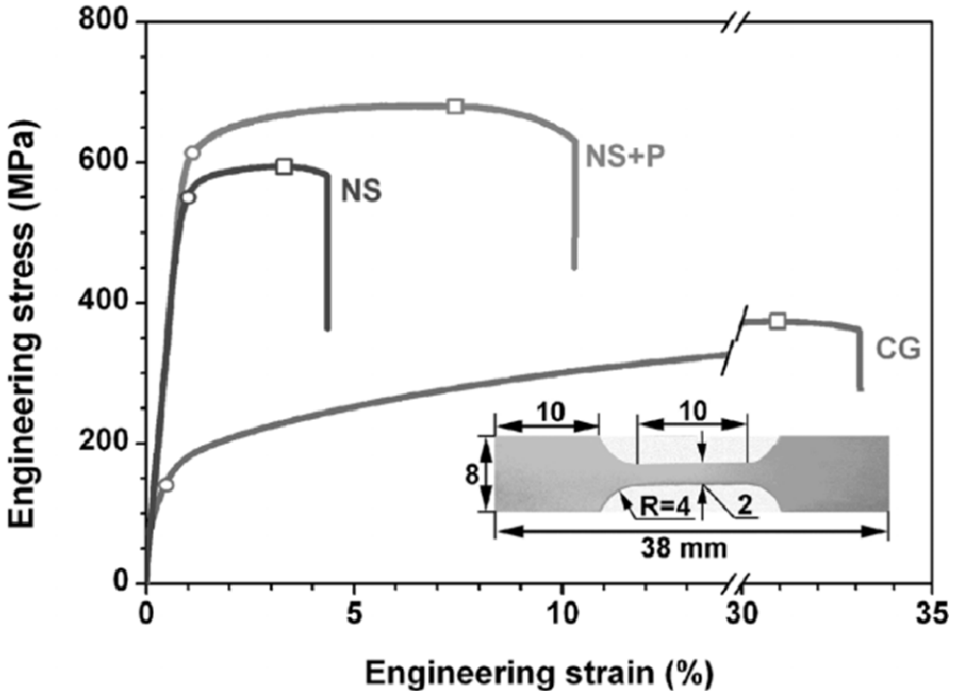

Figure 16. Engineering stress-strain curves for the CG, NS, and NS+P (nanostructured with very small second-phase particles) Al 7075 alloy [50].

Although dislocations can slip across twin boundaries, such a process requires very high stress. Therefore, twin boundaries are also effective barriers for blocking and accumulating dislocations. In addition, twin boundaries can also act as dislocation sources and effectively emit dislocations. Therefore, UFG microstructure with high density of twins should produce both high strength and high ductility. The pre-existing twins can be produced in bulk UFG Cu via SPD methods in combination with cryogenic deformation, for example by ECAP followed by cryogenic drawing and cryogenic rolling to introduce twins in the grains [123]. As it was shown, the cryogenic process after ECAP increased both the strength and ductility of the UFG Cu sample because of the twins introduced in the microstructure.

In the case of UFG materials that do not have either twins or second-phase particles, others options to increase the ductility of UFG materials are related to enhanced strain hardening rate or strain rate sensitivity. Since strain hardening rate is a balance between nucleation and annihilation of dislocations, it can also be increased by decreasing recovery rate. For suppressing recovery, the material should be deformed at low temperatures and/or high strain rates. Deforming at cryogenic temperatures avoids dynamic recovery and the thermally activated cross slip and climb of dislocations. Therefore, dislocation density is effectively increased promoting higher uniform elongation. Deforming at high strain rates involves similar effects on plastic deformation.

Following the Hart criterion (Equation 20), ductility can be enhanced by increasing strain rate sensitivity of metal. A metal with increased strain rate sensitivity index, *m*, should be able to maintain higher uniform elongation as well as elongation to failure due to gradual and progressive necking [113]. Strain rate sensitivity index is related to activation volume by Equation 23. This is an inverse relationship where restraining dislocation motion increases ***m***.

$$\boldsymbol{m} = \frac{\sqrt{3}\boldsymbol{kT}}{\boldsymbol{\sigma v}*} \qquad \textbf{Equation 23}$$

Strain rate sensitivity index is almost negligible for CG metals at RT (*m*~0.003 for the CG Al 6082 alloy in [27]). It follows upward trend as grains are refined in FCC metals. For example, *m*~0.03 was reported for UFG Al 6082 alloy in [27]. It should be noted

that this strategy cannot be applied to bcc metals since they undergo a decrease of *m* while grain size is reduced as was reported for NS Fe and Ta [124]. This opposite behavior with respect to FCC metals might be due to kink-pairs nucleation mechanism which still takes place in the UFG microstructure where the effect of screw dislocations on plastic deformation is almost insignificant. Athermal contribution to flow stress related to internal stresses of metal is dramatically increased by the Hall-Petch effect. Therefore, bcc metals are not temperature and strain rate sensitive.

One of the structural features that often exist in UFG materials produced by SPD is their high-dislocation density and LAGBs. The high dislocation density limits the strain hardening during tensile deformation, whereas it is hard to isolate the precise influence of LAGBs. Recent reports suggest that accumulated redundant plastic strain introduced during material processing could reduce the dislocation density thereby altering mechanical behaviour. For example, increasing the ECAP strain was found to increase the ductility of CP Cu [108]. In [125], ARB was used to process pure Al and significant increase in both strength and ductility with increasing ARB strain was found.

1.5. Fracture behavior of UFG metallic materials

In materials science, fracture toughness is a property which describes the ability of a material containing a crack to resist fracture and is one of the most important properties of any material for many design applications. Fracture failure criteria are closely related to surface energy or energy to overcome the cohesive force of the atoms to create new crack surfaces. Macroscopically, fracture is usually referred as ductile or brittle fracture depending on the stable or unstable character of crack propagation, respectively. Brittle cleavage fracture is a consequence of direct separation of crystallographic planes by simple atomic de-bonding while ductile fracture is defined by formation, growth and coalescence of micro-voids. Cleavage fracture is typically observed in bcc metals as tungsten, molybdenum, chromium or HCP metals as magnesium, zinc and beryllium. FCC metals do not exhibit this brittle behaviour under conventional circumstances.

In spite of the growing interest to the UFG metallic materials, experimental research on their fracture properties is limited. However, first steps to a deep understanding of their fracture behaviour have been already taken. A degradation of fracture toughness of CP Ti after ECAP processing due to the limited ductility of the UFG microstructure was

reported in [126]. In UFG Ni processed via HPT remarkable fracture toughness in combination with very high strength was found [127]. Additionally, a significant anisotropy of the fracture behaviour was observed. Anisotropy of fracture behaviour was reported in a pearlitic steel after HPT processing since a NS composite consisting of ferrite and cementite or cementite like amorphous layers aligned to shear direction was developed during HPT processing [128,129]. A strong deterioration of fracture toughness was observed when tested along shear direction while fracture properties remained high in other directions. Subsequently annealing treatments led to microstructure transformation to bimodal one consisting of globular UFG ferrite and spherical cementite dispersoids which fractured in a micro-ductile way [130]. In fact, homogeneously distributed fine precipitates and dispersoids combine high strength and high fracture toughness since formation of micro-voids was avoided thus the undesirable fracture failure was delayed [131]. Another example found in literature is a peculiar tailored microstructure composed of micro-sized grains embedded into a matrix of ultrafine grains of CP Al nanopowder consolidated by hot isostatic pressing. In this case, crack propagation was impeded by profuse dislocation slip while deformation mechanism in the UFG matrix was based on cooperative grain boundary sliding [132].

1.6. Commercialization of UFG metals

Metals as aluminium, titanium and their alloys are widely used in structural applications above all in automotive and aerospace engineering due to their good corrosion resistance, light weight-strength relationship and their easy machinability. Their mechanical and physical properties are found to be dramatically improved by manipulating the microstructure. Following the Hall-Petch equation, reducing grain size involves an increase in strength and fatigue properties. However, the main researching stone is to find out a processing method that also enables an enhancement of ductility. This is actually viable with a proper microstructure design i.e. a NS metal with high volume fraction of HAGBs and uniform distribution of nanosized second-phase particles [121]. Moreover, large bulks or UFG and NS semi-products can be easily manufactured by some SPD processes such as ECAP-based techniques and HE [17].

An example where UFG metals benefits are actually appealing is pure copper. Copper has been widely used in electric and electronic devices due to its low cost and excellent

thermal and electrical conductivity. In fact, pure copper screws for electrical contact are mechanized by cold forming, Deringer-Ney Company (USA). The main obstacle to wider application of pure copper is its very low mechanical strength. Alloying of pure copper, strain hardening, or precipitation strengthening can be employed to increase mechanical strength of pure Cu, but all these strategies lead to dramatic degradation of its electrical conductivity since it is determined by the scattering of electrons due to disturbances in the crystal structure including thermal vibrations, impurities, and defects [133]. For instance, the electrical conductivity in some of Cu alloys ranges from 10% to 70% of IACS (International Annealed Copper Standard) [134]. It has been recently demonstrated that intelligent microstructural design based on grain refinement down to ultra-fine or nano scale via SPD can be a good strategy to increase dramatically mechanical strength of pure Cu at no expense of its electrical conductivity [133,134,135,136]. The UFG Cu would be also an ideal material for MEMS (micro-electro-mechanical systems) having geometrical features of a few micrometers since the average grain size in the micro-parts should be smaller than the smallest dimension of the structural features in order to ensure their reliable property control [137,138].

Several commercial applications of NS and UFG materials have been found in literature. For example, micro bolts of UFG titanium or carbon steel are used in aircraft industries. As well, there is a recent progress on the fabrication of hard magnetic devices as permanent magnet because hysteresis properties are significantly improved after SPD processing [139].

Sub-micron grained Al and Cu sputtering targets processed by ECAP are already commercialized by Honeywell Electronic Materials and Praxair Electronics (Figure 17 b) [140,141]. These targets are effective tools for fabricating advanced uniform thin deposition films materials for semiconductor and photovoltaic markets. Lifetime and performance consistency of these targets have been significantly improved by grain refinement.

Ti-6Al-4V alloy is a common material for fabrication of medical implants as well as surgery devices. Alloying of pure Ti by other elements effectively improves its mechanical strength but reduces its corrosion resistance. Moreover, the Ti-6Al-4V alloy is toxic for human body because of the presence of vanadium. Recently, a standard dental implant made from the Ti alloy has been replaced by one made of fully

biocompatible NS pure titanium [142]. Not only mechanical properties of dental implant have been significantly improved, but also its diameter was reduced by 32% causing less damage in the jaw during operation (Figure 17 a).

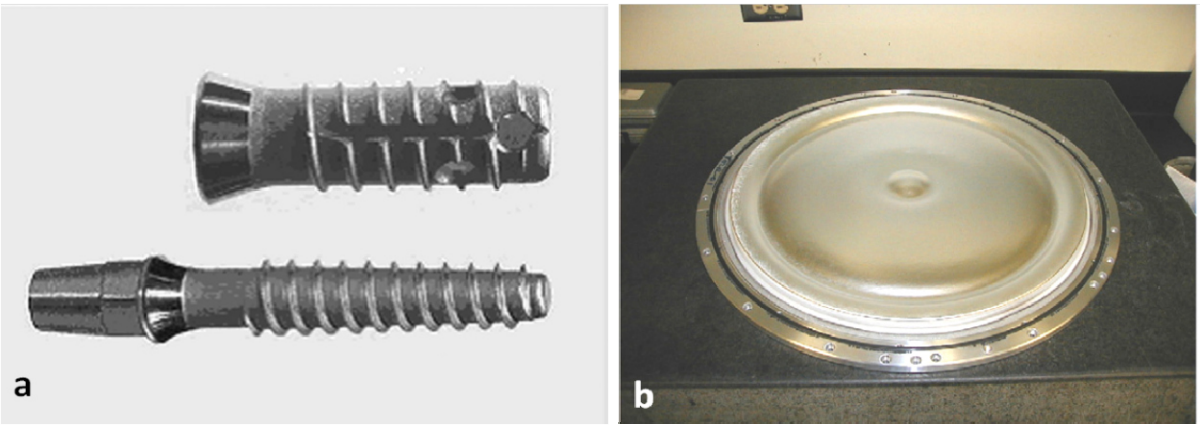

Figure 17 (a) Dental implants Ø 3.5 mm Timplant® (top) and Ø 2.4 mm Nanoimplant®; (b) Flat 300 mm monolithic ECAP processed Al-0.5Cu target. The images are reproduced from [141,142].

Nowadays, simple mechanizing as turning and drilling are the most common methods for metal-forming of final products from a nanocrystalline UFG or NS materials. A good example is a novel dental implant described above which is produced from rods of NS pure Ti having a diameter of ~5 mm. However, metalforming processing methods are required for fabrication of the complex shape products. It should be noted that there is no industrial application for complex shape parts/tools made from the UFG and NS metallic materials made via metalforming up to date.

2 MOTIVATION AND OBJECTIVES

2. MOTIVATION AND OBJECTIVES

As it is seen from the Introduction section, most of the studies on mechanical properties and ductility of UFG and NS metallic materials were carried out using uni-axial tensile testing. Figure 18 represents a tri-axial stress state in a cell unit where hydrostatic stress and mean stress are defined by following equations (Equation 24, Equation 25). The ratio of mean stress to hydrostatic stress represents stress triaxiality which is equal to 1/3 under uni-axial tensile testing (since both σ_2 and σ_3 are zero). Necking during tensile testing leads to increase of this factor [143]. It has been experimentally demonstrated that in UFG and NS metallic materials, mechanisms operating during plastic deformation in the necking area might be different from those operating during uni-axial homogeneous tensile deformation. For example, activation of extensive microshear banding along with cooperative grain boundary sliding in the necking area was observed in the UFG Pd and UFG Pd [144]. From these experimental data, it can be concluded that there is an effect of stress state on deformation mechanisms of plastic deformation. Moreover, it is well know that ductility of UFG metallic materials is determined by the mechanisms operating during plastic deformation. Therefore, there should be effect of stress state on ductility/formability of UFG metals. Since the metals in metalforming typically undergo plastic deformation under complex stress state (in multi-axial mode), the UFG metals deformed along complex strain path might show higher ductility compared to that in the case of the uni-axial tensile testing.

By the beginning of my work on this PhD thesis in 2010, there were no publications focused on formability of the UFG metallic materials in bi-axial stretching and on a fundamental understanding between the microstructure, stress state, and ductility/formability in the UFG metallic materials. Thus, the major goal of this work was to gain fundamental understanding between the microstructure, stress state, and formability in the UFG metallic materials.

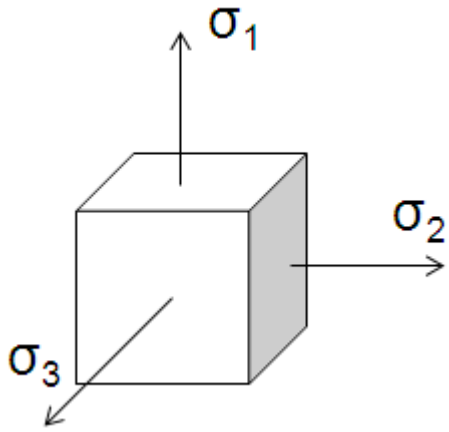

Figure 18. Schematic draw of tri-axial stress state where principal stresses are represented as σ_1, σ_2, σ_3.

$$\sigma_m = \frac{\sigma_1 + \sigma_2 + \sigma_3}{3}$$ **Equation 24**

$$\sigma_{eq} = \frac{1}{\sqrt{3}}\sqrt{(\sigma_1 - \sigma_2)^2 + (\sigma_1 - \sigma_3)^2 + (\sigma_2 - \sigma_3)^2}$$ **Equation 25**

$$T = \frac{\sigma_m}{\sigma_{eq}}$$ **Equation 26**

Thus, the main objectives of the present work were:

I. To fabricate a range of UFG metallic materials via various SPD techniques;

II. To investigate the effect of SPD processing on the microstructure;

III. To study mechanical behaviour and mechanical properties of UFG metallic materials deformed in uni-axial (stress triaxiality 1/3) and bi-axial (stress triaxiality 2/3) tensile mode;

IV. To understand the microstructure - stress state - deformation mechanisms – formability relationship in UFG metallic materials.

3 Materials and Experimental Procedures

3. MATERIALS AND EXPERIMENTAL PROCEDURES

This section describes the materials and provides justification for their choice, SPD processing methods and processing parameters applied to the materials are described in detail, along with the experimental methods and techniques used for the microstructural, mechanical characterization of the processed materials as well as for analysis of their mechanical behaviour.

3.1. Materials and processing

CP Cu, CP Ti, and an Al2024 alloy were chosen as materials for this investigation. Such a choice is rationalized based on the objective of this work to explore the effect of microstructure on formability of UFG metals. CP Cu was chosen to study purely the effect of grain size on the formability of FCC metals. Since HCP metals can show significant anisotropy of their mechanical behaviour depending on their texture, CP Ti was selected to analyze the combined effect of grain size and texture on formability of HCP metal. Finally, the Al2024 alloy provides us with opportunity to evaluate the effect of grain size and precipitates/dispersoids on formability of a FCC alloy.

3.1.1. Commercially pure Cu

CP Cu having a purity of 99.9% was received in form of bars having diameter of 20 mm. The as-received copper was subjected to annealing at 600^{o}C for 2h. The annealed material shows a homogeneous microstructure with an average grain size of ~50 μm. Hereafter, this material condition will be referred to as coarse-grained (CG) CP Cu.

The diameter of the annealed bars was reduced down to 18 mm. These bars with a length of 100 mm were subjected to ECAP processing at room temperature for 2 and 12 passes. The ECAP die had the internal channel angle φ = 90º and the outer arc curvature angle ψ = 0º (Figure 1). The processing route B_c was employed where the bar is rotated by 90^{o} around the pressing direction after each ECAP pass since it leads to the most efficient grain refinement in metallic materials [26,27,30,31]. The selection of the number of passes was rationalized by the previous works where the microstructure effect on deformation behaviour under uni-axial tensile testing was analyzed [30]. The strain produced in each pass was about 1, so the cumulative strain the specimens underwent as a result of the ECAP processing were about 2 and 12,

respectively [3]. Hereafter, these material conditions will be referred to as 2P Cu and 12P Cu, respectively.

As it was demonstrated in section 1.2.1, the ECAP processing is usually applied for fabrication of large billets. The processed Cu billets can be used for fabrication of high strength tools (as large conductive screws) or their further processing for manufacturing of parts for micro-electro-mechanical systems (MEMS).

3.1.2. An Al2024 alloy

An Al2024 alloy was received in form of billets having a diameter of 50 mm. The as-received material was in the hot extruded condition. In order to evaluate the grain size effect in addition to dispersoids and second phases' role in deformation behaviour, a commercial aluminium alloy was chosen as material for this investigation. Al2024 is an excellent candidate because of its extended use in engineering field. For instance, 61% of structure of A380 aircraft from AIRBUS is made of aluminium alloys. Lower cover of wings where high fracture toughness is required is made of this Al-Cu alloy. Their excellent strength-weight ratio besides of good workability enables their use as fuselage frames. Other numerous applications of aluminium alloys are gears, bolts, computer parts, couplings, hydraulic valve bodies, missile parts, munitions, nuts, pistons, fastening devices, veterinary and orthopaedic equipment, structures, etc.

Chemical composition of the selected alloy is detailed in Table 2. The as-received material was subjected to solution treatment at 490ºC for 10 hours after being annealed at 450ºC for 10 hours.

Table 2. Chemical composition of the Al2024 alloy.

	Si	Fe	Cu	Mn	Mg	Cr	Zn	Ti	Zr+Bi	others	Al
%	≤0.50	≤0.50	3.80-4.90	0.30-0.90	1.20-1.80	0.10	≤0.25	≤0.15	≤0.20	≤0.15	balance

The billets of the Al2024 alloy were subjected to single-pass hydrostatic extrusion at room temperature using a 45º die in order to refine their microstructure. The strain rate was 3.54 s^{-1} which corresponds to the linear extrusion speed above 5.9 mm/s. The total

true strain induced into sample was 1.19. The parameters of hydrostatic extrusion applied to material are presented in Table 3.

Hydrostatic extrusion is usually accompanied by significant adiabatic heating which might significantly affect the microstructure developed during processing [145]. The temperature rise due to adiabatic heating was estimated by the commonly accepted Equation 27 [145,146] where $\boldsymbol{p}$ is the extrusion pressure, $\boldsymbol{c}$ the specific heat, $\boldsymbol{\rho}$ the density, and $\boldsymbol{\beta}$ denotes the fraction of the plastic work converted into heat during deformation. For HE with good lubrication, $\boldsymbol{\beta}$~0.9 [145]. The calculated $\Delta\boldsymbol{T}$-value is also given in Table 3.

$$\Delta T = \beta \frac{p}{c\rho} \qquad \textbf{Equation 27}$$

Table 3. Processing parameters during hydrostatic extrusion of Al2024 alloy.

	Solution treatment	Entry die angle (º)	Reduction ratio	True strain	Linear extrusion speed (cm/s)	Pressure (MPa)	Strain rate at exit (s^{-1})	Adiabatic heating, ΔT (ºC)
HE-Al2024	490ºC/10h water quenching	45	3.29	1.19	5.9	727	3.54	284

This work was carried out by UNIPRESS, Institute of High Pressure Physics of the Polish Academy of Sciences, (Warsaw, Poland) as a part of European LIMEDU project. Figure 11 describes HE process [145]. Different combinations of lubricant paste based on ~60% MoS and refined oil, copper and PTFE aerosols and aluminium layer superimposed by physical vapor deposition (PVD) were tried as lubricants. The rods after hydrostatic extrusion showed smooth surface without any (micro)-cracks.

It should be noted that high strength HE rods Al 2024 alloy can be used in construction engineering.

3.1.3. Commercially pure Titanium

CP Ti (Grade 3) with specification corresponding to the ASTM B348-09 standard [147] was received in form of billets having a diameter of 50 mm. Equiaxed grains with average size of 42 μm are observed in the microstructure of the as-received titanium bars. Hereafter, this material condition is referred to AR-Ti.

Large bars of CP titanium were subjected to HE processing at room temperature using a 45º die in order to refine their microstructure. This work was carried out by the project partners from UNIPRESS, Institute of High Pressure Physics, the Polish Academy of Sciences as part of the European LIMEDU project. Different combinations of lubricant paste based on ~60% MoS and refined oil, copper and PTFE aerosols and aluminum layer superimposed by physical vapor deposition (PVD) were tried as lubricants. The rods after HE processing showed smooth surface without any (micro)cracks.

Table 4 summarizes the HE processing parameters (diameter reduction percentage, the final diameter, number of extrusion passes, cumulative extrusion ratio and cumulative strain) of CP Ti. Extrusion pressure was in the range of 827-1092 MPa. The strain rate was 10 s^{-1} which corresponds to the linear extrusion speed of 60.6 mm/s. Additionally, rotary swaging (RS) was imposed into some rods after HE processing.

Adiabatic heating during HE processing was calculated using Equation 27. For $\boldsymbol{c}$ = 0.523 $Jg^{-1}K^{-1}$ and $\boldsymbol{\rho}$ = 4.5 gcm^{-3} this estimation leads to $\Delta \boldsymbol{T}$ = 240-400 ^{o}C.

The HE processed rods are perfect semi-products for further manufacturing of micro-parts for fabrication of dental implants with minimum waste of expensive material.

Table 4. Processing parameters during hydrostatic extrusion of CP Ti and additional rotary swaging.

	Diameter reduction (%)	Final diameter (mm)	Number of extrusion steps	Cumulative extrusion ratio	Cumulative strain
AR-Ti	0	50	0	0	0
$HE_{0.7}$-Ti	50.2	10	1	2.01	0.70
$HE_{1.30}$-Ti	71.9	10	1	3.56	1.30
$HE_{3.24}$-Ti	40.6	10	4	25.41	3.24
$HE_{3.7}$-Ti	84	8	3	41.64	3.7
HE-RS-Ti	84	8	3	39.16	3.67

3.2. Mechanical testing

3.2.1. Uni-axial tensile testing

Uni-axial tensile testing is one of the most widely used methods for mechanical characterization of metallic materials [66]. Mechanical tensile strength and tensile ductility as well as strain hardening ability of the metallic materials can be quantitatively estimated using this technique.

3.2.1.1. Uni-axial tensile testing of CP Cu

Tensile specimens with a gauge length of 7.5 mm, gauge width of 1.5 mm and a thickness of 1 mm were machined from the CG and ECAP processed Cu bars. The tensile axis of the specimens coincided with the pressing direction. The surface of the specimens was polished to the mirror-like surface for further surface relief analysis. Tensile tests were carried out using Kammrath&Weiss module at room temperature with constant cross head speed corresponding to the initial strain rate of 10^{-3} s^{-1}. At least three specimens were tested for each materials condition and the results were found to be reproducible.

3.2.1.2. Uni-axial tensile testing of CP Ti and Al2024 alloy

Tensile specimens with a gauge length of 3.2 mm, a gauge width of 0.8 mm, and a gauge thickness of ~0.8 mm were machined from the longitudinal (L) and transversal

(T) sections of both as-received and hydrostatically extruded bars (Figure 19). The tensile axis of T-specimens was perpendicular to the bar axis and L-specimens was parallel to the bar axis, as indicated in Figure 19. These tensile specimens were mechanically polished to mirror-like surface using colloidal silica solution at the final stage. Tensile tests were carried out at room temperature using a Kammrath&Weiss testing module. Tensile specimens were deformed to failure with constant cross-head speed corresponding to the initial strain rate of 10^{-3} s^{-1}. At least three tensile specimens were tested for each material's condition and the results were reproducible.

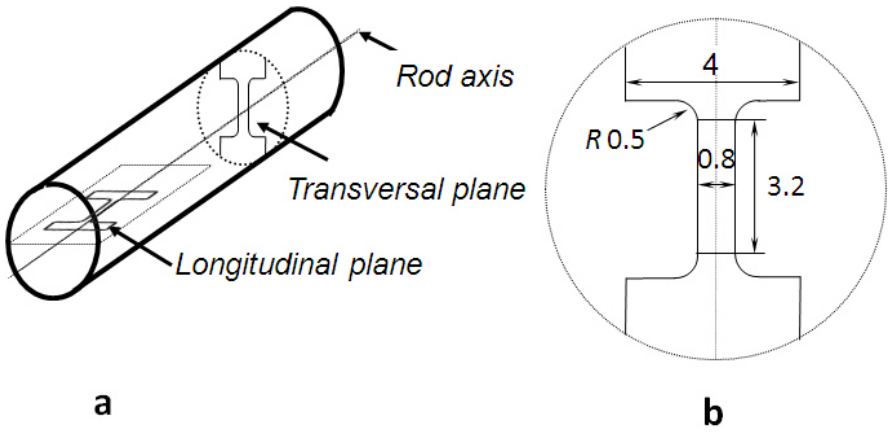

Figure 19. (a) Rod axis, transversal and longitudinal planes in the extruded rod; (b) schematic drawing of specimen dimensions.

3.2.2. Small-punch testing

In last decades, small-punch testing has been widely used for assessment of the damage level over repair-welded and heat affected areas of steel pipes for energy and thermal facilities [148,149,150,151]. European Committee of Standardization coordinated by the European Pressure Equipment Research Council set a code of practice for application and use of small-punch tests as a tool for prediction of creep failure and toughness and properties of in-service materials [152]. Similar die-punch designs are common in literature for evaluating bi-axial stretching formability of miniaturized thin specimens.

Flat specimens for small punch testing were cut from the T-section of the ECAP processed CP Cu billets and in both T- and L-sections of the HE processed rods of the Al2024 alloy and CP Ti as indicated in Figure 19. Both sides of the flat specimens were grinded and polished to mirror-like surfaces using colloidal silica at the final stage. The

final thickness of specimens was 0.4 mm. Small-punch tests were carried out at room temperature. Schematic diagram of the test is represented in Figure 20. A flat thin specimen is clamped between upper and bottom parts of the die and it is deformed using a well-lubricated hemispherical, rigid punch having a diameter of 2.4 mm (Figure 21). The cross-head speed during small punch testing was 0.5 mm/min. Readings from punch load (F) and central deflection (h) were taken during testing.

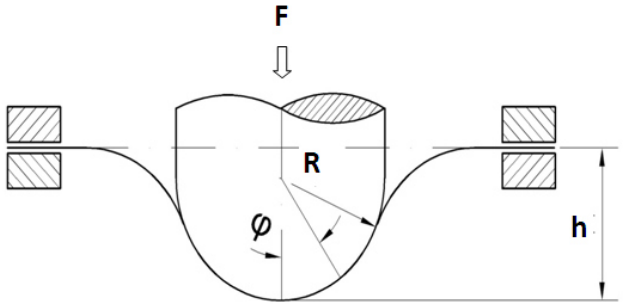

Figure 20. Schematic drawing of small punch testing.

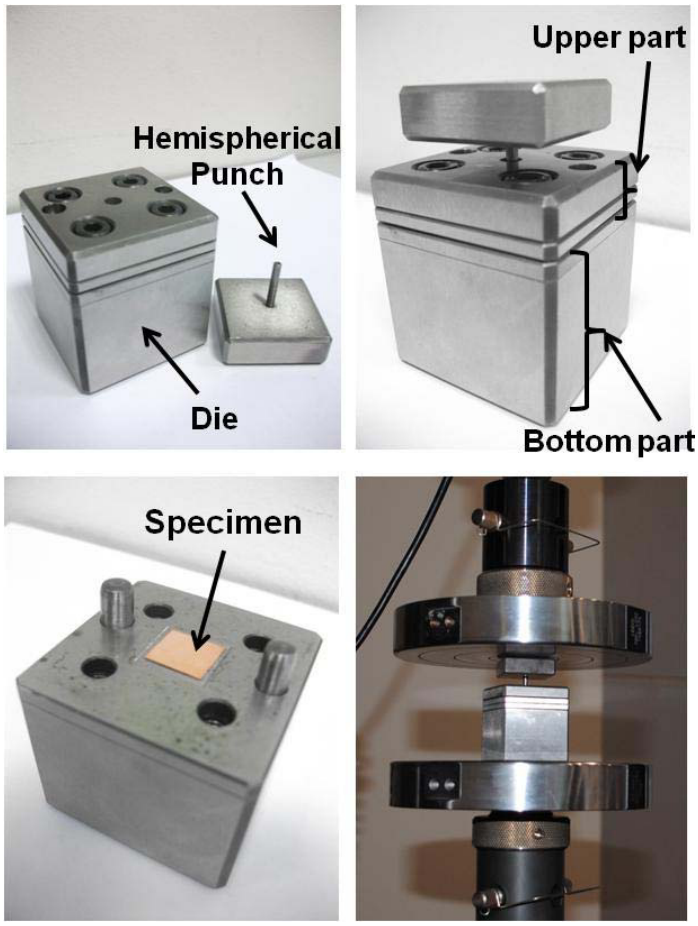

Figure 21. Experimental set-up for small-punch testing.

Figure 22 shows the typical punch load-central deflection curve where all deformation stages are marked [149]. Elastic bending is the first stage marked as I. This stage is related to the local surface micro-yielding. Plastic flow begins and spreads through punch-specimen contact area during plastic bending, stage II. Stage III corresponds to membrane (bi-axial) stretching. A flat specimen transforms into dome-shaped cup following the punch profile during this stage. It is considered that uniform deformation takes place along an annular section of specimen. Once maximum load is reached, unstable plastic flow onsets leading to formation of cracks and specimen failure.

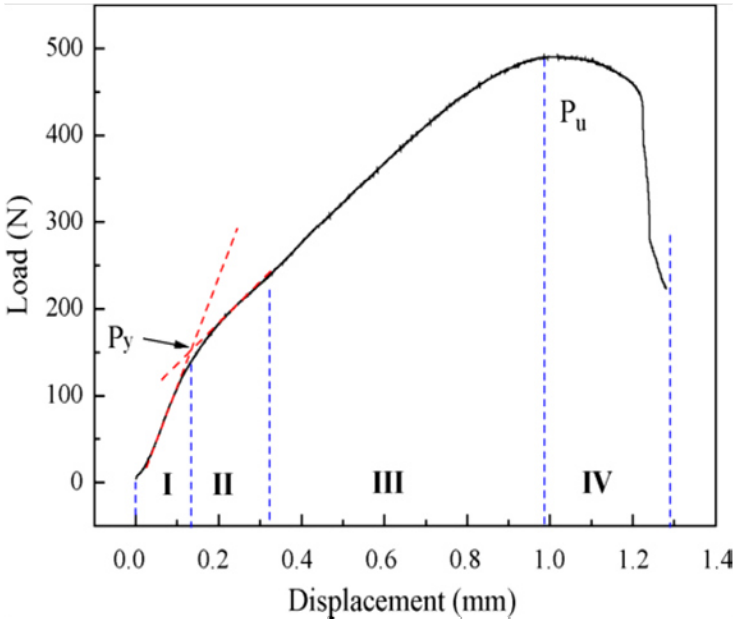

Figure 22. Typical punch load-displacement curve for 0.4 mm thickness small-punch specimen [149].

At least 3 specimens for each material condition were deformed up to the appearance of plastic instabilities. Uniform true strain was estimated taking into account the initial thickness, t_0 and the final thickness, t_f (Equation 28) over the area deformed in bi-axial stretching. This area was found to be placed at 20-60º with respect to the punch axis (Figure 20).

$$\varepsilon = ln\left(\frac{t_0}{t_f}\right)$$ **Equation 28**

3.2.3. Fracture characterization

An important limitation for fracture testing of most of SPD processed UFG and NS samples is their small size. Therefore, a novel technique to evaluate fracture toughness of miniaturized samples was successfully developed [127,128,130,153]

Compact tension specimens for fracture characterization were extracted with two different crack plane orientations from the HE processed bars of the Al2024 alloy and CP Ti. Nomenclature of specimens depends on the crack propagation direction where C-R specimens are mechanized as disc-shaped compact specimens with crack propagation direction perpendicular to the extrusion axis. In the R-L specimens, crack propagates in the extrusion direction (Figure 23).

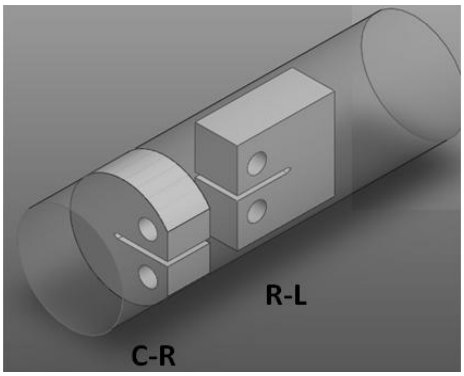

Figure 23. Orientation of fracture specimens.

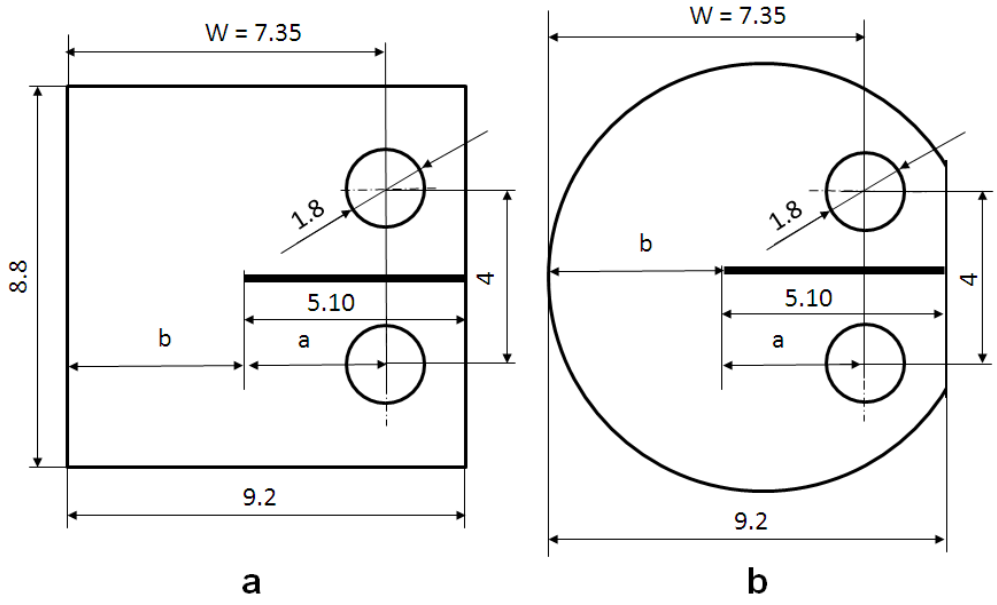

Figure 24. Drawing of fracture specimens: (a) R-L specimen; (b) C-R specimen. Specimen thickness is B=3.7 mm.

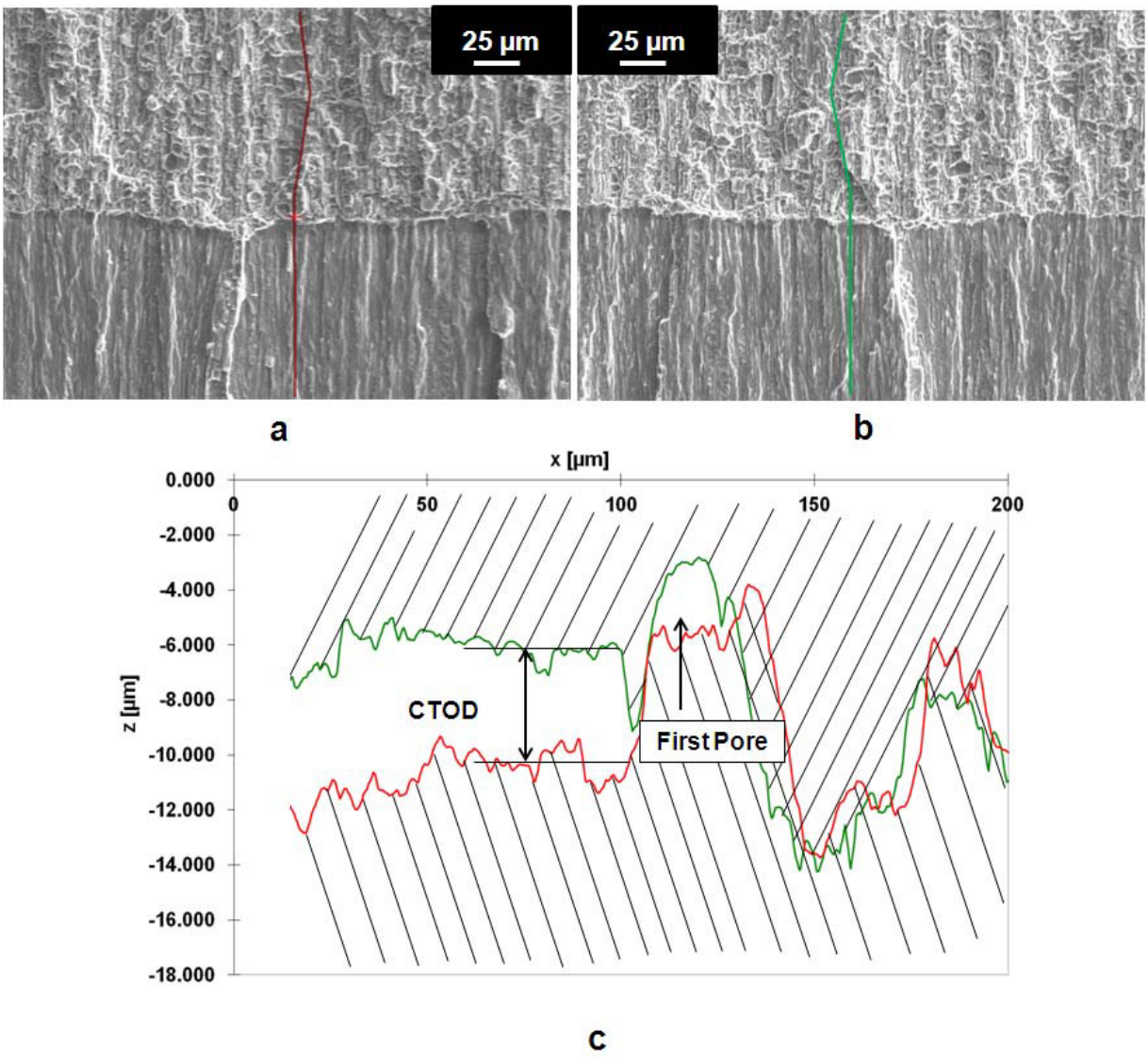

Figure 25. (a) and (b) SEM images of corresponding regions on both R-L specimen halves of the HE processed CP Ti; (c) Profiles through a fracture surface element at the moment of local failure.

A sharp fatigue pre-crack was introduced before fracture testing (Figure 26). Initial crack length was a_0 ~3.4 mm (a_0=W/2) (Figure 24). Fracture tests were performed at room temperature according to the ASTM standards (Figure 24) [154]. At least 3 specimens were tested for each material condition and the results were reproducible.

A fracture surface of broken compact tensile specimens was analyzed using an automatic fracture surface analysis system [126,155]. This system generates a digital elevation model (DEM) of surface in a stereoscopic image from two images taken in scanning electron microscope (SEM) LEO EVO MA 15 by tilting the specimen 5º. The

software automatically finds homologue points in SEM images taken at two different angles and computes the three-dimensional coordinates of the surface points, thus reconstructing the fracture surface (Figure 25). Fracture surfaces profiles can be extracted from the DEM in order to automatically evaluate the surface roughness parameters and the fractal dimensions. The system has been widely used for experimental study of fracture surfaces of diverse metallic materials [127,128,156]. The crack profiles can be drawn over the stereoscopic images of both halves in such a way that the crack propagation can be reconstructed.

Crack tip opening displacement (***CTOD***) and crack opening angle (***COA***) are the measurements of local fracture initiation toughness and total crack growth resistance, respectively. ***CTOD*** is estimated by separating the crack profiles from each other until the coalescence point of the first pore with the fatigue pre-crack is reached (Figure 25 c). The ***CTOD***-value is related to the ***J***-integral which characterizes the intensity of elastic-plastic crack-tip field and is understood as the difference of potential energy between two identically loaded specimens with different crack length. The total crack growth resistance (R_{tot}) is calculated according to Equation 29-Equation 31 where ***b*** is the ligament length ($b = W - a$), d_N is a dimensionless parameter depending on the strain hardening exponent (n), yield stress (σ_0) and elastic modulus (E) and η is a pre-factor to calculate ***J*** from the area below load versus load-line displacement curve [153,154]. The R_{tot}-value can be calculated using Equation 32 and Equation 33.

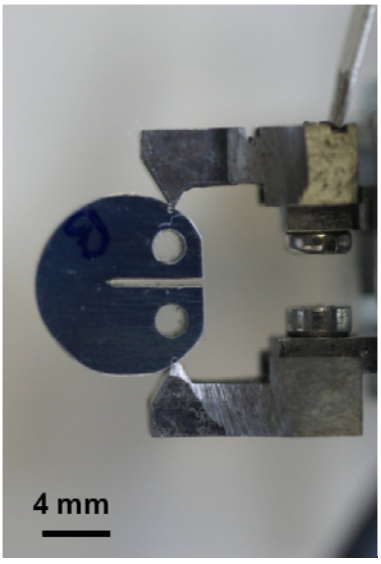

Figure 26. Set-up for the fracture testing of a C-R specimen.

$$J = \frac{1}{d_N}\sigma_0 COD$$ **Equation 29**

$$d_N = f(n, \sigma_0/E)$$ **Equation 30**

$$R_{tot} \approx \frac{dJ}{d(\Delta a)}\frac{b}{\eta}$$ **Equation 31**

$$R_{tot} = \frac{m\sigma_y b}{\eta} COA$$ **Equation 32**

$$m = \frac{\sigma_{UTS}}{\sigma_Y}\frac{\exp(n)}{(1+n)n^n}$$ **Equation 33**

3.2.4. Nanoindentation

Instrumented nanoindentation technique allows to measure hardness and elastic modulus of a material from load-displacement curves obtained by indenting small volumes of material with a diamond tip and recording force and displacement with resolutions of <30 nN and <1 nm, respectively.

However, an elastoplastic material usually exhibits pile-up or sink-in phenomenon around imprint and the measured area by the nanoindenter as a function of the depth could be unrealistic. Therefore, it is advisable to image the imprint in order to check the validity of the calculated elastoplastic properties from the load-displacement curves. The strain hardening ability of the material entails a strong influence on pile-up/sink-in behaviour [157] i.e. materials with lower strain hardening coefficient tend to form larger pile-up of material around the imprint.

Another influential factor to take into account is the size effect. As indenter penetrates into material, dislocations are generated and advance along grain interior toward grain boundaries and dislocation density increases with indenter penetration. In the NS materials the proximity between dislocations source (indenter) and sink (boundaries, nanosize precipitates, etc.) leads to the appearance of this so-called size effect [158].

Figure 27 is an example of a load–displacement curve where P_{max} is the peak indentation load, h_{max} is the displacement at peak load and h_f is the final depth of the

contact impression after unloading [159]. A portion of the contact area under load may not be plastically deformed since there is some elastic recovery of material after unloading. The contact area of imprints for elastoplastic materials is usually estimated following Oliver and Pharr's model where the contact area is measured from the measured depth of penetration assuming elastic unloading response [159]. ***S*** is the contact stiffness which is calculated from the derivate of load with respect to displacement at the maximum displacement point (the slope at the beginning of unloading curve) and ***A*** is the projected area of the elastic contact, calculated from the area function of the indenter tip $A=f(h_c)$ which relates area with contact depth, h_c. For non-rigid indenters, the resultant modulus is defined as reduced elastic modulus, E_r since it includes the contribution of the indenter to the measured stiffness. The Yong's modulus can be obtained from Equation 35, where E and ϑ are the Young's modulus and the Poison ratio for the specimen and E_i and ϑ_i are the same parameters for the indenter. As mentioned, this model has some limitations regarding pile-up or sink-in effect as contact area is calculated accounting elastic correction but it does not reflect the influence of the strain hardening coefficient.

$$E_r = \frac{\sqrt{\pi}}{2\sqrt{A}} S$$ **Equation 34**

$$\frac{1}{E_r} = \frac{(1-\vartheta^2)}{E} + \frac{(1-\vartheta_i{}^2)}{E_i}$$ **Equation 35**

$$H = \frac{P_{max}}{A}$$ **Equation 36**

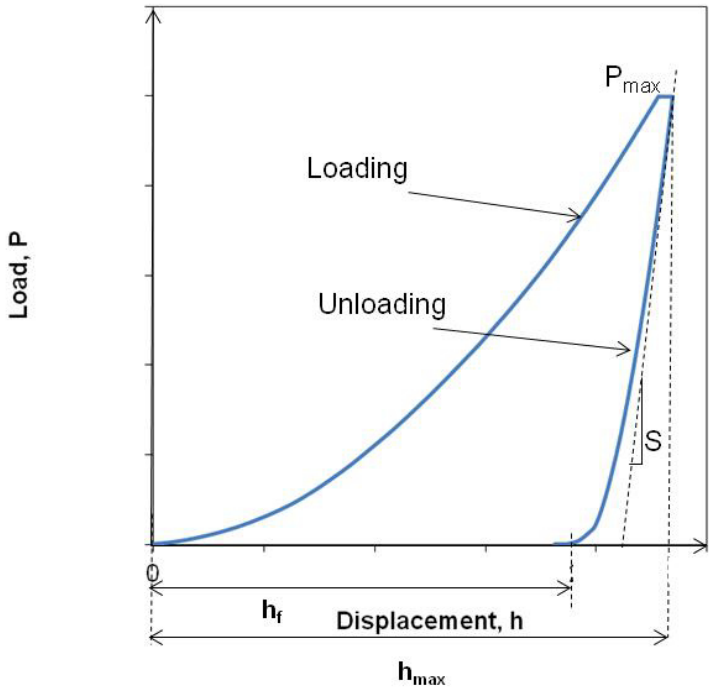

Figure 27. Schematic representation of load – nanoindenter displacement curve.

Nanohardness measurements with a Berkovich (pyramidal) indenter were performed at room temperature onto longitudinal HE processed specimens ($HE_{3.24}$-Ti) and (HE-RS-Ti) before and after bi-axial stretching at 300ºC. Small-punch specimens were firmly stuck over a wedge of 30º using adhesive based on cyanocrylate, as bi-axial stretching areas are found to be located at 25-60º with respect to the dome axis. At the same time, this wedge was placed on a metallic disc that was fixed to the stage (Figure 28).

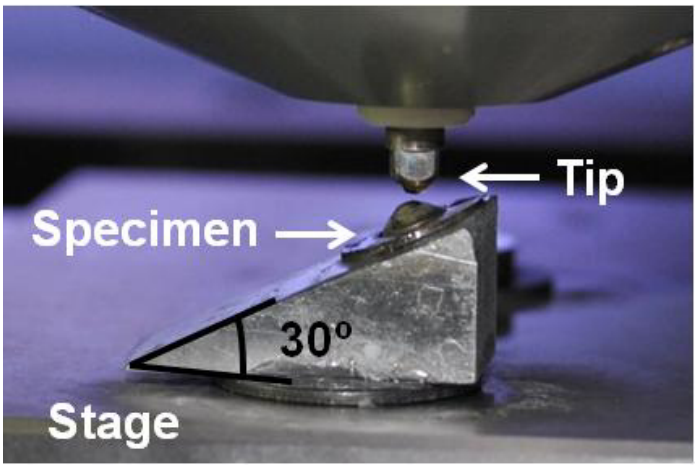

Figure 28. Experimental set-up for nanoindentation test.

Preliminary load-partial unload nanoindentation cycles were performed at maximum load of 700 mN in order to estimate the contribution of the frame (instrument plus mounting set-up) stiffness to the measured contact stiffness for setting the real stiffness since domes are not fully supported by a rigid substrate (specimens are hollow). Afterwards, at least 10 nanoindentations for each material condition were performed at room temperature and at constant loading with loading, holding and unloading times of 10 s, 5 s and 5 s respectively and maximum load of 500 mN using high load HYSITRON nanoindentation system T1950®.

3.3. Techniques for microstructural analysis

3.3.1. Optical microscopy

Optical microscopy observations were carried out using an Olympus BX-51 light microscope equipped with a digital camera. Quantitative characterization of the microstructure of the CG materials as well as shape and thickness of the small-punch specimens was performed using the ANALYSIS software.

3.3.2. Transmission electron microscopy

To study the microstructure in details, transmission electron microscopy (TEM) studies were carried out. The samples for TEM study were cut from the L-sections of the ECAP processed Cu samples and HE processed Al2024 alloy and CP Ti rods and then thinned down to the thickness of ~100 μm.

The Cu samples were prepared by twin jet electropolishing with electrolyte (25% orthophosphoric acid, 25% ethanol, and 50% distilled water) at 20ºC at a voltage of 9-10 V. TEM study of the Cu specimens was performed using a JEOL-2000 microscope operating at 200 kV. Observations were made in both bright and dark field imaging modes. Selected area electron diffraction (SAED) patterns were recorded from the areas of interest using an aperture of 1 μm nominal diameter.

The Al2024 specimens were prepared by twin jet electropolishing in TENUPOL 5 using 1:2 solution of nitric acid in methanol. Electropolishing was performed at -25ºC at voltage of 12V. TEM analysis of the Al2024 specimens was carried out in a TECNAI-20-FEG microscope operated at 200 kV by the research group of Carlos III University of

Madrid in frames of the LIMEDU project. Observations were made in both bright and dark field imaging modes. Selected area electro diffraction (SAED) patterns were recorded from the areas of interest.

The Ti specimens were prepared by electropolishing in a TENUPOL 5 twin-jet polisher using a 1:4 solution of nitric acid in methanol at T~-30ºC. Part of samples was characterized by the research group of Carlos III University of Madrid with a TECNAI-20-FEG microscope operated at 200 kV. Most of the samples were characterized by myself using a JEOL-2000 microscope operating at 200 kV. Observations were made in both bright and dark field imaging modes. SAED patterns were also recorded from the areas of interest.

3.3.3. Scanning electron microscopy

Examination of surface relief of the tested samples was performed using SEM EVO MA 15 SEM operating at 20kV. Surface relief of deformed tensile specimens was analyzed in the area of homogeneous plastic deformation and in the necking area. In the case of small-punch specimens, inspections were carried out over areas deformed by bi-axial stretching.

Fracture surface characterization was performed after fracture test of miniaturized specimens. The SEM images consisting of 1024x768 pixels at 256 gray levels were taken in the SEM at 0º and 5º tilting angles.

3.3.4. Atomic force microscopy

Atomic force microscopy enables to study the surface morphology of a material with a lateral precision depending on the tip radius, which is in the range 2-10 nm.

A quantitative characterization of surface relief of small-punch specimens of Cu over the area deformed by bi-axial stretching was carried out using atomic force microscopy, Park XE150 AFM Instrument. Three-dimensional (3D) topography images of the scanned areas were generated using WSxM Develop 5.2 software developed by Nanotec. At least 10 profiles were analyzed for each material condition in order to estimate dimensions of microshear bands. Local volume fraction of shear bands was

calculated as a ratio of length of the kinked profile (corresponding to the shear bans) to the total length of the profile.

Imprints from nanoindentation tests were scanned using AFM technique. Dimensions of at least 5 imprints were measured for each material condition for a proper nanohardness estimation of the small-punch specimens. Photoshop® software was used for selecting and measuring areas over a picture.

3.3.5. Texture measurements

Texture is the distribution of crystallographic orientations of a polycrystalline sample. A sample in which these orientations are fully random is said to have no texture. If the crystallographic orientations are not random, but have some preferred orientation, then the sample has a weak, moderate or strong texture. Texture measurements were performed at the CAI DRX using a Phillips Xpert'PRO diffractometer furnished with a PW3050/60 goniometer. Measurements were taken in a range of Psi angles from 0° to 75° at 3° steps.

For the Al2024 alloy after HE processing, the pole figures for the planes (111), (200), (222) and (311) were plotted. Crystallographic planes in a cubic system are schematically presented in Figure 29. For pure Ti after HE processing, the pole figures for the planes (0001), (10-10), (10-11), (10-12), (10-13), and (10-20) were plotted. Basal plane (0001), prismatic plane (10-10), and pyramidal plane (10-12) in the HCP lattice are schematically presented in Figure 30.

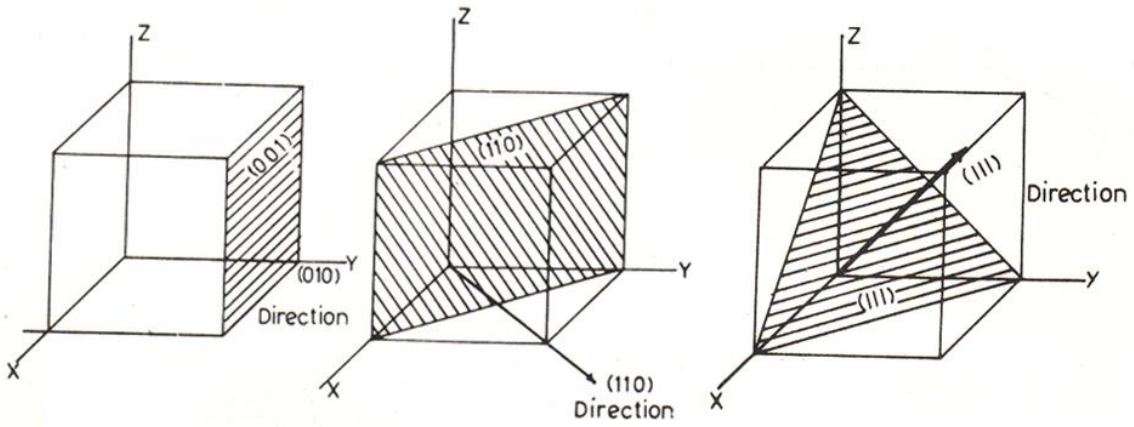

Figure 29. Planes and slip directions in the face centered cubic crystal structure of Al.

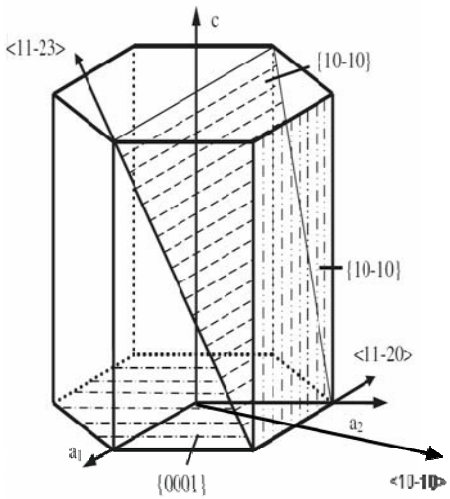

Figure 30. Planes and slip directions in the hexagonal close packed crystal structure of α-Ti.

4 RESULTS AND DISCUSSION

4. RESULTS AND DISCUSSIONS

4.1. Effect of SPD processing on microstructure of the studied materials

4.1.1. Evolution of microstructure in CP Cu during ECAP processing

Figure 31 illustrates evolution of microstructure during ECAP processing of CP Cu. The as-received and annealed CP Cu shows homogeneous microstructure with the average grain size of ~50 μm (Figure 31 a, d). Two ECAP passes lead to formation of a complex inhomogeneous microstructure consisting of lamellaes and subgrains having a size of 250-650 nm. Small areas consisting of ultra-fine grains having size of 150 to 300 nm are also observed (Figure 31 b, e). Shear bands formed during ECAP processing have a width of 200…300 nm and are inclined at 40…50º to the pressing direction. ECAP processing for 12 passes results in formation of a homogeneous UFG microstructure consisting mainly of equiaxed ultra-fine grains having a size of 100…250 nm. The interior of most of the grains is free of dislocations. It should be noted that these microstructural observations are in a very good accordance with the results presented earlier in numerous manuscripts focused on the microstructure evolution during ECAP processing of pure Cu [30,108,160,161].

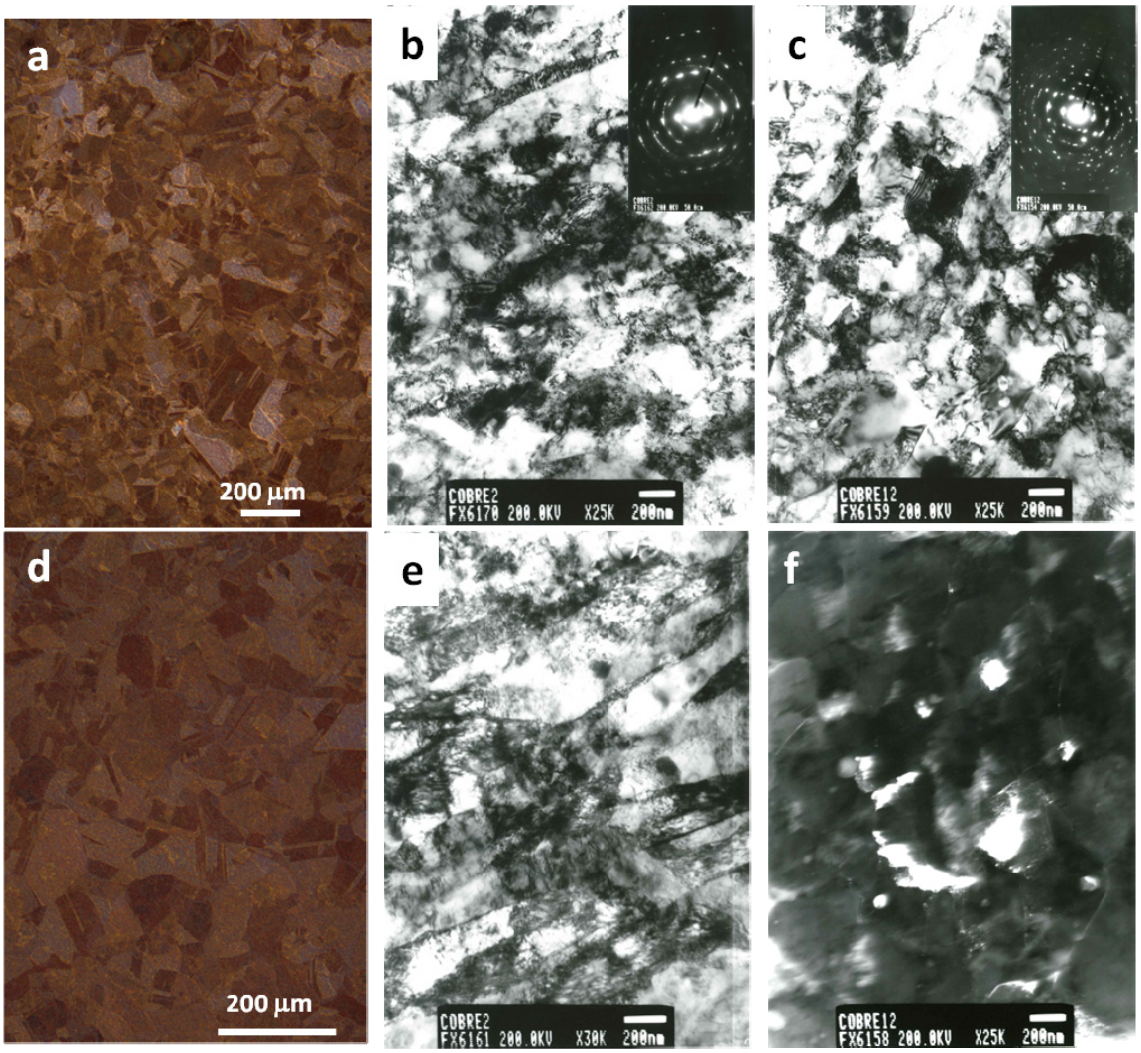

Figure 31. Microstructure of CP Cu: (a, d) Optical images of coarse grained Cu; (b, e) bright field TEM images and SAED pattern of CP Cu after 2 ECAP passes; (c,f) bright and dark field TEM images and SAED pattern of CP Cu after 12 ECAP passes.

4.1.2. Effect of HE processing on the microstructure and texture of the Al2024 alloy.

HE processing results in formation of complex microstructure consisting of elongated grains having a high dislocation density and subgrains (Figure 32 a). The grains have a length of 500-750 nm and a width of 200-500 nm. Homogeneous fine dispersion of rod-like $Al_{20}Cu_2Mn_3$ precipitates indentified as T-phase was found (Figure 32 b) as well as coarse and elongated particles of Al-Cu-Mg so-called S'-phase. It should be noted that similar microstructures were also observed in the Al2024 alloys subjected to low deformation strain via cryorolling [15].

HE processing introduces high dislocation density. Dislocations interaction promotes the formation of dislocation tangles and formation of subgrains with increasing deformation ratio.

Figure 33 shows pole figures for the transversal section of the HE processed Al2024 alloy. It is clearly seen that HE processing promotes the development of a very strong fiber texture with the <111> direction parallel to the extrusion axis. Similar textures were reported for the extruded Al alloys in [162,163].

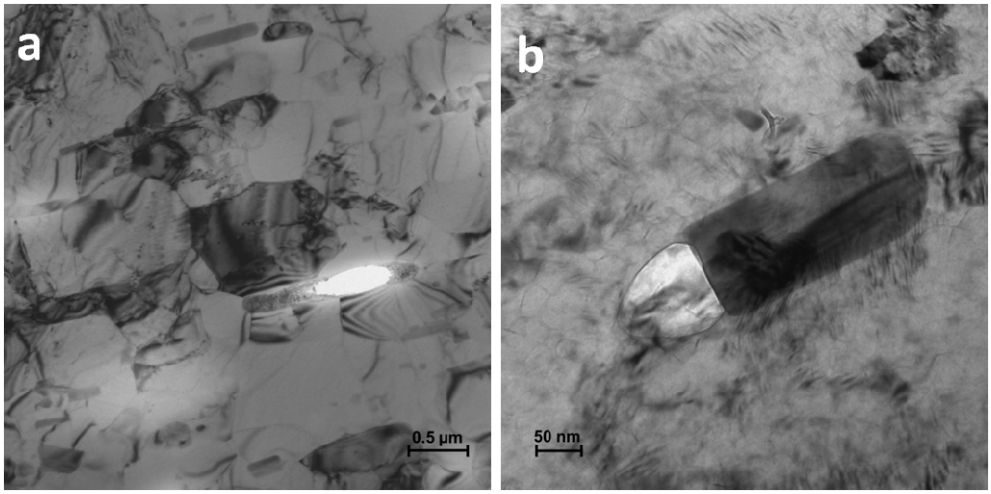

Figure 32. Bright field TEM images of: (a) microstructure of HE Al2024 alloy; (b) higher magnification of T-phase (courtesy of Carlos III University).

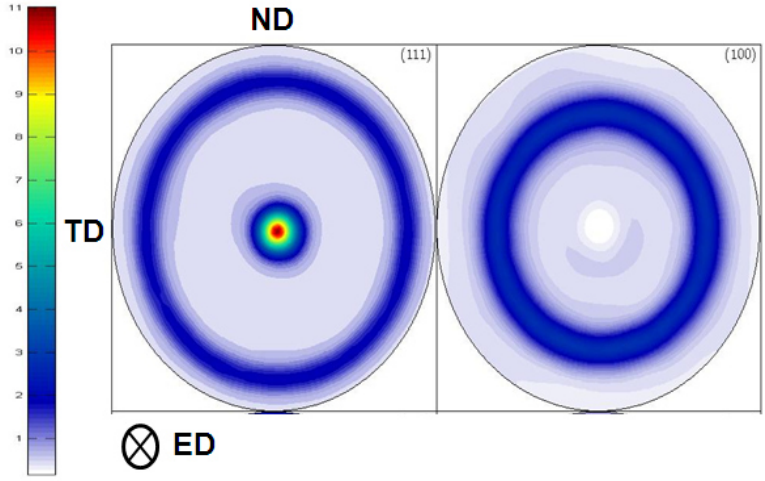

Figure 33. Pole figures for the transversal section of hydrostatically extruded Al2024 alloy.

4.1.3. Evolution of microstructure in CP Ti during HE processing

Figure 34 shows representative optical micrograph of longitudinal section of the as-received CP Titanium samples. It is seen that the microstructure of the CG CP Ti consists of homogeneous equiaxed coarse grains with an average size of 42 μm (Figure 34 a). Detailed examination of the microstructure of the processed samples showed that hydrostatic extrusion leads to the microstructure refinement and enables the formation of elongated grains/subgrains in form of lamellas aligned along extrusion direction (Figure 34 b, Figure 35). Lamellae width decreases as cumulated strain increases from 800 nm after ε=0.70 (Figure 34 b) to values below 100 nm after ε=3.24. After ε=3.24, microstructure consists of lamellae having a length of up to 1 μm and a width ranging from 50 to 150 nm (Figure 35 a, b). A high density of dislocations is observed in the lamellae interior and the formation of equi-axed grains/subgrains having a size of 100…200 nm is also seen (Figure 35). They present straight boundaries intersecting at high angles with neighbour lamellae. The grain boundaries are ill-defined and SAED patterns are spread indicating non-equilibrium character of grain boundaries [70,164]. The fraction of equiaxed grains increases with increasing cumulative strain to 3.7 (Figure 35 c, d). Combination of hydrostatic extrusion with rotary swaging with cumulative strain of 3.67 leads to very similar microstructure (Figure 35 e, f).

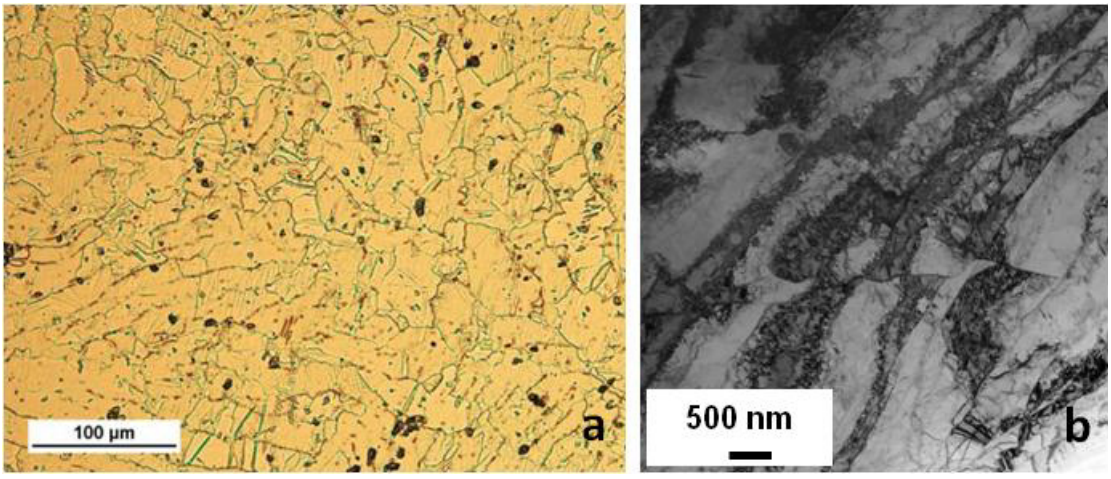

Figure 34. (a) Optical microscopy images of microstructure of the as-received CP Ti; (b) Bright field TEM images of CP Ti after HE to up to ε=0.70 ($HE_{0.7}$-Ti). Courtesy of Carlos III University.

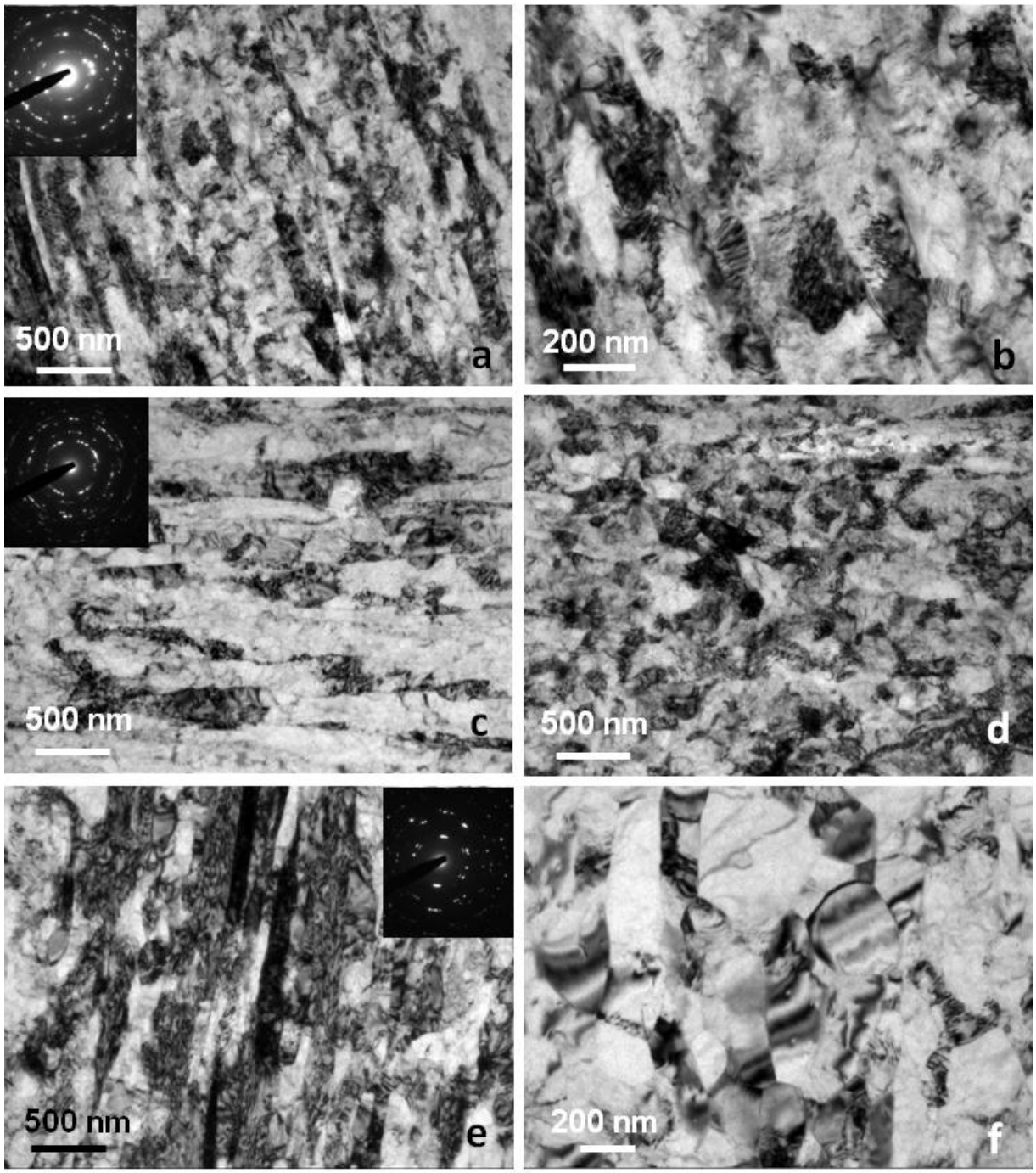

Figure 35. Bright field TEM images and SAED pattern of CP Ti subjected to SPD to up to (a, b) ε=3.24 ($HE_{3.24}$-Ti); (c, d) ε≈3.7 ($HE_{3.7}$-Ti); (e, f) after hydrostatic extrusion and additional rotary swaging ε≈3.67 (HE-RS-Ti).

The formation of these microstructures can be related explicitly to twinning and dislocation glide operating in the material during hydrostatic extrusion/rotary swaging. Despite hydrostatic extrusion results in significant adiabatic heating of metallic materials [145], the temperature of adiabatic heating in our hydrostatically extruded pure Ti

estimated using (Equation 27) is well below the recrystallization temperatures of 620-760^{o}C (Table 4) reported for severely deformed pure Ti [165,166]. Moreover, it should be noted that the samples during hydrostatic extrusion are heated only in the local deformed area just less 1 s followed by immediate cooling down to room temperature, that is not sufficient neither for recrystallization nor for significant recovery of the developed microstructure [165,166]. It should be noted that HE processing was more efficient for microstructure refinement in CP Ti than in the Al2024 alloy. This can be related to the higher melting point of CP Ti compared to that of the Al2024 alloy [59].

Figure 36 illustrates pole figures for the transversal section of the CG and HE processed Ti bars at various cumulative strains. The as-received CG Ti shows a weak texture similar to that developed in the hot rolled Ti (Figure 36 a) [64,167]. It is seen that α-fibre texture is developed during hydrostatic extrusion with the <10-10> direction and the basal plane (0001) parallel to the rod axis. Such fibre texture is typical for CP Ti subjected to extrusion, drawing or swaging [168]. The intensity of the texture component tends to increase dramatically with increasing cumulative strain. The maximum intensity on the (10-10) pole figure increases from ~4 for CP Ti after deformation with cumulative true strain of 0.7 up to ~18 in the rod after deformation with cumulative true strain of 3.24. A saturation of crystallographic texture after deformation to this strain is observed. A significant anisotropy of mechanical properties and deformation behaviour in longitudinal and transverse directions is expected in the material due to such strong crystallographic fibre texture.

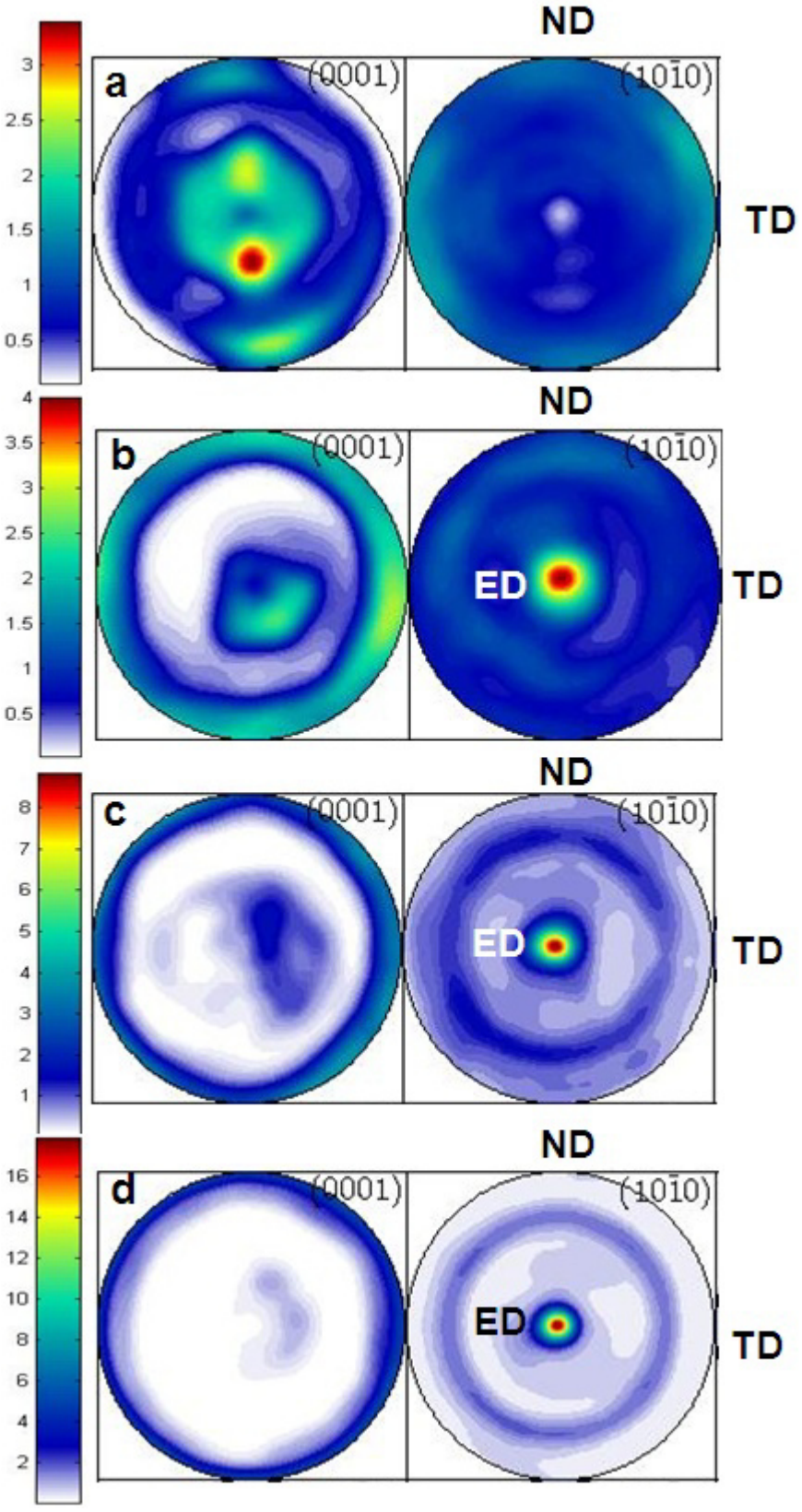

Figure 36. Pole figures for the transversal section of the as-received and the HE processed CP Ti: (a) As received Ti; (b) HE Ti to ε= 0.7 ($HE_{0.7}$-Ti); (c) HE Ti to ε=1.30 ($HE_{1.30}$-Ti); (d) HE Ti to ε=3.24 ($HE_{3.24}$-Ti).

4.2. Uni-axial behavior of studied materials

This section focuses on the microstructure and texture effect on uni-axial tensile behaviour of the studied materials.

4.2.1. Grain size effect on tensile mechanical properties of CP Cu

Typical engineering stress - engineering strain curves obtained from tensile tests of the CG Cu and ECAP-processed Cu are represented in Figure 37. Data on mechanical properties determined from tensile tests (0.2% proof strength, $\sigma_{0.2}$, ultimate tensile strength, σ_{UTS}, strain hardening coefficient, n, uniform elongation, ε_u and elongation to failure ε_f) are listed in Table 5. It is clearly seen that grain refinement leads to increase of mechanical strength properties following the Hall-Petch law [62,63], whereas both uniform elongation and elongation to failure dramatically drop with decreasing grain size (Table 5). The strain hardening exponent drops in CP Cu after ECAP processing due to lower ability of the processed material to accumulate dislocations during plastic deformation (Table 5). It should be noted that similar effect of ECAP processing on mechanical properties and deformation behavior of pure Cu was reported earlier in [30,160,161]

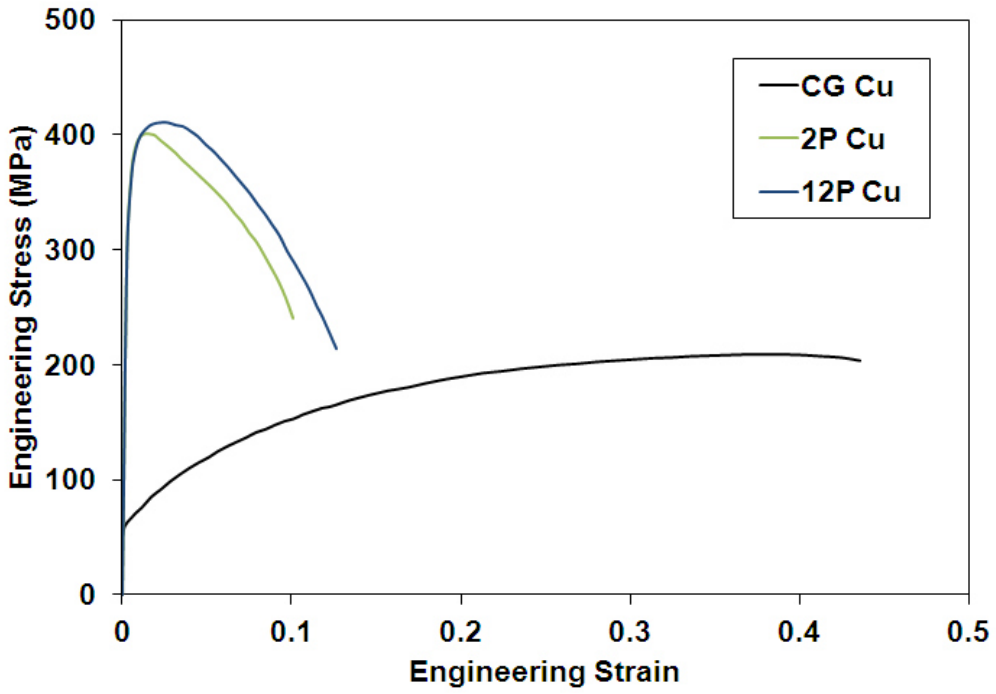

Figure 37. Engineering stress-engineering strain curves for CG Cu and CP Cu after 2 and 12 ECAP passes.

Table 5. Mechanical properties of CG Cu, 2P and 12P Cu.

	$\sigma_{0.2}$ (MPa)	σ_{UTS} (MPa)	n	ε_u	ε_f
CG Cu	61±2	206±8	0.40	0.437±0.031	0.465±0.049
2P Cu	363±1	400±1	0.05	0.012±0.001	0.099±0.001
12P Cu	359±3	410±1	0.03	0.026±0.001	0.119±0.007

To analyze deformation behaviour of the CG Cu during tensile testing, a surface relief developed in the area of homogeneous plastic flow and in the necking area of the tested specimens was analyzed in SEM (Figure 38). Slip lines verify that dislocation slip is the main deformation mechanisms in the CG CP Cu (Figure 38 a). Necking does not affect significantly the morphology of surface relief of the CG CP Cu. No evidences of localization of plastic deformation were found on homogeneously deformed areas of the CP Cu after 2 and 12 ECAP passes. However, some localization of plastic flow in form of microshear bands is observed in the necking area of ECAP processed Cu (marked by white arrows in Figure 38 b, c).

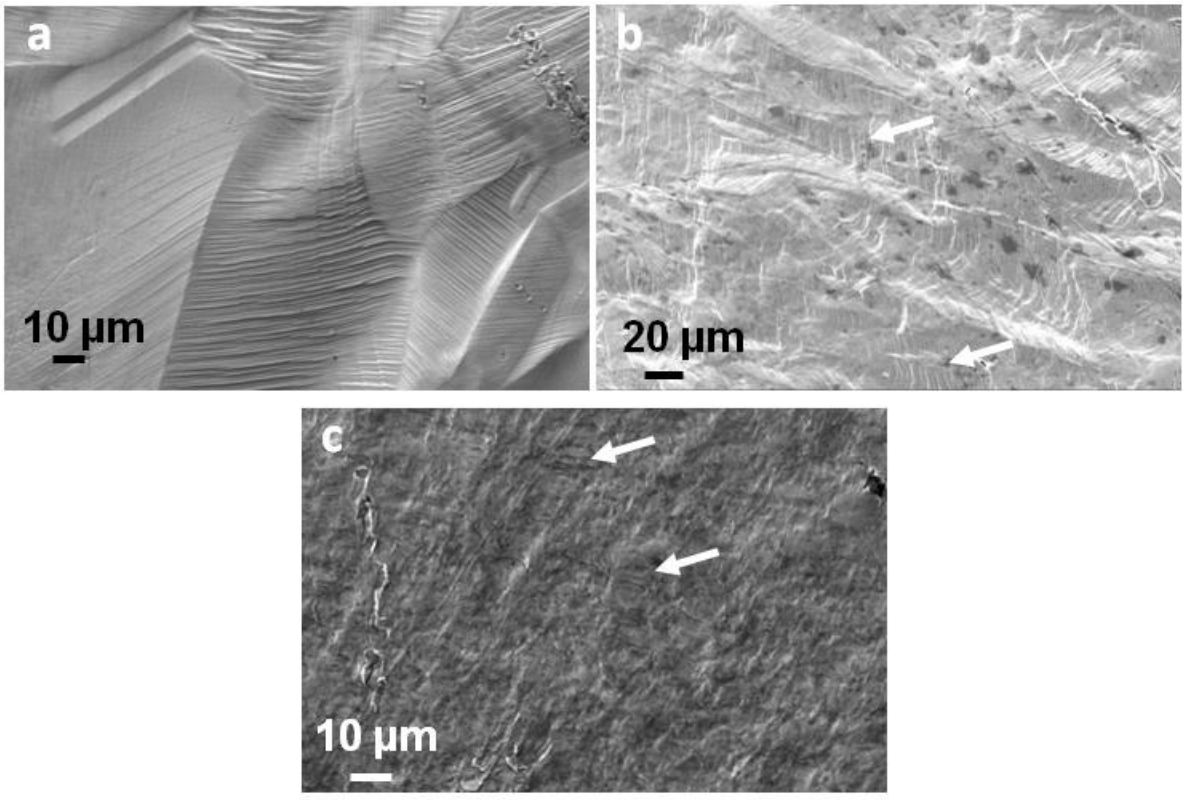

Figure 38. SEM images of surface relief in necking area of tensile specimens: (a) CG Cu; (b) 2P Cu; (c) 12P Cu.

4.2.2. Mechanical properties of the Al2024 alloy after HE processing

Figure 39 shows engineering stress – engineering strain curves for the solution treated and naturally aged Al2024 alloy and the HE processed Al2024 alloy. The grain refinement leads to increase mechanical strength significantly at the expenses of the reduction of uniform elongation and elongation to failure. Mechanical properties extracted from tensile testing are listed below (Table 6). Anisotropy of tensile mechanical behaviour in the extrusion direction and transverse direction of the Al2024 alloy is clearly observed which is related to the microstructure and crystallographic texture developed during HE processing: grains elongated along the extrusion direction and the second phase *S'*-precipitates aligned along the extrusion direction as well as the fibre texture where <111> direction is parallel to extrusion direction. Ductility in both testing directions is limited, less than 6% (Table 6).

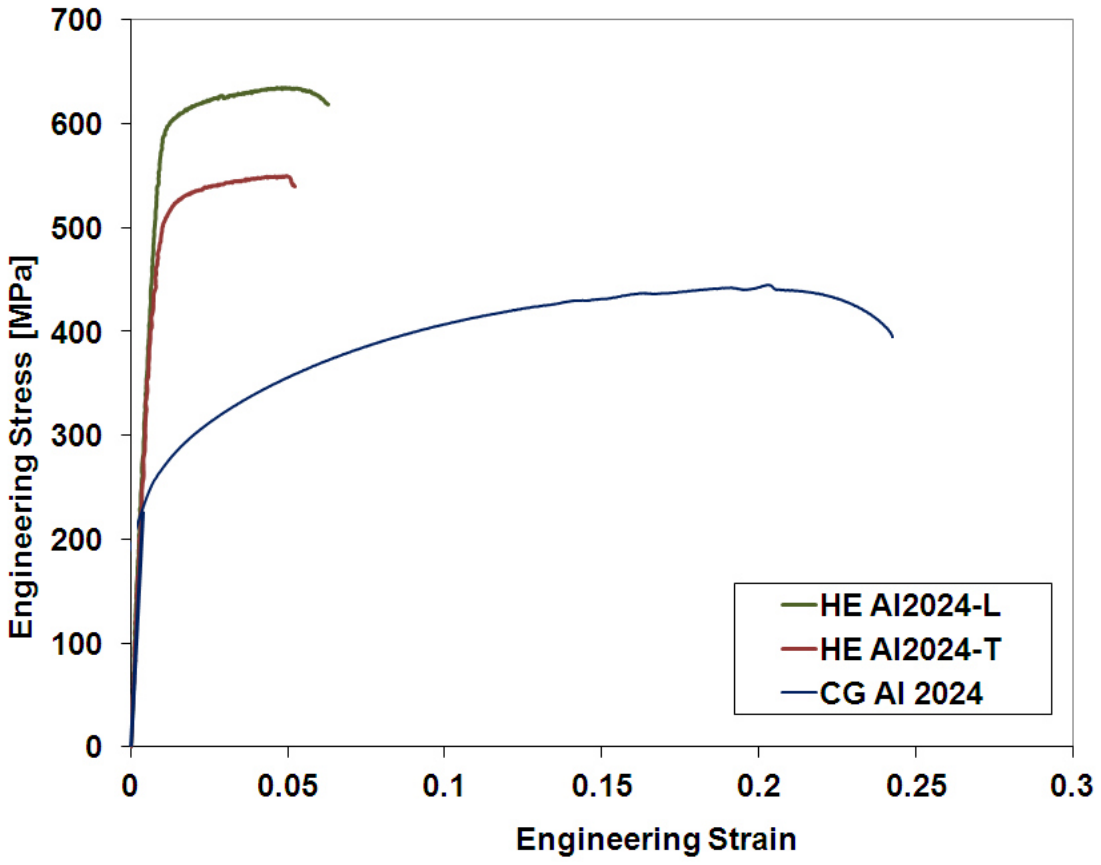

Figure 39. Engineering stress-engineering strain curves for the CG solution treated Al2024 alloy and longitudinal (L) and transversal (T) specimens of HE processed Al2024 alloy.

Table 6. Mechanical properties of CG and HE processed Al2024 alloy from uni-axial tensile testing on transversal (T) and longitudinal (L) planes.

	σ_y (MPa)	$\sigma_{0.2}$ (MPa)	σ_{UTS} (MPa)	ε_u (%)	ε_f (%)
CG Al2024	238	265	440	18	22.3
HE Al2024-T	390	450	550	4.4	5.3
HE Al2024-L	490	570	640	4.1	4.4

4.2.3. Grain size and texture effect on tensile mechanical behavior of the CP Ti

As a result of experimental data from microstructure characterization of CP Ti, specimens for tensile testing were mechanized from the as-received and the HE processed bars to cumulative true strain of 3.24 (material condition called as $HE_{3.24}$-Ti) as additional straining does not affect microstructure formation. At this material condition, the finest microstructure was obtained and the maximum intensity on the (10-10) pole figures was reached. Hereafter, this condition will be presented as hydrostatically extruded material.

Figure 40 illustrates the engineering stress - engineering strain curves from tensile testing at room temperature for longitudinal and transversal sections of the as-received and hydrostatically extruded Ti bars. Mechanical properties obtained from tensile testing are listed below (Table 7). Despite the as-received CG Ti specimens show a slight anisotropy of mechanical properties, pronounced anisotropy of mechanical behaviour is observed after hydrostatic extrusion. It is in good agreement with the literature data where strong mechanical anisotropy was observed for Ti billets processed via different SPD routes [16,169]. The T-specimens of the CG specimens tend to show somewhat higher mechanical strength and tensile ductility compared to the L-specimens due to the weak crystallographic texture (Figure 40). No significant effect of the sample orientation on the work hardening behaviour is observed (Figure 40, Table 7). The mechanical strength of CP Ti dramatically increases after hydrostatic extrusion due to grain refinement whereas both uniform elongation and elongation to failure show an opposite trend. After HE processing, the L-specimens display very high 0.2% proof strength of 915 MPa but low work hardening capacity, so the ultimate tensile strength of the material is 970 MPa. The T-specimens show much lower 0.2%

proof strength of 562 MPa, which is much higher compared to that of the as-received material though (Table 7). However, very high work hardening capacity of the T-specimens from hydrostatically extruded material leads to very high ultimate tensile strength of 995 MPa which slightly exceeds that of the L-specimens (Table 7).

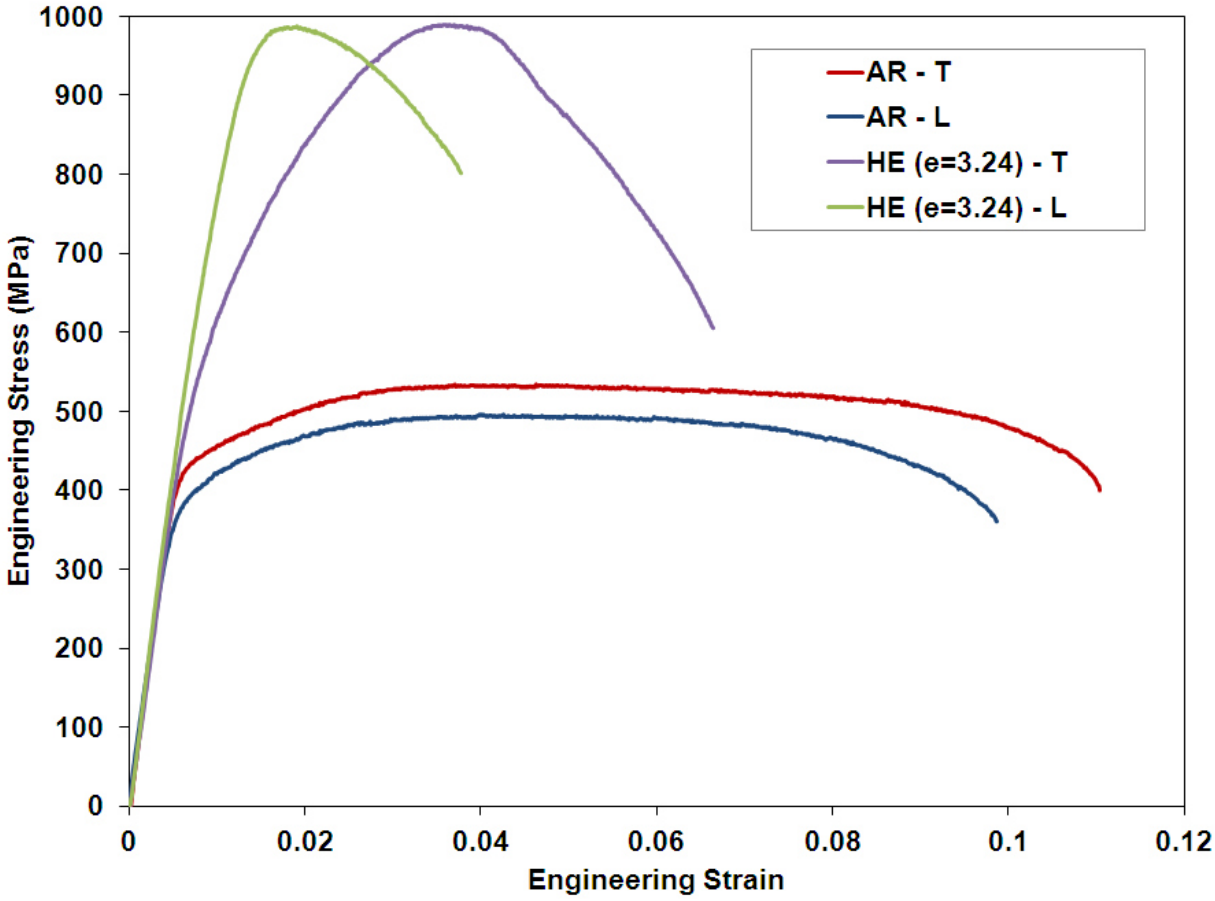

Figure 40. Engineering stress-engineering strain curves for longitudinal (L) and transversal (T) specimens of the as-received CP Ti and hydrostatically extruded CP Ti.

Table 7. Mechanical properties of the as-received and HE processed bars of CP Ti from tensile testing on transversal (T) and longitudinal (L) planes.

	σ_y (MPa)	$\sigma_{0.2}$ (MPa)	σ_{UTS} (MPa)	ε_u (%)	ε_f (%)
AR-T	390±17	445±13	537±12	4.43±0.65	9.82±0.75
AR-L	345±7	395±7	494±1	4.95±0.63	8.97±0.67
$HE_{3.24}$-T	420±29	495±35	995±7	2.65±0.07	5.95±0.07
$HE_{3.24}$-L	573±30	750±70	970±17	0.87±0.16	3.06±0.33

This anisotropy in mechanical properties of the extruded CP Ti may be rationalized based on the crystallographic macrotexture developed in the microstructure during processing. It is well known that dislocation glide and twinning are the main mechanisms operating during plastic deformation of CP Ti [170,171]. The main dislocation slip modes in CP Ti at room temperature are the prismatic <11-20>{10-10} slip system and the basal <11-20>{0001} slip system (Figure 30) having the lowest critical resolved shear stresses [170,172]. Additionally, dislocation glide on pyramidal systems <11-20>{10-11} and <11-23>{10-11} can be also activated. The operating systems are generally determined by the Von Misses criterion, the Schmid factors and the critical resolved shear stress. In the L-specimens, basal planes are suppressed since they are parallel to the tensile axis and two of the prismatic slip planes are suppressed since they are perpendicular to the tensile axis. The remaining four slip planes are inclined at 60º to the tensile axis and can be active. So, the high yield strength of the material can be related to the limited number of prismatic slip systems available. In the T-specimens, the c-axis of the HCP lattice of individual grains is randomly inclined with respect to the tensile axis. Thus, the microstructure will be formed by a combination of soft and hard grains, depending on the individual orientations. The grains that are most favourably orientated for prismatic and basal slip can be easily deformed at lower values of applied stress (soft grains). Localization of plastic slip within these grains results in local strain hardening, and, in turn, in an increase of the flow stress, and in the spread of plastic slip to grains that are less favourably oriented for prismatic and basal slip. This scenario leads to overall high work hardening capacity of the T-specimens. It should be also noted that a higher work hardening ability of these T-specimens delays macro-localization of plastic flow resulting in higher work uniform elongation (~2.7%) and higher elongation to failure (~6%) compared to those for the L-specimens (~0.9% and ~3.1%) according to the well-known Considère criterion [66].

4.3. Bi-axial stretching and formability of studied materials

This section focuses on bi-axial deformation behaviour and formability of the studied metallic materials in the coarse-grained and SPD processed conditions. The effect of microstructure and texture on bi-axial deformation behaviour and formability is analyzed.

4.3.1. Grain size effect on formability of pure copper.

The appearance of specimens of CG CP Cu and ECAP processed CP Cu after small punch testing is demonstrated on Figure 41. It is clearly seen that small punch testing led to formation of dome-shaped cups without specimen failure and the height of domes is not significantly affected by the processing condition.

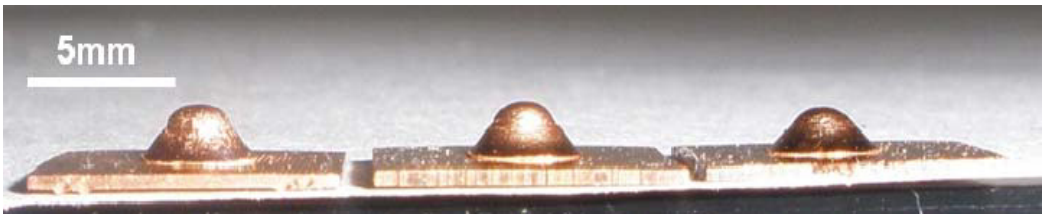

Figure 41. Small punch specimens after testing: left – CG Cu, centre – 2P Cu, right – 12P Cu.

Figure 42 shows load – central deflection curves for all material's conditions. Typical stages of formability curves can be easily identified in all curves and are marked for the 2P Cu on Figure 42 (see Section 3.2.2). The results of small punch testing (maximum load F_{max}, maximum central deflection at maximum load h_{max}, and uniform strain ε) are listed in Table 8. It is seen that the maximum values of load recorded for the 2P Cu and 12P Cu are higher compared to that for the CG Cu. The highest value of the maximum central deflection in stable flow (near the maximum load) is shown by 2P Cu followed by CG Cu and 12P Cu (Table 8).

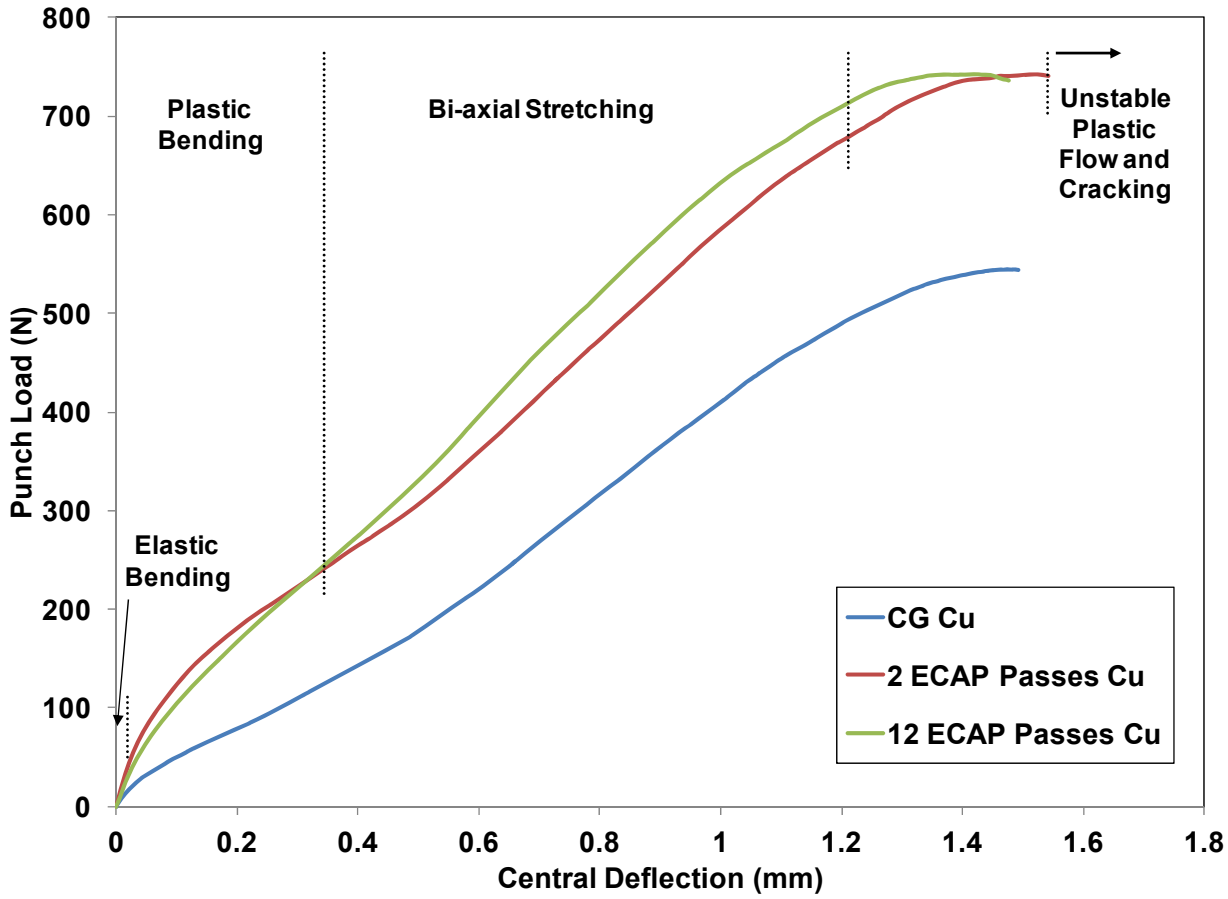

Figure 42. Punch load-central deflection curves for CG Cu and Cu subjected to 2 and 12 ECAP passes.

Table 8. Small punch testing results of CP Cu.

Cu	F_{max} (N)	h_{max} (mm)	$\varepsilon=\ln(t_0/t)$
CG	557±18	1.48±0.10	0.55±0.04
2P	692±24	1.45±0.10	0.68±0.02
12P	712±39	1.40±0.04	0.48±0.01

Equivalent strain was estimated over areas deformed under bi-axial stretching using Equation 28. As it was pointed in experimental procedures (see Section 3.2.2), bi-axial stretching occurs in an annular section of the disc in tension. The areas deformed under bi-axial stretching were located at φ = 20 to 45 deg with respect to the vertical axis of the dome as illustrated in Figure 20. This area is characterized by constant reduction of thickness following the profile of the punch. The estimated values of true equivalent strain are 0.57, 0.66, and 0.47 for CG, 2P, and 12P Cu, respectively. As

seen, these values are in a good correlation with the data on maximum central deflection (Table 8).

SEM observations over surface relief of dome-shaped cups might reveal key features to visualize deformation mechanisms under bi-axial loading. SEM inspections of surface relief on both top of domes and areas deformed by bi-axial stretching were performed (Figure 43 and Figure 44). It can be asserted that CG Cu is bi-axially deformed by dislocation slip the surface relief is similar to that developed during uni-axial tensile testing (Figure 38). Surface relief morphology of the 2P and 12P specimens is somewhat similar to that observed in the necking area of tensile specimens though it shows much higher roughness compared to that of the surface relief in the necking area of the tensile specimens. Profuse microshear banding is observed over the surface of 2P Cu; some small surface areas free of microshear bands are also present. Quantitative analysis of the surface area of 280 x 180 μm^2 showed that the areas free of microshear bands have a diameter up to 30 μm and their surface fraction is nearly 35%.

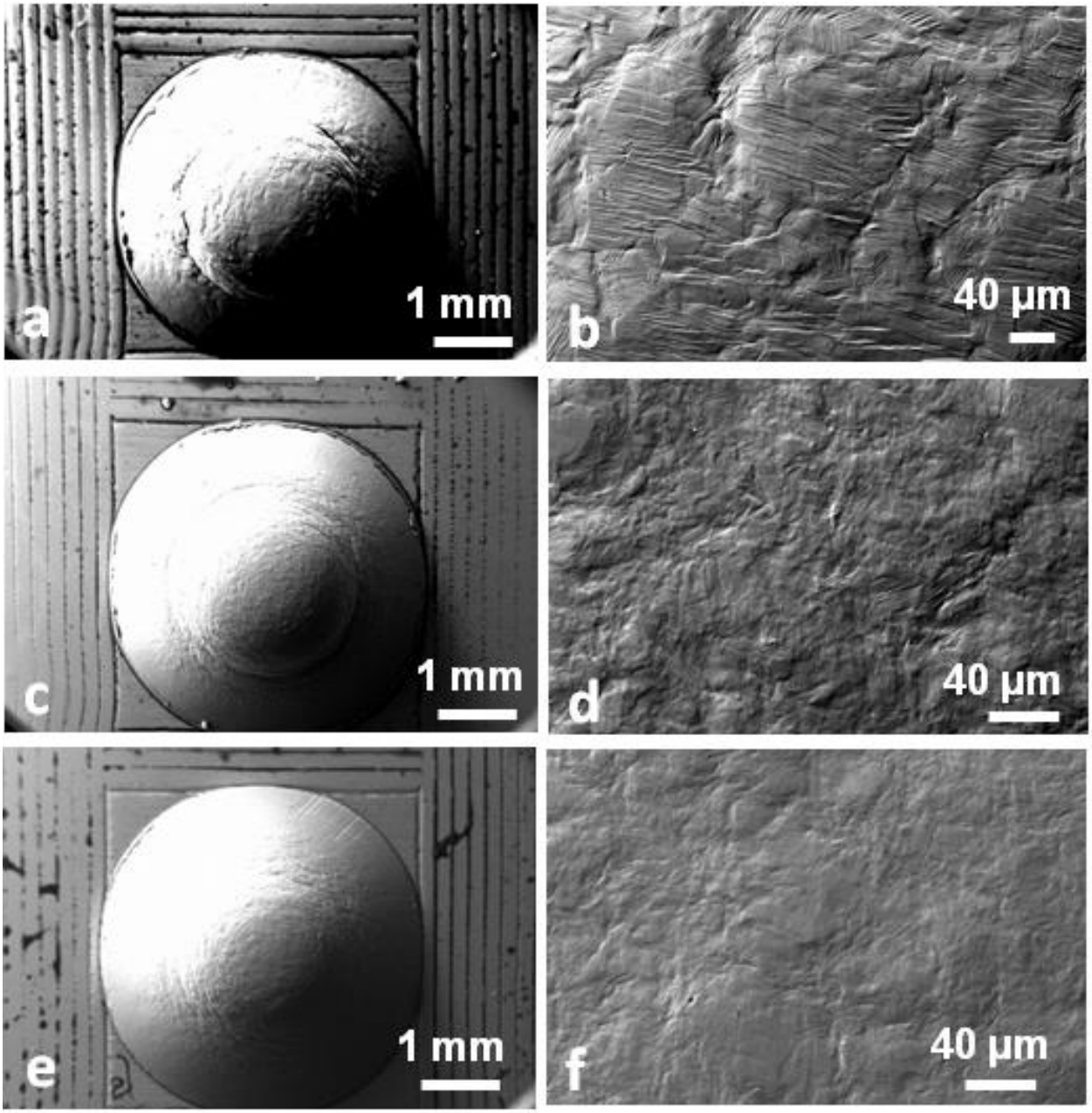

Figure 43. SEM images of small punch specimens: (a) a view of CG Cu; (b) surface relief on the top of the dome in CG Cu; (c) a view of 2P Cu; (d) surface relief on the top of the dome in 2P Cu; (e) a view of 12P Cu; (f) surface relief on the top of the dome in 12P Cu.

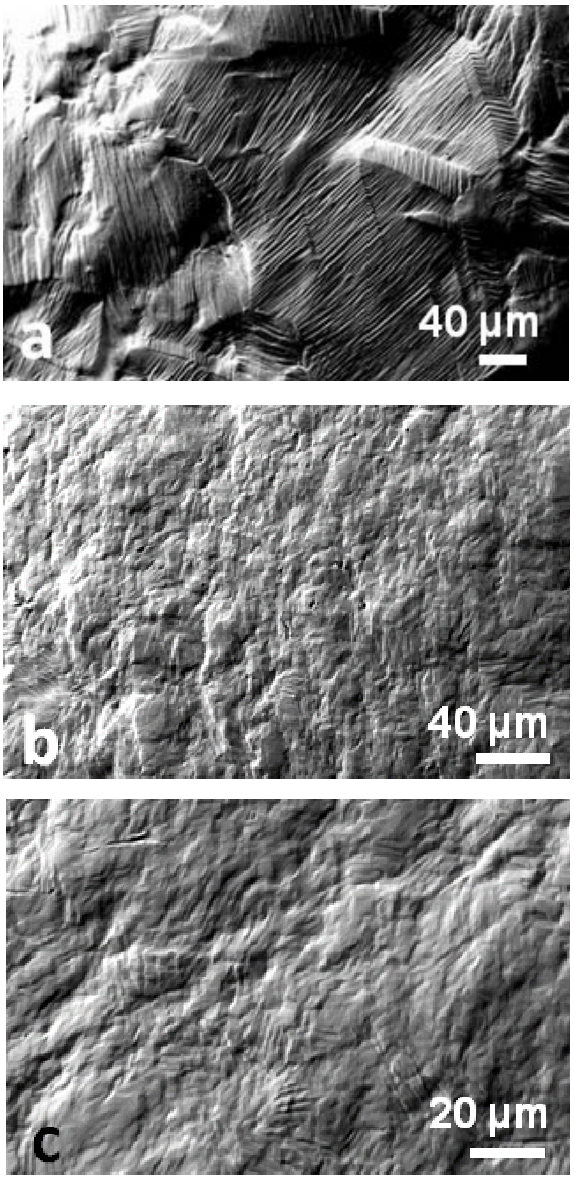

Figure 44. SEM images of surface relief of the small punch specimens in the area of bi-axial stretching for: (a) CG Cu; (b) 2P Cu; (c) 12P Cu.

The very inhomogeneous character of surface relief after small punch testing was confirmed by results of the AFM analysis. Figure 45 shows 3D AFM topography images in the area of bi-axial deformation of the 2P and 12P Cu specimens after small punch testing. The results of the quantitative analyses of surface profiles through 3D AFM topography images are presented in Table 9. Surface relief of 2P Cu is characterized by a high density of step-like micro shear bands having average length in the range of 7-25 µm and a width in the range 30-810 nm (Table 9). Their volume fraction is about 34%. The surface relief of the 12P Cu specimen is inhomogeneous, as well (Table 9). The morphology and dimensions of the microshear bands are similar to those observed

in the 2P Cu specimen, though the 12P Cu has a lower volume fraction of microshear bands, 25%.

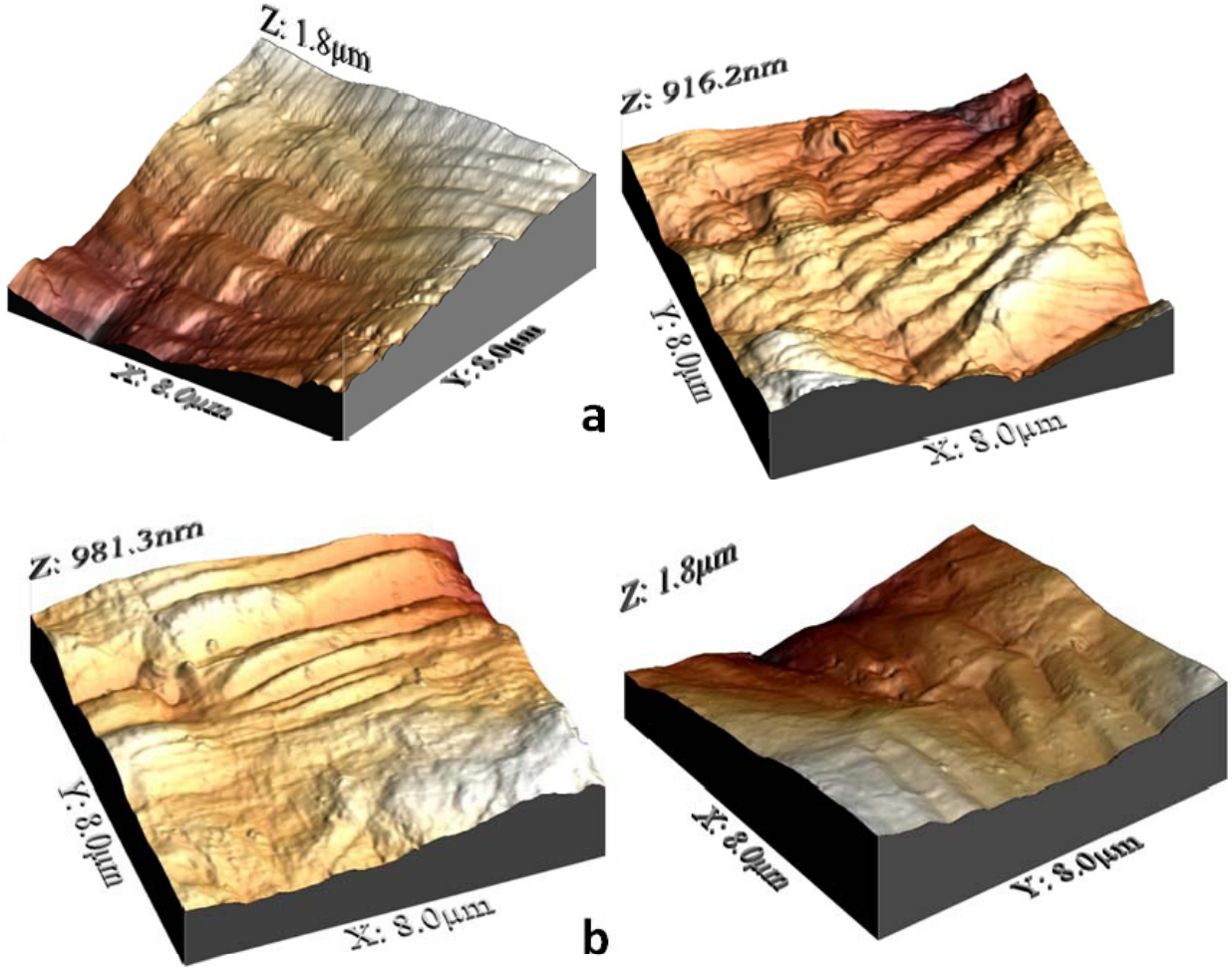

Figure 45. Typical 3D AFM topography images in bi-axial stretching areas for (a) 2P Cu and (b) 12P Cu.

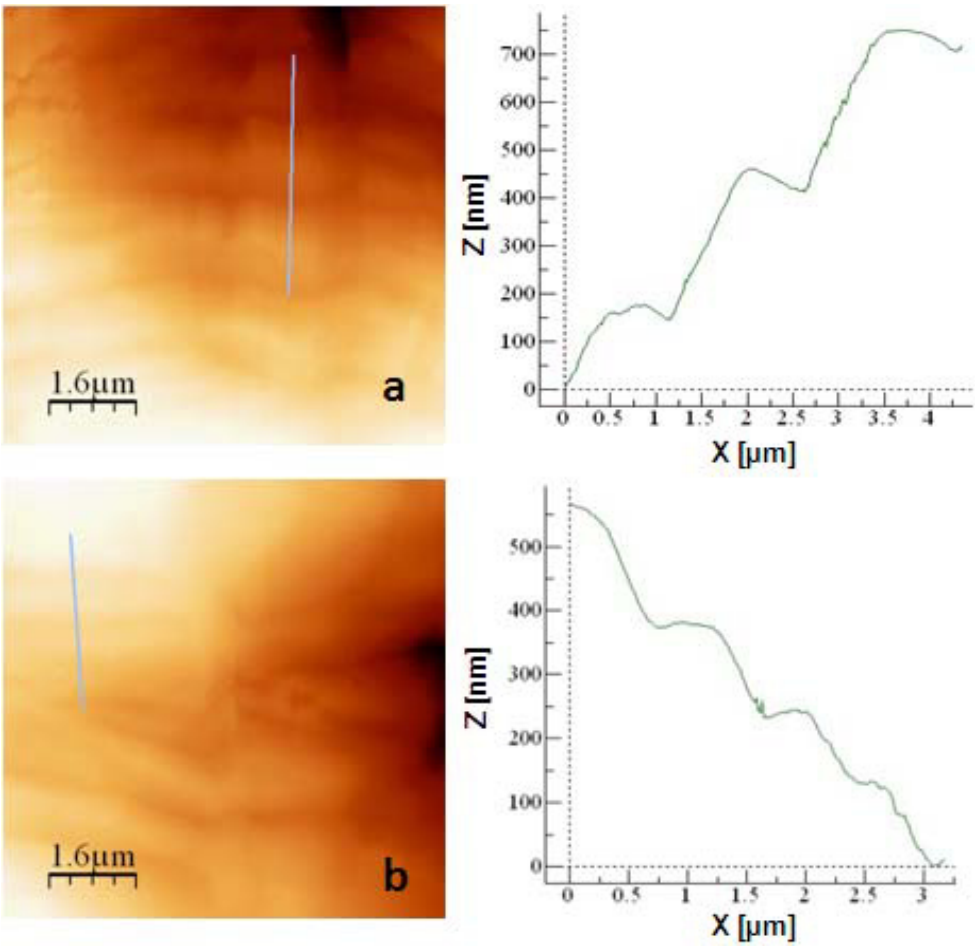

Figure 46. 2D AFM topography images and profiles for (a) 2P Cu; (b) 12P Cu.

Table 9. Dimensions, local surface fraction of micro shear bands, and surface fraction of areas containing micro shear bands on surface relief for the as-ECAP processed CP Cu.

Number of ECAP passes	Dimensions of shear bands			Average local volume fraction of shear bands (%)	Surface fraction of areas containing shear bands (%)
	Length (µm)	Width (nm)	Step height (nm)		
2	7-25	30-810	50-280	34	96
12	4-23	100-900	50-200	25	65

Numerous publications have documented the appearance of shear bands in the UFG and NS materials [27,106,107,112,173,174,175,176,177,178]. It should be note that the contribution of this profuse microshear bands activity into plastic flow can be very significant [175,179]. For example, the contribution of microshear banding during uni-

axial tensile deformation of the UFG AA6082 provided 9% out of 20% of uniform elongation, i.e. almost half of the total plastic deformation [179]. In the case of bi-axial stretching, the calculation of contribution of microshear banding into uniform elongation is a complex task and it has not been carried out in frames of this work. However, the qualitative analysis of the experimental results presented above clearly shows higher contribution of microshear banding into plastic deformation of the 2P Cu, thus, leading to its higher formability compared to that of the 12P Cu.

What could be the reasons for such extensive microshear banding during bi-axial stretching of ECAP processed Cu at room temperature? The first most obvious reason could be related to the microstructure inhomogeneities that allow stress redistribution at the micro-scale and localization of plastic flow in form of microshear bands. Indeed, 2P Cu specimens show higher activity of microshear bands due to more inhomogeneous microstructure compared to that of 12P Cu. The second mechanism might be linked to the presence of microshear bands inserted in the microstructure during ECAP processing. Bi-axial stretching can trigger their further growth. This assumption is also well supported by a good correlation between width of microshear bands observed in the microstructure of 2P Cu and those observed on surface relief of the 2P Cu small punch specimens. A body of research has shown that cooperative grain boundary sliding might also trigger formation of microshear banding in the UFG metallic materials [144,178]. Clear evidences of grain boundary sliding were found on the surface relief of specimens after small punch testing so this mechanism of microshear banding formation might play an important role.

It was reported that nanovoids and second phase precipitates often act as nucleation sites for microshear bands [106]. However these mechanisms can be ruled out since these microstructural features are not present in the ECAP processed CP Cu.

An earlier study on uni-axial tensile deformation of nanocrystalline pure copper demonstrated near-perfect elastoplasticity of the material at room temperature [113]. Nanocrystalline Cu deformed uniformly up to high strains without any work hardening and necking. This was explained by grain boundary-mediated mechanisms. Our results reveal that UFG pure copper undergoes work hardening during uni-axial tensile deformation (Figure 37, Table 5). Work hardening is also seen in the load-central deflection curves during plastic bending and bi-axial stretching stages (Figure 42). Flow

stress is a function of load and some other parameters related to specimen and die geometry. Since all these parameters are common for all tested material conditions, flow stress should be linearly proportional to the load applied. In spite of grain boundary sliding does provide some slight contribution to the total plastic deformation, the predominance of grain boundary-mediated mechanisms during bi-axial stretching of the as-ECAP Cu can be ruled out as well.

4.3.2. The effect of grain size and dispersoids on formability of the Al2024 alloy

Figure 47 shows typical punch load – central deflection curves of the longitudinal and transversal specimens of the extruded Al2024 alloy and for its coarse grained counterpart. The results of analysis of these tests are summarized in Table 10. It is clearly seen that the hydrostatic extrusion leads to significant reduction of maximum central deflection and true strain induced in the area of bi-axial stretching. In the hydrostatically extruded material, and effect of specimen orientation on both parameters can be noted. The T-specimens demonstrate somewhat higher load (515.7 N), higher maximum central deflection (0.41 mm) and true strain (0.04) compared to those of the L-specimens (398 N), (0.40 mm) and (0.02), respectively.

It should be noted that the coarse-grained Al2024 alloy shows much lower values of the maximum central deflection compared to that reported for this material in [180] (see Figure 47 and Figure 48). The same tendency can be noted for the hydrostatically extruded materials: the h_{max}-values are lower compared to those reported for the ECAP processed Al2024 alloy in [180]. The load-displacement curves from our tests (Figure 47) and for the Al2024 alloy studied in [180] show that our material fails already at the stage of plastic bending not even having reached the stage of bi-axial stretching. Analysis of the surface relief of our specimens after small punch testing (Figure 49) shows that coarse dispersoids having a size of 10 μm act as nucleation sites for formation of micro-cracks: the cracks are easily formed at these dispersoids and grow into the matrix, thus, leading to specimen failure. Taking into account that hydrostatic extrusion resulted in cracking of coarse dispersoids as well as T-particles and formation of voids in the material, it can be suggested that no any further manipulation with the microstructure of the supplied Al2024 alloy after hydrostatic extrusion can lead to improvement of its formability.

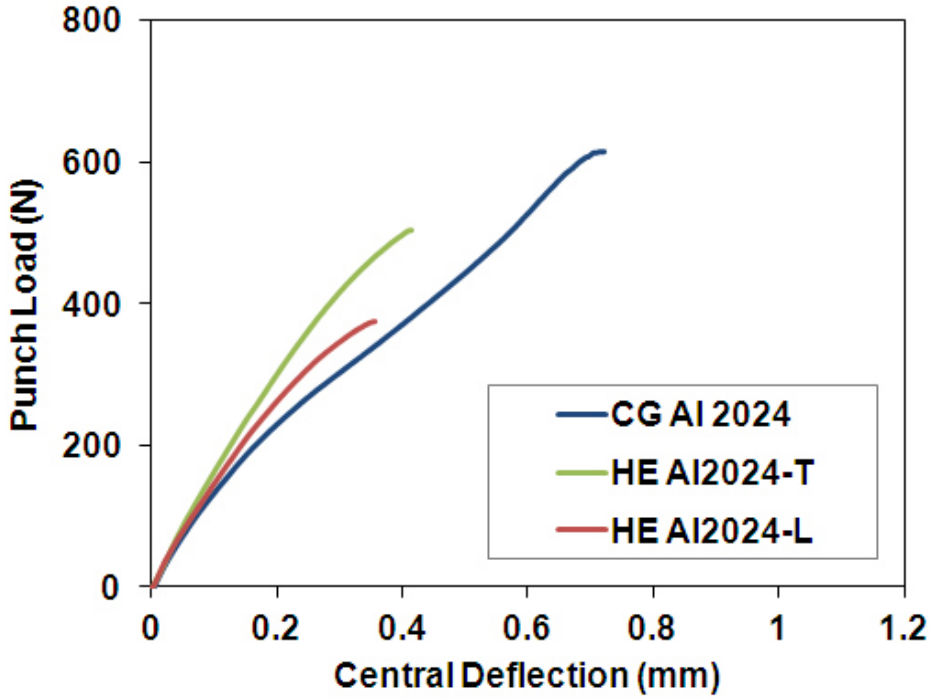

Figure 47. Load – central deflection curves of longitudinal (L) and transversal (T) specimens for coarse grained and hydrostatic extruded Al2024 alloy.

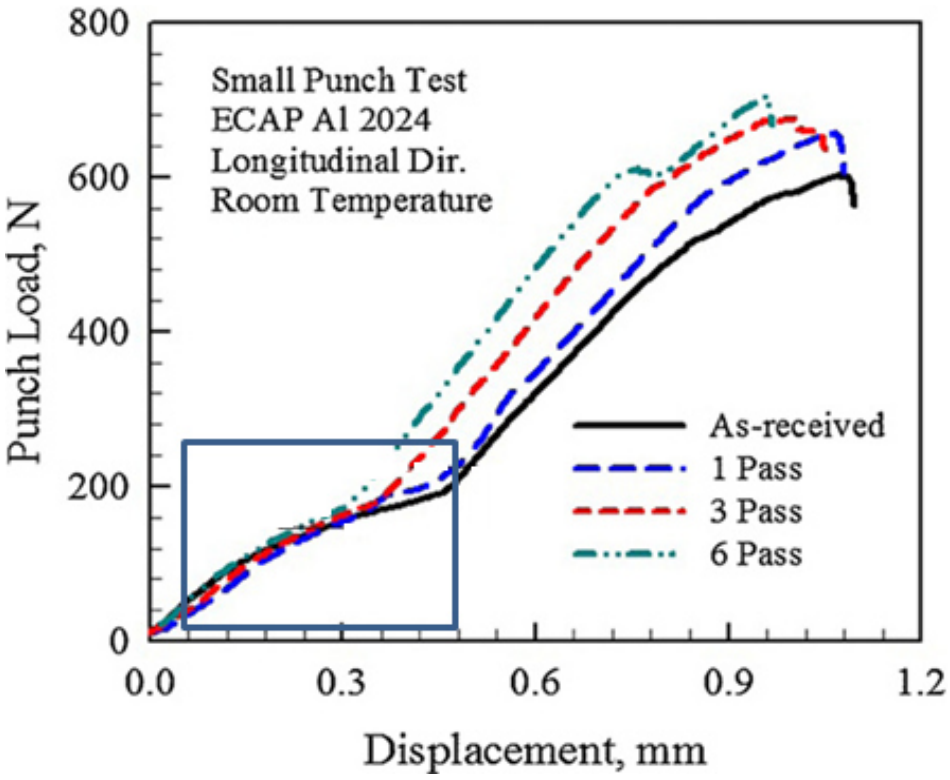

Figure 48. Results of small punch test for L-specimens machined along the longitudinal direction of over-aged aluminum 2024 alloy subjected to one, three and six ECAP passes at 150ºC. The curves are reproduced from [180].

Table 10. Results of small punch testing of coarse grained (CG) Al2024 alloy and the HE processed Al2024 alloy in longitudinal (L) and transversal (T) sections.

Sample	F_{max} (N)	h_{max} (mm)	ε
CG	617±5	0.74±0.03	0.14
HE-T	515±7	0.41±0.03	0.04
HE-L	398±32	0.35±0.03	0.02
CG alloy tested in [180]	~590	~1.05	n/a

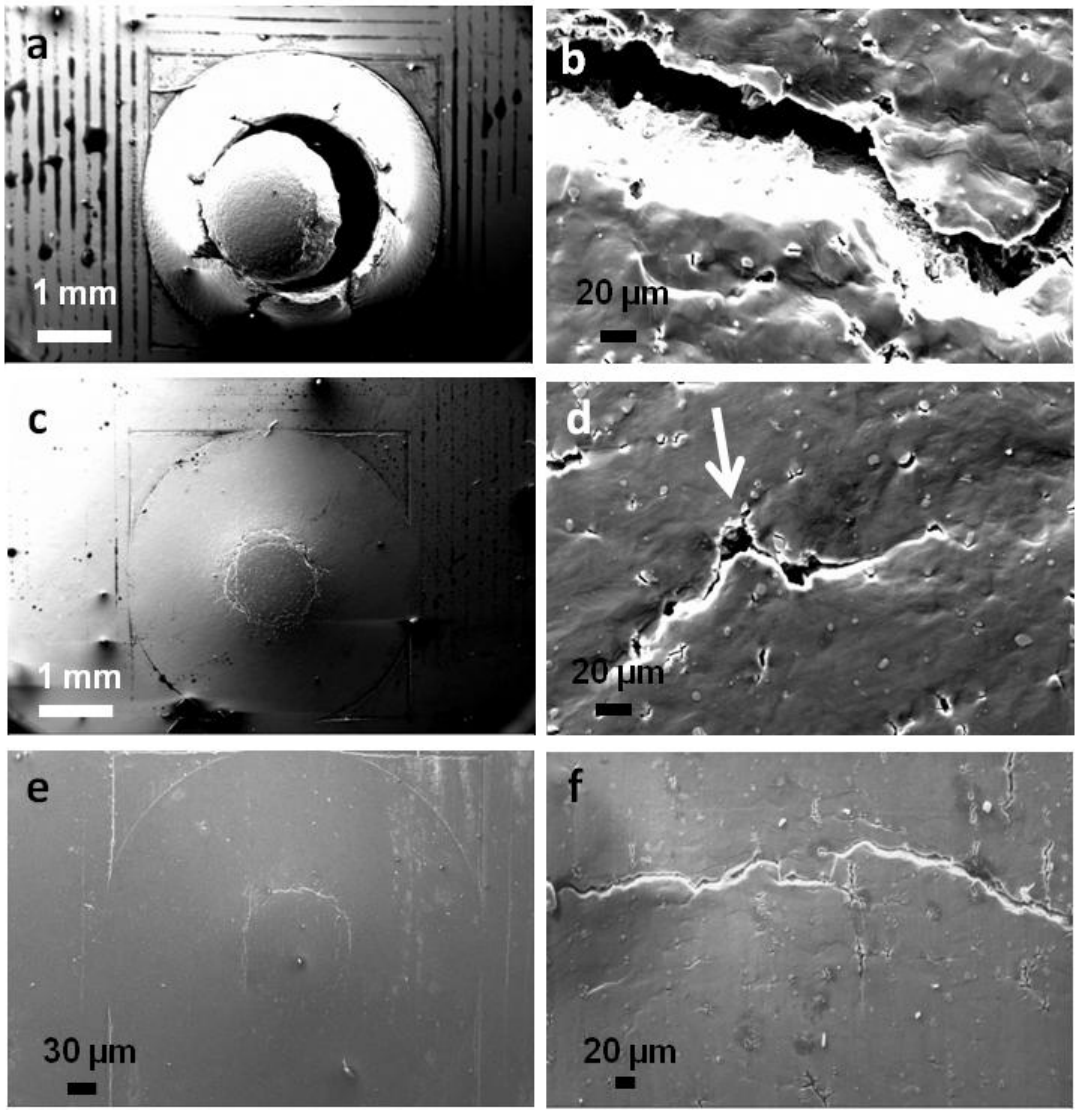

Figure 49. SEM images of the surface relief for the small punch Al2024 specimens: (a) general view of the CG specimen; (b) crack at higher magnification for the CG condition; (c) general view of the HE-T specimen; (d) crack at higher magnification for the HE-T condition; (e) general view of the HE-L specimen; (f) crack at higher magnification for the HE-L condition.

Some anisotropy of bi-axial deformation behaviour in the HE processed Al2024 alloy can be related mainly to the microstructure developed in the material during hydrostatic extrusion, namely, (1) T-phase particles elongated along the extrusion direction and (2) grains/subgrains elongated along the extrusion direction. The micro-cracks formed (or already present) during small punch testing can easily grow along the grain boundaries in the L-specimens or, in other words, in the direction perpendicular to the punch axis along the extrusion direction forming long macro-cracks which lead to the material failure. It can be generally concluded that the formability of the studied Al2024 alloy is limited due to the presence of coarse dispersoids. No further manipulation of microstructure can lead an increase of formability unless the coarse dispersoids are dissolved.

4.3.3. Grain size and texture effect on formability of CP Ti

The appearance of the CG and hydrostatically extruded Ti specimens after small-punch testing is demonstrated on Figure 50. A visual inspection reveals that the dome height of the coarse-grained specimens is remarkably higher compared to that of the hydrostatically extruded material.

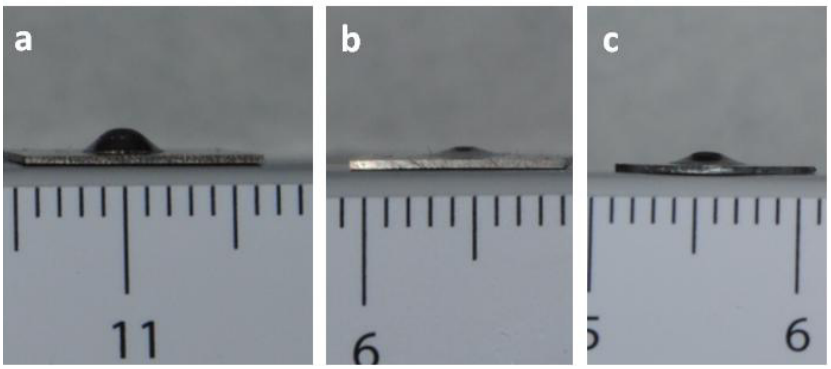

Figure 50. Appearance of Ti specimens after small-punch testing: (a) the as-received L-specimen; (b) the HE processed L-specimen; (c) the HE processed T-specimen.

The load-central deflection curves from small punch testing of the as-received and extruded CP Ti are presented on Figure 51. The typical stages of formability behaviour are marked on the curve for the as-received specimens (see Section 3.2.2). The results of small punch testing are listed in Table 11. No anisotropy of the bi-axial deformation behavior is observed in the as-received CG material, it is seen that the load-central deflection curves for the L- and T- small punch specimens nearly coincide and have the

same maximum central deflection of ~1.3 mm (Figure 51) and true uniform strain of 0.35-0.4 induced in the specimens during small punch testing. It is also seen that hydrostatic extrusion leads to significant increase of the load required for deformation of small punch specimens to the same central deflection as well as to significant reduction of the maximum central deflection leading to the lower values of the true strain which can be induced in the specimens during small punch testing (Table 11). The HE processed material shows anisotropy of bi-axial deformation behaviour. First, the load-central deflection curves tend to show somewhat higher load required for bi-axial deformation of the L-specimens in the bi-axial stretching regime (Figure 51). Second, the L-specimens display lower maximum central deflection (~0.6 mm) and lower value of true uniform strain induced into sample during small punch testing (0.12) compared to those for the T-specimens (~0.8 and 0.06 mm, respectively) (Table 11).

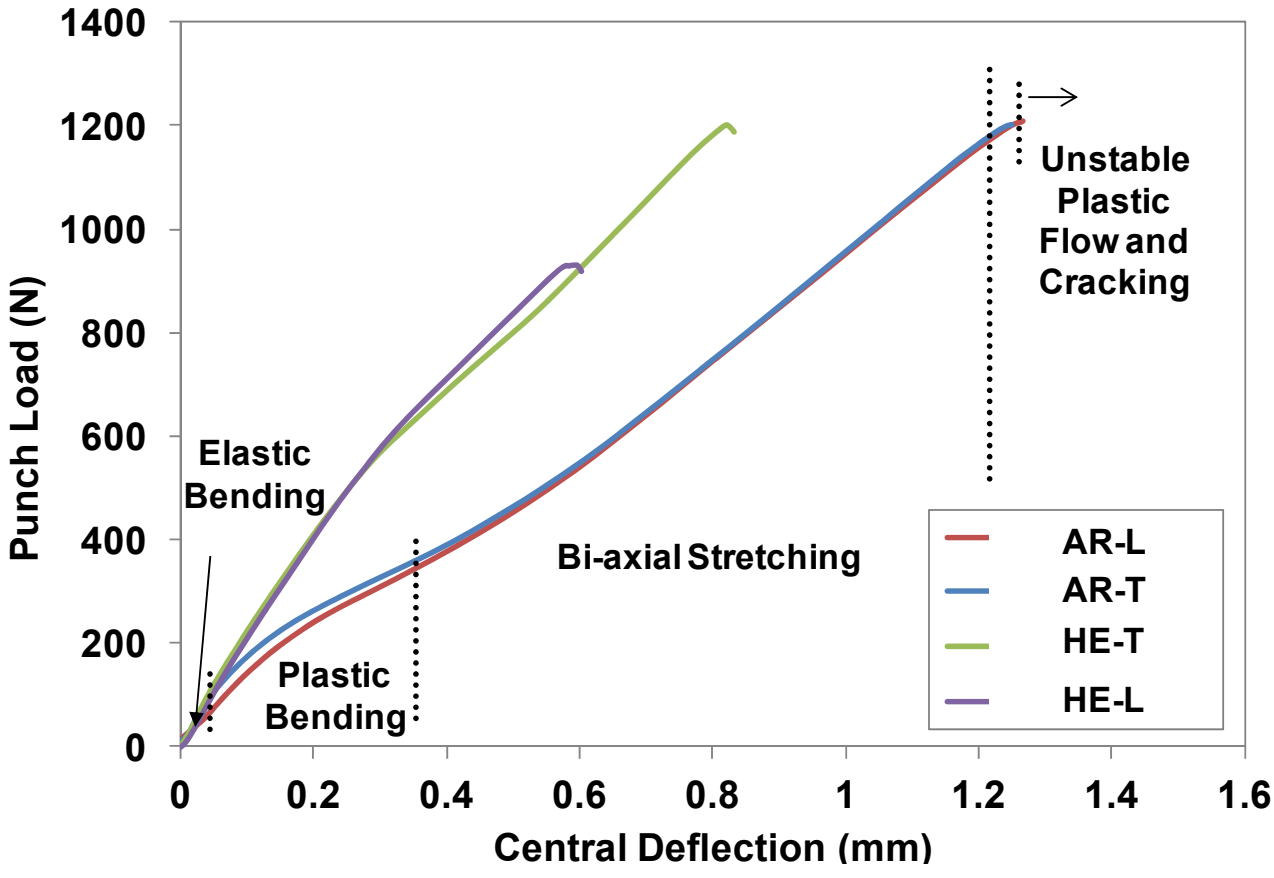

Figure 51. Punch load-central deflection curves for transversal (T) and longitudinal (L) sections of the as-received and the HE processed CP Ti.

Table 11. Results of small punch testing for transversal (T) and longitudinal (L) specimens of the as-received and the HE processed CP Ti.

Sample	F_{max} (N)	h_{max} (mm)	ε
AR-T	1243±47	1.3±0.05	0.4±0.01
AR-L	1213±23	1.27±0.05	0.35±0.02
$HE_{3.24}$-T	1163±34	0.79±0.03	0.12±0.03
$HE_{3.24}$-L	910±59	0.60±0.02	0.05±0.008

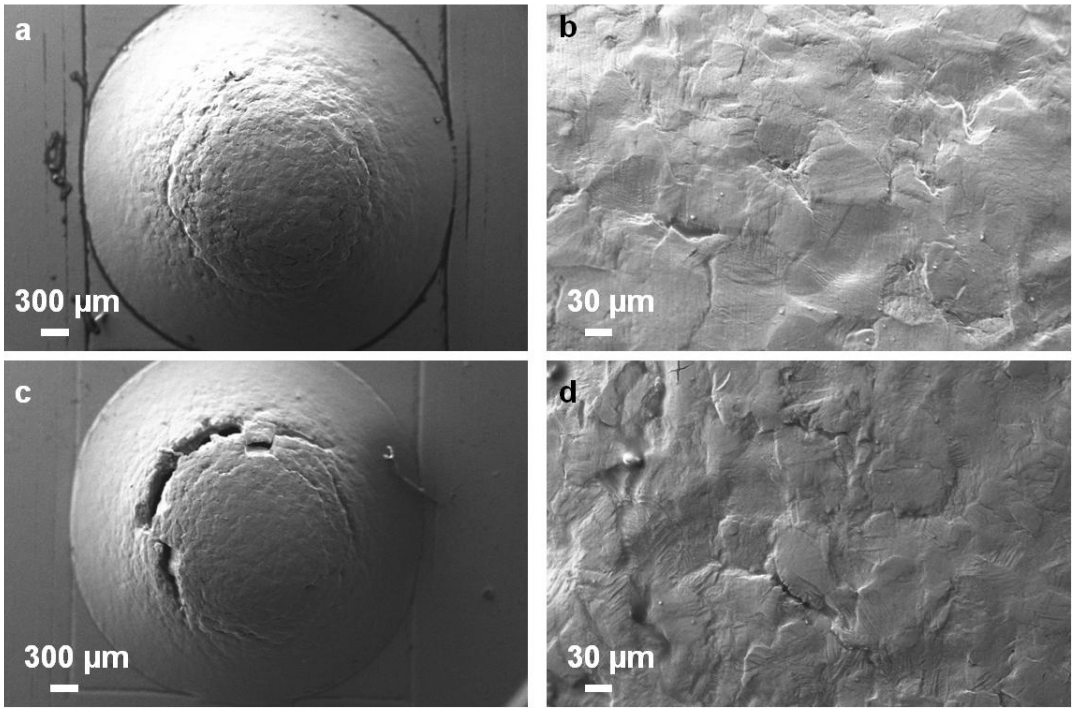

Figure 52. SEM images of surface relief on the coarse-grained CP Ti after small punch testing: (a) general view of the dome and (b) area at *φ*~30º of the T-specimen; (c) general view of the dome and (d) area at *φ*~30º of the L-specimen.

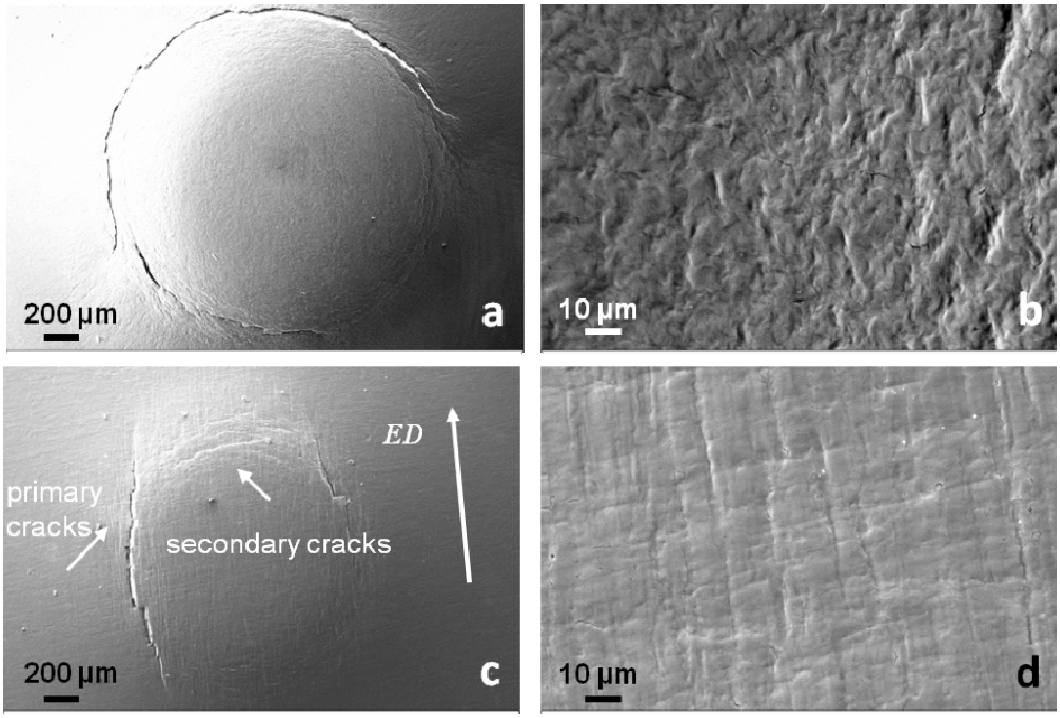

Figure 53. SEM images of surface relief on the hydrostatically extruded CP Ti after small punch testing (a) general view of the dome and (b) area at φ~30º of the T-specimen; (c) general view of the dome and (d) area at φ~30º of the L-specimen.

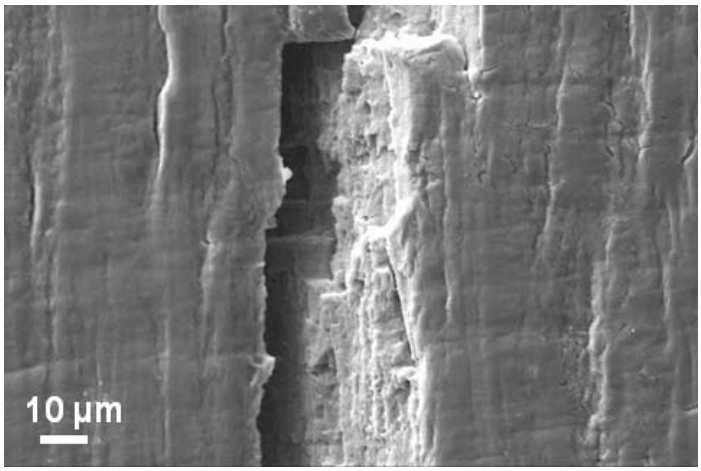

Figure 54. SEM image of a primary crack on L-specimen at higher magnification.

Surface analysis of the small punch specimens tested up to cracking showed a significant anisotropy in failure behaviour of the L- and T-specimens after hydrostatic extrusion. This anisotropy is not observed in the coarse-grained specimens (Figure 52) where dislocation and twinning activity are the mean deformation mechanisms in both planes of the CG Ti bars. The hydrostatically extruded T-specimens showed formation

of cracks at φ~60^{o} (Figure 20) which are concentric to the dome (Figure 53 a). These cracks were formed in the symmetric manner with respect to the dome axis. Some evidence of microshear banding was observed in the area of bi-axial stretching and the length of microshear bands was in the range of 5-15 μm (Figure 53 b). Two types of cracks were observed in the L-specimens: primary long cracks were formed along the extrusion direction at φ~50...60^{o} and their further growth to the length of 200...400 μm was accompanied by formation of secondary cracks which were perpendicular to the extrusion direction (Figure 53 c, d and Figure 54). The anisotropy in bi-axial deformation and failure behaviour of the hydrostatically extruded material can be related to (1) the lamellar-type microstructure and (2) to the very strong crystallographic fibre texture developed during hydrostatic extrusion. Indeed, in the T-specimens, the *c*-axis and two prismatic planes of the HCP lattice are perpendicular and all basal planes are parallel to the punch axis, thus, resulting in homogeneous bi-axial plastic deformation in the area of bi-axial stretching followed by failure which is symmetrical with respect to the dome axis (Figure 55 a). In the L-specimens, the *c*-axis, basal planes, and prismatic planes are randomly inclined with respect to the punch axis (Figure 55 b). Therefore, combinations of grains with various crystallographic orientations can be present in the microstructure of the L-specimens. Some combinations of soft grains and hard grains can lead to formation of the quasi-cleavage facets [181] which, in turn, can easily lead to their quick growth along lamellae boundaries since SPD processed Ti tends to show a low crack growth resistance [16].

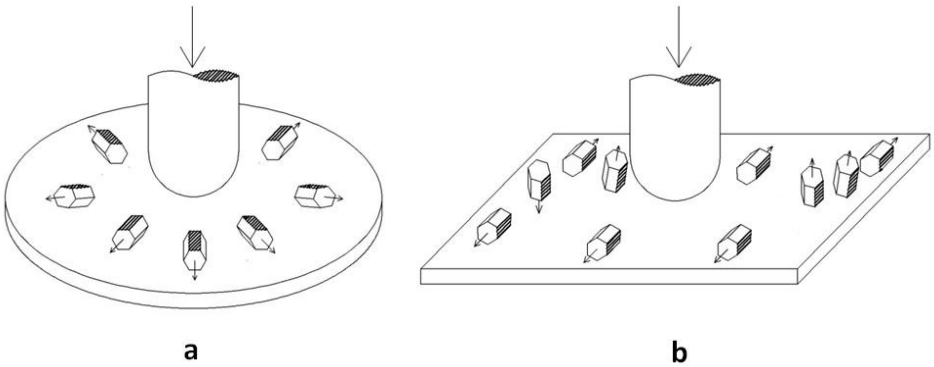

Figure 55. Schematic drawing of crystallographic texture of extruded CP Ti during small-punch testing (a) of T-specimen; (b) of L- specimen.

4.3.4. Temperature effects on formability of CP Ti

As it is seen from the previous section, the hydrostatically extruded Ti samples show very low formability compared to the CG material. How can one increase its formability? In [182], the SPD processed pure Ti rods were subjected to annealing treatments at 350ºC for 6 h leading to recovery and change of grain boundary structure. The UFG pure Ti after this annealing treatment showed higher ductility and enhanced fatigue life without any loss of its strength. Moreover, it was demonstrated that in biaxial deformation, the annealed cryo-rolled pure aluminium showed relatively good elongations [183]. Therefore, the first approach could be to study the possibility of improvement of materials formability applying annealing treatments.

It is well known that ductility/formability of metallic materials including Ti tends to increase with increasing temperature [184]. Therefore, the bi-axial stretching at elevated temperatures of the UFG pure Ti could be another strategy to increase its formability. Other deformation mechanisms such as enhanced diffusion and dislocation climb can be activated at elevated temperatures, thus, providing higher formability. However, one should be aware of the fact that UFG metals and alloys can easily undergo deformation induced grain growth and/or dynamic recrystallization during metalforming operations at elevated temperatures that can lead to significant decrease of their final mechanical strength.

4.3.4.1. Annealing temperature effect

To choose the correct temperature for annealing treatments, the HE processed samples ($HE_{3.24}$-Ti) were subjected to annealing at 300ºC, 350ºC and 400ºC for 1 and 5 h. the selection of this temperature range is rationalized based on the earlier work [182] as well as the fact that the annealing temperatures should be much less than recrystallization temperature in the SPD processed pure Ti which was reported to be in the range of 620-760ºC [165,166].

Figure 56 illustrates the effect of annealing treatments on the microhardness of the specimens. It is clearly seen that the HE processed material retains its microhardness after annealing at 300ºC and 350ºC. However, it was observed the slight detriment of microhardness after annealing at 400ºC. Thus, the temperature of 350ºC appears as the most appropriate annealing temperature for this work. The TEM analysis of the

specimens annealed at 350ºC for 5 h has demonstrated that the annealing led to decrease of dislocation density in the grain/lamellae interior due to the climb of statistically stored dislocations and their annihilation or their absorption by grain boundaries acting as dislocations sinks (Figure 57). The grain boundaries became well defined as annealing leads to relaxation of non-equilibrium grain boundaries and to decrease of their excess energy (Figure 57) [70].

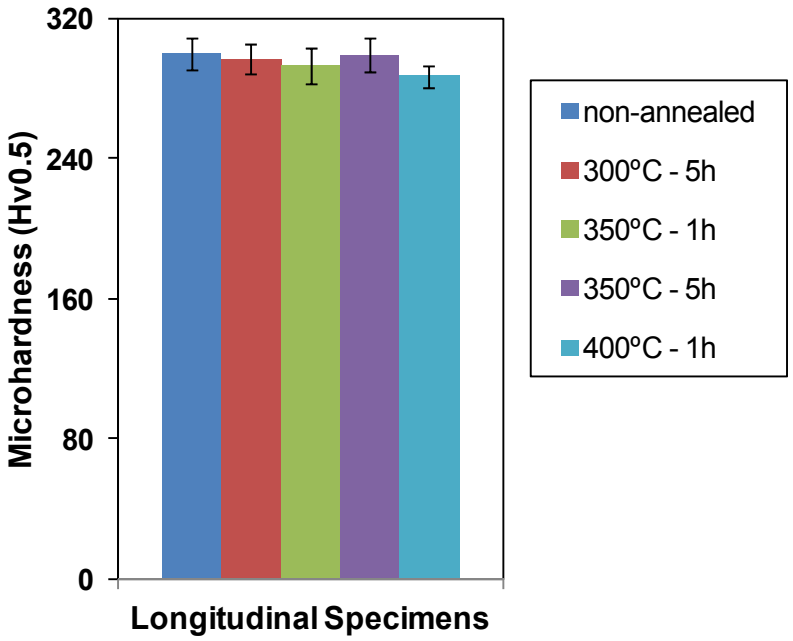

Figure 56. Microhardness values for the non-annealed and annealed (at different conditions) L-specimens of the HE processed CP Ti.

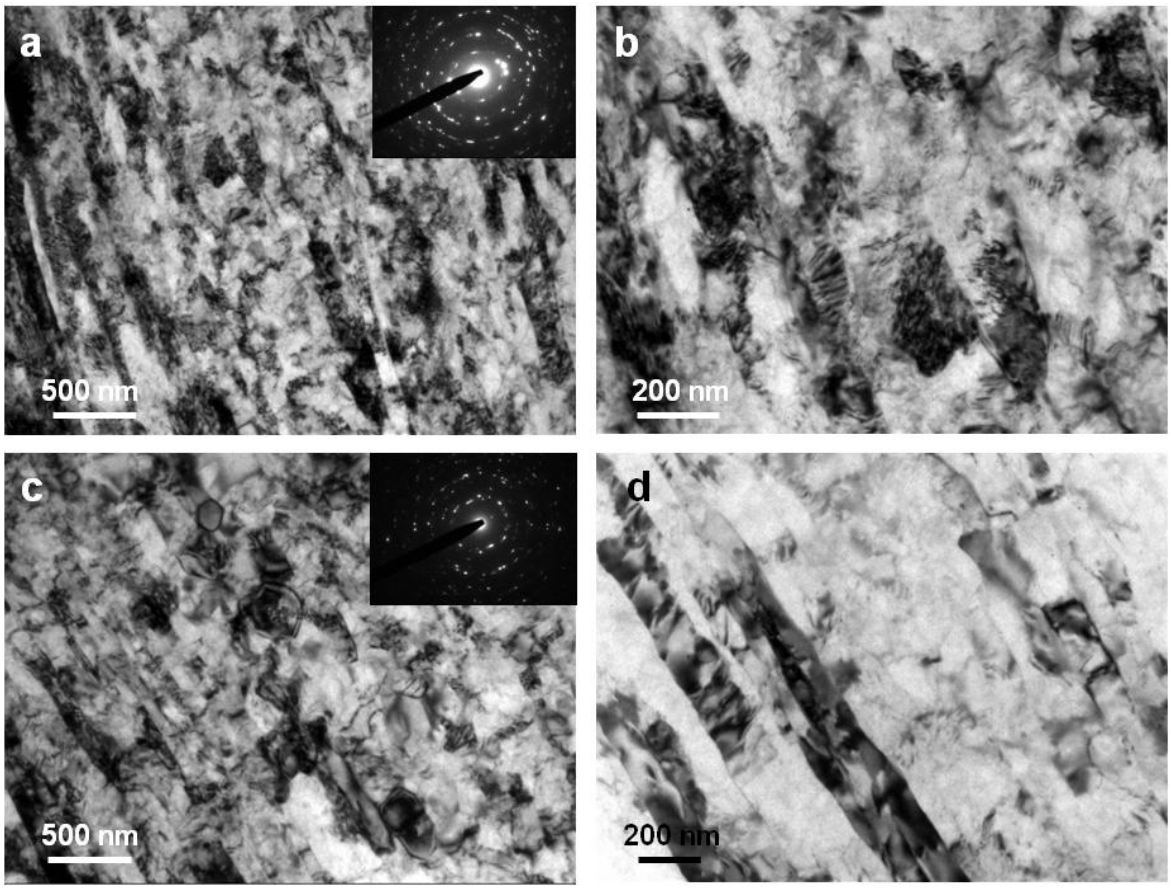

Figure 57. Bright field TEM images and SAED patterns of (a, b) hydrostatically extruded Ti and (c, d) hydrostatically extruded and annealed Ti at 350ºC for 5h.

The uni-axial tensile behaviour of the annealed specimens was carefully analyzed. Engineering stress – engineering strain curves show that tensile strength and ductility properties are not significantly affected by this annealing treatment (Figure 58). However, a slight enhancement of work hardening and ductility for L-specimens is promoted and, in turn, it leads to a slight increase of the ultimate tensile strength.

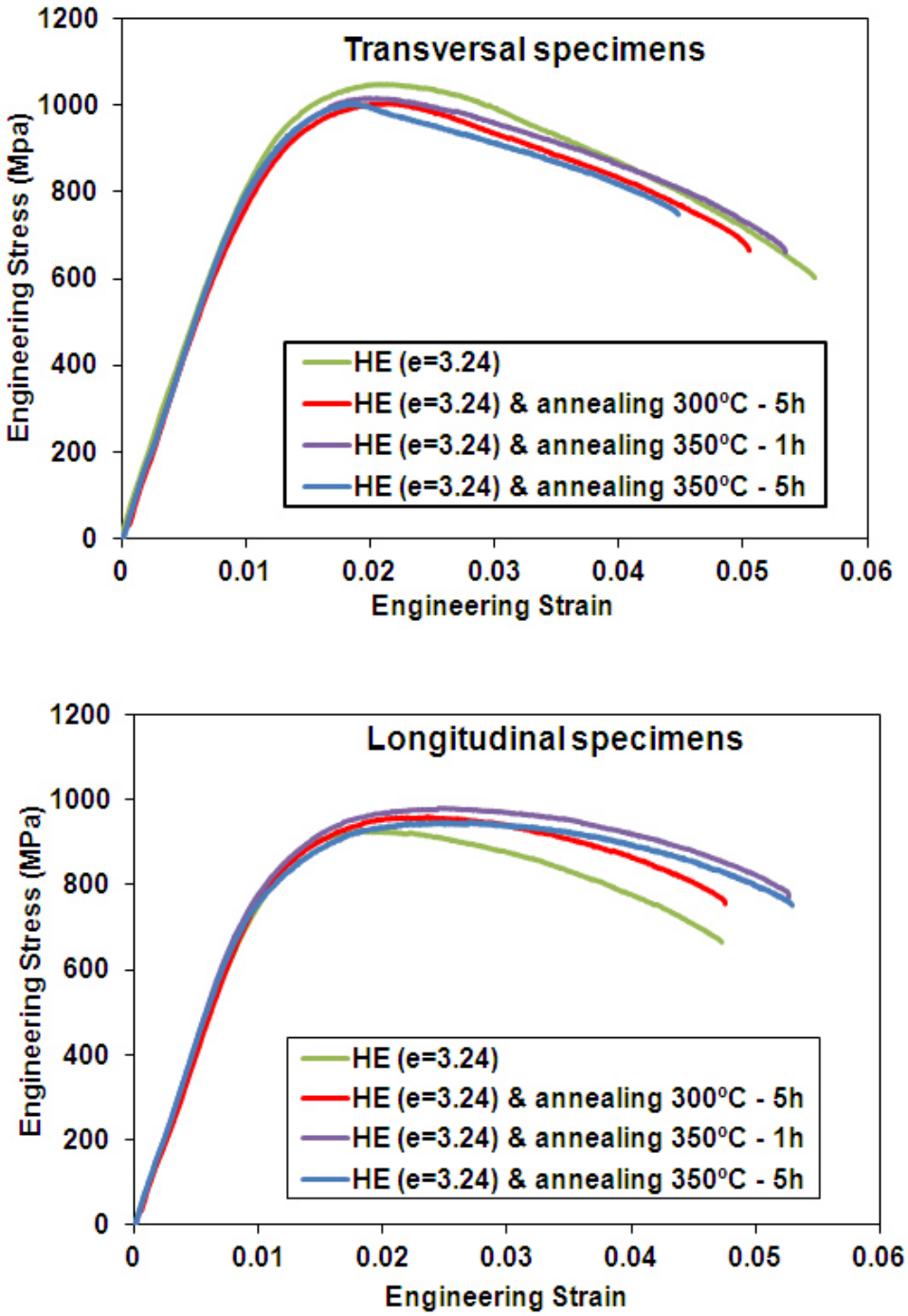

Figure 58. Engineering stress – strain curves for T- and L-specimens after hydrostatic extrusion and annealing treatments.

The effect of annealing treatments on the appearance of the specimens after small punch testing is illustrated in Figure 59. Typical load – central deflection curves obtained from small punch testing of the annealed specimens are presented in Figure 60. It is seen that the annealing leads to some decrease of load during small punch testing (Figure 60, Table 12). No any improvement of maximum central deflection and

true strain induced into specimens during bi-axial stretching is observed in the T-specimens (Figure 60), whereas the L-specimens demonstrate an increase of these parameters (Figure 60), though the ability of the material to undergo bi-axial stretching in the L-plane still remains low compared to that on the T-plane. This small increase can be related to the higher ability of the annealed HE material to accumulate dislocations in the grain interior. Thus, it can be outlined that application of annealing treatments is not an effective way to improve formability of the UFB CP Ti produced via HE processing.

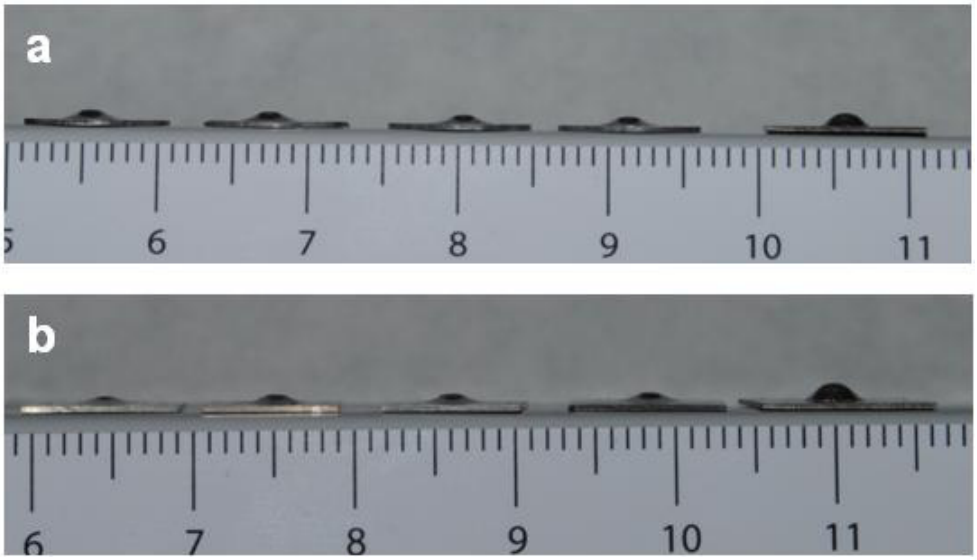

Figure 59. Appearance of the small-punch specimens (a) from the T- section; (b) from L-section of the CP Ti bars. From left to right: hydrostatically extruded specimen, hydrostatically extruded and annealed specimen at 300ºC for 5 h, at 350ºC for 1 h, at 350ºC for 5 h and the as-received CG condition.

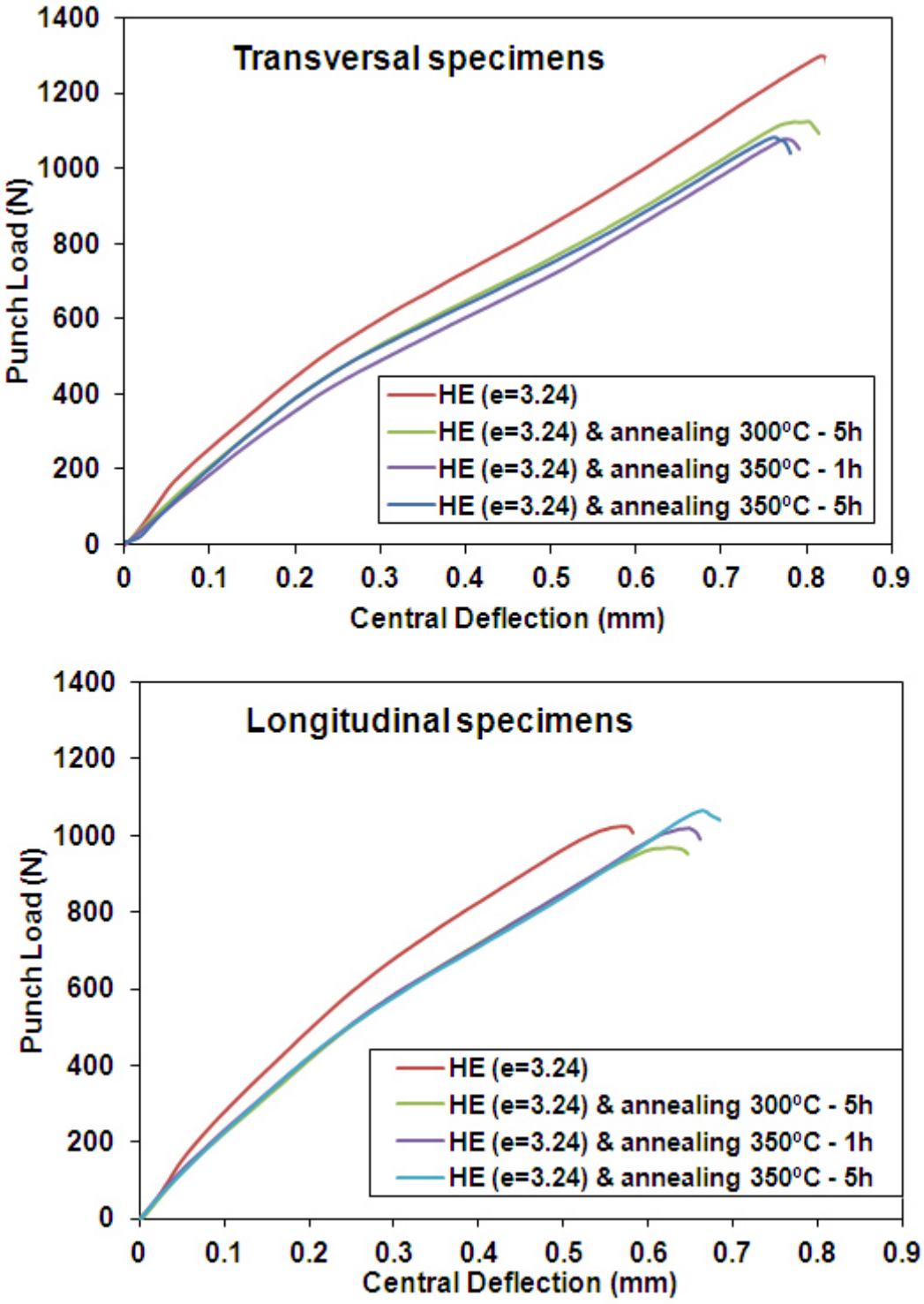

Figure 60. Load – central deflection curves for L- and T-specimens after hydrostatic extrusion and annealing treatments.

Table 12. Results of small punch testing for transversal (T) and longitudinal (L) of hydrostatically extruded and annealed CP Ti.

		F_{max} (N)	h_{max} (mm)	ε
$HE_{3.24}$	**T**	1163±34	0.79±0.03	0.12
	L	910±59	0.60±0.02	0.05
$HE_{3.24}$ & annealing at 300ºC for 5 h	**T**	1120±10	0.78±0.02	0.12
	L	945±35	0.63±0.01	0.07
$HE_{3.24}$ & annealing at 350ºC for 1 h	**T**	1073±12	0.76±0.06	0.1
	L	1030±26	0.67±0.01	0.07
$HE_{3.24}$ & annealing at 350ºC for 5 h	**T**	1070±17	0.76±0.06	0.08
	L	1080±28	0.67±0.07	0.07

Analysis of the surface relief of the small-punch specimens reveals that there is no significant effect of annealing treatments on the surface relief of hydrostatically extruded Ti (Figure 61). Transversal specimens deform and fracture in a symmetric way, while in the L-specimens, the primary and secondary cracks are found parallel and perpendicular to extrusion direction, respectively.

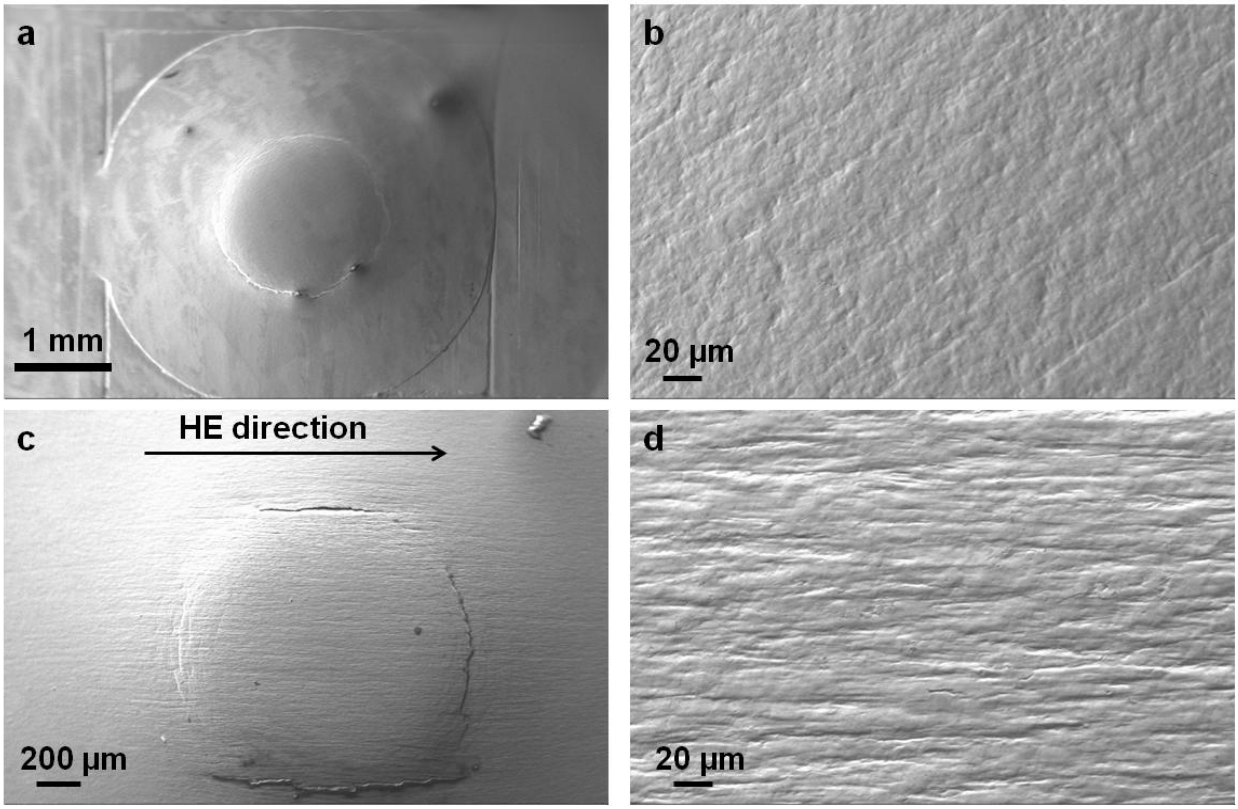

Figure 61. SEM images of the surface relief of the HE processed specimens subjected to annealing at 350ºC for 5 h (a) view of dome of the T-specimen; (b) area at φ~30º of T-specimen; (c) view of the dome of the L-specimen and (d) area at φ~30º of the L-specimen.

4.3.4.2. Testing temperature effect

As well known, the strength of metallic materials tends to decrease with increasing temperature whereas their ductility increases. The same trend is usually demonstrated by the UFG and NS metallic materials. Therefore, the UFG metallic materials tested at elevated temperatures should demonstrate higher formability. However, the UFG metallic materials usually show a low thermostability. Grain growth or recrystallization during plastic deformation at elevated temperatures can significantly degrade their mechanical strength. Therefore, the testing temperature should be carefully chosen to prevent any grain growth and should be well below recrystallization temperature.

Based on the results of the annealing treatments (see previous Section 4.3.4.1) 300ºC was chosen as the temperature for small punch testing. Figure 62 and Figure 63 illustrate images of the specimens after small punch testing at 300ºC compared to those tested at room temperature. The load – central deflection curves for AR-Ti,

$HE_{3.24}$-Ti and HE-RS-Ti samples are compared in Figure 64. Unlike load – central deflection curves for extruded bars at room temperature, curves at 300ºC follow the profile of those for the coarse grained specimens and formability stages can be clearly identified as in Figure 51. It is clearly seen that the $HE_{3.24}$ and HE-RS specimens show the same level of formability as the AR counterpart at room temperature. The maximum central deflection and true strain induced into $HE_{3.24}$ and HE-RS specimens are comparable to that of the AR material at room temperature (Table 13). Regardless cumulative strain of the processed specimens, the punch load at 300ºC at the stage of bi-axial stretching is significantly lower for the T-specimens compared to the L-specimens (Table 13). It is also remarkable the significant increase of central deflection and uniform strain of L-specimens after small-punch testing at 300ºC in spite of the required punch load is retained with respect to the extruded L-specimens.

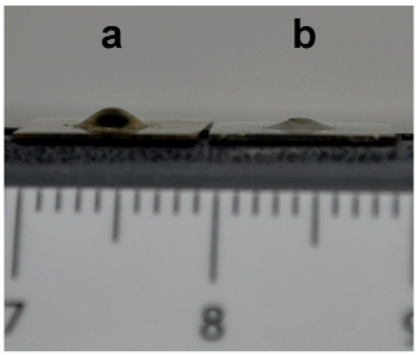

Figure 62. Appearance of the $HE_{3.24}$-Ti L-specimens of CP Ti after small-punch testing (a) at 300ºC and (b) at RT.

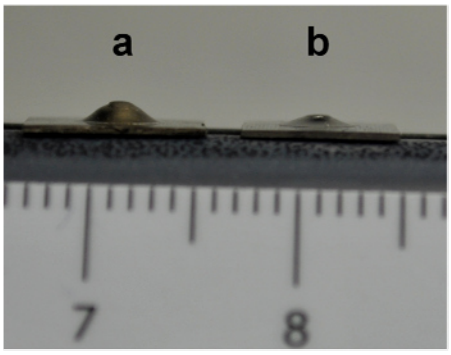

Figure 63. Appearance of the HE-RS L-specimens of CP Ti after small-punch testing (a) at 300ºC and (b) at RT.

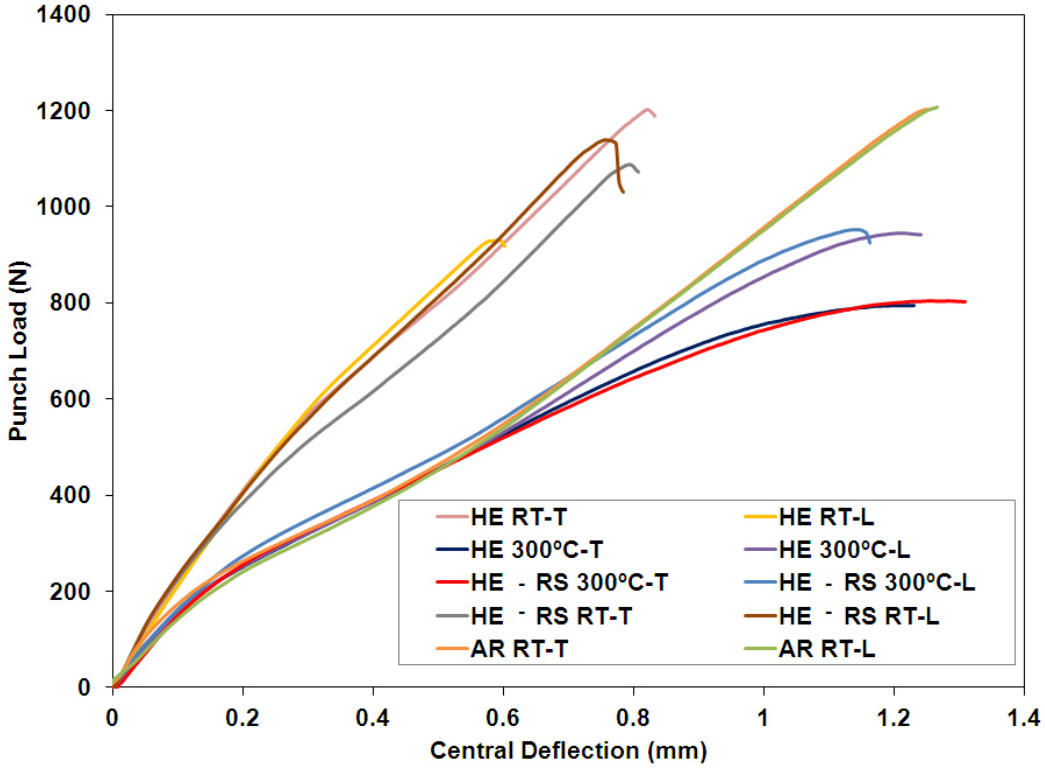

Figure 64. Punch load – central deflection curves at 300ºC and room temperature for L- and T- specimens of the as-received (AR) Ti and the HE processed ($HE_{3.24}$-Ti) Ti and additional rotary swaging (HE-RS) Ti.

Table 13. Results of small punch testing at 300ºC and room temperature (RT) for L- and T-specimens of the as-received and the HE processed CP Ti and additionally rotary swaged CP Ti.

Sample	F_{max} (N)	h_{max} (mm)	ε
AR RT-T	1243±47	1.3±0.05	0.4±0.01
AR RT-L	1213±23	1.27±0.05	0.35±0.02
$HE_{3.24}$ RT-T	1163±34	0.79±0.03	0.12±0.03
$HE_{3.24}$ RT-L	910±59	0.60±0.02	0.05±0.008
$HE_{3.24}$ Ti 300ºC-T	798±10	1.25±0.03	0.39±0.01
$HE_{3.24}$ 300ºC-L	912±53	1.17±0.05	0.37±0.01
HE - RS RT-T	1053±40	0.78±0.01	0.11±0.01
HE - RS RT-L	1150±10	0.73±0.06	0.07±0.01
HE - RS 300ºC-T	800±20	1.27±0.02	0.37±0.1
HE - RS 300ºC-L	963±120	1.14±0.11	0.32±0.01

Analysis of surface relief of specimens after small-punch testing at 300ºC confirms that microstructure anisotropy and the strong crystallographic texture developed during hydrostatic extrusion still play an important role in bi-axial deformation behavior (Figure 65 and Figure 67). Evidences of profuse plastic deformation are easily found in specimens confirming that the T-specimens deform in a symmetric manner with respect to the dome axis while it is not the case for the L-ones. The high roughness in bi-axial stretching areas of both T- and L-specimens can be noted. Some microshear the banding is observed in bi-axial stretching areas (φ~30º) of T-specimens promoting larger uniform strain. The length of microshear bands is in the range of 2-20 μm. At φ~60º from the punch axis, the primary and secondary cracks which are respectively parallel and perpendicular to the extrusion direction are identified on the surface relief of the L-specimens (Figure 66 a, b and Figure 68 a, b). This massive micro-localization of plastic flow might result in a significant increase of formability being comparable to those for the CG Ti at room temperature.

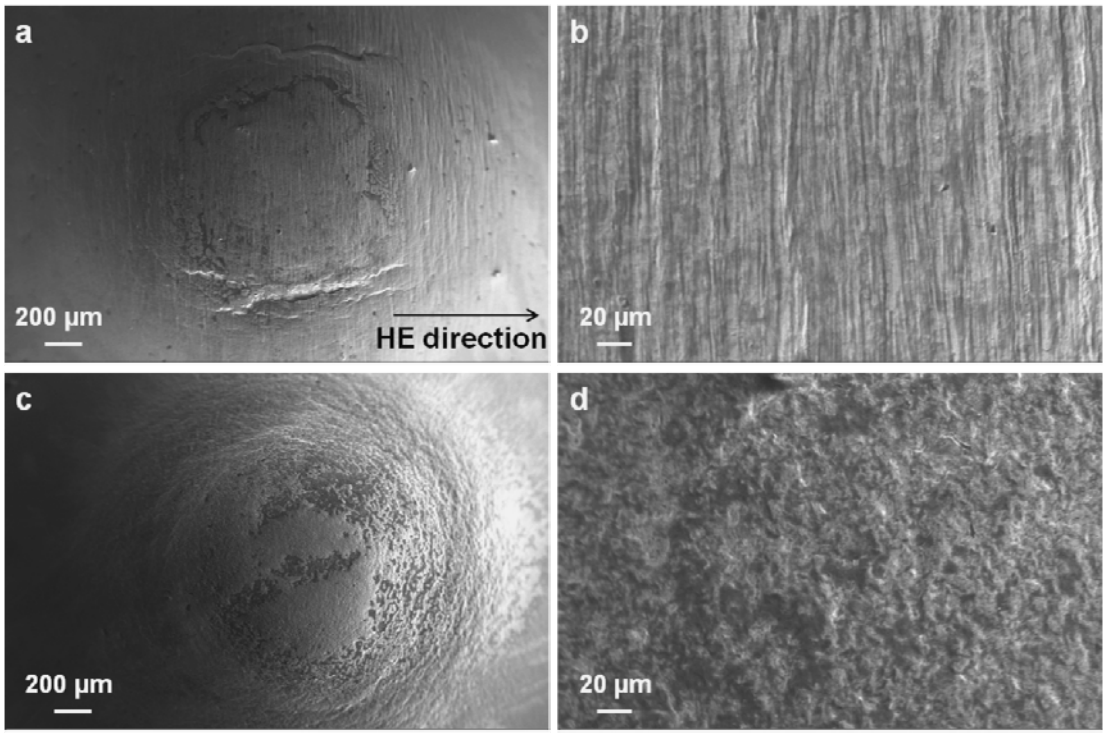

Figure 65. SEM images of the surface relief of the $HE_{3.24}$ specimens subjected to small-punch test at 300ºC (a) the view of dome of the L-specimen; (b) area at φ~30º of the L-specimen; (c) the view of the dome of the T-specimen and (d) area at φ~30º of the L-specimen.

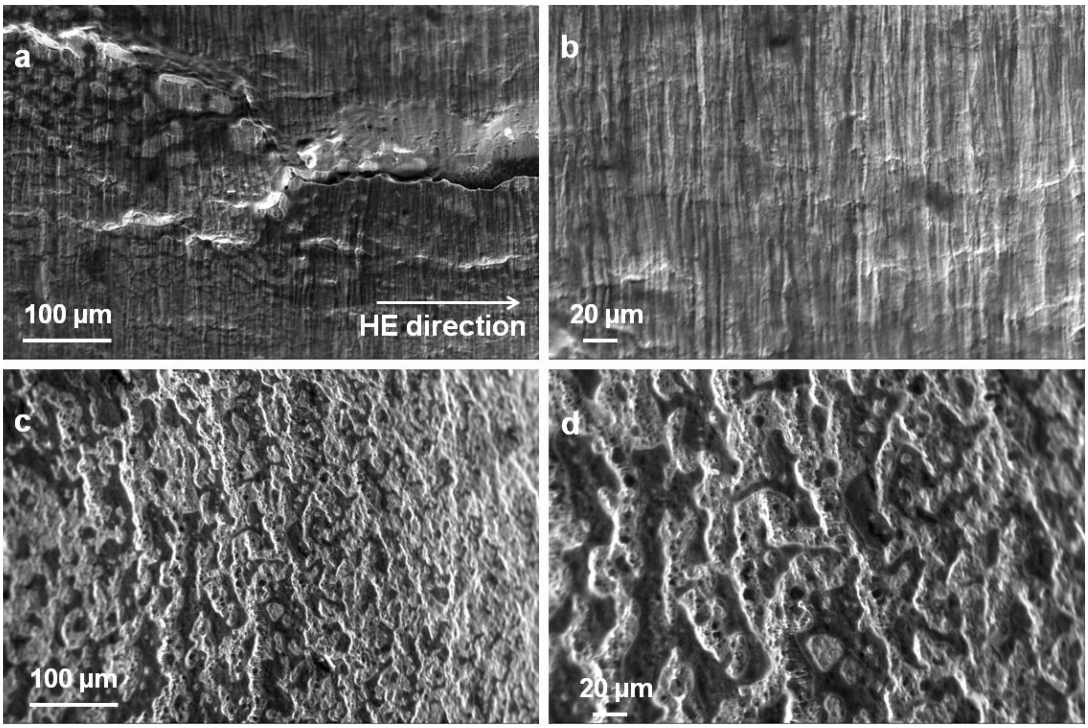

Figure 66. SEM images of the surface relief of the $HE_{3.24}$ specimens after small punch testing at φ~60º for (a, b) L-specimens and (c, d) T-specimens.

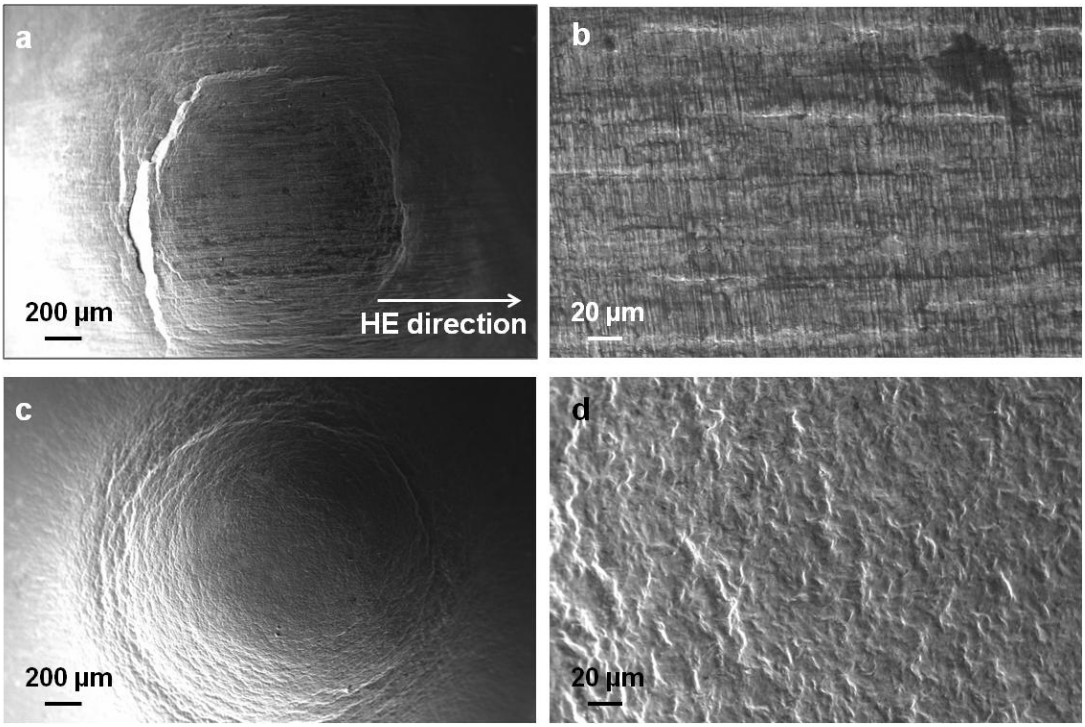

Figure 67. SEM images of the surface relief of the HE-RS specimens subjected to small-punch test at 300ºC (a) the view of dome of the L-specimen; (b) area at φ~30º of the L-specimen; (c) the view of the dome of the T-specimen and (d) area at φ~30º of the L-specimen.

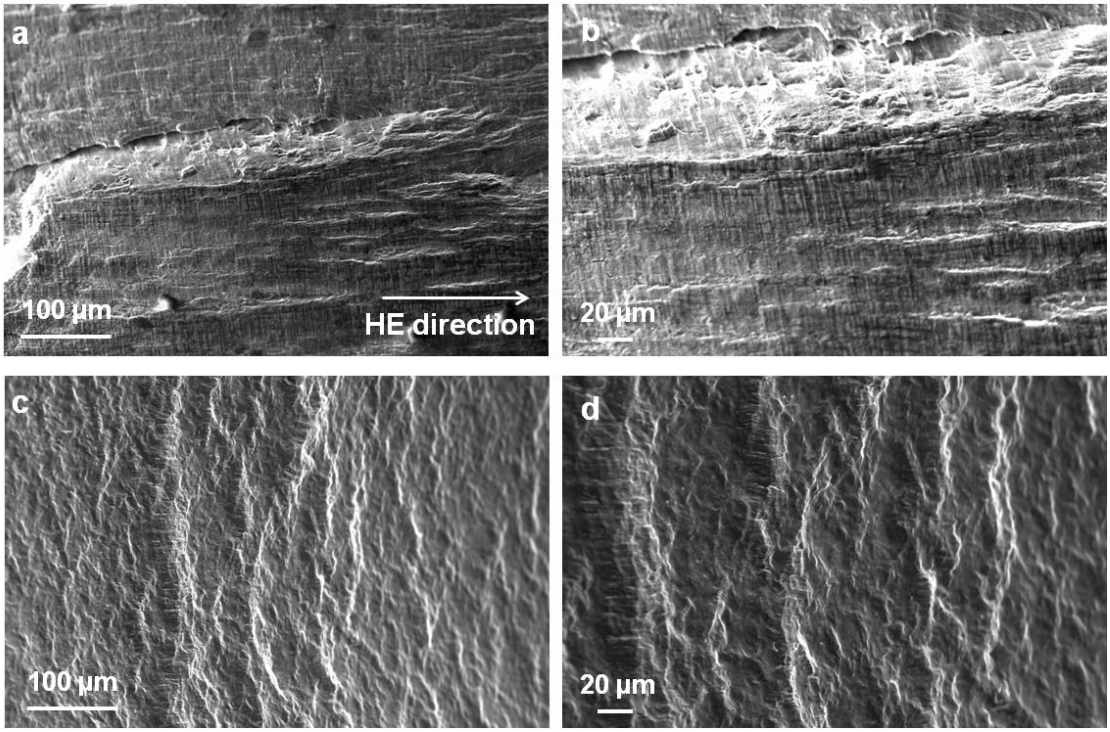

Figure 68. SEM images of the surface relief of the HE-RS specimens after small punch testing at *φ*~60º for (a, b) L-specimens and (c, d) T-specimens.

4.3.4.3. Nanocharacterization of domes

Table 14 summarizes the elastoplastic properties (hardness and modulus) extracted from nanoindentation curves of the $HE_{3.24}$-Ti and HE-RS-Ti specimens before and after bi-axial stretching at 300ºC. These values were estimated taking into account the indenter shape function for hardness estimation as suggested by Oliver and Pharr [159]

Table 14. Data on hardness and reduced Young's modulus for extruded ($HE_{3.24}$-Ti) and additionally rotary swaged CP Ti specimens (HE-RS-Ti) before and after bi-axial stretching at 300ºC. The average values from at least 10 nanoindentation curves are listed.

Material condition	Hardness (GPa)		Er (GPa)	
	Before bi-axial stretching	Bi-axially stretched at 300ºC	Before bi-axial stretching	Bi-axially stretched at 300ºC
$HE_{3.24}$	3.8±0.3	3.1±0.6	152.1±6.1	101.8±9.8
HE- RS	3.7±0.3	3.7±0.5	144.6±7.1	132.2±9.7

In [185], a theoretical model for indentation of metals was developed and validated by experimental data, the model correlates hardness and tensile strength (Equation 37). The mean contact pressure, ***Pm***, is directly proportional to tensile strength, ***Y***, by the constrain factor, ***c***, which is considered to be ≈2.8 for work-hardened metals. Based on our results, nanoindentation resulted in an overestimation of hardness values when compared to theoretical hardness values calculated from Equation 37. Experimental hardness of the $HE_{3.24}$ CP Ti is ≈3.8 GPa (Table 14) while *Y* is ≈ 1 GPa for this condition (Table 7), which corresponds to a theoretical hardness value of ~2.8 GPa.

$$P_m = cY$$ **Equation 37**

This discrepancy can be related to the pile-up effect as well as the high surface roughness in bi-axial deformed specimens since the model used for computing hardness does not account for these effects for the calculation of the projected area. Pile-up was expected to occur due to the low strain hardening ability of UFG and NS metallic materials [157]. For these cases, Oliver and Pharr model tends to underestimate the projected area which results in an overestimation of the hardness values. Based on work done in [186], residual indentation imprints were scanned using AFM (Figure 69, Figure 70) and hardness was estimated by measuring areas directly from the AFM images (Equation 36, Table 15). The presence of pile-up around residual imprints is confirmed in the 3-D topography images and line cross-section profiles. It could be asserted that hardness slightly decreases due to the dynamic recovery and dislocation annihilation by climbing since recrystallization process had not taken place at such temperature as was demonstrated with TEM analysis (Figure 57).

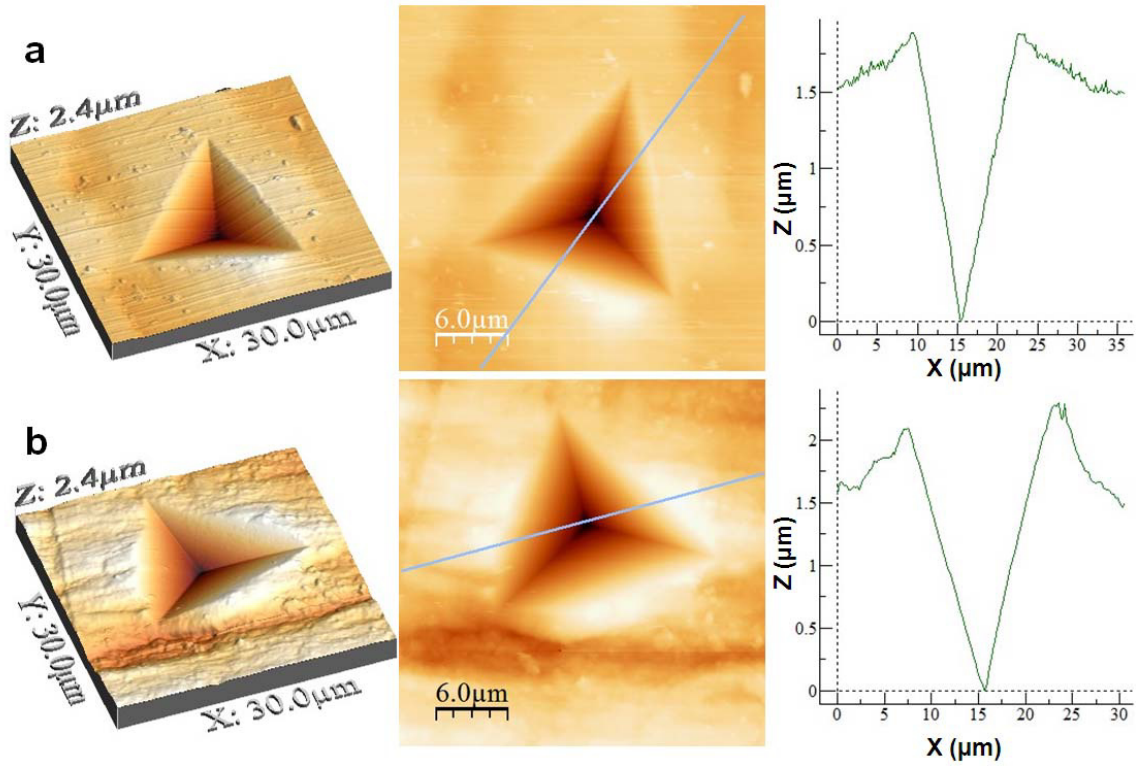

Figure 69. 3D and 2D AFM topography images and line profiles of residual indentation imprints in (a) $HE_{3.24}$ specimen; (b) bi-axially stretched $HE_{3.24}$ specimen at 300ºC.

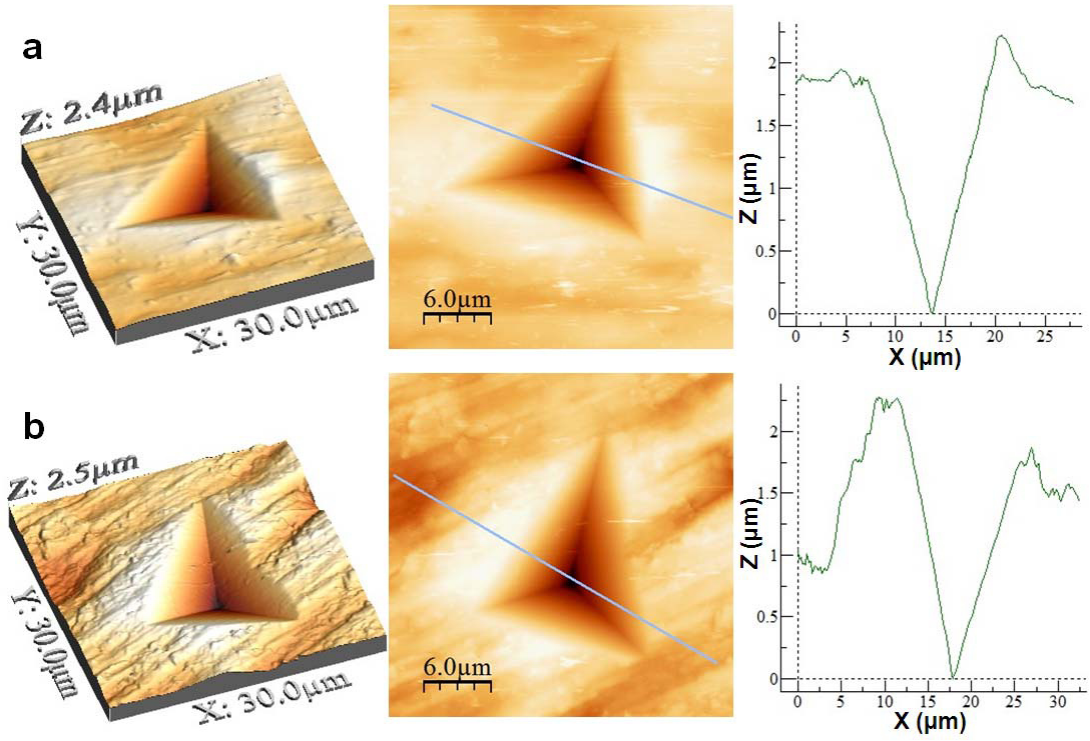

Figure 70. 3D and 2D AFM topography images and line profiles of residual indentation imprints in (a) HE-RS specimen; (b) bi-axially stretched HE-RS specimen at 300ºC.

Table 15. Hardness results for $HE_{3.24}$ and HE-RS specimens before and after bi-axial stretching at 300ºC. The data are extracted from indentation imprints analysis using AFM.

Specimen	Hardness (GPa)
$HE_{3.24}$	3.06±0.07
$HE_{3.24}$ bi-axially stretched at 300ºC	2.84±0.07
HE-RS	3.10±0.07
HE-RS bi-axially stretched at 300ºC	2.98±0.95

4.4. Fracture behavior of HE processed Al2024 alloy and CP Ti

4.4.1. Microstructure effect on fracture toughness of HE processed Al alloy

Figure 71 corresponds to SEM images of fracture surfaces of C-R and R-L extruded Al2024 specimens. The fatigue pre-crack area and fracture surface can be easily identified on the images. It is clearly seen that material has undergone ductile fracture via formation of voids, their growth and coalescence resulting in formation of dimple fracture surface. The size of dimples is in the range of 5-15 μm. It is clearly seen that the dimples are somewhat elongated along the extrusion direction: i.e. they are elongated perpendicular to the crack front in the C-R specimens (Figure 71 a, b) and parallel to the crack front in the R-L specimens (Figure 71 c, d). It can be concluded that the microstructure formed during HE processing plays an important role in fracture behavior of the material which shows a significant anisotropy.

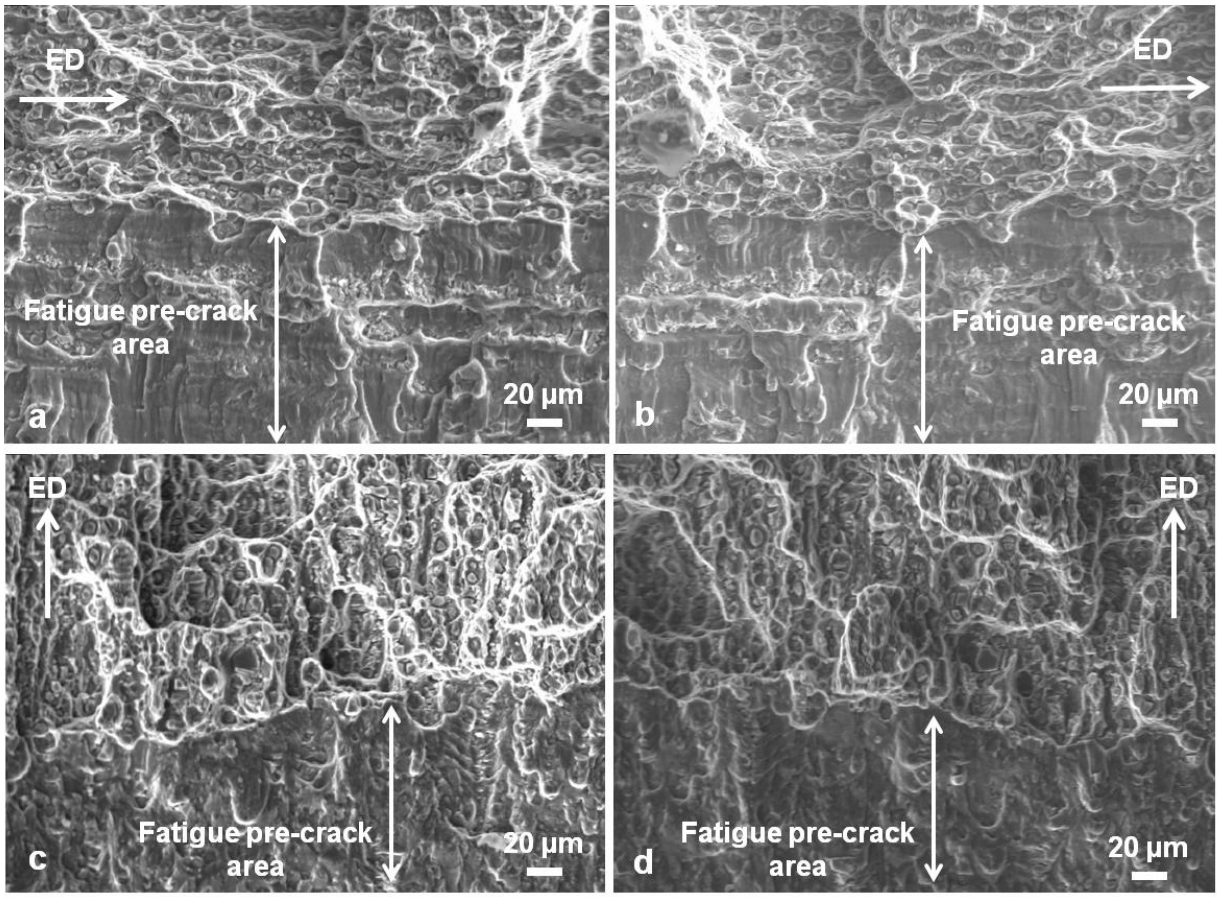

Figure 71. SEM images of fracture surfaces on both halves of the broken specimens of the HE processed Al2024 alloy: (a, b) C-R specimen; (c, d) R-L specimen. The extrusion direction is marked by white arrow.

Table 16 summarizes estimated fracture parameters (CTOD, COA, J_i-integral and crack growth resistance, R_{tot}) extracted from fracture testing using Equation 29 - Equation 33. Yield stress, σ_0 was extracted from tensile testing results and the dimensionless parameter d_N was calculated using an estimation of strain hardening exponent and following calculations for plane strain conditions [187]. Anisotropy of fracture behavior observed in the SEM images is supported by calculations. The average CTOD-value for the C-R specimens is ≈5.4 µm while the average CTOD-value for the R-L specimens less than 4 µm (Table 16). Thus, the COA- and J_i-values are higher for the C-R specimens, 2.5º and 4.9 kJ/m^2 versus 1.8º and 3.4 kJ/m^2 for the R-L specimens, respectively. It should be noted that it is given a qualitative value of R_{tot} due to the pre-factor η (Equation 32) is independent of specimen orientation. The ratio of the R_{tot}-value for both samples can be determined: the crack growth resistance of the C-R specimens is by a factor of 1.4 times higher compared to the R-L specimens.

Table 16. Results of fracture testing of C-R and R-L specimens for the HE processed Al2024 alloy.

Specimen orientation	σ_0 (MPa)	d_N	CTOD (μm)	COA (º)	J_i (kJ/m^2)	R_{tot}
C-R Al2024	390	0.43	5.4±2.4	2.5±0.5	4.9±2.1	1.4R
R-L Al24024	390	0.43	3.8±1.3	1.8±0.4	3.4±1.2	1R

The anisotropic fracture behavior of the Al2024 alloy may be related to the elongated grains/subgrains and elongated second phase precipitates aligned along the extrusion direction. Interface between elongated and coarse dispersoids and metal matrix is a preferential site for dimples and nanovoids nucleation and their coalescence promotes crack propagation. Since the grains/subgrains are elongated along the extrusion direction, the crack growth resistance is lower in the extrusion direction due to the crack can easily grow along the grains/cells boundaries, whereas the crack growing in the perpendicular direction has to kink more often. Also, the length of dimples along the direction of crack propagation is larger in the R-L specimens compared to the C-R specimens. This is also supported by the estimated values of J_i and R_{tot} (Table 16).

4.4.2. Microstructure and texture effect on fracture toughness of HE processed CP Ti

Anisotropy of microstructure and texture also affects as well the fracture behavior of the HE processed CP Ti (Figure 72). Similar to the Al2024 alloy, elongated dimples having a size of 3-10 μm along extrusion direction are easily identified over fracture surfaces regardless specimen orientation indication ductile fracture mode. Again, the dimples are elongated along the crack propagation direction in the R-L specimens (Figure 72 a, b) and perpendicular to the of C-R specimens (Figure 72 c, d). This observation can be rationalized based on the lamellae-type microstructure developed during HE processing of the material (see Section 4.1.3). Quantitative analysis of the surface roughness parameters was performed and the CTOD- and COA-values were determined for both specimen orientations. The results are listed in Table 17. The J_i- and R_{tot}-values were calculated.

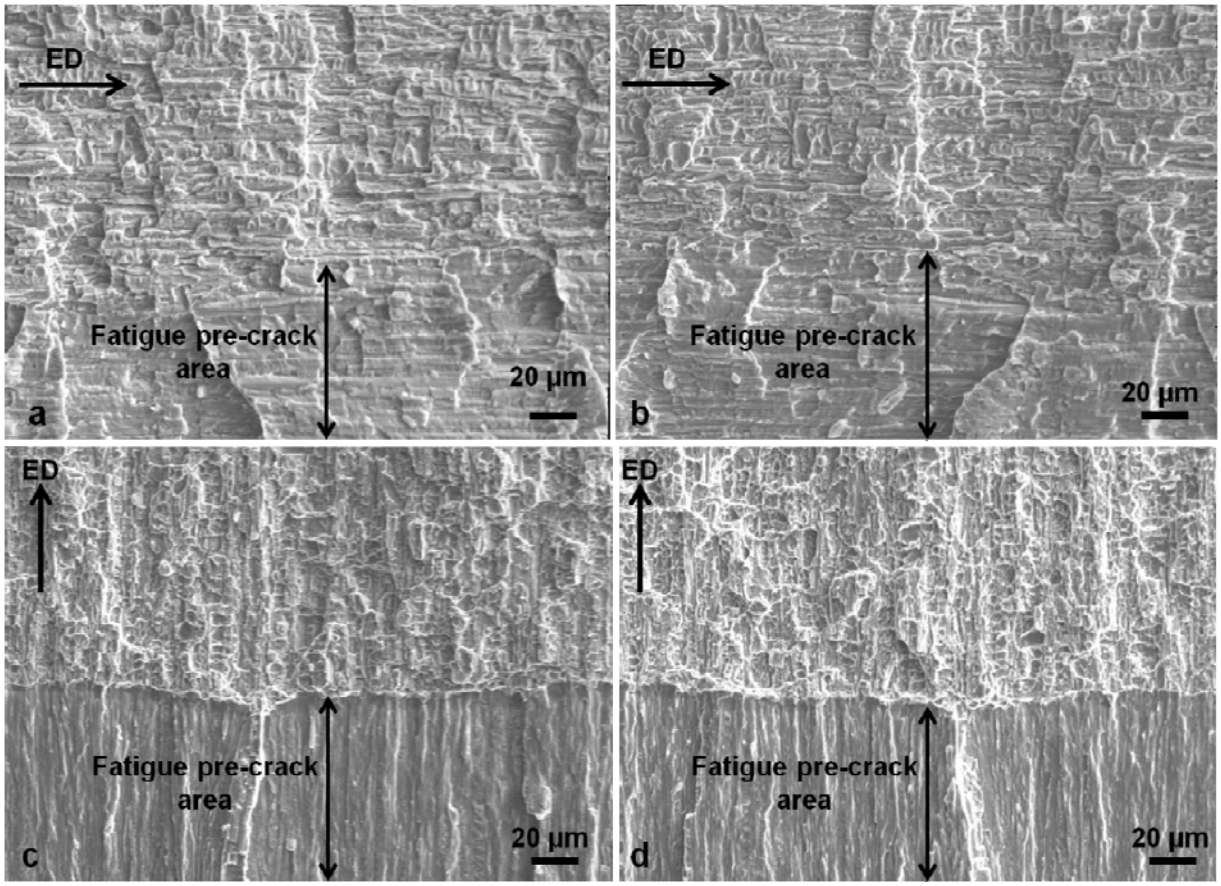

Figure 72. SEM images of fracture surface of both halves for (a, b) C-R specimen, (c, d) R-L specimen from the HE processed CP Ti bars. The extrusion direction is marked by black arrow.

Table 17. Results of fracture testing of the C-R and R-L specimens for the HE processed CP Ti.

Specimen orientation	σ_0 (MPa)	d_N	CTOD (µm)	COA (º)	J_i (kJ/m2)	R_{tot}
C-R	420	0.2	2.6±0.5	2.2±0.7	5.2±0.9	1.5R
R-L	420	0.2	2.3±0.3	1.5±0.6	4.7±1.0	1R

Anisotropy of fracture properties in the HE processed CP Ti is similar to that observed in the Al2024 alloy. The C-R specimens show higher fracture initiation toughness and total crack growth resistance compared to the R-L specimens (Table 17). This effect can be related to the microstructure developed in the material during HE processing. The crack propagates easier along the lamellae boundaries in the direction of their elongation than in the perpendicular direction.

4.5. A recipe to increase bi-axial stretching formability of the UFG metals

The results of this investigation clearly show that the deformation mode (stress state) does not affect the plastic deformation mechanisms, homogeneity of plastic flow, and mechanical properties of the CG metallic materials. However, an opposite trend can be observed in the UFG metallic materials. The homogeneity of plastic flow and the plastic deformation mechanisms in the UFG metals and alloys as well as their formability strongly depend on the initial microstructure, crystallographic texture and deformation mode during plastic deformation. The analysis of outcomes from this experimental work has lead to a general recipe how to improve formability of the UFG metallic materials which is presented below.

I. Extensive microshear banding can play a very important role in the enhancement of bi-axial stretching formability of the UFG FCC metallic materials. The UFG FCC metals can show even higher bi-axial stretching formability than their coarse-grained counterparts if extensive microshear banding is activated. The mechanisms for activation of extensive microshear banding might include inhomogeneous microstructure containing ultra-fine grains/subgrains, cells, as well as appropriate choice of testing parameters for activation of grain boundary sliding. It should be noted that the positive effect of microshear banding on enhancement of uni-axial tensile ductility [107] and fatigue ductility [188] of FCC metals was already reported earlier.

II. Formability of the UFG metallic materials is determined by crystallographic and metallographic texture developed during fabrication of these materials. Elongated grains/lamellae can significantly degrade bi-axial stretching formability if the material is deformed in the plane of elongated grains. Crystallographic texture can play a very important role during bi-axial stretching of HCP metals. The crystallographic texture symmetrical with respect to the applied stress does not seem to degrade the bi-axial stretching formability of the HCP metals, whereas combination of “soft” and “hard” grains in the “scenario” of the crystallographic texture unsymmetrical with respect to the applied stress can significantly degrade bi-axial stretching formability. A general approach to increase formability of the UFG materials is to generate UFG microstructures consisting of equiaxed ultra-fine grains with no preferred orientation of crystals.

III. Presence of coarse dispersoids or cracked particles in the microstructure can significantly degrade bi-axial stretching formability of the UFG metallic materials. The coarse dispersoids and/or cracked particles can act as nucleation sites for formation of microcracks and their further quick propagation. Thus, it is recommended to avoid presence of coarse dispersoids/particles and cracked precipitates in the microstructure of the UFG metallic materials.

IV. High dislocation density in the interior of ultra-fine grains and/or non-equilibrium grain boundaries can also degrade formability of the UFG metallic materials since such ultra-fine grains have no any ability to accumulate dislocations. Generation of the UFG microstructures with grains free of dislocations could slightly improve bi-axial stretching formability. Such microstructures can be also obtained if the UFG material is subjected to annealing treatments in order to decrease dislocation density in the grain interior as well as to perform relaxation of the non-equilibrium grain boundaries. It should be noted that such strategy was successfully employed to increase uni-axial tensile ductility and fatigue life of the UFG Ti-based materials [182].

V. The UFG metallic materials can demonstrate enhanced formability at elevated temperatures and retain their high mechanical strength after metalforming. However, the testing (metalforming) temperature should be carefully chosen to prevent any grain growth or recrystallization during testing (metalforming) at elevated temperatures.

5 CONCLUSIONS

5. CONCLUSIONS

Following conclusions can be drawn based on the analysis of the outcomes of this work.

1. Equal channel angular pressing (ECAP) and hydrostatic extrusion (HE) can be utilized for grain refinement in commercially pure Cu, Ti and Al2024 alloy. ECAP for 2 passes of pure Cu led to formation of inhomogeneous microstructure consisting of ultra-fine grains and highly deformed coarse grains containing cells and shear bands, whereas ECAP for 12 passes resulted in formation of homogeneous ultra-fine grained microstructure with grain size of 100-250 nm. HE of pure Ti led to formation of ultra-fine lamellar-type microstructure having a very strong crystallographic fibre texture with the C-axis perpendicular to the extrusion axis and (10-10) direction parallel to the extrusion axis. Similar microstructure containing coarse dispersoids, T-particles and second phase precipitates was formed after hydrostatic extrusion in the Al2024 alloy.

2. The ECAP processed Cu, HE processed pure Ti and Al2024 alloys demonstrated very high mechanical strength, but low tensile uniform elongation and elongation to failure. The transversal specimens showed much lower yield strength but much higher strain hardening capacity compared to those of the longitudinal specimens. Significant anisotropy of uni-axial tensile deformation behaviour of the HE processed pure Ti is related to its very strong crystallographic (10-10) fibre texture and specific microstructure developed during hydrostatic extrusion. Metallographic and (111) texture developed during HE of the Al2024 alloy led to anisotropy of its uni-axial tensile mechanical properties.

3. Small punch testing showed that formability in bi-axial stretching of the ECAP processed Cu was comparable to that of the coarse-grained Cu. Inhomogeneous plastic flow in form of profuse microshear banding played an important role in bi-axial stretching of the ECAP processed Cu providing significant amount of plastic deformation and, therefore, formability. Activity of microshear banding and formability of the ECAP processed Cu can be controlled via microstructural design (choosing optimum processing parameters) and/or stress triaxiality. Other mechanisms active during bi-axial stretching of the ECAP processed Cu included dislocation glide and grain boundary sliding.

4. There is anisotropy of bi-axial deformation behaviour and failure during small punch testing of the HE processed pure Ti. A higher load is required for bi-axial deformation of the longitudinal specimens in the bi-axial stretching regime and the longitudinal specimens show lower maximum central deflection and lower value of true uniform strain compared to those for the transversal specimens. The transversal specimens are deformed and fail in symmetric manner with respect to the punch axis since all grains have symmetrical orientation. Combinations of grains with various crystallographic and metallographic orientations with respect to the punch axis can be present in the microstructure of the longitudinal specimens. Some combinations of soft grains and hard grains can lead to rotation of the quazi-cleavage facets which, in turn, can easily lead to their quick growth along lamellae boundaries, thus forming primary longitudinal cracks (parallel to the extrusion direction) and their growth followed by formation of secondary cracks (perpendicular to the extrusion direction).

5. Annealing treatments of the HE processed pure Ti led to a slight increase of its bi-axial stretching in the longitudinal plane at room temperature. At 300ºC, the HE processed Ti showed the same level of formability as the coarse-grained CP Ti at room temperature.

6. Bi-axial stretching formability of the HE processed Al2024 alloy is limited by presence of coarse dispersoids and cracked T-particles which act as nucleating sites for microcracks.

7. A recipe for improvement of bi-axial stretching formability of the UFG metallic materials includes:

- activation of microshear banding via microstructural design;

- generation of microstructures with equi-axed ultra-fine grains free of dislocations with no or minimum crystallographic texture;

- absence of coarse dispersoids or particles in the microstructure;

- metalforming operations at elevated temperatures provided that there is no recrystallization or grain growth during plastic deformation

6 BIBLIOGRAPHY

6. **BIBLIOGRAPHY**

1. Polmear, I. J. *Light Alloys-Metallurgy of the Light Metals*. London: Arnold, 1995.

2. Valiev, R. Z.; Islamgaliev, R. K.; and Alexandrov, I. V. "Bulk nanostructured materials from severe plastic deformation." *Progress in Materials Science* 45 (2000): 103-189.

3. Valiev, R. Z.; and Langdon, T. G. "Principles of equal-channel angular pressing as a processing tool for grain refinement." *Progress in Materials Science* 51 (2006): 881-981.

4. Zhilyaev, A. P.; and Langdon, T. G. "Using high-pressure torsion for metal processing: Fundamentals and applications." *Progress in Materials Science* 53 (2008): 893-979.

5. Liddicoat, P. V.; Liao, X. Z.; Zhao, Y. H.; Zhu, Y. T.; Murashkin, M. Y.; Lavernia, E. J.; and al., e. "Nanostructural hierarchy increases the strength of aluminum alloys." *Nature Communications* 1 (2010): 1-7.

6. Langdon, T. G. "Twenty-five years of ultrafine-grained materials: Achieving exceptional properties through grain refinement." *Acta Materialia* 61 (2013): 7035-7059.

7. Witkin, D. B.; and Lavernia, E. J. "Synthesis and mechanical behavior of nanostructured materials via cryomilling." *Progress in Materials Science* 51 (2006): 1-60.

8. Valiev, R. Z.; Krasilnikov, N. A.; and Tsenev, N. K. "Plastic deformation of alloys with submicron-grained structure." *Materials Science and Engineering: A* 137 (1991): 35-40.

9. Stolyarov, V. V.; Zhu, Y. T.; Lowe, T. C.; and Valiev, R. Z. "Microstructure and properties of pure Ti processed by ECAP and cold extrusion." *Materials Science and Engineering: A* 303 (2001): 82-89.

10. Kang, D. H.; and Kim, T. W. "Mechanical behavior and microstructural evolution of commercially pure titanium in enhanced multi-pass equal channel angular pressing and cold extrusion." *Materials and Design* 31, Supplement 1 (2010): S54-S60.

11. Fan, Z.; Jiang, H.; Sun, X.; Song, J.; Zhang, X.; and Xie, C. "Microstructures and mechanical deformation behaviors of ultrafine-grained commercial pure (grade 3) Ti processed by two-step severe plastic deformation." *Materials Science and Engineering: A* 527 (2009): 45-51.

12. Kulczyk, M.; Pachla, W.; Krasilnikov, N.; Mazur, A.; Sus-Ryszkowska, M.; and Kurzydlowski, K. J. "Producing bulk nanocrystalline materials by combined hydrostatic extrusion and equal-channel angular pressing " *Materials Science-Poland* 25 (2007): 991-999.

13. Lewandowska, M. "Dependence of the deformation microstructure of aluminium alloys on the strain path." *Materials Chemistry and Physics* 81 (2003): 555-557.

14. Nurislamova, G.; Sauvage, X.; Murashkin, M.; Islamgaliev, R.; and Valiev, R. Z. "Nanostructure and related mechanical properties of an Al-Mg-Si alloy processed by severe plastic deformation." *Philosophical Magazine Letters* 88 (2008): 459-466.

15. Cheng, S.; Zhao, Y. H.; Zhu, Y. T.; and Ma, E. "Optimizing the strength and ductility of fine structured 2024 Al alloy by nano-precipitation." *Acta Materialia* 55 (2007): 5822-5832.

16. Sabirov, I.; Perez-Prado, M. T.; Molina-Aldareguia, J. M.; Semenova, I. P.; Salimgareeva, G. K.; and Valiev, R. Z. "Anisotropy of mechanical properties in high-strength ultra-fine-grained pure Ti processed via a complex severe plastic deformation route." *Scripta Materialia* 64 (2011): 69-72.

17. Pachla, W.; Kulczyk, M.; Sus-Ryszkowska, M.; Mazur, A.; and Kurzydlowski, K. "Nanocrystalline titanium produced by hydrostatic extrusion." *Journal of Materials Processing Technology* 205 (2008): 173-182.

18. Semenova, I. P.; Yakushina, E. B.; Nurgaleeva, V. N.; and Valiev, R. Z. "Nanostructuring of Ti alloys by SPD processing to achieve superior fatigue properties." *International Journal of Material Science* 100 (2009): 1691-1696.

19. Ma, A.; Jiang, J.; Saito, N.; Shigematsu, I.; Yuan, Y.; Yang, D.; and Nishida, Y. "Improving both strength and ductility of a Mg alloy through a large number of ECAP passes." *Material Science and Engineering: A* 513–514 (2009): 122–127.

20. Foley, D. C.; Al-Maharbi, M.; Hartwig, K. T.; Karaman, I.; J., K. L.; and Mathaudhu, S. N. "Grain refinement vs. crystallographic texture: Mechanical anisotropy in a magnesium alloy." *Scripta Materialia* 64 (2011): 193–196.

21. Ding, S. X.; Lee, W. T.; Chang, C. P.; W., C. L.; and Kao, P. W. "Improvement of strength of magnesium alloy processed by equal channel angular extrusion." *Scripta Mater.* 59 (2008): 1006–1009.

22. Estrin, Y.; and Vinogradov, A. "Extreme grain refinement by severe plastic deformation: A wealth of challenging science." *Acta Materialia* 61 (2013): 782-817.

23. Sun, P. L.; Yu, C. Y.; Kao, P. W.; and Chang, C. P. "Influence of boundary characters on the tensile behavior of sub-micron-grained aluminum." *Scripta Materialia* 52 (2005): 265-269.

24. Soliman, M. S.; El-Danaf, E. A.; and Almajid, A. A. "Enhancement of static and fatigue strength of 1050 Al processed by equal-channel angular pressing using two routes." *Materials Science and Engineering: A* 532 (2012): 120-129.

25. El-Danaf, E. A.; Soliman, M. S.; Almajid, A. A.; and El-Rayes, M. M. "Enhancement of mechanical properties and grain size refinement of commercial purity aluminum 1050 processed by ECAP." *Materials Science and Engineering: A* 458 (2007): 226-234.

26. Sun, P. L.; Yu, C. Y.; Kao, P. W.; and Chang, C. P. "Microstructural characteristics of ultrafine-grained aluminum produced by equal channel angular extrusion." *Scripta Materialia* 47 (2002): 377-381.

27. Sabirov, I.; Barnett, M. R.; Estrin, Y.; and Hodgson, P. D. "The effect of strain rate on the deformation mechanisms and the strain rate sensitivity of an ultra-fine-grained Al alloy." *Scripta Materialia* 61 (2009): 181-184.

28. Venkatachalam, P.; Ramesh Kumar, S.; Ravisankar, B.; Thomas Paul, V.; and Vijayalakshmi, M. "Effect of processing routes on microstructure and mechanical properties of 2014 Al alloy processed by equal channel angular pressing." *Transactions of Nonferrous Metals Society of China* 20 (2010): 1822-1828.

29. Horita, Z.; Fujinami, T.; Nemoto, M.; and Langdon, T. G. "Equal-channel angular pressing of commercial aluminum alloys: Grain refinement, thermal stability and tensile properties." *METALLURGICAL AND MATERIALS TRANSACTIONS A* 31 (2000): 691-701.

30. Dalla Torre, F.; Lapovok, R.; Sandlin, J.; Thomson, P. F.; Davies, C. H. J.; and Pereloma, E. V. "Microstructures and properties of copper processed by equal channel angular extrusion for 1–16 passes." *Acta Materialia* 52 (2004): 4819-4832.

31. Blum, W.; Li, Y. J.; Zhang, Y.; and Wang, J. T. "Deformation resistance in the transition from coarse-grained to ultrafine-grained Cu by severe plastic deformation up to 24 passes of ECAP." *Materials Science and Engineering: A* 528 (2011): 8621-8627.

32. Stolyarov, V. V.; Zhu, Y. T.; Alexandrov, I. V.; Lowe, T. C.; and Valiev, R. Z. "Influence of ECAP routes on the microstructure and properties of pure Ti." *Materials Science and Engineering: A* 299 (2001): 59-67.

33. Sakai, G.; Nakamura, K.; Horita, Z.; and Langdon, T. G. "Developing high-pressure torsion for use with bulk samples." *Materials Science and Engineering: A* 406 (2005): 268-273.

34. Liu, M.; Roven, H.; Murashkin, M.; Valiev, R.; Ungár, T.; and Balogh, L. "Structure and mechanical properties of nanostructured Al-Mg alloys processed by severe plastic deformation." *Journal of Materials Science* 45 (2010): 4659-4664.

35. Zhang, J.; Gao, N.; and Starink, M. J. "Al-Mg-Cu based alloys and pure Al processed by high pressure torsion: The influence of alloying additions on strengthening." *Materials Science and Engineering: A* 527 (2010): 3472-3479.

36. Loucif, A.; Figueiredo, R. B.; Baudin, T.; Brisset, F.; Chemam, R.; and Langdon, T. G. "Ultrafine grains and the Hall-Petch relationship in an Al-Mg-Si alloy processed by high-pressure torsion." *Materials Science and Engineering: A* 532 (2012): 139-145.

37. Jiang, H.; Zhu, Y. T.; Butt, D. P.; Alexandrov, I. V.; and Lowe, T. C. "Microstructural evolution, microhardness and thermal stability of HPT-processed Cu." *Materials Science and Engineering: A* 290 (2000): 128-138.

38. Islamgaliev, R. K.; Kazyhanov, V. U.; Shestakova, L. O.; Sharafutdinov, A. V.; and Valiev, R. Z. "Microstructure and mechanical properties of titanium (Grade 4) processed by high-pressure torsion." *Materials Science and Engineering: A* 493 (2008): 190-194.

39. Sergueeva, A. V.; Stolyarov, V. V.; Valiev, R. Z.; and Mukherjee, A. K. "Advanced mechanical properties of pure titanium with ultrafine grained structure." *Scripta Materialia* 45 (2001): 747-752.

40. Sergueeva, A. V.; Stolyarov, V. V.; Valiev, R. Z.; and Mukherjee, A. K. "Superplastic behaviour of ultrafine-grained Ti–6A1–4V alloys." *Materials Science and Engineering: A* 323 (2002): 318-325.

41. Kai, M.; Horita, Z.; and Langdon, T. G. "Developing grain refinement and superplasticity in a magnesium alloy processed by high-pressure torsion." *Materials Science and Engineering: A* 488 (2008): 117-124.

42. Hosseini, S. A.; and Manesh, H. D. "High-strength, high-conductivity ultra-fine grains commercial pure copper produced by ARB process." *Materials & Design* 30 (2009): 2911-2918.

43. Saito, Y.; Tsuji, N.; Utsunomiya, H.; Sakai, T.; and Hong, R. G. "Ultra-fine grained bulk aluminum produced by accumulative roll-bonding (ARB) process." *Scripta Materialia* 39 (1998): 1221-1227.

44. Tsuji, N.; Saito, Y.; Utsunomiya, H.; and Tanigawa, S. "Ultra-fine grained bulk steel produced by accumulative roll-bonding (ARB) process." *Scripta Materialia* 40 (1999): 795-800.

45. Hidalgo-Manrique, P.; Cepeda-Jiménez, C. M.; Ruano, O. A.; and Carreño, F. "Effect of warm accumulative roll bonding on the evolution of microstructure, texture and creep properties in the 7075 aluminium alloy." *Materials Science and Engineering: A* 556 (2012): 287-294.

46. Schmidt, C. W.; Knieke, C.; Maier, V.; Höppel, H. W.; Peukert, W.; and Göken, M. "Accelerated grain refinement during accumulative roll bonding by nanoparticle reinforcement." *Scripta Materialia* 64 (2011): 245-248.

47. Yang, D.; Cizek, P.; Hodgson, P.; and Wen, C. E. "Ultrafine equiaxed-grain Ti/Al composite produced by accumulative roll bonding." *Scripta Materialia* 62 (2010): 321-324.

48. Duan, X.; and Sheppard, T. "The influence of the constitutive equation on the simulation of a hot rolling process." *Journal of Materials Processing Technology* 150 (2004): 100-106.

49. Panigrahi, S. K.; and Jayaganthan, R. "Development of ultrafine grained high strength age hardenable Al 7075 alloy by cryorolling." *Materials and Design* 32 (2011): 3150-3160.

50. Zhao, Y. H.; Liao, X. Z.; Cheng, S.; Ma, E.; and Zhu, Y. T. "Simultaneously increasing the ductility and strength of nanostructured alloys." *Advanced Materials* 18 (2006): 2280-2283.

51. Panigrahi, S. K.; Jayaganthan, R.; and Chawla, V. "Effect of cryorolling on microstructure of Al–Mg–Si alloy." *Materials Letters* 62 (2008): 2626-2629.

52. Rangaraju, N.; Raghuram, T.; Krishna, B. V.; Rao, K. P.; and Venugopal, P. "Effect of cryo-rolling and annealing on microstructure and properties of commercially pure aluminium." *Materials Science and Engineering: A* 398 (2005): 246-251.

53. Yang, D. K.; Hodgson, P. D.; and Wen, C. E. "Simultaneously enhanced strength and ductility of titanium via multimodal grain structure." *Scripta Materialia* 63 (2010): 941-944.

54. Wang, Y.; Chen, M.; Zhou, F.; and Ma, E. "High tensile ductility in a nanostructured metal." *Nature* 419 (2002): 912-915.

55. Lewandowska, M.; Krawczynska, A. T.; Kulczyk, M.; and Kurzydlowski, K. J. "Structure and properties of nano-sized Eurofer 97 steel obtained by hydrostatic extrusion." *Journal of Nuclear Materials* 386-388 (2009): 499-502.

56. Lewandowska, M.; Garbacz, H.; Pachla, W.; Mazur, A.; and Kurzydlowski, K. "Grain refinement in aluminium and the aluminium Al–Cu–Mg–Mn alloy by hydrostatic extrusion " *Materials Science-Poland* 23 (2005): 279-286.

57. Lewandowska, M.; and Kurzydlowski, K. "Thermal stability of a nanostructured aluminum alloy." *Materials Characterization* 55 (2005): 395-401.

58. Zherebtsov, S.; Lojkowski, W.; Mazur, A.; and Salishchev, G. "Structure and properties of hydrostatically extruded commercially pure titanium." *Materials Science and Engineering: A* 527 (2010): 5596-5603.

59. Lewandowska, M.; and Kurzydlowski, K. J. "Recent development in grain refinement by hydrostatic extrusion." *Journal of Materials Science* 43 (2008): 7299-7306.

60. Hummel, R. Understanding materials science: History, properties, applications. Gainesville: Universtity of Florida, 2004.

61. Cahn, R.; and Haasen, P. *Physical Metallurgy*. The Netherlands: Elsevier, 1996.

62. Hall, E. O. "The deformation and ageing of mild steel." *Procedings of the Physical Society* B 64 (1951): 747.

63. Petch, N. J. "The cleavage strength of polycrystals." *Journal of Iron Steel Institute* 174 (1953): 25.

64. Kocks, U. F.; Tome, C. N.; and Wenk, H. R. "Texture and anisotropy." *Cambridge University Press* (2000).

65. Kumar, K. S.; Van Swygenhoven, H.; and Suresh, S. "Mechanical behavior of nanocrystalline metals and alloys." *Acta Materialia* 51 (2003): 5743-5774.

66. Dieter, G. E. *Mechanical Metallurgy*. Boston, MA: McGraw-Hill, 1986.

67. Sabirov, I.; Murashkin, M. Y.; and Valiev, R. Z. "Nanostructured aluminium alloys produced by severe plastic deformation: New horizons in development." *Materials Science and Engineering: A* 560 (2013): 1-24.

68. Chokshi, A. H.; Rosen, A.; Karch, J.; and Gleiter, H. "On the validity of the hall-petch relationship in nanocrystalline materials." *Scripta Metallurgica* 23 (1989): 1679-1683.

69. Ryen, O.; Nijs, O.; Sjolander, E.; Holmedal, B.; Ekstrom, H. E.; and Nes, E. "Strengthening mechanisms in solid solution aluminum alloy." *Metallurgical and Materials Trasactions A* 37 (2006): 1999-2006.

70. Sauvage, X.; Wilde, G.; Divinski, S. V.; Horita, Z.; and Valiev, R. Z. "Grain boundaries in ultrafine grained materials processed by severe plastic deformation and related phenomena." *Materials Science and Engineering: A* 540 (2012): 1-12.

71. Starink, M. J.; and Wang, S. C. "The thermodynamics of and strengthening due to co-clusters: General theory and application to the case of Al–Cu–Mg alloys." *Acta Materialia* 57 (2009): 2376-2389.

72. Sauvage, X.; Murashkin, M.; and Valiev, R. Z. "Atomic scale investigation of dynamic precipitation and grain boundary segregation in a 6061 aluminum alloy nanostructured by ECAP." *Kovove Materialy* 49 (2011): 11-15.

73. Sha, G.; Marceau, R. K. W.; Gao, X.; Muddle, B. C.; and Ringer, S. P. "Nanostructure of aluminium alloy 2024: Segregation, clustering and precipitation processes." *Acta Materialia* 59 (2011): 1659-1670.

74. Sha, G.; Yao, L.; Liao, X. Z.; Ringer, S. P.; Chao Duan, Z.; and Langdon, T. G. "Segregation of solute elements at grain boundaries in an ultrafine grained Al–Zn–Mg–Cu alloy." *Ultramicroscopy* 111 (2011): 500-505.

75. Moreno-Valle, E. C.; Sabirov, I.; Perez-Prado, M. T.; Murashkin, M. Y.; Bobruk, E. V.; and Valiev, R. Z. "Effect of the grain refinement via severe plastic deformation on strength properties and deformation behavior of an Al6061 alloy at room and cryogenic temperatures." *Materials Letters* 65 (2011): 2917-2919.

76. Valiev, R. Z.; Enikeev, N. A.; Murashkin, M. Y.; Kazykhanov, V. U.; and Sauvage, X. "On the origin of the extremely high strength of ultrafine-grained Al alloys produced by severe plastic deformation." *Scripta Materialia* 63 (2010): 949-952.

77. Clark, B. G.; Robertson, I. M.; and Dougherty, L. M. "High-temperature dislocation-precipitate interactions in Al alloys: An in situ Transmission Electron Microscopy deformation study." *Journal of Materials Research* 20 (2005): 1792-1801.

78. Islamgaliev, R. K.; Yunusova, N. F.; Nikitina, M. A.; and Nesterov, K. M. "The effect of alloying elements on superplasticity in an ultrafine-grained aluminum alloy." *Reviews on Advanced Materials Science* 25 (2010): 241-248.

79. Horita, Z.; and Langdon, T. "Achieving exceptional superplasticity in a bulk aluminum alloy processed by high-pressure torsion." *Scripta Materialia* 58 (2008): 1029-1032.

80. Gutierrez-Urrutia, I.; Muñoz-Morris, M. A.; and Morris, D. G. "The effect of coarse second-phase particles and fine precipitates on microstructure refinement and mechanical properties of severely deformed Al alloy." *Materials Science and Engineering: A* 394 (2005): 399-410.

81. Valdes Leon, K.; Muñoz-Morris, M. A.; and Morris, D. G. "Optimisation of strength and ductility of Cu–Cr–Zr by combining severe plastic deformation and precipitation." *Materials Science and Engineering: A* 536 (2012): 181-189.

82. Huskins, E. L.; Cao, B.; and Ramesh, K. T. "Strengthening mechanisms in an Al–Mg alloy." *Materials Science and Engineering: A* 527 (2010): 1292-1298.

83. Courtney, T. H. *Mechanical behavior of materials*. New York: McGraw-Hill, 2000.

84. Gutierrez-Urrutia, I.; Muñoz-Morris, M. A.; and Morris, D. G. "Recovery of deformation substructure and coarsening of particles on annealing severely plastically deformed Al–Mg–Si alloy and analysis of strengthening mechanisms." *Journal of Materials Research* 21 (2006): 329-342.

85. Murayama, M.; Horita, Z.; and Hono, K. "Microstructure of two-phase Al–1.7 at% Cu alloy deformed by equal-channel angular pressing." *Acta Materialia* 49 (2001): 21-29.

86. Lechner, W.; Puff, W.; Mingler, B.; Zehetbauer, M. J.; and Würschum, R. "Microstructure and vacancy-type defects in high-pressure torsion deformed Al–Cu–Mg–Mn alloy." *Scripta Materialia* 61 (2009): 383-386.

87. Brodova, I. G.; Shirinkina, I. G.; and Antonova, O. V. "Phase and structural transformations in the Al-Cr-Zr alloy after rapid melt quenching and high-pressure torsion." *The Physics of Metals and Metallography* 104 (2007): 281-288.

88. Sha, G.; Wang, Y. B.; Liao, X. Z.; Duan, Z. C.; Ringer, S. P.; and Langdon, T. G. "Influence of equal-channel angular pressing on precipitation in an Al–Zn–Mg–Cu alloy." *Acta Materialia* 57 (2009): 3123-3132.

89. Huang, Y.; Robson, J. D.; and Prangnell, P. B. "The formation of nanograin structures and accelerated room-temperature theta precipitation in a severely deformed Al–4wt.% Cu alloy." *Acta Materialia* 58 (2010): 1643-1657.

90. Gubicza, J.; Schiller, I.; Chinh, N. Q.; Illy, J.; Horita, Z.; and Langdon, T. G. "The effect of severe plastic deformation on precipitation in supersaturated Al–Zn–Mg alloys." *Materials Science and Engineering: A* 460–461 (2007): 77-85.

91. Zhao, Y. H.; Liao, X. Z.; Jin, Z.; Valiev, R. Z.; and Zhu, Y. T. "Microstructures and mechanical properties of ultrafine grained 7075 Al alloy processed by ECAP and their evolutions during annealing." *Acta Materialia* 52 (2004): 4589-4599.

92. Chinh, N. Q.; Gubicza, J.; Czeppe, T.; Lendvai, J.; Xu, C.; Valiev, R. Z.; and Langdon, T. G. "Developing a strategy for the processing of age-hardenable alloys by ECAP at room temperature." *Materials Science and Engineering: A* 516 (2009): 248-252.

93. Cepeda-Jiménez, C. M.; García-Infanta, J. M.; Ruano, O. A.; and Carreño, F. "Mechanical properties at room temperature of an Al–Zn–Mg–Cu alloy processed by equal channel angular pressing." *Journal of Alloys and Compounds* 509 (2011): 8649-8656.

94. El-Danaf, E. A. "Mechanical properties, microstructure and texture of single pass equal channel angular pressed 1050, 5083, 6082 and 7010 aluminum alloys with different dies." *Materials & Design* 32 (2011): 3838-3853.

95. Jayaganthan, R.; Brokmeier, H. G.; Schwebke, B.; and Panigrahi, S. K. "Microstructure and texture evolution in cryorolled Al 7075 alloy." *Journal of Alloys and Compounds* 496 (2010): 183-188.

96. Kamikawa, N.; Huang, X.; Tsuji, N.; and Hansen, N. "Strengthening mechanisms in nanostructured high-purity aluminium deformed to high strain and annealed." *Acta Materialia* 57 (2009): 4198-4208.

97. Beyerlein, I. J.; and Tóth, L. S. "Texture evolution in equal-channel angular extrusion." *Progress in Materials Science* 54 (2009): 427-510.

98. Schmid, E.; and Boas, W. *Plasticity of Crystals*. London: Hughes & Co, 1950.

99. Lobemeier, D.; Klein, H.; and Nembach, E. "Grain boundary strengthening of copper-base copper–manganese and copper–gallium solid solutions." *Acta Materialia* 46 (1998): 2909-2912.

100. Conrad, H. "Grain size dependence of the plastic deformation kinetics in Cu." *Materials Science and Engineering: A* 341 (2003): 216-228.

101. Conrad, H. "Grain-size dependence of the flow stress of Cu from millimeters to nanometers." *METALLURGICAL AND MATERIALS TRANSACTIONS A* 35A (2004): 2681-2695.

102. Conrad, H.; and Jung, K. "Effect of grain size from mm to nm on the flow stress and plastic deformation kinetics of Au at low homologous temperatures." *Materials Science and Engineering: A* 406 (2005): 78-85.

103. Wang, Z. W.; Wang, Y. B.; Liao, X. Z.; Zhao, Y. H.; Lavernia, E. J.; Zhu, Y. T.; Horita, Z.; and Langdon, T. G. "Influence of stacking fault energy on deformation mechanism and dislocation storage capacity in ultrafine-grained materials." *Scripta Materialia* 60 (2009): 52-55.

104. Weertman, J. "Crack growth for the double slip plane crack model-I. The R-curve." *Acta Metallurgica* 32 (1984): 563-573.

105. Meyers, M. A.; Mishra, A.; and Benson, D. J. "Mechanical properties of nanocrystalline materials." *Progress in Materials Science* 51 (2006): 427-556.

106. Hayes, R. W.; Witkin, D. B.; Zhou, F.; and Lavernia, E. J. "Deformation and activation volumes of cryomilled ultrafine-grained aluminum." *Acta Materialia* 52 (2004): 4259-4271.

107. Sabirov, I.; Estrin, Y.; Barnett, M. R.; Timokhina, I.; and Hodgson, P. D. "Tensile deformation of an ultrafine-grained aluminium alloy: Micro shear banding and grain boundary sliding." *Acta Materialia* 56 (2008): 2223-2230.

108. Valiev, R. Z.; Alexandrov, I. V.; Zhu, Y. T.; and Lowe, T. C. "Paradox of strength and ductility in metals processed by severe plastic deformation." *Journal of Materials Research* 17 (2002): 5-8.

109. Sergueeva, A. V.; Mara, N. A.; and Mukherjee, A. K. "Plasticity at really diminished length scales." *Materials Science and Engineering: A* 463 (2007): 8-13.

110. Straumal, B. B.; Baretzky, B.; Mazilkin, A. A.; Phillipp, F.; Kogtenkova, O. A.; Volkov, M. N.; and Valiev, R. Z. "Formation of nanograined structure and decomposition of supersaturated solid solution during high pressure torsion of Al-Zn and Al-Mg alloys." *Acta Materialia* 52 (2004): 4469-4478.

111. Han, B.; Huang, J.; Zhu, Y.; and Lavernia, E. *Scripta Materialia* 54 (2006): 1175.

112. Cheng, S.; Ma, E.; Wang, Y. M.; Kecskes, L. J.; Youssef, K. M.; Koch, C. C.; Trociewitz, U. P.; and Han, K. "Tensile properties of in situ consolidated nanocrystalline Cu." *Acta Materialia* 53 (2005): 1521-1533.

113. Champion, Y.; Langlois, C.; Guérin-Mailly, S.; Langlois, P.; Bonnentien, J. L.; and Hÿtch, M. J. "Near-perfect elastoplasticity in pure nanocrystalline copper." *Science* 300 (2003): 310-311.

114. Van Swygenhoven, H.; and Derlet, P. M. "Grain-boundary sliding in nanocrystalline fcc metals." *Physical Review B* 64 (2001): 224105.

115. Huang, Y. i.; and Langdon, T. G. "Advances in ultrafine-grained materials." *Materials Today* 16 (2013): 85-93.

116. Guduru, R.; Murty, K.; Youssef, K. M.; Scattergood, R. O.; and Koch, C. C. "Mechanical behavior of nanocrystalline copper." *Materials Science and Engineering: A* 463 (2007): 14-21.

117. Zhao, Y.; Zhu, Y.; and Lavernia, E. J. "Strategies for improving tensile ductility of bulk nanostructured materials." *Advanced Engineering Materials* 12 (2010): 769-778.

118. Hart, E. V. "Theory of the tensile test." *Acta Materialia* 15 (1967): 351-355.

119. Dalla Torre, F.; Pereloma, E. V.; and Davies, C. H. J. "Strain rate sensitivity and apparent activation volume measurements on equal channel angular extruded Cu processed by one to twelve passes." *Scripta Materialia* 51 (2004): 367-371.

120. Wang, Y. M.; and Ma, E. "Three strategies to achieve uniform tensile deformation in a nanostructured metal." *Acta Materialia* 52 (2004): 1699-1709.

121. Ovid´ko, I. A.; and Sheinerman, A. G. "Enhanced ductility of nanomaterials through optimization of grain boundary sliding and diffusion processes." *Acta Materialia* 57 (2009): 2217-2228.

122. Han, B. Q.; Huang, J. Y.; Zhu, Y. T.; and Lavernia, E. J. "Strain rate dependence of properties of cryomilled bimodal 5083 Al alloys." *Acta Materialia* 54 (2006): 3015-3024.

123. Zhao, Y. H.; Bingert, J. F.; Liao, X. Z.; Cui, B. Z.; Han, K.; Sergueeva, A. V.; Mukherjee, A. K.; Valiev, R. Z.; Langdon, T. G.; and Zhu, Y. T. "Simultaneously increasing the ductility and strength of ultra-fine-grained pure copper." *Advanced Materials* 18 (2006): 2949-2953.

124. Wei, Q.; Cheng, S.; Ramesh, K. T.; and Ma, E. "Effect of nanocrystalline and ultrafine grain sizes on the strain rate sensitivity and activation volume: fcc versus bcc metals." *Materials Science and Engineering: A* 381 (2004): 71-79.

125. Höppel, H. W.; May, J.; and Göken, M. "Enhanced strength and ductility in ultrafine-grained aluminium produced by accumulative roll bonding." *Advanced Engineering Materials* 6 (2004): 781-784.

126. Sabirov, I.; Valiev, R. Z.; Semenova, I. P.; and Pippan, R. "Effect of equal channel angular pressing on the fracture behavior of commercially pure titanium." *Material Science and Engineering A* 41 A (2010): 727-732.

127. Hohenwarter, A.; and Pippan, R. "Fracture toughness evaluation of ultrafine-grained nickel." *Scripta Materialia* 64 (2011): 982-985.

128. Hohenwarter, A.; and Pippan, R. "Anisotropic fracture behavior of ultrafine-grained iron." *Materials Science and Engineering: A* 42A (2011): 1609-1618.

129. Wetscher, F.; Pippan, R.; Sturm, S.; Kauffmann, F.; Scheu, C.; and Dehm, G. "TEM Investigations of the Structural Evolution in a Pearlitic Steel Deformed by High-Pressure Torsion." *Mater. Sci. Eng. A.* 37 (2006): 1963-1968.

130. Kammerhofer, C.; Hohenwarter, A.; Scheriau, S.; Brantner, H. P.; and Pippan, R. "Influence of morphology and structural size on the fracture behavior of a nanostructured pearlitic steel." *Materials Science and Engineering: A* 585 (2013): 190–196.

131. Sabirov, I.; Kolednik, O.; Valiev, R. Z.; and Pippan, R. "Equal channel angular pressing of metal matrix composites: Effect on particle distribution and fracture toughness." *Acta Materialia* 53 (2005): 4919-4930.

132. Billard, S.; Fondère, J. P.; Bacroix, B.; and Dirras, G. F. "Macroscopic and microscopic aspects of the deformation and fracture mechanisms of ultrafine-grained aluminum processed by hot isostatic pressing." *Acta Materialia* 54 (2006): 411-421.

133. Chen, X. H.; Lu, L.; and Lu, K. "Electrical resistivity of ultrafine-grained copper with nanoscale growth twins." *Journal of Applied Physics* 102 (2007): 083708.

134. Takata, N.; Lee, S.; and Tsuji, N. "Ultrafine grained copper alloy sheets having both high strength and high electric conductivity." *Materials Letters* 63 (2009): 1757-1760.

135. Zhang, Y.; Li, Y. S.; Tao, N. R.; and Lu, K. "High strength and high electrical conductivity in bulk nanograined Cu embedded with nanoscale twins." *Applied Physics Letters* 91 (2007): 211901.

136. Shangina, D. V.; Bochvar, N. R.; and Dobatkin, S. V. "The effect of alloying with hafnium on the thermal stability of chromium bronze after severe plastic deformation." *Journal of Materials Science* 47 (2012): 7764-7769.

137. Champion, Y.; and Bréchet, Y. "Effect of grain size reduction and geometrical confinement in fine grained copper: Potential applications as a material for reversible electrical contacts." *Advanced Engineering Materials* 12 (2010): 798-802.

138. Valiev, R. Z.; Zehetbauer, M. J.; Estrin, Y.; Höppel, H. W.; Ivanisenko, Y.; Hahn, H.; Wilde, G.; Roven, H. J.; Sauvage, X.; and Langdon, T. G. "The innovation potential of bulk nanostructured materials." *Advanced Engineering Materials* 9 (2007): 527-533.

139. Fischer, R.; Schrefl, T.; Kronmüller, H.; and Fidler, J. "Grain-size dependence of remanence and coercive field of isotropic nanocrystalline composite permanent magnets." *Journal of Magnetism and Magnetic Materials* 153 (1996): 35-49.

140. Lowe, T.; and Zhu, Y. "Commercialization of Nanostructured Metals Produced by Severe Plastic Deformation Processing." *Advanced Engineering Materials* 5 (2003): 373-378.

141. Ferrasse, S.; Alford, F.; Grabmeier, S.; Düvel, A.; Zedlitz, R.; Strothers, S.; Evans, J.; and B., D. "ECAE® Targets with Sub-Micron Grain Structures Improve Sputtering Performance and Cost-of-Ownership." Technology White Paper:Honeywell Electronic Materials Inc. , 2003.

142. Valiev, R. Z.; Semenova, I. P.; Latysh, V. V.; Rack, H.; Lowe, T. C.; Petruzelka, J.; Dluhos, L.; Hrusak, D.; and Sochova, J. "Nanostructured titanium for biomedical applications." *Advanced Biomaterials B* (2008): 15-17.

143. Argon, A. S.; Im, J.; and Needleman, A. "Distribution of plastic strain and negative pressure in necked steel and copper bars." *Metallurgical Transactions A* 6 (1975): 815-824.

144. Yang, K.; Ivanisenko, Y.; Caron, A.; Chuvilin, A.; Kurmanaeva, L.; Scherer, T.; Valiev, R. Z.; and Fecht, H. J. "Mechanical behaviour and in situ observation of shear bands in ultrafine grained Pd and Pd–Ag alloys." *Acta Materialia* 58 (2010): 967-978.

145. Pachla, W.; Kulczyk, M.; Świderska-Środa, A.; Lewandowska, M.; Garbacz, H.; Mazur, A.; and Kurzydłowski, K. J. "Nanostructuring of metals by hydrostatic extrusion." Proc. of 9th Int. Conf. on Mat. Forming ESAFORM-2006. Glasgow, UK, 2006;535-538.

146. Ryazanov, A. I.; Pavlov, S. A.; and Kiritani, M. "Effective temperature rise during propagation of shock wave and high-speed deformation in metals." *Materials Science and Engineering: A* 350 (2003): 245-250.

147. ASTM. Standard specification for Titanium and Titanium alloy bars and billets. ASTM B 348-09, 2013.

148. Milička, K.; and Dobeš, F. "Small punch testing of P91 steel." *International Journal of Pressure Vessels and Piping* 83 (2006): 625-634.

149. Wang, Z.; Shi, H.; Lu, J.; Shi, P.; and Ma, X. "Small punch testing for assessing the fracture properties of the reactor vessel steel with different thicknesses." *Nuclear Engineering and Design* 238 (2008): 3186-3193.

150. Gülçimen, B.; Durmuş, A.; Ülkü, S.; Hurst, R. C.; Turba, K.; and Hähner, P. "Mechanical characterisation of a P91 weldment by means of small punch fracture testing." *International Journal of Pressure Vessels and Piping* 105–106 (2013): 28-35.

151. Isselin, J.; and Shoji, T. "Crack initiation resistance characterization of weld by small-punch test in boiling water reactor environment." *International Journal of Pressure Vessels and Piping* 93–94 (2012): 22-28.

152. Blagoeva, D. T.; and Hurst, R. C. "Application of the CEN (European Committee for Standardization) small punch creep testing code of practice to a representative repair welded P91 pipe." *Materials Science and Engineering: A* 510–511 (2009): 219-223.

153. Stampfl, J.; and Kolednik, O. "The separation of the fracture energy in metallic materials." *International Journal of Fracture* 101 (2000): 321-345.

154. ASTM. Standard test method for measurement of fracture toughness. ASTM E1820-01. Philadelphia, 2001.

155. Tatschl, A.; and Kolednik, O. "A new tool for the experimental characterization of micro-plasticity." *Material Science and Engineering A* 339 (2003): 265-280.

156. Hohenwarter, A.; and Pippan, R. "A comprehensive study on the damage tolerance of ultrafine-grained copper." *Materials Science and Engineering: A* 540 (2012): 89-96.

157. Norbury, A. L.; and Samuel, T. "The recovery and sinking-in or piling-up in the Brinell test, and the effects of these factors on the correlation of the Brinell with certain other hardness tests." *Journal of Iron Steel Institute* 117 (1928): 673-687.

158. Nix, W. D.; and Gao, H. "Indentation size effects in crystalline materials: A law for strain gradient plasticity." *Journal of the Mechanics and Physics of Solids* 46 (1998): 411-425.

159. Oliver, W. C.; and Pharr, G. M. "An improved technique for determining hardness and elastic modulus using load and displacement sensing indentation experiments." *Journal of Materials Research* 7 (1992): 1564-1583.

160. Dalla Torre, F. H.; Pereloma, E. V.; and Davies, C. H. J. "Strain hardening behaviour and deformation kinetics of Cu deformed by equal channel angular extrusion from 1 to 16 passes." *Acta Materialia* 54 (2006): 1135-1146.

161. Huang, C. X.; Wu, S. D.; Li, S. X.; and Zhang, Z. F. "Strain hardening behavior of ultrafine-grained Cu by analyzing the tensile stress-strain curve." *Advanced Engineering Materials* 10 (2008): 434-438.

162. Chowdhury, S.; Xu, C.; and Langdon, T. "Texture evolution in an aluminum alloy processed by ECAP with concurrent precipitate fragmentation." *Materials Science and Engineering: A* 473 (2008): 219-225.

163. Li, J. X.; Zhai, T.; Garratt, M. D.; and Bray, G. H. "Four-point-bend fatigue of AA 2026 aluminum alloys." *METALLURGICAL AND MATERIALS TRANSACTIONS A* 36 (2005): 2529-2539.

164. Horita, Z.; Smith, D. J.; Furukawa, M.; Nemoto, M.; Valiev, R. Z.; and Langdon, T. G. "Evolution of grain boundary structure in submicrometer-grained Al-Mg alloy." *Materials Characterization* 37 (1996): 285-294.

165. Hajizadeh, K.; Ghobadi Alamdari, S.; and Eghbali, B. "Stored energy and recrystallization kinetics of ultrafine grained titanium processed by severe plastic deformation." *Physica B: Condensed Matter* 417 (2013): 33-38.

166. Contieri, R. J.; Zanotello, M.; and Caram, R. "Recrystallization and grain growth in highly cold worked CP-Titanium." *Materials Science and Engineering: A* 527 (2010): 3994-4000.

167. Wang, Y. N.; and Huang, J. C. "Texture analysis in hexagonal materials." *Materials Chemistry and Physics* 81 (2003): 11-26.

168. Nemat-Nasser, S.; Guo, W. G.; and Cheng, J. Y. "Mechanical properties and deformation mechanisms of a commercially pure titanium." *Acta Materialia* 47 (1999): 3705-3720.

169. Yapici, G. G.; Karaman, I.; and Maier, H. J. "Mechanical flow anisotropy in severely deformed pure titanium." *Materials Science and Engineering: A* 434 (2006): 294-302.

170. Conrad, H. "Effect of interstitial solutes on the strength and ductility of titanium." *Progress in Materials Science* 26 (1981): 123-403.

171. Myshlyaev, M. M.; and Mironov, S. Y. "On the mechanism of deformation in submicrocrystalline titanium." *Physics of the Solid State* 44 (2002): 738-743.

172. Gong, J.; and Wilkinson, A. J. "Anisotropy in the plastic flow properties of single-crystal α titanium determined from micro-cantilever beams." *Acta Materialia* 57 (2009): 5693-5705.

173. Cheng, S.; Ma, E.; Wang, Y.; Kecskes, L.; Youssef, K.; Koch, C.; and al., e. *Acta Materialia* 53 (2005): 1521.

174. Wang, Y. M.; Wang, K.; Pan, D.; Lu, K.; Hemker, K. J.; and Ma, E. "Microsample tensile testing of nanocrystalline copper." *Scripta Materialia* 48 (2003): 1581-1586.

175. Jia, D.; Ramesh, K. T.; and Ma, E. "Effects of nanocrystalline and ultrafine grain sizes on constitutive behavior and shear bands in iron." *Acta Materialia* 51 (2003): 3495-3509.

176. Malekjani, S.; Hodgson, P. D.; Cizek, P.; Sabirov, I.; and Hilditch, T. B. "Cyclic deformation response of UFG 2024 Al alloy." *International Journal of Fatigue* 33 (2011): 700-709.

177. Kashyap, B. P.; Hodgson, P. D.; Estrin, Y.; Timokhina, I.; Barnett, M. R.; and Sabirov, I. "Plastic Flow Properties and Microstructural Evolution in an Ultrafine-Grained Al-Mg-Si Alloy at Elevated Temperatures." *METALLURGICAL AND MATERIALS TRANSACTIONS A* 40 (2009): 3294-3303.

178. Vinogradov, A.; Hashimoto, S.; Patlan, V.; and Kitagawa, K. "Atomic force microscopic study on surface morphology of ultra-fine grained materials after tensile testing." *Materials Science and Engineering: A* 319–321 (2001): 862-866.

179. Sabirov, I.; Estrin, Y.; Barnett, M. R.; Timokhina, I.; and Hodgson, P. D. "Enhanced tensile ductility of an ultra-fine-grained aluminum alloy." *Scripta Materialia* 58 (2008): 163-166.

180. Ma, Y. W.; Choi, J. W.; and Yoon, K. B. "Change of anisotropic tensile strength due to amount of severe plastic deformation in aluminum 2024 alloy." *Materials Science and Engineering: A* 529 (2011): 1-8.

181. Dunne, F. P. E.; and Rugg, D. "On the mechanisms of fatigue facet nucleation in titanium alloys." *Fatigue & Fracture of Engineering Materials & Structures* 31 (2008): 949-958.

182. Semenova, I. P.; Salimgareeva, G. K.; Latysh, V. V.; Lowe, T.; and Valiev, R. Z. "Enhanced fatigue strength of commercially pure Ti processed by severe plastic deformation." *Materials Science and Engineering: A* 503 (2009): 92-95.

183. Taylor, A. S.; Weiss, M.; Hilditch, T.; Stanford, N.; and Hodgson, P. D. "Formability of cryo-rolled aluminium in uniaxial and biaxial tension." *Materials Science and Engineering: A* 555 (2012): 148-153.

184. Lütjering, G.; and Williams, J. *Titanium*: Springer, 2007.

185. Tabor, D. *The hardness of metals*: Clarendon Press, 1951.

186. Randall, N. X.; Julia-Schmutz, C.; and Soro, J. M. "Combining scanning force microscopy with nanoindentation for more complete characterisation of bulk and coated materials." *Surface and Coatings Technology* 108–109 (1998): 489-495.

187. Shin, C. F. "Tables of HRR Singular Field Quantities, MRL E-147." Providence, RI, USA:Materials Research Laboratory, Brown University, 1983.

188. Malekjani, S.; Hodgson, P. D.; Stanford, N. E.; and Hilditch, T. B. "The role of shear banding on the fatigue ductility of ultrafine-grained aluminium." *Scripta Materialia* 68 (2013): 269-272.

7 APPENDIX

7. APPENDIX

7.1. Current research activities: Formability of ultra-fine grained Al-Mg-Si alloy

The current research activities are focused on improvement of formability of the UFG heat-treatable Al-Mg-Si alloys with low content of alloying elements.

Billets with a diameter of 18 mm and a length of 120 mm were machined from the Al-0.6Mg-0.5Si alloy. They were subjected to solution treatment at 530°C for 2h and quenched in water. Hereafter, this condition will be referred to as CG material. The as-quenched billets were subjected to equal channel angular pressing with parallel channels (ECAP-PC) at 100°C for 1 and 4 passes so the accumulative strain induced into the samples was 1.6 and 6.4, respectively. The angle of ECAP-PC die was 100° and the distance between axes of parallel channels, **K**, was 18 mm (Figure 73). Some billets after ECAP-PC processing were artificially aged at 130ºC for 24 hours.

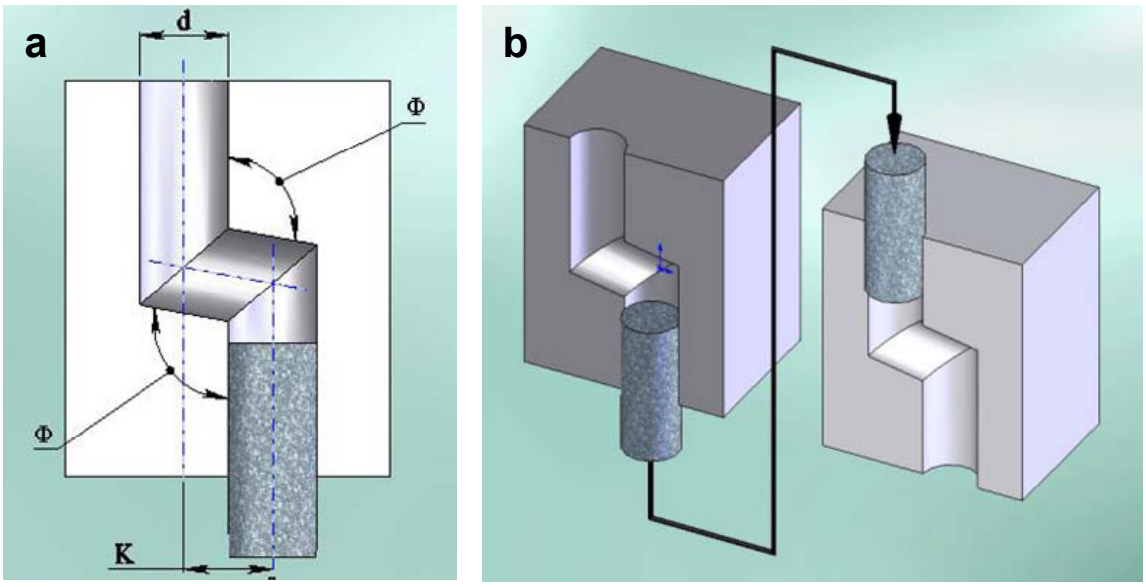

Figure 73. a) Schematic presentation of ECAP-PC processing die: d – diameter of channels, K – distance between axes of parallel channels, Φ – intersection angle between parallel channels and the connecting channel; b) ECAP-PC processing.

Figure 74 illustrates typical microstructure of the Al-0.6Mg-0.5Si alloy after ECAP-PC processing at 100°C for 4 passes. Formation of a very homogeneous microstructure is observed. Elongated grains having a length of 560 nm and aspect ratio of ~2 are seen

on longitudinal section (Figure 74 a). On transversal cross section, ultra-fine grains having a length of 515 nm and aspect ratio of ~1.5 are observed. Nanosized spherical second phase precipitates having an average size of 10 nm are observed along the grain boundaries and in the interior of ultra-fine grains (Figure 74 a). According to the earlier studies on the SPD processed Al-Mg-Si alloys, these nanosized precipitates can be identified as β'-Mg_2Si precipitates and they are formed due to dynamic aging [1,2]. Subsequent artificial aging leads to further decomposition of solid solution and formation of nanoscale needle-type β''-Mg_2Si precipitates (Figure 75)

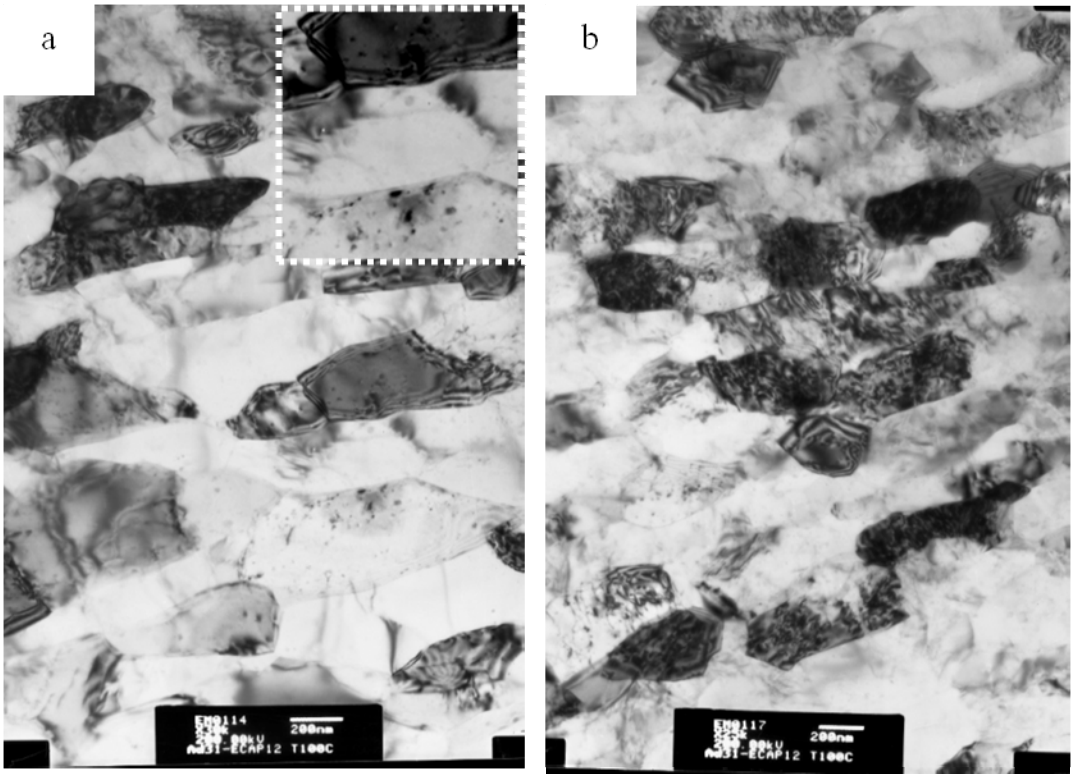

Figure 74. Microstructure of the Al-0.6Mg-0.5Si alloy after ECAP-PC processing at 100°C for 4 passes: (a) longitudinal section, (b) transversal section.

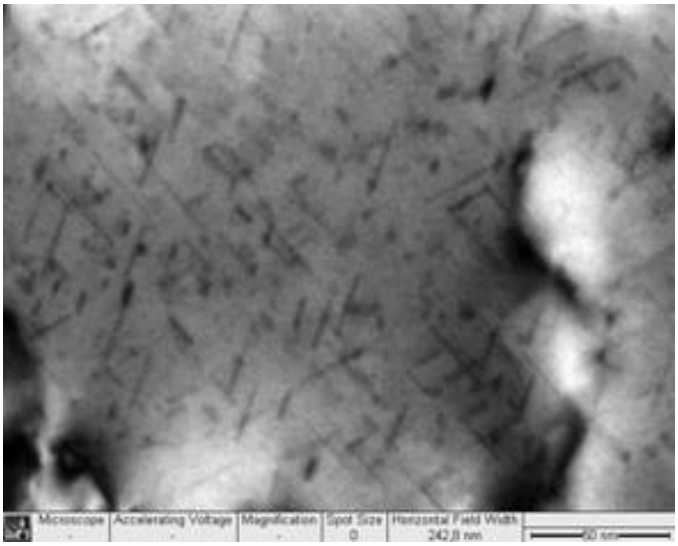

Figure 75. The needle-like β''- Mg_2Si precipitates in the grain interior of the Al-0.6Mg-0.5Si alloy after ECAP-PC processing at 100°C for 4 passes followed by artificial aging.

Appearance of small punch specimens after testing is shown in Figure 76. Figure 77 illustrates punch load – central deflection curves for some conditions. Values for the maximum punch load, the central deflection at maximum punch load and uniform strain are listed in Table 18. It is clearly seen that refining the microstructure down to the ultra-fine scale leads to the increase of the load required for bi-axial stretching of material, whereas the values of central deflection and uniform strain are significantly reduced. However, the alloy after 4 ECAP-PC passes and artificial aging demonstrates bi-axial stretching formability similar to that of the coarse-grained material (Table 18). This could be rationalized based on the increased strain hardening ability of the alloy due to the presence of the nanosized needle-like precipitates which are able to promote the dislocation accumulation in the grain interior [3].

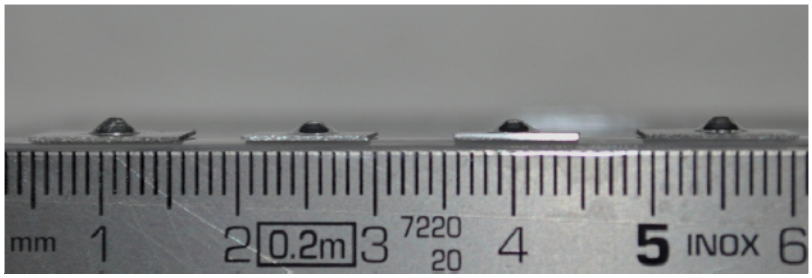

Figure 76. Small punch specimens of the Al-Mg-Si alloy after testing from left to right: CG condition, 1 ECAP passes and CR, 6 ECAP passes and CR and 4 ECAP-PP passes and artificially aged conditions.

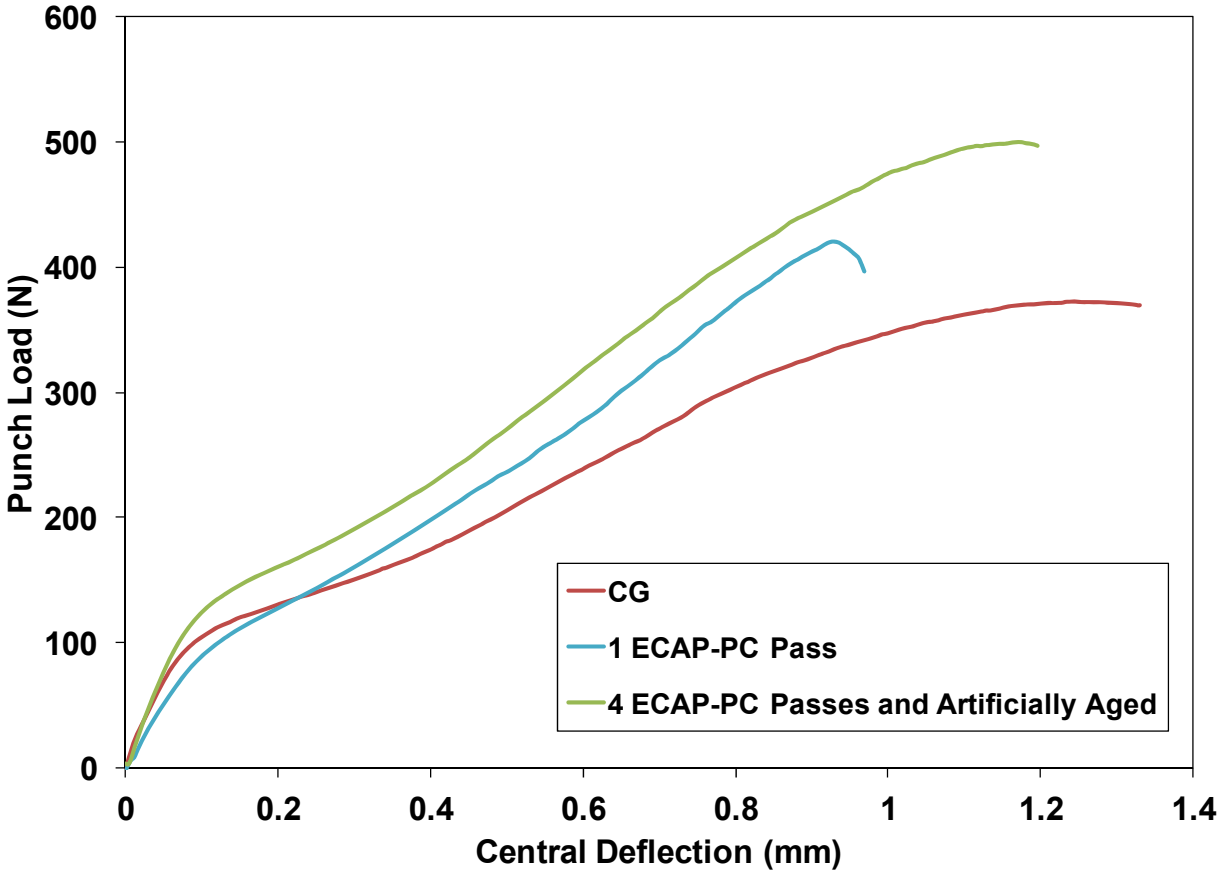

Figure 77. Load – central deflection curves of Al-Mg-Si alloy specimens for the coarse grained condition and ECAP-PC processing for 1 and 4 passes and subsequently artificial aging.

Table 18. Results of small punch testing of coarse grained (CG) Al-Mg-Si and the ECAP-PC Al-Mg-Si alloy and after artificial aging (AA).

Sample	F_{max} (N)	h_{max} (mm)	ε
CG	370	1.25	0.47
1ECAP-PC Pass	420	0.93	0.23
4 ECAP-PC Passes & AA	500	1.18	0.40

Therefore, the introduction of nano-scale precipitates in the ultra-fine grains can be considered as another approach to improve formability of the ultra-fine grained metallic materials. Current research activities have been focused on more detailed analysis of the processing-microstructure—formability relationship in the Al-0.6Mg-0.5Si alloy.

Bibliography

1. X. Sauvage, M. Murashkin, R.Z. Valiev, Kovove Materialy, 49 (2011) 11-15.

2. A. Cuniberti, A. Tolley, M.V.C. Riglos, R. Giovachini, Materials Science and Engineering: A, 527 (2010) 5307-5311.

3. J.K. Kim, H.G. Jeong, S.I. Hong, Y.S. Kim, W.J. Kim, Scripta Materialia, 45 (2001) 901-907.

7.2. Published Manuscripts

E.C. Moreno-Valle, W. Pachla, M. Kulczyk, B. Savoini, M.A. Monge, C. Ballesteros, I. Sabirov. “Anisotropy of uni-axial and bi-axial deformation behaviour of pure Titanium after hydrostatic extrusion*” Material Science and Engineering A* 588 (2013) 7–13.

E.C. Moreno-Valle, M.A. Monclus, J.M. Molina-Aldareguia, N. Enikeev, I. Sabirov, *“*Bi-axial deformation behavior and enhanced formability of ultrafine-grained pure copper” *Metallurgical and Materials Transactions A* 44 (2013) 2399-2408.

E.C. Moreno-Valle, I. Sabirov, M.T. Perez-Prado, M.Yu. Murashkin, E.V. Bobruk, R.Z. Valiev. “Effect of the grain refinement via severe plastic deformation on strength properties and deformation behavior of an Al6061 alloy at room and cryogenic temperatures” *Materials Letters* 65 (2011) 2917–2919.

Materials Science & Engineering A 588 (2013) 7–13

Contents lists available at ScienceDirect

Materials Science & Engineering A

journal homepage: www.elsevier.com/locate/msea

Anisotropy of uni-axial and bi-axial deformation behavior of pure Titanium after hydrostatic extrusion

E.C. Moreno-Valle [a,*], W. Pachla [b], M. Kulczyk [b], B. Savoini [c], M.A. Monge [c], C. Ballesteros [c], I. Sabirov [a]

[a] IMDEA Materials Institute, Calle Eric Kandel 2, Getafe 28906, Madrid, Spain
[b] Institute of High Pressure Physics, Polish Academy of Sciences (Unipress), ul. Sokolowska 29, 01-142 Warsaw, Poland
[c] Departamento de Física, Universidad Carlos III de Madrid, Av. Universidad 30, 28911 Madrid, Spain

ARTICLE INFO

Article history:
Received 10 July 2013
Received in revised form
15 August 2013
Accepted 22 August 2013
Available online 30 August 2013

Keywords:
Titanium
Hydrostatic extrusion
Texture
Uni-axial deformation behavior
Bi-axial deformation behavior
Anisotropy

ABSTRACT

Coarse-grained commercially pure (CP) Titanium is subjected to hydrostatic extrusion resulting in the formation of ultrafine lamellar-type microstructure having very strong fiber texture. Uni-axial tensile tests of longitudinal and transverse specimens are carried out to study anisotropy of uni-axial deformation behavior of hydrostatically extruded CP Titanium. Small punch testing of longitudinal and transverse specimens is performed to study the anisotropy of its bi-axial deformation behavior. It is demonstrated that there is significant anisotropy of both uni-axial and bi-axial deformation of CP Titanium after hydrostatic extrusion which is related to the specific microstructure and texture developed in the material during hydrostatic extrusion.

1. Introduction

Commercially pure (CP) Ti has been widely used in various sectors of engineering including biomedical industry due to its high corrosion resistance and good biocompatibility [1]. However, CP Ti has relatively low mechanical strength limiting its application [1]. Alloying can significantly enhance mechanical performance of CP Ti, but some alloying elements such as vanadium increase the toxicity and degrade its corrosion properties [2]. Nowadays, development of severe plastic deformation (SPD) techniques [3] has enabled formation of ultrafine-grained (UFG) microstructure in CP Ti leading to its enhanced mechanical strength. These SPD methods include equal-channel angular pressing (ECAP) [4,5], ECAP in combination with extrusion (or rolling, swaging, drawing) [6–8], high pressure torsion (HPT) [9,10], cryo-rolling followed by annealing [11], cross rolling [12,13], etc. Hydrostatic extrusion appears as one of the most promising SPD methods for fabrication of UFG CP Ti since it has some advantages [14]. First, very long rods can be processed via hydrostatic extrusion and, second, the method has a very high efficiency due to the very high processing strain rates, usually $>10\,s^{-1}$ but can exceed $10^4\,s^{-1}$. A body of research on the microstructure and mechanical properties of pure Ti after hydrostatic extrusion exists in the literature [15–18]. It was demonstrated that grain size can be successfully refined down to the nanoscale if a strain of 5.47 is induced into rods during hydrostatic extrusion, leading to a mechanical yield strength of 1245 MPa in the longitudinal direction [15]. The effect of hydrostatic extrusion temperature (in the temperature range of 20–450 °C) on the microstructure, texture and mechanical properties of CP Ti was analyzed in [17]. It was shown that extrusion at room temperature leads to formation of a lamellar-type microstructure with the width of lamellae in the range of 100–500 nm, whereas extrusion at 300–450 °C results in formation of a bi-modal microstructure consisting of packs of lamellae and ultrafine grains. Significant increase of mechanical strength was observed after hydrostatic extrusion at all temperatures. As is well known, being hcp metal, α-Ti can show significant anisotropy of mechanical properties depending on the texture developed during materials processing [7,19]. However, no detailed studies on the anisotropy of mechanical properties in the hydrostatically extruded Ti rods have been performed yet. Fundamental understanding of the effect of hydrostatic extrusion on the anisotropy of mechanical behavior of pure Ti is necessary in order to predict the performance of the final engineering components.

The objective of the present work is to study the effect of hydrostatic extrusion on the microstructure, texture, and mechanical properties of pure Ti with greater respect to the anisotropy of uni-axial and bi-axial deformation behavior in the processed material. In most

* Corresponding author. Tel.: +34 91 549 34 22; fax: +34 91 550 30 47.
E-mail address: eva.moreno@imdea.org (E.C. Moreno-Valle).

0921-5093/$ - see front matter © 2013 Published by Elsevier B.V.
http://dx.doi.org/10.1016/j.msea.2013.08.044

Table 1
Parameters of hydrostatic extrusion applied to CP Ti (Grade 3).

Number of extrusion steps	Total cumulative reduction ratio, R_{cum}	Total cumulative true strain, ε_{cum}	Extrusion pressure [MPa]	Linear extrusion speed [mm/s]	Strain rate [s^{-1}]	Adiabatic heating, ΔT [°C]
4	25.41	3.24	630–1050	24–60	6–10	240–400

of metalforming operations, material is deformed in multi-axial mode along complex strain path [20]. Therefore, understanding of anisotropy of bi-axial deformation behavior of the extruded Ti is necessary if metalforming operations will be required for fabrication of complex shape parts from extruded Ti. It should be noted that research on bi-axial deformation behavior of SPD processed metals is very limited [21–23] and anisotropy of bi-axial deformation behavior of the SPD processed metals has not been studied yet.

2. Material and processing

CP Ti (Grade 3) with specification corresponding to the ASTM B348-09 standard [24] was supplied in the form of bars having a diameter of 50 mm. The as-received bar was subjected to hydrostatic extrusion at room temperature in four extrusion steps to the cumulative strain of 3.24 using a 45° die. Detailed description of hydrostatic extrusion process can be found in [25]. The strain rate at the last extrusion step was 10 s^{-1} which corresponds to the linear extrusion speed above 60 mm/s. Different combinations of lubricant paste based on ~60% MoS and refined oil, copper and PTFE aerosols, an aluminum layer deposited by physical vapor deposition (PVD) were tried as lubricants. The parameters of hydrostatic extrusion are outlined in Table 1. The rods after hydrostatic extrusion showed smooth surface without any (micro)cracks.

Hydrostatic extrusion is usually accompanied by significant adiabatic heating which might significantly affect the microstructure developed during processing [25]. The temperature rise due to adiabatic heating was estimated by the commonly accepted equation [25–27],

$$\Delta T = \beta \frac{W}{c\rho} = \beta \frac{p}{c\rho} \quad (1)$$

where W is the plastic deformation work per unit volume, c the specific heat, ρ the material density, p the extrusion pressure, and the dimensionless parameter β denotes the fraction of plastic work converted into heat during deformation. For hydrostatic extrusion with a good insulation by a lubrication layer around the work-piece and high extrusion speed, β is taken as 0.9 [25]. For $c = 0.523$ J g^{-1} K^{-1} and $\rho = 4.5$ g cm^{-3}, Eq. (1) gives a temperature increase, ΔT, in the range of 240–400 °C.

3. Experimental procedures

The specimens for light optical microscopy studies were cut from the extruded rods on the longitudinal L-section (parallel to the rod axis/extrusion direction) and transverse T-section (perpendicular to the rod axis/extrusion direction), as shown in Fig. 1. The specimens were grinded and polished to mirror-like surface using standard metallographic technique. The final step was a chemical–mechanical polishing with a mixture of colloidal silica oxide polishing suspension (OPS) and 5% vol of H_2O_2. Optical microscopes Nikon Eclipse LV150 and OLYMPUS BX 51 were employed for the microstructural analysis.

The specimens for transmission electron microscopy (TEM) studies were cut from the L- and T-sections of the processed rods. The specimens were thinned by electropolishing in a TENUPOL 5 twin-jet polisher using a 1:4 solution of nitric acid in methanol at $T \sim -30$ °C. The TEM analyses were carried out in a TECNAI-20-FEG microscope operated at 200 kV equipped with an X-ray energy dispersive spectrometer. For Z-contrast measurements, a scanning transmission electron microscopy (STEM) modulus with a dark-field high angle annular detector (HAADF) was employed. Selected area electron diffraction (SAED) patterns were recorded from the areas of interest.

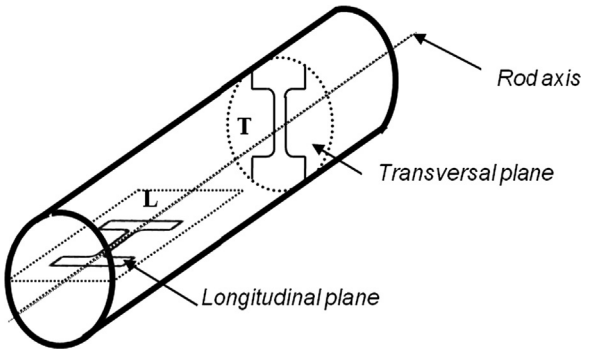

Fig. 1. Rod axis, longitudinal and transverse planes and orientation of specimens in the extruded rod.

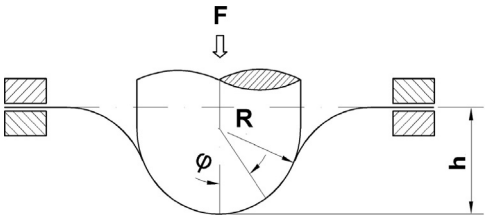

Fig. 2. Schematic drawing of small punch testing.

Texture measurements were performed at the CAI DRX at the Complutense University of Madrid using a Phillips Xpert'PRO diffractometer equipped with a PW3050/60 goniometer. Measurements were taken in a range of Φ angles from 0° to 75° at 3° steps. The pole figures for the planes (0001), (10 – 10), (10 – 11), (10 – 12), (10 – 13), and (10 – 20) were plotted.

To study uni-axial tensile behavior of the material, specimens for tensile testing were cut from the extruded rods so their tensile axis was perpendicular to the rod axis (T-specimens) and parallel to the rod axis (L-specimens), as shown in Fig. 1. Tensile specimens of gauge length 3.2 mm and gauge width of 0.8 mm were mechanically polished to mirror-like surface using colloidal silica solution at the final stage. Tensile tests were carried out at room temperature using the universal tensile/compression module 'Kammrath&Weiss'. Tensile specimens were deformed to failure with constant cross-head speed corresponding to the initial strain rate of 10^{-3} s^{-1}. The mechanical properties (0.2% proof strength $\sigma_{0.2}$, ultimate tensile strength, σ_{UTS}, uniform elongation, ε_u, and elongation to failure, ε_f) were determined from the obtained engineering stress–strain curves. At least three specimens were tested for each condition and the results were reproducible.

To study bi-axial deformation behavior of the material, flat specimens for small punch testing were cut in the T- and L-sections of the extruded rods (Fig. 1). Both sides of the flat

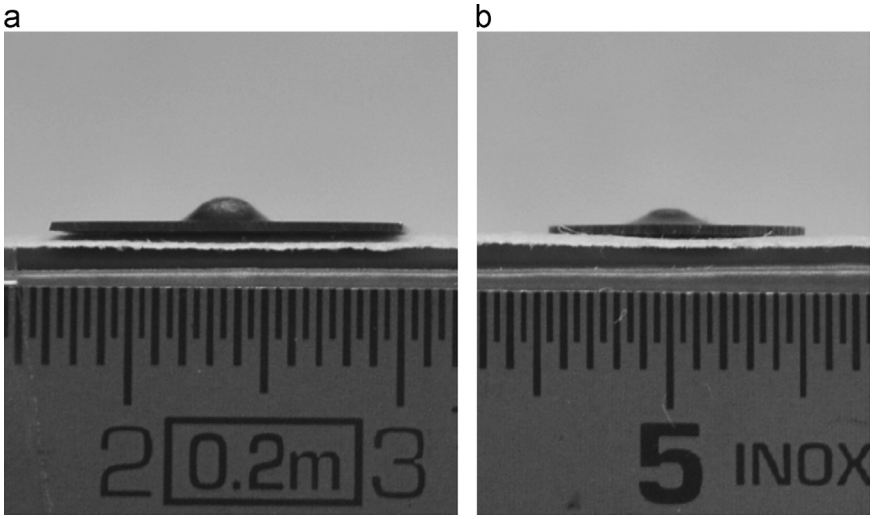

Fig. 3. Appearance of specimens after small punch testing of CP Ti: (a) as-received T-specimen and (b) hydrostatically extruded T-specimen.

specimens were grinded and polished to mirror-like surfaces using colloidal silica at the final stage. The final thickness of specimens was 0.4 mm. A schematic diagram of a small punch testing is illustrated in Fig. 2. A flat punch specimen is clamped between upper and bottom dies. It is deformed at room temperature by a well lubricated hemi-spherical rigid punch having a diameter of 2.4 mm. The die design is similar to that widely used for small punch testing [28–33]. Punch speed during testing was 0.5 mm/min. Load F and central deflection h readings were taken during testing (Fig. 2). Small punch tests were stopped at the moment of onset of plastic instability on the load–central deflection curve. Fig. 3 illustrates appearance of specimens after small punch testing. It is clearly seen that specimens are deformed into a dome shaped cap. To estimate the equivalent strain induced in these small punch specimens, final thickness was measured over areas deformed under membrane (bi-axial) stretching. The true strain was estimated as

$$\varepsilon = \ln\left(\frac{t_0}{t}\right) \tag{2}$$

where t_0 is the initial thickness and t the final thickness of the small punch specimen. At least three specimens were tested per each condition and the results were found to be reproducible.

Qualitative examination of surface relief after deformation of small punch specimens was performed using an EVO MA 15 SEM operating at 20 kV. Surface relief was analyzed in the area of bi-axial stretching.

4. Results and discussions

4.1. Effect of hydrostatic extrusion on microstructure and texture of CP Ti

Optical microscopy images of the as-received CP Titanium are presented in Fig. 4a. A homogeneous microstructure consisting of equiaxed grains having the average size of 42 μm is observed. Fig. 4b shows a representative optical micrograph of a longitudinal section of the CP Titanium samples after hydrostatic extrusion. It is seen that hydrostatic extrusion led to fragmentation and elongation of grains along extrusion direction resulting in the complex microstructure which cannot be clearly resolved with light optical microscope. TEM examination of the samples showed that hydrostatic extrusion leads to a microstructure consisting of lamellae aligned along the extrusion axis and having a length up to 1 μm

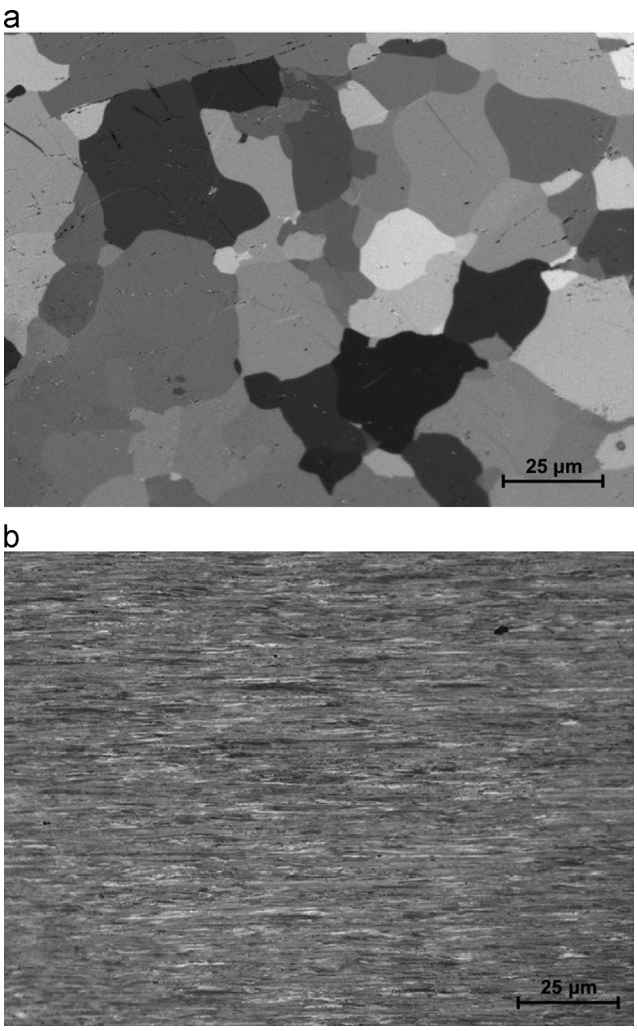

Fig. 4. Optical images of microstructure of CP Ti: (a) as-received; (b) hydrostatically extruded (L plane). Extrusion direction is horizontal.

and a width ranging from 10 to 100 nm (Fig. 5a). A high density of dislocations is observed in the lamellae interior and the formation of equiaxed grains/subgrains is also seen (Fig. 5b). They present straight boundaries intersecting at high angles with neighbor

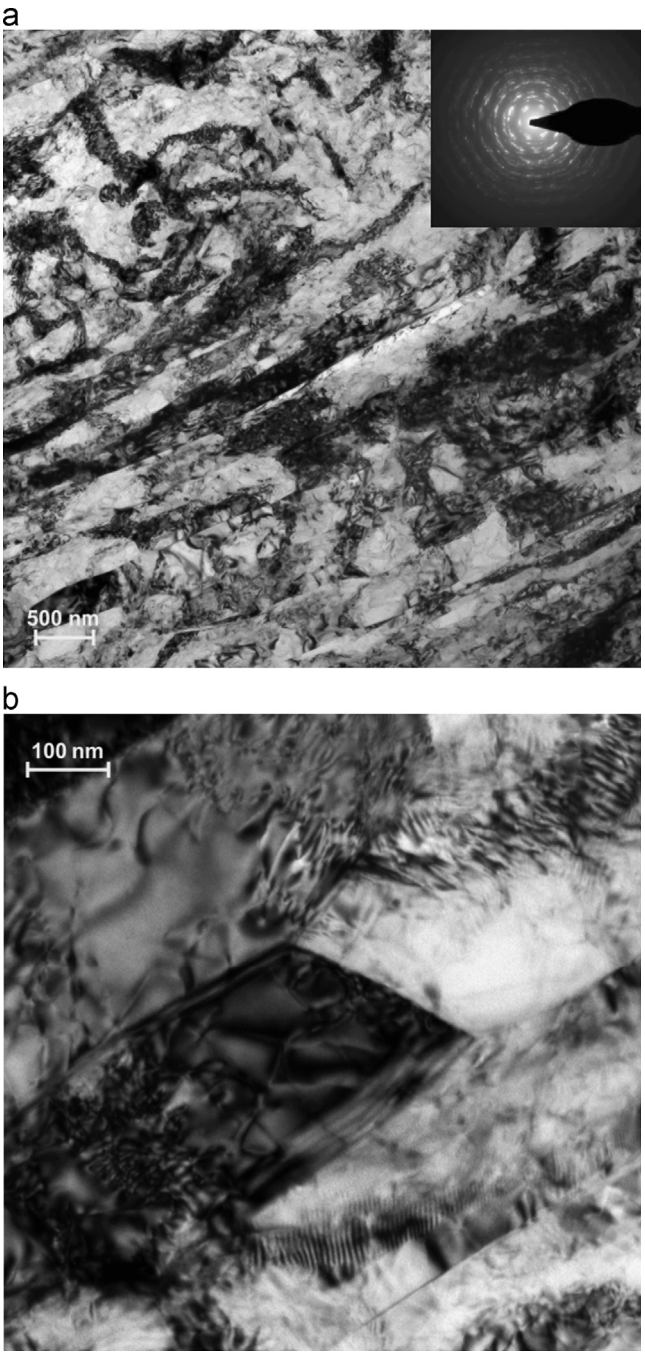

Fig. 5. TEM images of the microstructure of CP Ti after hydrostatic extrusion (L plane).

lamellae. The formation of this microstructure can be related explicitly to twinning and dislocation glide operating in the material during hydrostatic extrusion. Despite hydrostatic extrusion results in significant adiabatic heating of metallic materials [25], the temperature of adiabatic heating in our hydrostatically extruded pure Ti estimated using Eq. (1) (Table 1) is well below the recrystallization temperatures of 620–760 °C reported for severely deformed pure Ti [35,36]. Moreover, it should be noted that the samples during hydrostatic extrusion are heated only in the local deformed volume within the die work-piece during milliseconds and they are immediately cooled down (water quenched) to room temperature, that is insufficient in case of CP Titanium neither for recrystallization nor for significant recovery of the developed microstructure [34,35].

Fig. 6 illustrates pole figures for the T-section of pure Ti before and after hydrostatic extrusion. The as-received material shows a weak texture somewhat similar to that demonstrated by hot rolled pure Ti (Fig. 6a) [36]. Hydrostatic extrusion breaks up the initial texture and leads to formation of very strong fiber texture with $\langle 10-10\rangle$ direction parallel to the rod axis and basal planes (0001) parallel to the rod axis (Fig. 6b). The maximum intensity on the $(10-10)$ pole figure increases up to $\sim$17. Such fiber texture is typical for CP Ti subjected to conventional extrusion, drawing or swaging [37].

4.2. Effect of hydrostatic extrusion on mechanical behavior and its anisotropy

4.2.1. Uni-axial tensile behavior and its anisotropy

Fig. 7 shows the engineering stress–strain curves from tensile tests at room temperature in the L- and T-directions of the as-received and hydrostatically extruded CP Ti. Mechanical properties are listed in Table 2. A slight anisotropy of mechanical properties is observed in the as-received CP Titanium. The T-specimens tend to show higher mechanical properties compared to the L-specimens (Fig. 7, Table 2) due to the weak crystallographic texture present in the as-received material (Fig. 6a). No significant effect of the sample orientation on the work hardening capacity defined as $\sigma_{UTS}/\sigma_{0.2}$ is observed (Fig. 7). The mechanical strength of CP Ti dramatically increases after hydrostatic extrusion due to grain refinement whereas both uniform elongation and elongation to failure show an opposite trend (Table 2). Significant anisotropy of uni-axial tensile mechanical behavior is observed. The L-specimens display very high $\sigma_{0.2}$-value, 915 MPa, but low work hardening capacity, so the σ_{UTS}-value of the material is 970 MPa (Fig. 7, Table 2). On the other hand, the T-specimens show a much lower $\sigma_{0.2}$-value, 562 MPa, but a similar σ_{UTS}-value, 995 MPa, indicating a very high work hardening capacity of the T-specimens (Fig. 7, Table 2). This anisotropy of mechanical behavior can be rationalized based on the very strong crystallographic macrotexture developed in the material during hydrostatic extrusion (Fig. 6b) [7,19]. It is well known that dislocation glide and twinning are the main mechanisms operating during plastic deformation of CP Ti at room temperature [37,38]. Deformation twinning is suppressed in the UFG CP Ti [38,39]. The main dislocation slip modes in CP Ti at room temperature having the lowest critical resolved shear stresses are the prismatic $\langle 11-20\rangle\{10-10\}$ slip system and the basal $\langle 11-20\rangle\{0001\}$ slip system [38,40]. Additionally, dislocation glide on pyramidal systems $\langle 11-20\rangle\{10-11\}$ and $\langle 11-23\rangle\{10-11\}$ can be also activated [40]. The operating systems are generally determined by the Von Misses criterion, the Schmid factors, and the critical resolved shear stress. In the L-specimens, basal planes are suppressed since they are parallel to the tensile axis and two of the prismatic slip planes are suppressed since they are perpendicular to the tensile axis. The remaining four prismatic slip planes are inclined at 60° to the tensile axis and can be active. So, the high yield strength of the material can be related to the limited number of prismatic slip systems available. In the T-specimens, the *c*-axis of the h.c.p. lattice of individual grains is randomly inclined with respect to the tensile axis. Thus, the microstructure will be formed by a combination of soft and hard grains, depending on the individual orientations. The grains that are most favorably oriented for prismatic and basal slip can be easily deformed at lower values of applied stress (soft grains). Localization of plastic slip within these grains results in local strain hardening, and, in turn, in an increase of the flow stress, and in the spread of plastic slip to grains that are less favorably oriented for prismatic and basal slip. This scenario leads to overall high work hardening capacity of the T-specimens. It should be also noted that a higher work hardening

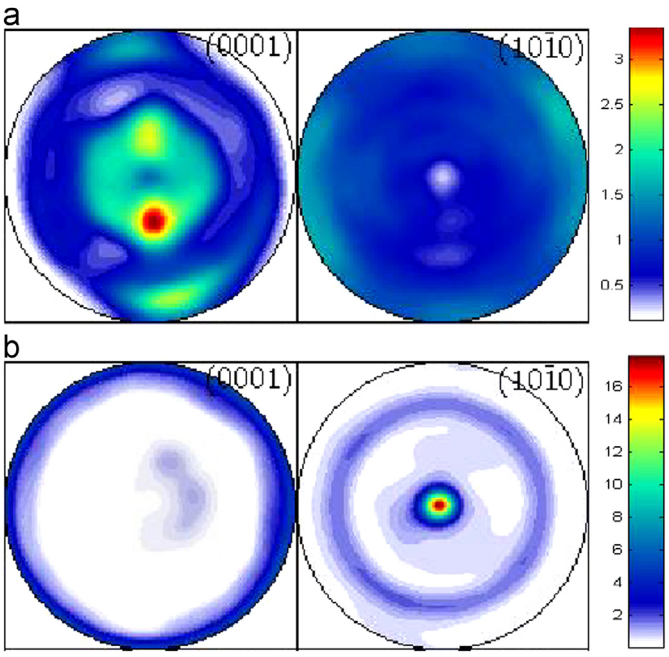

Fig. 6. Pole figures for CP Ti: (a) in the as-received condition; (b) after hydrostatic extrusion. Scale represents multiples of random distribution (mrd).

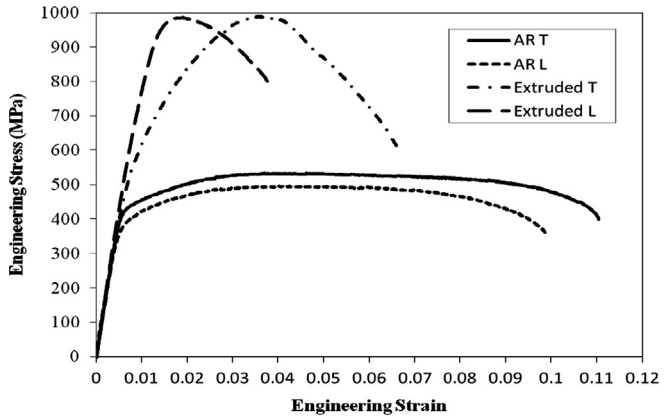

Fig. 7. Engineering stress–strain curves from tensile testing of CP Ti in the as-received (AR) condition and after hydrostatic extrusion.

ability of these T-specimens delays macro-localization of plastic flow resulting in higher uniform elongation (~2.7%) and higher elongation to failure (~6%) compared to those for the L-specimens (~0.9% and ~3.1%) according to the well-known Considere criterion [41].

4.2.2. *Bi-axial deformation behavior and its anisotropy*

Load–central deflection curves from small punch testing of the as-received and extruded CP Ti are presented in Fig. 8. Typical stages of formability behavior are marked on the curve for the as-received specimens. The first stage corresponds to elastic bending that is associated with local surface micro-yielding. During the second stage, plastic bending, plastic flow begins and spreads within the specimen-punch contact zone. Bi-axial deformation of flat specimen into dome shaped cap occurs during the next stage, membrane stretching [42]. Once maximum load capacity is reached, unstable plastic flow begins resulting in the formation of cracks and specimen failure. The results of small punch testing are listed in Table 3. No any anisotropy of bi-axial deformation behavior is observed in the as-received material, since the load-central deflection curves for the

Table 2
Mechanical properties of CP Ti (Grade 3) in the as-received (AR) condition and after hydrostatic extrusion. T indicates transverse section and L longitudinal section.

	$\sigma_{0.2}$ [MPa]	σ_{UTS} [MPa]	ε_u [%]	ε_f [%]
AR-T	396 ± 1	537 ± 12	4.43 ± 0.65	9.82 ± 0.75
AR-L	344 ± 14	494 ± 1	4.95 ± 0.63	8.97 ± 0.67
Extruded-T	562 ± 32	995 ± 7	2.65 ± 0.07	5.95 ± 0.07
Extruded-L	915 ± 70	970 ± 17	0.87 ± 0.16	3.06 ± 0.33

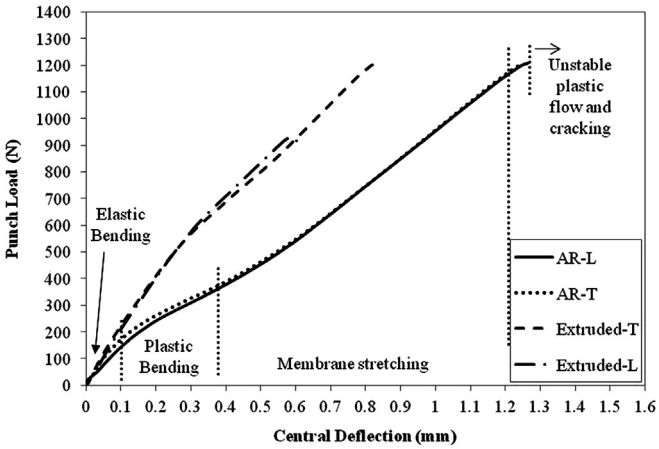

Fig. 8. Load–central deflection curves from small punch testing of CP Ti: as-received (AR) material and hydrostatically extruded material.

Table 3
Results of small punch testing.

Sample	F_{max} [N]	h_{max} [mm]	ε
AR-T	1243 ± 47	1.3 ± 0.05	0.32
AR-L	1213 ± 23	1.27 ± 0.05	0.30
Extruded-T	1163 ± 34	0.79 ± 0.03	0.12
Extruded-L	910 ± 59	0.60 ± 0.02	0.05

L- and T- small punch specimens nearly coincide and have the same maximum central deflection of ~1.3 mm (Fig. 8) and true uniform strain $\varepsilon \sim 0.3$. Fig. 8 shows that hydrostatic extrusion results in a significant increase of the load required for deformation of small punch specimens to the same central deflection as well as to significant reduction of the maximum central deflection leading to the lower values of the true strain which can be induced in the specimens during small punch testing (Table 3). The hydrostatically extruded material shows anisotropy of bi-axial deformation behavior. First, the load-central deflection curves show higher load required for bi-axial deformation of the L-specimens in the membrane stretching regime (Fig. 8). Second, the L-specimens display lower maximum central deflection, ~0.6 mm, and lower value of true uniform strain, 0.12, compared to those for the T-specimens, ~0.8 mm and 0.05, respectively (Table 3).

Surface analysis of the small punch specimens tested up to cracking showed a significant anisotropy in failure behavior of the L- and T-extruded specimens. The T-specimens showed formation of cracks at $\varphi \sim 60^\circ$ which are concentric to the dome as shown in Fig. 9a. These cracks were formed in symmetric manner with respect to the dome axis. Evidence of micro-shear band formation, with deformation bands having a length in the range of 5–15 μm, is observed in Fig. 9b. Two types of cracks were observed in the L-specimens: primary long cracks were formed along the extrusion direction at $\varphi \sim 50$–60° and their further growth to the length of 200–400 μm was accompanied by formation of secondary cracks

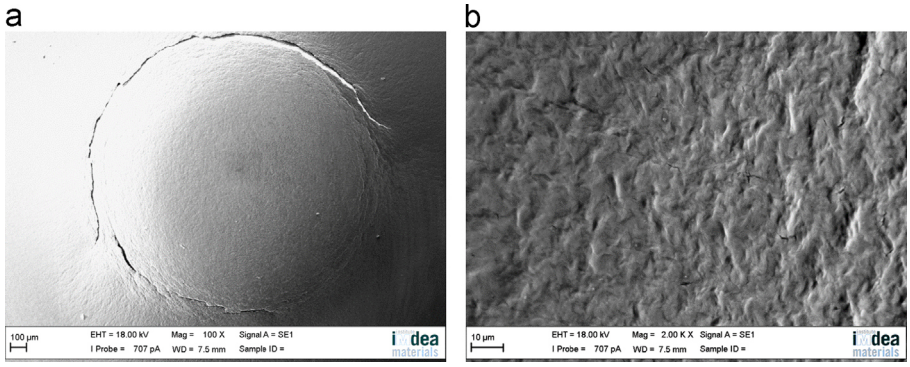

Fig. 9. SEM images of surface relief on the hydrostatically extruded T-specimen after small punch testing: (a) general view of the tested specimen and (b) at $\varphi \sim 30^{\circ}$.

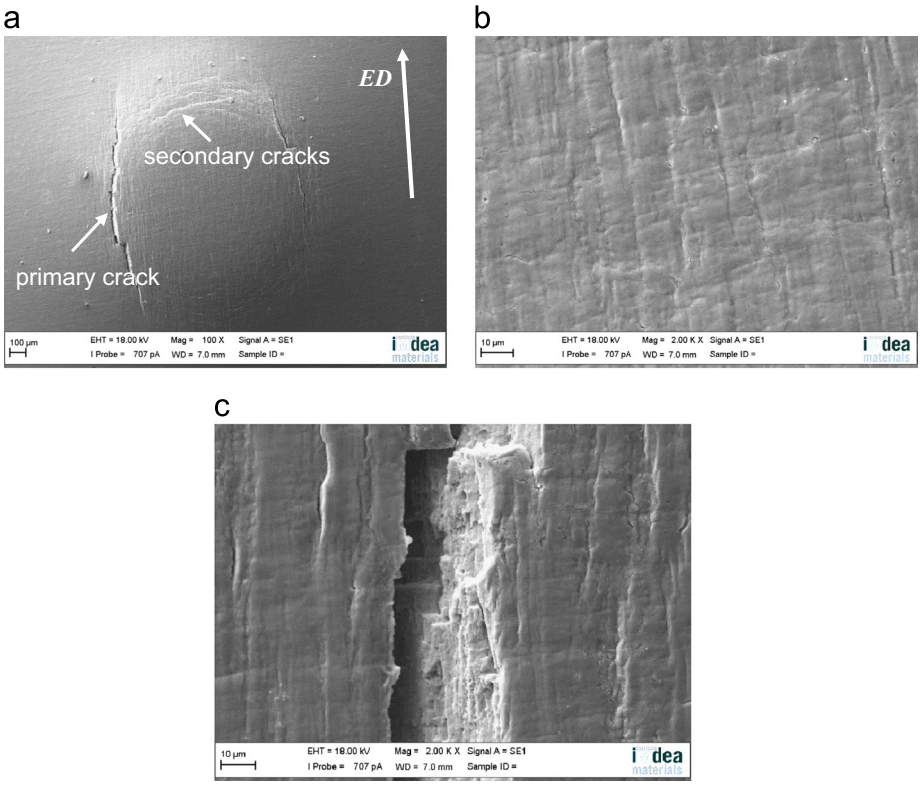

Fig. 10. SEM images of surface relief on hydrostatically extruded L-specimen after small punch testing: (a) general view of the tested specimen, (b) at $\varphi \sim 30^{\circ}$, (c) a primary crack at higher magnification.

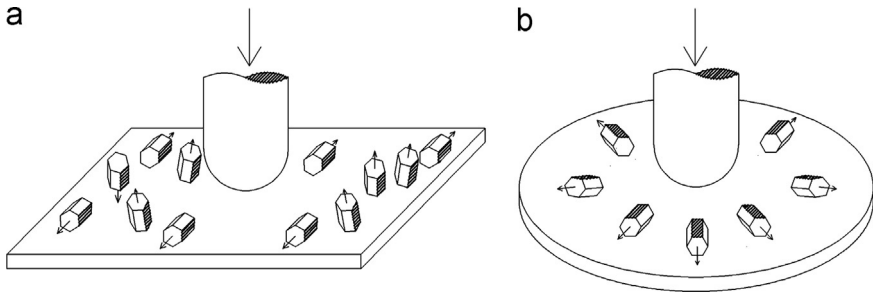

Fig. 11. Schematic drawings of crystallographic texture of extruded specimens during small punch testing: (a) L-specimen and (b) T-specimen.

perpendicular to the extrusion direction, as shown in Fig. 10. The anisotropy in bi-axial deformation and failure behavior of the hydrostatically extruded material can be related to (1) the lamellar-type microstructure and (2) the very strong crystallographic fiber texture developed during hydrostatic extrusion, though we suggest that the latter effect plays the major role. In the T-specimens, the *C*-axis and two prismatic planes of the hcp lattice are perpendicular and all basal planes are parallel to the punch axis (Fig. 11a), thus, resulting in homogeneous bi-axial plastic deformation in the area of bi-axial stretching followed by failure which is symmetrical with respect to the dome axis (Fig. 9a). In the L-specimens, the *C*-axis, basal planes, and prismatic planes are randomly inclined with

respect to the punch axis (Fig. 11b). Therefore, combinations of grains with various crystallographic orientations can be present in the microstructure of the L-specimens. Some combinations of soft grains and hard grains can lead to formation of the quazi-cleavage facets [43] which, in turn, can easily lead to their quick growth along lamellae boundaries since SPD processed Ti tends to show a low crack growth resistance [44].

5. Conclusions

1. Hydrostatic extrusion of CP Ti leads to the formation of ultrafine lamellar-type microstructure having a very strong crystallographic fiber texture with the *C*-axis perpendicular to the extrusion axis and $(10-10)$ direction parallel to the extrusion axis.
2. Hydrostatic extrusion of CP Ti leads to a significant increase of mechanical strength at the expense of ductility. There is a significant anisotropy of uni-axial tensile behavior of hydrostatically extruded CP Ti. The T-specimens show much lower yield strength but much higher strain hardening capacity compared to those of the L-specimens due to the strong crystallographic texture developed during hydrostatic extrusion.
3. There is anisotropy of bi-axial deformation behavior and failure of the hydrostatically extruded CP Ti during small punch testing. A higher load is required for bi-axial deformation of the L-specimens in the membrane stretching regime and the L-specimens show lower maximum central deflection and lower value of true uniform strain compared to those for the T-specimens. The T-specimens are deformed and fail in symmetric manner with respect to the punch axis whereas the failure of the L-specimens begins with formation of primary longitudinal cracks (parallel to the extrusion direction) and their growth followed by formation of secondary cracks (perpendicular to the extrusion direction). This anisotropy is related to the specific microstructure and texture developed in CP Ti during hydrostatic extrusion.

Acknowledgments

This work was carried out in frames of the European project LIMEDU (FP7 ERA-NET MATERA+ 2009, Project No MATERA/ESM-1889) funded by Fundacion MADRI+D and by the National Centre for Research and Development (Project NCBiR/ERA-NET MATERA+/03/2011). IS acknowledges gratefully the Spanish Ministry of Economy and Competitiveness for financial support through the Ramon y Cajal Fellowship. The authors thank the Laboratorio de Microscopía Electrónica de Transmisión (LABMET) for the TEM measurements.

References

[1] G. Lutjering, J.C. Williams, Titanium, Springer, Germany, 2003.
[2] D.M. Brunette, P. Tengvall, M. Textor, P. Thomsen, Titanium in Medicine, Springer, Germany, 2001.
[3] R.Z. Valiev, M.J. Zehetbauer, Y. Estrin, H.W. Hoeppel, Y. Ivanisenko, H. Hahn, G. Wilde, H.J. Roven, X. Sauvage, T.G. Langdon, Adv. Eng. Mater. 9 (2007) 527–533.
[4] Y.G. Ko, D.H. Shin, K.T. Park, C.S. Lee, Scr. Mater. 54 (2006) 1785–1789.
[5] D.H. Shin, I. Kim, J. Kim, Y.S. Kim, S.L. Semiatin, Acta Mater. 51 (2003) 983–996.
[6] J. Gubicza, Zs. Fogarassy, Gy. Krallics, J. Labar, T. Torkoly, Mater. Sci. Forum 589 (2008) 99–104.
[7] I. Sabirov, M.T. Perez-Prado, J.M. Molina-Aldareguia, I.P. Semenova, G.K. H. Salimgareeva, R.Z. Valiev, Scr. Mater. 64 (2011) 69–72.
[8] D.V. Gunderov, A.V. Polyakov, I.P. Semenova, G.I. Raab, A.A. Churakova, E. I. Gimaltdinova, I. Sabirov, J. Segurado, V.D. Sitdikov, I.V. Alexandrov, N. A. Enikeev, R.Z. Valiev, Mater. Sci. Eng. A 562 (2013) 128–136.
[9] A.V. Sergueeva, V.V. Stolyarov, R.Z. Valiev, A.K. Mukherjee, Scr. Mater. 45 (2001) 747–752.
[10] R.Z. Valiev, A.V. Sergueeva, A.K. Mukherjee, Scr. Mater. 49 (2003) 669–674.
[11] D.K. Yang, P.D. Hodgson, C.E. Wen, Scr. Mater. 63 (2010) 941–944.
[12] H.S. Kim, Mater. Sci. Eng. A 328 (2002) 317–323.
[13] H.S. Kim, S.J. Kim, J.W. Kim, D.H. Kim, W.J. Kim, Mater. Sci. Eng. A 528 (2011) 8479–8485.
[14] M. Lewandowska, K.J. Kurzydlowski, J. Mater. Sci. 43 (2008) 7299–7306.
[15] W. Pachla, M. Kulczyk, M. Sus-Ruszkowska, A. Mazur, K.J. Kurzydlowski, J. Mater. Process. Technol. 205 (2008) 173–182.
[16] K. Topolski, H. Garbacz, W. Pachla, K.J. Kurzydlowski, Phys. Status Solidi 7 (2010) 1391–1394.
[17] S. Zherebtsov, W. Lojkowski, A. Mazur, G. Salishchev, Mater. Sci. Eng. A 527 (2010) 5596–5603.
[18] K. Topolski, H. Garbacz, K.J. Kurzydlowski, Mater. Sci. Forum 584–586 (2008) 777–782.
[19] G.G. Yapici, I. Karaman, H.J. Maier, Mater. Sci. Eng. A 434 (2006) 294–302.
[20] R. Lapovok, P.D. Hodgson, J. Mech. Phys. Solids 57 (2009) 1851–1864.
[21] A. Taylor, M. Weiss, T. Hilditch, N. Stanford, P.D. Hodgson, Mater. Sci. Eng. A 555 (2012) 148–153.
[22] R. Yoda, K. Shibata, T. Morimitsu, D. Terada, N. Tsuji, Scr. Mater. 65 (2011) 175–178.
[23] E.C. Moreno-Valle, M.A. Monclus, J.M. Molina-Aldareguia, N. Enikeev, I. Sabirov, Metal. Mater. Trans. A 44 (2013) 2399–2408.
[24] ASTM B 348-09. Standard Specification for Titanium and Titanium Alloy Bars and Billets.
[25] W. Pachla, M. Kulczyk, A. Świderska-Środa, M. Lewandowska, H. Garbacz, A. Mazur, K.J. Kurzydłowski, Nanostructuring of metals by hydrostatic extrusion, in: Proceedings of the 9th International Conference on Mat. Forming ESAFORM-2006, Glasgow, UK, 26–28 April 2006, pp. 535–538.
[26] I. Alexander, S.S. Pavlov, M. Kiritani, Mater. Sci. Eng. A 350 (2003) 245–250.
[27] A. el-Domiaty, S.Z. Kassab, J. Mater. Process. Technol. 83 (1998) 72–83.
[28] J.M. Garcia-Infanta, A.P. Zhilyaev, A. Sharafutdinov, O.A. Ruano, F. Carreno., J. Alloys Compd. 473 (2009) 163–166.
[29] Z.X. Wang, H.J. Shi, J. Lu, P. Shi, X.F. Ma, Nucl. Eng. Des. 238 (2008) 3186–3193.
[30] Y.W. Ma, K.B. Yoon, Mater. Sci. Eng. A 527 (2010) 3630–3638.
[31] J.S. Ha, E. Fleury, Int. J. Pres. Ves. Pip. 75 (1998) 707–713.
[32] E. Fleury, J.S. Ha, Int. J. Pres. Ves. Pip. 75 (1998) 699–706.
[33] M.B. Toloczko, M.L. Hamilton, G.E. Lucas, J. Nucl. Mater. 283–287 (2000) 987–991.
[34] R.J. Contieri, M. Zanotello, R. Caram, Mater. Sci. Eng. A 527 (2010) 3994–4000.
[35] K. Hajizadeh, S. Ghobadi Alamdari, B. Eghbali, Physica B 417 (2013) 33–38.
[36] U.F Kocks, C.N. Tome, H.R. Wenk, Texture and Anisotropy, Cambridge University Press (2000) 203–207.
[37] S. Nemat-Nasser, W.G. Guo, J.Y. Cheng, Acta Mater. 47 (1999) 3705–3720.
[38] H. Conrad, Prog. Mater. Sci. 26 (1981) 123.
[39] M.M. Myshlyaev, S Yu, Mironov, Phys. Sol. State 44 (2002) 711–716.
[40] J. Gong, A.J. Wilkinson, Acta Mater. 57 (2009) 5693.
[41] G.E. Dieter, Mechanical Metallurgy, McGraw-Hill, Boston, MA, 1986.
[42] S.D. Norris, J.D. Parker, Mater. Sci. Technol. 12 (1996) 163–170.
[43] F.P.E. Dunne, D. Rugg, Fatigue Fract. Eng. Mater. Struct. 31 (2008) 949–958.
[44] I. Sabirov, R.Z. Valiev, I.P. Semenova, R. Pippan., Metal. Mater. Trans. A 41 (2010) 727–733.

Biaxial Deformation Behavior and Enhanced Formability of Ultrafine-Grained Pure Copper

E.C. MORENO-VALLE, M.A. MONCLUS, J.M. MOLINA-ALDAREGUIA, N. ENIKEEV, and I. SABIROV

Coarse-grained commercially pure Cu was subjected to equal channel angular pressing at room temperature for 2 passes and 12 passes resulting in grain refinement down to the ultrafine scale. Uniaxial tensile testing revealed that as-ECAP Cu samples have very high strength, but low uniform elongation and elongation to failure, whereas small punch testing showed that strain in biaxial stretching of the as-ECAP Cu specimens was comparable to that in the coarse-grained Cu. Analysis of surface relief demonstrated extensive microlocalization of plastic flow into microshear bands during biaxial stretching of the as-ECAP Cu specimens. The effect of microstructure and stress state on formability of the material and the mechanisms governing its plastic deformation are discussed. It is suggested that although the high strength as-ECAP Cu exhibits poor ductility in uniaxial tension, in other strain paths such as biaxial stretching, it can show high formability which is sufficient for metal-forming processes.

DOI: 10.1007/s11661-012-1576-8

I. INTRODUCTION

COPPER has been used in electric and electronic devices due to its low cost and excellent thermal and electrical conductivity and therefore appears as a good candidate for application in micro-electro-mechanical systems (MEMS).[1] The main obstacle to wider application of pure copper is its very low mechanical strength. Alloying of pure copper, strain hardening, or precipitation strengthening can be employed to increase mechanical strength of pure Cu, but all these strategies lead to dramatic degradation of its electrical conductivity since it is determined by the scattering of electrons due to disturbances in the crystal structure including thermal vibrations, impurities, and defects.[2] For instance, the electrical conductivities in some of Cu alloys range from 10 to 70 pct of IACS (international annealed copper standard).[3] It has been recently demonstrated that intelligent microstructural design based on grain refinement down to the ultrafine or nanoscale *via* severe plastic deformation can be a good strategy to dramatically increase mechanical strength of pure Cu at no expense to its electrical conductivity.[2–5] The ultrafine-grained (UFG) Cu would also be an ideal material for MEMS having geometrical features of a few micrometers since the average grain size in the microparts should be smaller than the smallest dimension of the structural features in order to insure their reliable property control.[6,7]

E.C. MORENO-VALLE, Research Assistant, M.A. MONCLUS, Junior Researcher, J.M. MOLINA-ALDAREGUIA and I. SABIROV, Senior Researchers, are with the IMDEA Materials Institute, Getafe, Madrid, Spain. Contact e-mail: eva.moreno@imdea.org N. ENIKEEV, Senior Researcher, is with the Institute of Physics of Advanced Materials, Ufa State Aviation Technical University, Ufa, Russia.

Manuscript submitted July 9, 2012.
Article published online December 14, 2012

A problem arises in application of the high strength UFG Cu. A significant body of literature related to research on mechanical properties and deformation behavior of UFG Cu exists.[8–19] It was demonstrated that UFG Cu shows very low ductility.[8,9,14,15] Tensile stress–strain curves attain peak stress at a small plastic strain and then drop due to strain localization leading to specimen failure. Thus, it has been suggested that low tensile ductility of the UFG material can cause problems with fabrication of complex shape parts due to its low formability. Various strategies have been developed to increase the ductility of the UFG and nanostructured metallic materials as shown in the overviews.[20–22] Those strategies are mostly based either on manipulation with testing parameters (such as strain rate and/or temperature[14]) or on intelligent microstructural design (*e.g.*, formation of bimodal microstructures,[15] introduction of second phase precipitates,[23] *etc.*). All these strategies lead to activation of mechanisms that lead to increase in ductility and/or suppression of mechanisms degrading ductility. However, not much attention has been paid to the fact that in most of metal-forming operations, material is deformed in the multiaxial mode along a complex strain path.[24] Plastic deformation of the UFG and nanostructured metallic materials in the multiaxial mode (when mean stress is increased) might lead to activation of other deformation mechanisms such as grain boundary sliding and/or extensive microshear banding, which are not active during plastic deformation of these materials in the uniaxial mode.[25] Activation of these mechanisms during plastic deformation in the multiaxial mode may also lead to improved formability of the UFG and nanostructured metallic materials. Therefore, the main objective of this work is to study the effect of grain size on biaxial deformation behavior of UFG Cu with respect to mechanisms operating during plastic deformation as well as their

effect on the material formability, which has not been done so far.

II. MATERIAL AND EXPERIMENTAL PROCEDURES

A. *Material and Processing*

Commercially pure (CP) copper (99.9 pct) was chosen as a material for this investigation. The as-received material was subjected to annealing at 873 K (600 °C) for 2 hours. The annealed material shows a homogeneous microstructure with an average grain size of ~50 μm. Hereafter, this material condition will be referred to as coarse-grained (CG) Cu. Bars with a diameter of 18 mm and a length of 100 mm were subjected to equal channel angular pressing (ECAP) at room temperature in a die with the internal channel angle $\varphi = 90$ deg and outer angle $\psi = 0$ deg using route B_c (bar is rotated by 90 deg around the pressing direction after each ECAP pass). The bars were subjected to 2 and 12 ECAP passes. The strain produced in each pass was about 1, so the cumulative strain the specimens underwent as a result of the ECAP processing was about 2 and 12.[26] Hereafter, these material conditions will be referred to as 2P Cu and 12P Cu.

B. *Mechanical Tensile Testing and Small Punch Testing*

Tensile specimens of gauge length 7.5 mm, gauge width 1.5 mm, and gauge thickness ~1.2 mm were machined from the CG Cu and ECAP-processed Cu bars. The tensile axis of specimens was perpendicular to the bar axis. These tensile specimens were mechanically polished to a mirror-like surface using colloidal silica solution at the final stage. Tensile tests were carried out at room temperature using a 2 kN INSTRON 3384 universal testing machine (Instron, MA). Tensile specimens were deformed to failure with constant cross-head speed corresponding to the initial strain rate of 10^{-3} s^{-1}. Three tensile specimens were tested for each material condition and the results thus obtained were found to be reproducible.

Specimens for small punch testing were cut in the transverse section of pressed bars. Both sides of the disks were ground and polished to mirror-like surfaces using colloidal silica at the final stage. The final thickness of specimens was 0.45 mm. A schematic diagram of small punch testing is illustrated in Figure 1. The small punch specimen is clamped between the upper and bottom dies. It is deformed at room temperature by a well-lubricated hemispherical rigid punch having a radius of 1.2 mm. Our die has a design similar to that widely used for small punch testing.[27–33] The punch speed during the test was 0.5 mm/min. Load F and central deflection h readings were taken during testing (Figure 1). Small punch tests were stopped at the onset of plastic instability on the load–central deflection curve. Figure 2 illustrates the appearance of specimens after small punch testing, showing that specimens are deformed into a dome-shaped cap. To estimate the

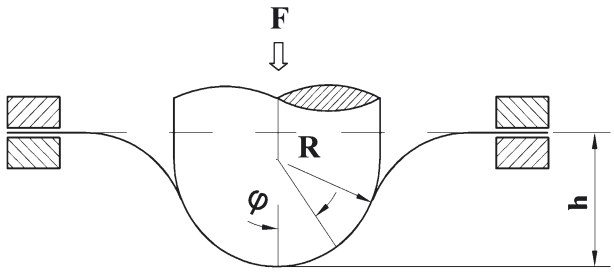

Fig. 1—Schematical drawing of punch testing.

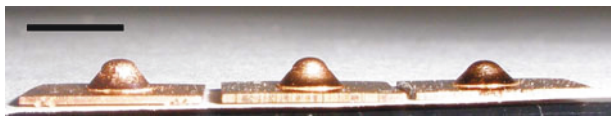

Fig. 2—Small punch specimens after testing: left—CG Cu; center—2P Cu; right—12P Cu. Scale bar length is 5 mm.

equivalent strain induced in these small punch specimens, the final thickness was measured over areas deformed under membrane (biaxial) stretching located at $\varphi = 20$ to 45 deg with respect to the vertical axis of the dome as illustrated in Figure 1. The true strain was estimated as

$$\varepsilon = \ln\left(\frac{t_0}{t}\right), \qquad [1]$$

where t_0 is the initial thickness and t is the final thickness of the punch specimen. At least three specimens were tested for each condition and the results were reproducible.

C. *Microstructure Analysis*

To study the microstructure, transmission electron microscopy (TEM) was carried out using a JEOL-2000 microscope (JEOL, Tokyo, Japan) operating at 200 kV. Samples for TEM study were prepared by twin jet electropolishing with electrolyte (25 pct orthophosphoric acid, 25 pct ethanol, and 50 pct distilled water) at room temperature at a voltage of 9 to 10 V. Observations were made in both bright and dark field imaging modes. Selected area electron diffraction (SAED) patterns were recorded from areas of interest using an aperture of 1.1 μm nominal diameter.

Qualitative examination of surface relief after deformation of both tensile specimens and small punch specimens was performed using an EVO MA 15 SEM (Carl Zeiss, NY) operating at 20 kV. Surface relief of deformed tensile specimens was analyzed in the area of homogeneous plastic deformation and in the necking area. Surface relief of deformed small punch specimens was analyzed in the area of biaxial stretching. For quantitative characterization of the surface relief in the area of biaxial stretching, atomic force microscopy (AFM) analysis was carried out using a Park XE150 AFM Instrument (Park Systems Corp., Suwon, Korea). Three-dimensional (3D) topography images of the

scanned areas were generated using WSxM Develop 5.2 software developed by Nanotec (Nanotec Electronica S.L, Madrid, Spain).[34] At least 10 profiles were analyzed for each material condition in order to estimate dimensions of microshear bands. Local volume fraction of shear bands was calculated as a ratio of length of the kinked profile (corresponding to the shear bands) to the total length of the profile.

III. RESULTS

A. *Effect of ECAP Processing on Microstructure of CP Cu*

Figure 3 illustrates TEM images of ECAP-processed Cu. It is seen that ECAP processing for two passes leads to formation of inhomogeneous microstructure consisting of coarse grains and small areas of ultrafine grains having a size of 150 to 300 nm. This is confirmed by SAED patterns where a mixture of low and high angle grain boundaries is observed (Figure 3(a)). Coarse grains contain shear bands having an average width of 200 nm and well-defined boundaries. These shear bands are inclined at nearly 45 deg to the extrusion axis (Figures 3(a) and (b)). Equiaxed subgrains of 250 to 650 nm are also observed within coarse grains. High dislocation density walls are seen (marked with arrows in Figure 3(a)). These defects promote the subgrain division and breakdown, which further refined the microstructure with increasing imposed strain.[10,11] Homogeneous UFG microstructure with equiaxed grains, of 100 to 250 nm in size and with well-defined grain boundaries, is formed after 12 ECAP passes (Figures 3(c) and (d)). Most grains are free of dislocations due to dynamic recovery by dislocation rearrangement during processing to large strains.[10,11] Analysis of SAED patterns shows that a majority of grain boundaries in the microstructure are high angle grain boundaries. These microstructural observations are in very good agreement with the results of microstructure investigations of ECAP-processed CP Cu reported earlier.[8–11,16]

B. *Mechanical Tensile Behavior*

Engineering stress–engineering strain curves from tensile tests at room temperature for CG, 2P, and 12P Cu are shown in Figure 4. Mechanical properties (flow stress at the onset of plastic deformation $\sigma_{\varepsilon=0}$, 0.2 pct proof strength $\sigma_{0.2}$, ultimate tensile strength σ_{UTS}, strain hardening exponent n, uniform elongation ε_u, and elongation to failure ε_f) are listed in Table I. It is clearly seen that grain refinement leads to significantly enhanced strength properties following the well-known Hall–Petch relationship.[35,36] However, the strength properties decrease very slightly with increasing the number of ECAP passes from 2 to 12 (Table I). This was rationalized based on dynamic recovery by dislocation rearrangement during processing to a larger number of ECAP passes.[10,11] ECAP processing leads to significant reduction of both uniform elongation and elongation to failure. Both ε_u and ε_f values somewhat increase with increasing number of ECAP passes (Figure 4; Table I).

It should be noted that the mechanical behavior of UFG copper has been studied in depth and numerous publications can be found in References 9, 10, 16. The results of our analysis of the mechanical behavior of the ECAP-processed Cu are in very good accordance with the data available in the literature.

C. *Mechanical Behavior During Small Punch Testing*

Figure 5 shows load–central deflection curves for all material conditions. Typical stages depicting the behavior of material during forming are marked on the curve for the 2P Cu specimen and can also be easily identified on other curves. The first stage, elastic bending, is associated with local surface microyielding. During the second stage, plastic bending, plastic flow begins and spreads within the specimen-punch contact zone. Biaxial deformation of a flat specimen into a dome-shaped cap occurs during the next stage, membrane stretching.[37] Once maximum load capacity is reached, unstable plastic flow begins leading to formation of cracks and specimen failure. The results of small punch testing are listed in Table II. It is seen that the maximum values of load recorded for the 2P Cu and 12P Cu are higher compared to that for the CG Cu (Table II). The highest value of the maximum central deflection in stable flow (at maximum load) is shown by CG Cu followed by 2P Cu and 12P Cu.

Equivalent strain was estimated over areas deformed under membrane stretching using Eq. [1]. Membrane stretching occurs in an annular section of the disk in tension.[37] This area is characterized by constant reduction of thickness following the profile of the punch. The estimated values of true equivalent strain are 0.55, 0.68, and 0.48 for CG, 2P, and 12P Cu, respectively.

D. *Surface Relief Analysis and Homogeneity of Plastic Flow*

To study homogeneity of plastic flow at the microscale and mechanisms operating during plastic deformation, the surface relief of tested tensile specimens and small punch specimens was carefully inspected in SEM. These observations reveal that CG Cu is deformed by dislocation slip under both uniaxial and biaxial deformation (Figures 6(a) and 7(a)). Necking in tensile CG Cu specimens also does not significantly affect morphology of surface relief (Figure 6(a)). No evidence of localized plastic flow was observed in the area of homogeneous plastic deformation of 2P Cu and 12P Cu tensile specimens. However, some localization of plastic deformation in the form of microshear banding is observed in the necking area of 2P and 12P Cu tensile specimens (Figures 6(b) and (c)). Surface relief observed in the area of biaxial stretching of small punch 2P and 12P Cu specimens is somewhat similar to those in the necking area of tensile specimens, though the surface relief has much higher roughness in both materials

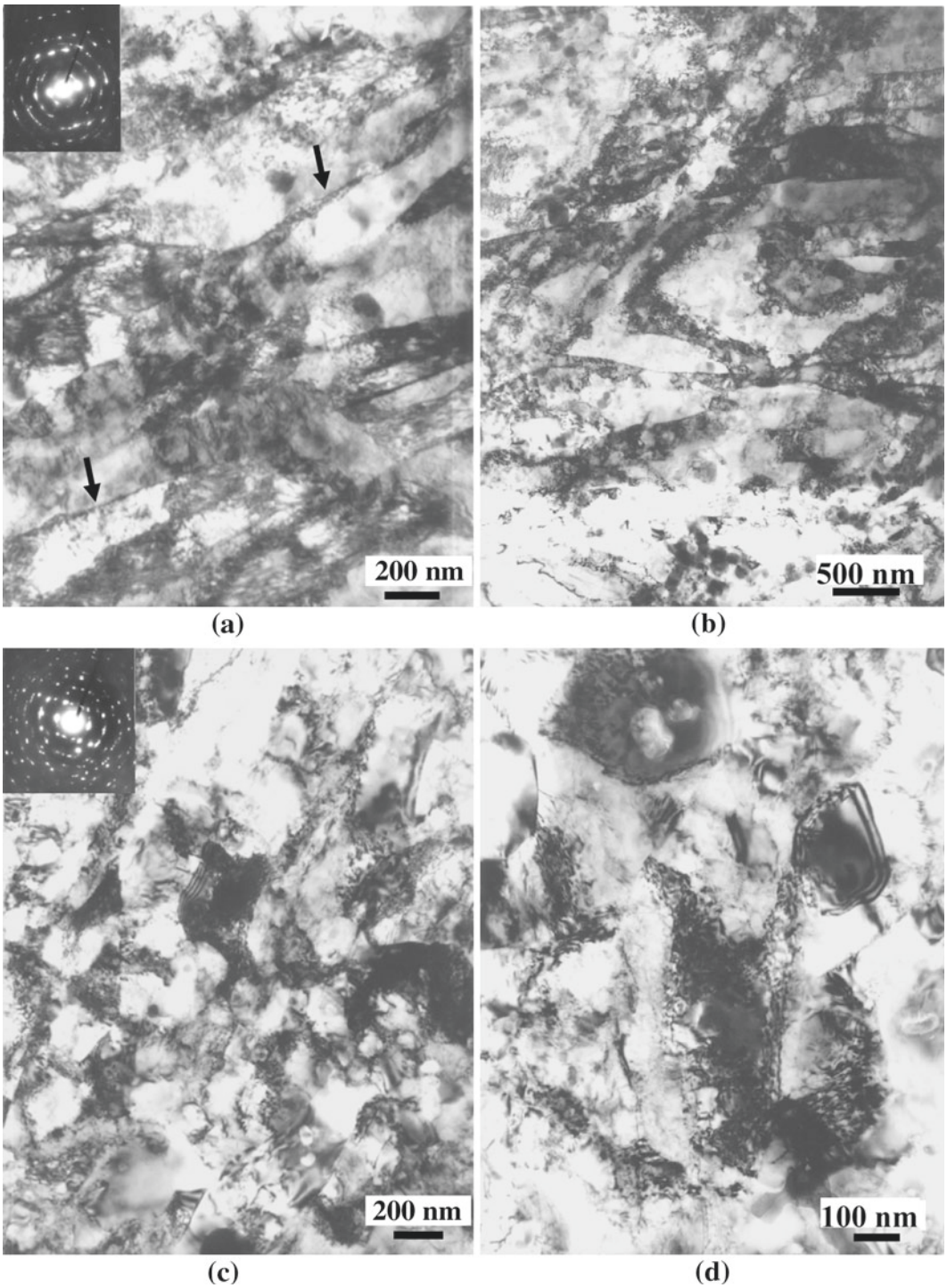

Fig. 3—Microstructure of Cu after ECAP processing: (*a*, *b*) bright field image and SAED pattern of 2P Cu; (*c*, *d*) bright field image and SAED pattern of 12P Cu.

(Figures 7(b) and (c)). Profuse microshear banding is observed over the surface of 2P Cu (marked with arrows in Figure 7b); some small surface areas free of microshear bands are present as well. Quantitative analysis of the surface area 280 × 180 μm^2 showed that the areas free of microshear bands have a diameter up to 30 μm and their surface fraction is just ~4 pct. A similar surface relief is also seen in the 12P Cu small punch specimen. However, the areas free of microshear bands have a larger diameter up to 60 μm and their surface fraction is nearly 35 pct (shear bands are marked with arrows in Figure 7(c)).

Figure 8 illustrates 3D AFM topography images of surface relief in the area of biaxial deformation of the 2P and 12P Cu small punch specimens after testing. The results of quantitative analyses of surface profiles through 3D AFM topography images are presented in Table III. The 3D AFM topography image (Figure 8(a)) and the surface profile (Figure 9(a)) confirm a very inhomogeneous character of surface relief in the 2P Cu specimen. It is characterized by a high density of step-like microshear bands having an average length in the range 7 to 25 μm and a width in the range 30 to 810 nm (Table III). Their volume fraction is about 34 pct. The surface relief of the 12P Cu specimen is inhomogeneous as well (Figures 8(b) and 9(b)). The morphology and dimensions of microshear bands are similar to those observed in 2P Cu specimen, though the 12P Cu has lower volume fraction of microshear bands, 25 pct (Figure 7; Table III).

IV. DISCUSSION

A. *Mechanisms Governing Plastic Deformation in Uniaxial and Biaxial Mode*

The results of this investigation clearly show that the deformation mode does not affect the plastic deformation mechanisms and mechanical properties of CG Cu much. The material is deformed mainly by dislocation glide and shows nearly the same ductility in both uniaxial and biaxial deformation modes (Tables I and II). At the same time, the homogeneity of plastic flow and the plastic deformation mechanisms in the 2P Cu and 12P Cu as well as their formability strongly depend on the initial (as-ECAP) microstructure and deformation mode (or stress state) during plastic deformation.

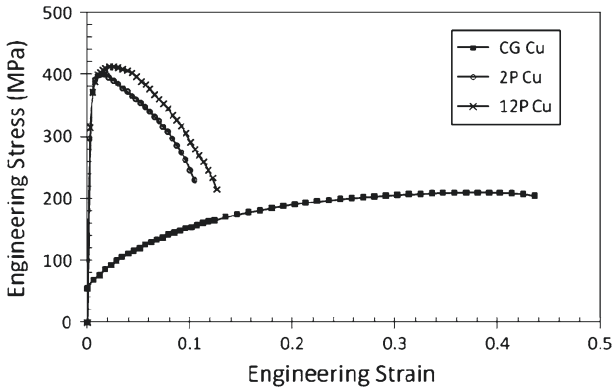

Fig. 4—Engineering stress–engineering strain curves for CG Cu, 2P Cu, and 12P Cu.

1. *Effect of microstructure on homogeneity of plastic flow and mechanisms operating during plastic deformation*

An analysis of experimental results shows that there is significant effect of microstructure on microshear banding activity in the as-ECAP Cu specimens. Numerous publications have documented the appearance of shear bands in the UFG and nanostructured materials.[17,18,38–44] What could be the main mechanism(s) leading to extensive microshear banding in the as-ECAP Cu during its biaxial stretching at room temperature? The first mechanism could be related to the microstructure inhomogeneities leading to significant stress redistribution at the microscale and, therefore, localization of plastic flow as was demonstrated earlier in Reference 38. Indeed, higher activity of microshear banding in the 2P Cu (Section III–D) having a more inhomogeneous microstructure compared to that of 12P Cu (Section III–A) supports this mechanism. The second mechanism could be related to the presence of microshear bands in the as-ECAP microstructure (which were induced during ECAP processing) before small punch testing since biaxial plastic deformation can trigger their further growth.[39] The presence of numerous microshear bands in the as-ECAP 2P Cu (Section III–A) showing a higher activity of microshear banding as well

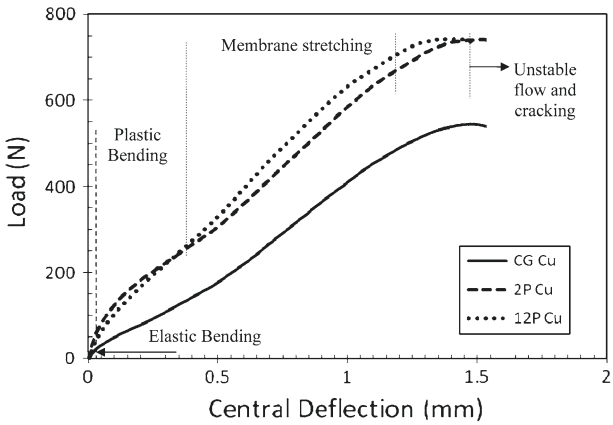

Fig. 5—Load–central deflection curves for CG Cu, 2P Cu, and 12P Cu. Stages of deformation are marked for 2P Cu.

Table II. Results of Small Punch Testing

Cu	F_{max} (*N*)	h_{max} (mm)	ε
CG	557 ± 18	1.48 ± 0.10	0.55 ± 0.04
2P	692 ± 24	1.45 ± 0.10	0.68 ± 0.02
12P	712 ± 39	1.40 ± 0.04	0.48 ± 0.01

Table I. Mechanical Properties of CG Cu, 2P Cu, and 12P Cu

Cu	$\sigma_{\varepsilon=0}$ (MPa)	$\sigma_{0.2}$ (MPa)	σ_{UTS} (MPa)	n	ε_u	ε_f
CG	27 ± 1	61 ± 2	206 ± 8	0.40	0.437 ± 0.031	0.465 ± 0.049
2P	255 ± 7	363 ± 1	400 ± 1	0.05	0.012 ± 0.001	0.099 ± 0.001
12P	240 ± 14	359 ± 3	410 ± 1	0.03	0.026 ± 0.001	0.119 ± 0.007

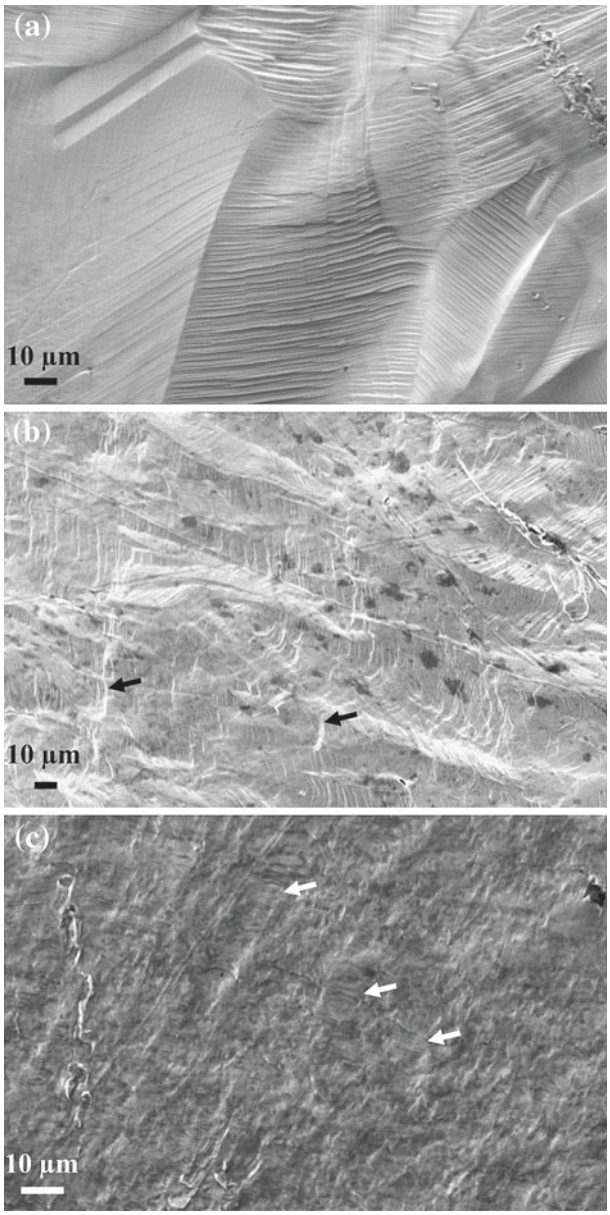

Fig. 6—SEM images of surface relief in necking area of tensile specimens: (*a*) CG Cu, (*b*) 2P Cu, and (*c*) 12P Cu.

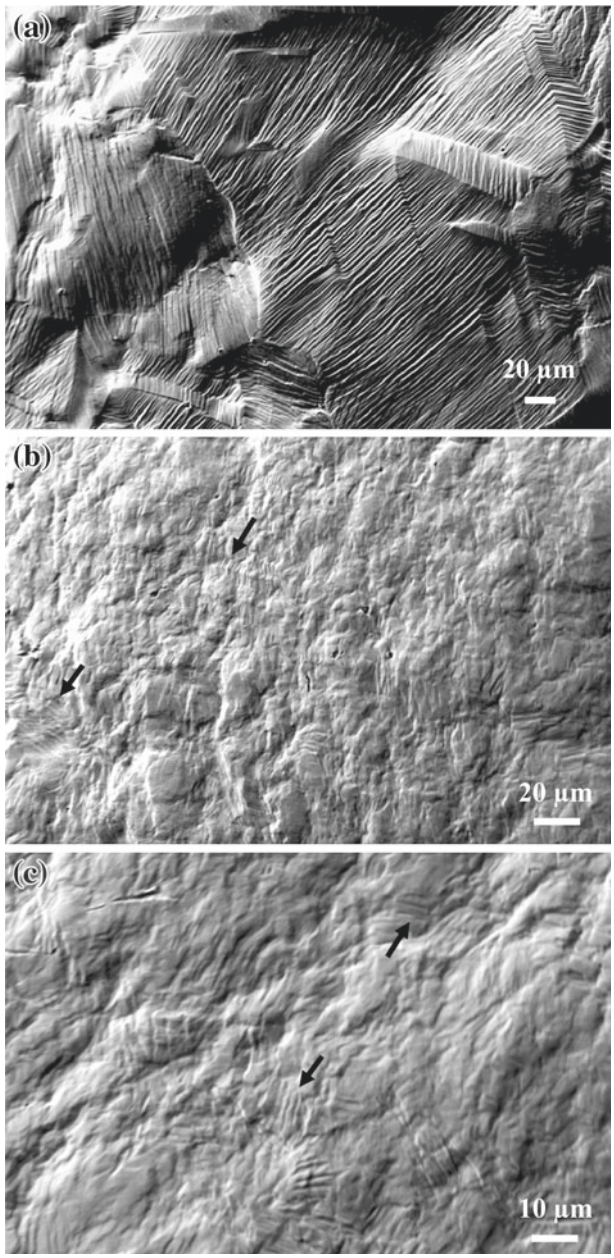

Fig. 7—SEM images of surface relief in area of biaxial stretching for (*a*) CG Cu, (*b*) 2P Cu, and (*c*) 12P Cu.

as a good correlation between the width of microshear bands in the as-ECAP 2P Cu (Section III–A) and 2P Cu after biaxial stretching (Section III–D) do support this assumption. Finally, activation of extensive microshear banding due to cooperative grain boundary sliding can be also considered as a mechanism responsible for formation of microshear bands[40,44] since cooperative grain boundary sliding can be active in UFG pure Cu at room temperature.[40] The evidence of cooperative grain boundary sliding observed in the 2P Cu specimen after punch testing is presented in Figure 10. Other mechanisms based on initiation of microshear bands at nanovoids and/or second phase precipitates[43] can be ruled out since these microstructural features are not present in the as-ECAP Cu (Section III–A).

As was demonstrated in the earlier works, the contribution of microshear banding to plastic deformation can be very significant.[38,44] For instance, microshear banding provided 9 pct out of 20 pct of uniform elongation during uniaxial tensile deformation of the UFG AA6082, which was almost half of the total plastic deformation.[44] We have not estimated quantitatively the contribution of microshear banding into total deformation in the as-ECAP Cu during biaxial stretching as it is a very complex task. Nevertheless, high volume fractions of microshear bands and their dimensions, comparable to those observed earlier in other materials,[38,44] clearly indicate significant contribution of microshear bands into the total strain of biaxially stretched 2P and 12P Cu specimens. Obviously,

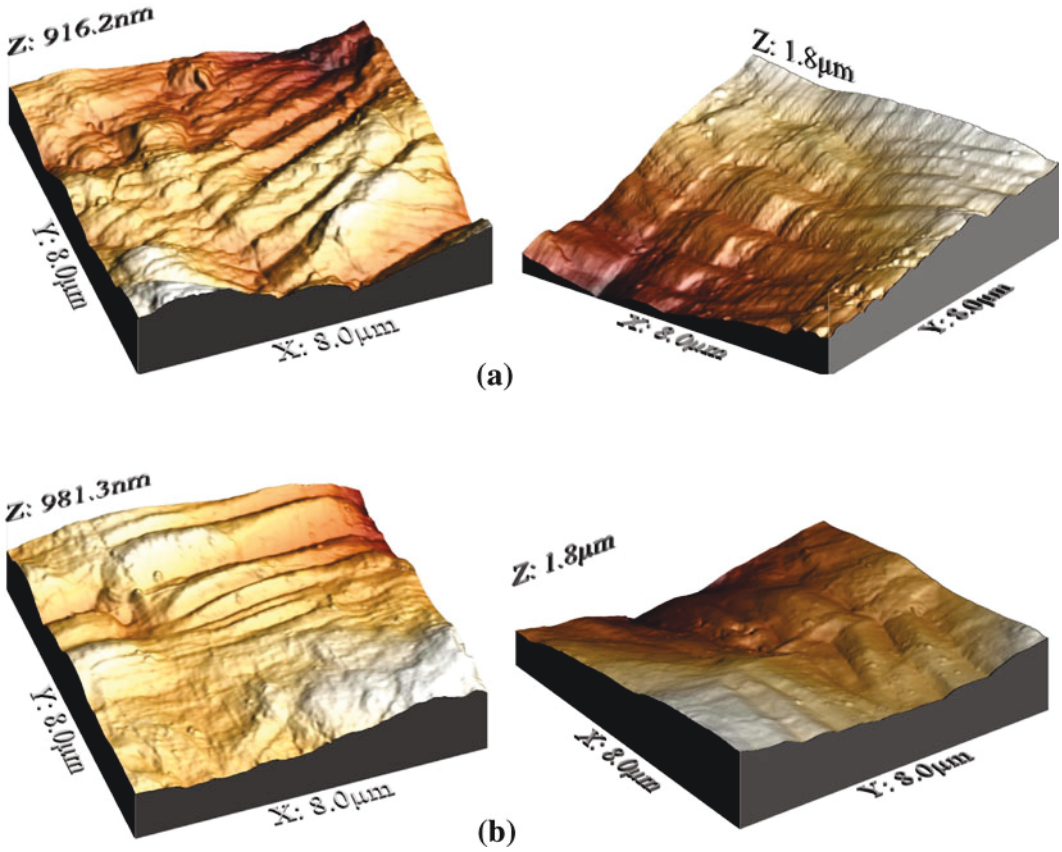

Fig. 8—Typical 3D AFM topography images of surface relief in area of biaxial stretching for (*a*) 2P Cu and (*b*) 12P Cu.

Table III. Dimensions, Local Surface Fraction of Microshear Bands, and Surface Fraction of Areas Containing Microshear Bands on Surface Relief for As-ECAP Cu

Number of ECAP Passes	Dimensions of Shear Bands			Average Local Volume Fraction of Shear Bands (pct)	Surface Fraction of Areas Containing Shear Bands (pct)
	Length (μm)	Width (nm)	Step height (nm)		
2	7 to 25	30 to 810	50 to 200	34	96
12	4 to 23	100 to 900	50 to 200	25	65

microshear banding should provide higher contribution to plastic deformation of the 2P Cu small punch specimens due to higher volume fraction of microshear bands in this material condition (Table III).[44]

An earlier study on uniaxial tensile deformation behavior of nanocrystalline Cu demonstrated near-perfect elastoplasticity of the material at room temperature.[19] Nanocrystalline Cu was deformed to large strains without any work hardening and necking, which was related to the predominance of grain boundary-mediated mechanisms. Analysis of our experimental results showed work hardening during tensile testing of the 2P and 12P pure Cu (Figure 4; Table I). From the character of the load–central deflection curves for the 2P and 12P Cu specimens (Figure 5), it is also seen that there is work hardening during plastic bending and biaxial (membrane) stretching before the onset of plastic instability. As known, the flow stress in the specimen during small punch testing is proportional to the load F and some parameters depending on the specimen and die geometry.[29,31] These parameters should be the same for all tested material conditions and, therefore, the flow stress in all three material conditions should be linearly proportional to the load applied (Figure 5). Thus, predominance of grain boundary-mediated mechanisms during biaxial stretching of the as-ECAP-processed Cu can be ruled out as well. On the other hand, cooperative grain boundary sliding does provide some slight contribution to the total plastic deformation (Figure 10).

2. *Effect of deformation mode on homogeneity of plastic flow in the as-ECAP copper*

Microlocalization of plastic deformation in necking areas of the UFG specimens is not a novel observation and has been already demonstrated on a range of UFG metallic materials.[18,25] For instance, the AFM study of the surface topography in the necking area of tensile

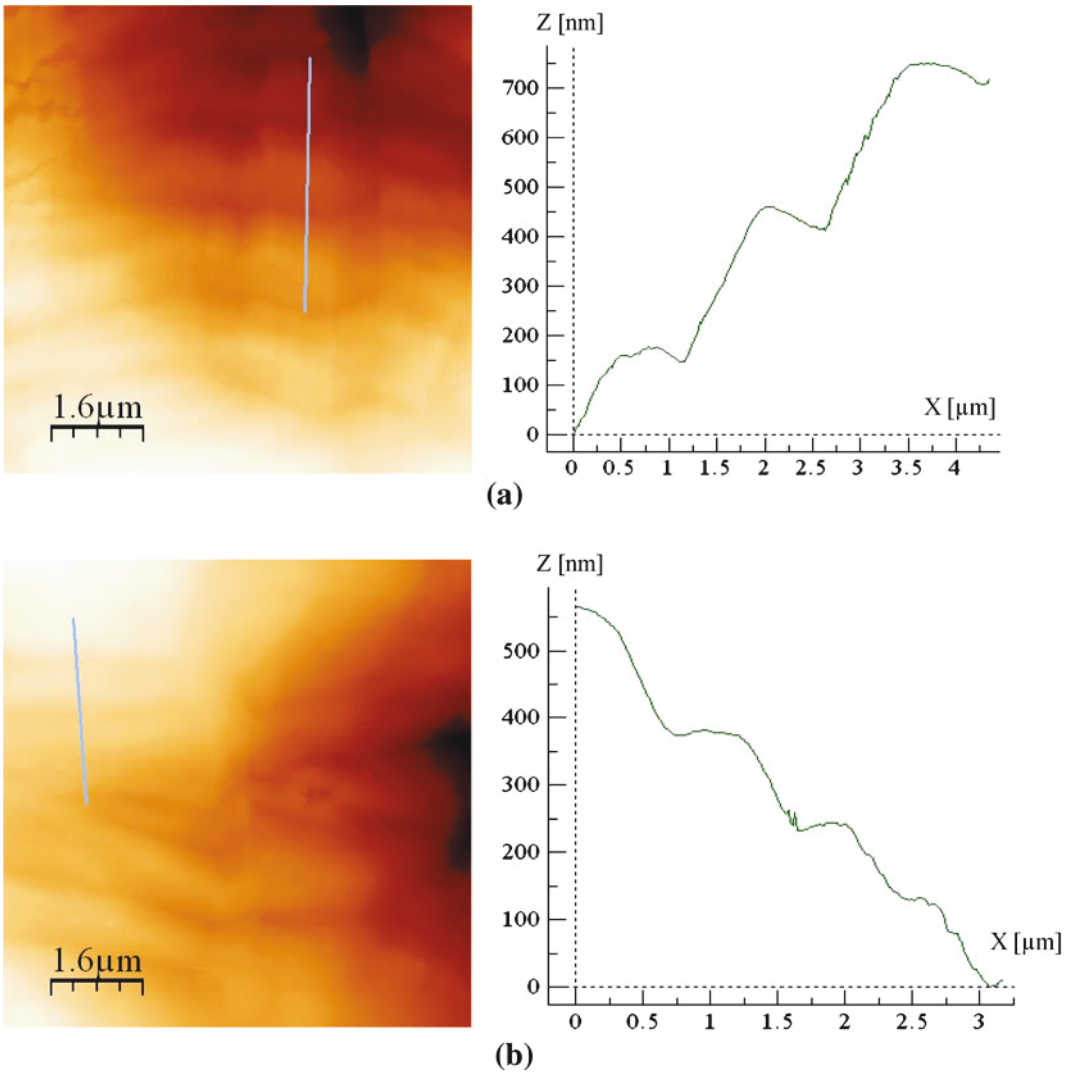

Fig. 9—2D AFM topography images and profiles for (*a*) 2P Cu and (*b*) 12P Cu.

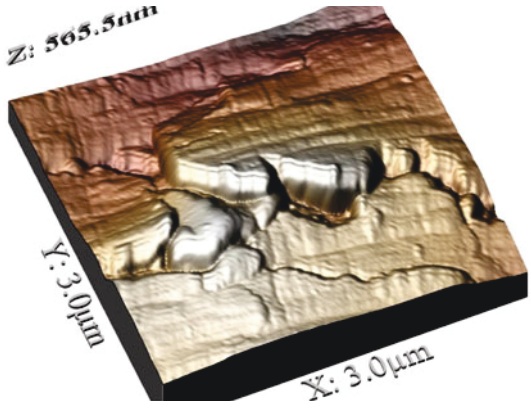

Fig. 10—3D AFM topography image of surface relief of 2P Cu in the area of biaxial stretching: evidence of cooperative grain boundary sliding.

specimens made from UFG pure Pd and UFG Pd-Ag alloys showed extensive microshear banding due to cooperative grain boundary sliding.[25] It can be hypothesized that the stress triaxiality T (a ratio of mean stress to hydrostatic stress) plays an important role in plastic deformation of UFG and nanostructured metallic materials. Increased stress triaxiality T in the necking area ($T > 1/3$) triggers some microshear banding, whereas this effect does not occur during homogeneous tensile deformation ($T = 1/3$). In the area of biaxial stretching of small punch specimens, T equals 2/3 which exceeds that T-value in the necking area of tensile specimens, thus leading to even higher surface roughness due to profuse microshear banding.

B. *About Formability of Ultrafine-Grained and Nanostructured Metallic Materials*

The results of the present investigation clearly show that high strength UFG Cu processed *via* ECAP can show very high formability in biaxial deformation at room temperature even though it has low tensile ductility. The enhanced formability is related to profuse microshear banding during biaxial deformation providing significant amount of plastic strain. The formability

of the UFG material in the multiaxial mode can be controlled *via* microstructural design (Section IV–A–1) and/or strain path (stress triaxiality) (Section IV–A–2). It should be noted that similar results have been very recently reported for UFG interstitial free steel fabricated by accumulative roll bonding[33] and UFG pure Al processed *via* cryorolling followed by recovery annealing.[45] Both materials showed very good stretch formability sufficient for metal-forming operations. Thus, it can be outlined that complex shape parts can be potentially fabricated from the UFG and nanostructured metallic materials *via* metal-forming operations for applications in various sectors of engineering.

V. CONCLUSIONS

(1) ECAP for 2 passes of pure Cu led to the formation of inhomogeneous microstructure consisting of ultrafine grains and highly deformed coarse grains containing subgrains and shear bands, whereas ECAP for 12 passes resulted in the formation of homogeneous UFG microstructure with a grain size of 100 to 250 nm.
(2) The ECAP-processed Cu demonstrated very high strength, but low uniform elongation and elongation to failure. Small punch testing showed that formability in biaxial stretching of the ECAP-processed Cu was comparable to that of the coarse-grained Cu.
(3) Inhomogeneous plastic flow in the form of profuse microshear banding plays an important role in biaxial stretching of the ECAP-processed Cu providing a significant amount of plastic deformation and, therefore, formability. The activity of microshear banding and formability of the ECAP-processed Cu can be controlled *via* microstructural design and/or stress triaxiality.
(4) Other mechanisms active during biaxial stretching of the ECAP-processed Cu include dislocation glide and grain boundary sliding.

ACKNOWLEDGMENTS

The authors acknowledge the financial support of the Spanish Ministry of Science and Innovation (MAT2009-14396) and the Comunidad de Madrid through the program ESTRUMAT (S2009/MAT-1585). IS gratefully acknowledges the Spanish Ministry of Science and Innovation for financial funding through the Ramon y Cajal Fellowship. NE gratefully acknowledges financial support by the RFBR (11-08-12098-ofi-m-2011).

REFERENCES

1. *ASM Handbook*: *Volume 2. Properties and Selection: Nonferrous Alloys and Special Purpose Materials*, ASM, 1990.
2. X.H. Chen, L. Lu, and K. Lu: *J. Appl. Phys.*, 2007, vol. 102, pp. 0837081–88.
3. N. Takata, S.H. Lee, and N. Tsuji: *Mater. Lett.*, 2009, vol. 63, pp. 1757–60.
4. Y. Zhang, Y.S. Li, N.R. Tao, and K. Lu: *Appl. Phys. Lett.*, 2007, vol. 91, pp. 2119011–13.
5. D.V. Shangina, N.R. Bochvar, and S.V. Dobatkin: *J. Mater. Sci.*, 2012, vol. 47, pp. 7764–69.
6. Y. Champion and Y. Brechet: *Adv. Eng. Mater.*, 2010, vol. 12, pp. 798–802.
7. R.Z. Valiev, M.J. Zehetbauer, Y. Estrin, H.W. Hoppel, Y. Ivanisenko, H. Hahn, G. Wilde, H.J. Roven, X. Sauvage, and T.G. Langdon: *Adv. Eng. Mater.*, 2007, vol. 9, pp. 527–33.
8. R.Z. Valiev, I.V. Alexandrov, T.C. Lowe, and Y.T. Zhu: *J. Mater. Res.*, 2002, vol. 17, pp. 5–8.
9. F.H. Dalla Torre, E.V. Pereloma, and C.H.J. Davies: *Acta Mater.*, 2006, vol. 54, pp. 1135–46.
10. C. Huang, S. Wu, S. Li, and Z. Zhang: *Adv. Eng. Mater.*, 2008, vol. 10, pp. 434–38.
11. N. Lugo, N. LLorca, J.J. Sunol, and J.M. Cabrera: *J. Mater. Sci.*, 2010, vol. 45, pp. 2264–73.
12. J. Gubicza, N.Q. Chinh, J.L. Lábár, S. Dobatkin, Z. Hegedus, and T.G. Langdon: *J. Alloy. Compd.*, 2009, vol. 483, pp. 271–74.
13. H. Conrad: *Mater. Sci. Eng. A*, 2003, vol. 341, pp. 216–28.
14. Y.M. Wang and E. Ma: *Acta Mater.*, 2004, vol. 52, pp. 1699–1709.
15. Y.M. Wang, M. Chen, F. Zhou, and E. Ma: *Nature*, 2002, vol. 419, pp. 912–15.
16. F. Dalla Torre, R. Lapovok, J. Sandlin, P.F. Thomson, C.H.J. Davies, and E.V. Pereloma: *Acta Mater.*, 2004, vol. 52, pp. 4819–32.
17. S. Cheng, E. Ma, Y.M. Wang, L.J. Kecskes, K.M. Youssef, C.C. Koch, U.P. Trociewitz, and K. Han: *Acta Mater.*, 2005, vol. 53, pp. 1521–33.
18. Y.M. Wang, K. Wang, D. Pan, K. Lu, K.J. Hemker, and E. Ma: *Scripta Mater.*, 2003, vol. 48, pp. 1581–86.
19. Y. Champion, C. Langlois, S. Guerin-Mailly, P. Langlois, J.L. Bonnentien, and M.J. Hytch: *Science*, 2003, vol. 300, pp. 310–11.
20. E. Ma: *JOM*, 2006, vol. 58 (4), pp. 49–56.
21. Y. Zhao, Y.T. Zhu, and E.J. Lavernia: *Adv. Eng. Mater.*, 2010, vol. 12, pp. 769–78.
22. I.A. Ovidko and T.G. Langdon: *Rev. Adv. Mater. Sci.*, 2012, vol. 30, pp. 103–11.
23. Y.H. Zhao, X.Z. Liao, S. Cheng, E. Ma, and Y.T. Zhu: *Adv. Mater.*, 2006, vol. 18, pp. 2280–83.
24. R. Lapovok and P.D. Hodgson: *J. Mech. Phys. Solids*, 2009, vol. 57, pp. 1851–64.
25. K. Yang, Yu. Ivanisenko, A. Caron, A. Chuvilin, L. Kurmanaeva, T. Scherer, R.Z. Valiev, and H.J. Fecht: *Acta Mater.*, 2010, vol. 58, pp. 967–78.
26. R.Z. Valiev and T.G. Langdon: *Prog. Mater. Sci.*, 2006, vol. 51, pp. 881–981.
27. J.M. Garcia-Infanta, A.P. Zhilyaev, A. Sharafutdinov, O.A. Ruano, and F. Carreno: *J. Alloy. Compd.*, 2009, vol. 473, pp. 163–66.
28. Z.X. Wang, H.J. Shi, J. Lu, P. Shi, and X.F. Ma: *Nucl. Eng. Des.*, 2008, vol. 238, pp. 3186–93.
29. Y.W. Ma and K.B. Yoon: *Mater. Sci. Eng. A*, 2010, vol. 527, pp. 3630–38.
30. J.S. Ha and E. Fleury: *Int. J. Press. Vessel. Pip.*, 1998, vol. 75, pp. 707–13.
31. E. Fleury and J.S. Ha: *Int. J. Press. Vessel. Pip.*, 1998, vol. 75, pp. 699–706.
32. M.B. Toloczko, M.L. Hamilton, and G.E. Lucas: *J. Nucl. Mater.*, 2000, vols. 283–287, pp. 987–91.
33. R. Yoda, K. Shibata, T. Morimitsu, D. Terada, and N. Tsuji: *Scripta Mater.*, 2011, vol. 65, pp. 175–78.
34. I. Horcas, R. Fernandez, J.M. Gomez-Rodriguez, J. Colchero, J. Gomez-Herrero, and A.M. Baro: *Rev. Sci. Instrum.*, 2007, vol. 78, pp. 0137051–58.
35. E.O. Hall: *Proc. Phys. Soc. B*, 1951, vol. 64, pp. 747–53.
36. N.J. Petch: *J. Iron Steel Inst.*, 1953, vol. 174, pp. 25–28.
37. S.D. Norris and J.D. Parker: *Mater. Sci. Technol.*, 1996, vol. 12, pp. 163–70.

38. D. Jia, K.T. Ramesh, and E. Ma: *Acta Mater.*, 2003, vol. 51, pp. 3495–3509.
39. S. Malekjani, P.D. Hodgson, P. Cizek, I. Sabirov, and T.B. Hilditch: *Int. J. Fatigue*, 2011, vol. 33, pp. 700–09.
40. A. Vinogradov, S. Hashimoto, V. Patlan, and K. Kitagawa: *Mater. Sci. Eng. A*, 2001, vols. 319–321, pp. 862–66.
41. B.P. Kashyap, P.D. Hodgson, Y. Estrin, I. Timokhina, M.R. Barnett, and I. Sabirov: *Metall. Mater. Trans. A*, 2009, vol. 40A, pp. 3294–3303.
42. I. Sabirov, M.R. Barnett, Y. Estrin, and P.D. Hodgson: *Scripta Mater.*, 2009, vol. 61, pp. 181–84.
43. R.W. Hayes, D. Witkin, F. Zhou, and E.J. Lavernia: *Acta Mater.*, 2004, vol. 52, pp. 4259–71.
44. I. Sabirov, Y. Estrin, M.R. Barnett, I. Timokhina, and P.D. Hodgson: *Acta Mater.*, 2008, vol. 56, pp. 2223–30.
45. A. Taylor, M. Weiss, T. Hilditch, N. Stanford, and P.D. Hodgson: *Mater. Sci. Eng. A*, 2012, vol. 555, pp. 148–53.

Materials Letters 65 (2011) 2917–2919

Contents lists available at ScienceDirect

Materials Letters

journal homepage: www.elsevier.com/locate/matlet

Effect of the grain refinement via severe plastic deformation on strength properties and deformation behavior of an Al6061 alloy at room and cryogenic temperatures

E.C. Moreno-Valle [a,*], I. Sabirov [a], M.T. Perez-Prado [a], M.Yu. Murashkin [b], E.V. Bobruk [b], R.Z. Valiev [b]

[a] Instituto Madrileño de Estudios Avanzados de Materiales, IMDEA Materials Institute, Madrid, Spain
[b] Institute of Physics of Advanced Materials, Ufa State Aviation Technical University, Ufa, Russia

ARTICLE INFO

Article history:
Received 19 May 2011
Accepted 14 June 2011
Available online 24 June 2011

Keywords:
Metals and alloys
Microstructure
Nanocrystalline materials
High pressure torsion
Mechanical properties
Cryogenic temperatures

ABSTRACT

A coarse-grained (CG) Al6061 alloy after solution treatment is subjected to high pressure torsion at room temperature resulting in the formation of a homogeneous ultra-fine grained (UFG) microstructure with average grain size of 170 nm. Tensile tests are performed at room and liquid nitrogen temperatures for both CG and UFG conditions. Analysis of the surface relief of the tested specimens is performed. The effect of microstructure on the mechanical properties and on the deformation behavior of the material is discussed.

1. Introduction

The 6xxx Al alloys are widely used in aerospace engineering due to their good corrosion resistance and low cost, along with good formability and weldability [1]. It is now realized that a better understanding of strengthening and flow properties of the Al alloys of the 6xxx series by manipulating the grain refinement processes can enable more effective exploitation of these alloys. It was demonstrated that severe plastic deformation can be successfully utilized for grain refinement in the Al alloys down to ultra-fine scale [2]. Despite a significant body of experimental research into the plastic deformation of the UFG 6xxx Al alloys at room temperature [3,4] and elevated temperatures [5,6], their deformation behavior at cryogenic temperatures has not been widely studied so far. However, these alloys in the UFG condition have a significant potential for application in engineering at temperatures well below zero. The objective of this work is to study the effect of grain refinement on the mechanical behavior of an Al6061 alloy at room and cryogenic temperatures.

2. Material and experimental procedures

Commercial grade Al–Mg–Si alloy of composition (in wt.%) 1.00 Mg, 0.61 Si, 0.12 Cu, 0.38 Cr, 0.60 Fe, 0.02 Ti, and balance Al was chosen for this investigation. Disks with a diameter of 20 mm and a thickness of 1 mm were solution treated at 530 °C for 2 h and water quenched. The average grain size of the Al6061 alloy after solution treatment and natural aging for a week (T4 condition) was found to be of ~100 μm. The Al6061 alloy in T4 condition also contains clusters of Mg and Si solute atoms homogeneously distributed in the microstructure [7].

Water quenched disks were subjected to high pressure torsion (HPT) for 10 turns at room temperature under a pressure of 6 GPa. Then the samples were naturally aged for a week. To study the microstructure, transmission electron microscopy (TEM) was carried out using a JEOL 2100 microscope. Observations were made in both the bright and the dark field imaging modes, and selected area electron diffraction (SAED) patterns were recorded from several areas of interest. At least 300 grains were analyzed by the lineal intercept method to estimate the average grain size. Tensile specimens of gage length 6 mm, gage width 1.5 mm, and thickness ~0.8 mm were machined from both CG and HPT processed disks. The central axis of the tensile specimens was located at a distance of 4.5 mm from the disk center. Tensile specimens were deformed to failure with the initial strain rate of 10^{-3} s^{-1} at room temperature (298 K) and liquid nitrogen temperature (77 K). At least three specimens were deformed at each condition and the results were found to be reproducible.

3. Results and discussion

3.1. Microstructure of the Al6061 alloy

HPT results in formation of a homogeneous UFG microstructure consisting of equiaxed grains (Fig. 1). The histogram of grain size distribution is presented in Fig. 2. The average grain size is 170 nm.

* Corresponding author. Tel.: +34 674 178 904; fax: +34 916 940 945.
E-mail address: eva.moreno@imdea.org (E.C. Moreno-Valle).

0167-577X/$ – see front matter © 2011 Elsevier B.V. All rights reserved.
doi:10.1016/j.matlet.2011.06.057

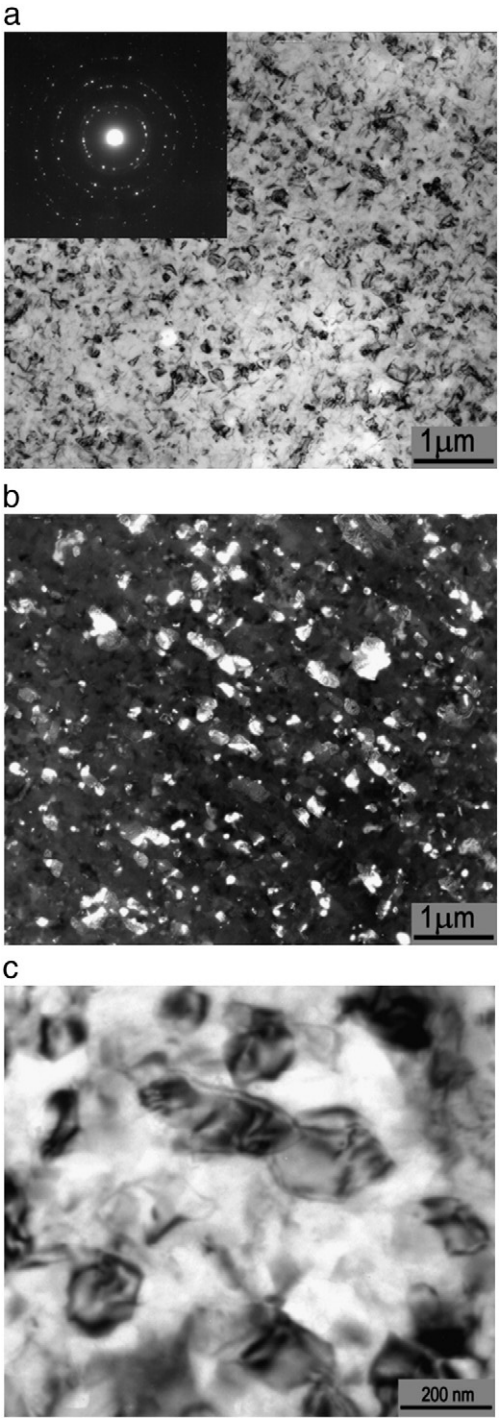

Fig. 1. TEM images of the Al6061 alloy after solution treatment and HPT processing: a) bright field image and SAED pattern; b) dark field image; c) bright field image.

Analysis of the SAED patterns shows that most of the boundaries are high angle grain boundaries (Fig. 1a); some low angle grain boundaries are also observed (Fig. 1c). Such microstructure is typical of HPT processed metallic materials [2]. Atom probe tomography studies performed on this material after HPT processing revealed massive segregations of the Mg, Si, and Cu solute atoms along grain boundaries [8].

3.2. Effect of grain size on mechanical behavior of the Al6061 alloy

Fig. 3 illustrates the engineering stress–engineering strain curves for both the CG and the UFG material. Data on the mechanical

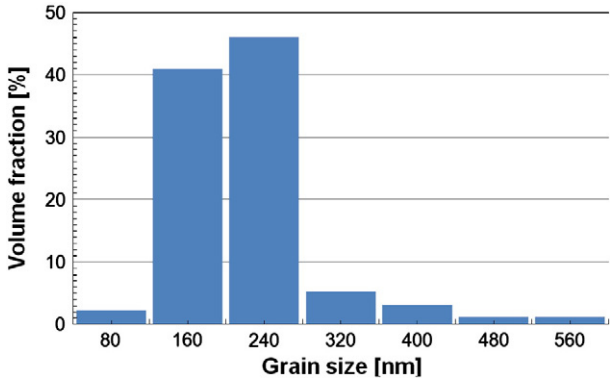

Fig. 2. Histogram of the grain size distribution for the Al6061 alloy after solution treatment and HPT processing.

properties of the material (stress at the onset of plastic deformation σ_o, 0.2% proof stress $\sigma_{0.2}$, ultimate tensile strength σ_{UTS}, uniform elongation ε_u, and elongation to failure ε_f) are listed in Table 1. It is seen that HPT results in a significant increase of strength properties of the material at both testing temperatures. However, the ductility decreases significantly. A decrease of the testing temperature results in a significant increase of σ_o, $\sigma_{0.2}$, and σ_{UTS} in both CG and UFG samples. It should be noted that the ratio $\sigma_o^{77K}/\sigma_o^{298K}$ is higher for the CG condition than for the UFG condition (Table 1). A similar trend can be also noted for the ratio $\sigma_{0.2}^{77K}/\sigma_{0.2}^{298K}$. The uniform elongation of the CG material increases slightly with decreasing temperature while the

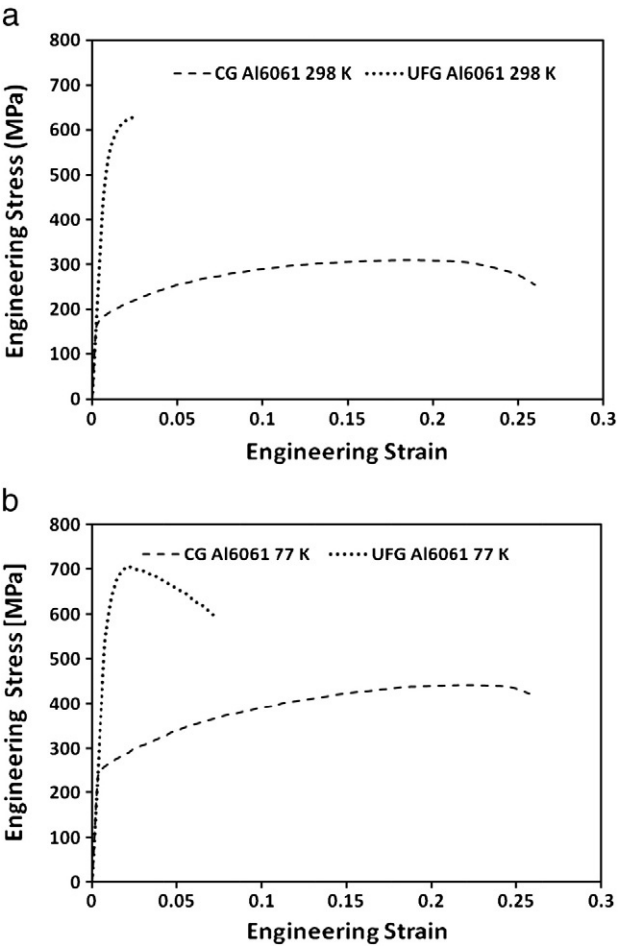

Fig. 3. Engineering stress–engineering strain curves for both CG and UFG Al6061 alloys: a) at 298 K and b) at 77 K.

Table 1
Mechanical properties of the coarse-grained and ultra-fine grained Al6061 at 298 K and 77 K.

		σ_o (MPa)	$\sigma_{0.2}$ (MPa)	σ_{UTS} (MPa)	ε_u (%)	ε_f (%)	n
CG	298 K	160	170	300	21	25.7	0.22
	77 K	235	245	430	26.8	28.3	0.26
	σ^{77K}/σ^{RT}	1.47	1.44				
UFG	298 K	430	545	630	1.5	1.8	0.07
	77 K	530	605	705	1.2	6.3	0.09
	σ^{77K}/σ^{RT}	1.23	1.11				

UFG material follows the opposite trend. The elongation to failure of the CG material slightly increases whereas in the UFG alloy this parameter increases dramatically. To estimate the strain hardening coefficient n, the true stress–true strain curves were fitted by a single power-law [9]

$$\frac{\sigma}{\sigma_o} = \alpha\left(\frac{\varepsilon}{\varepsilon_o}\right)^n \quad (1)$$

where $\varepsilon_o = \sigma_o/E$ and α is a dimensionless coefficient. It should be noted that for the UFG material, only the strain hardening coefficient at the early stage of plastic deformation can be determined due to its low uniform elongation. It is seen that grain refinement results in a significant decrease of the n-value at both temperatures (Table 1). A decrease of the testing temperature leads to a slight increase of the n-value in both CG and UFG materials. This can be related to increased ability of coarse grains and ultra-fine grains to accumulate dislocations due to the suppression of dislocation annihilation at 77 K that can stabilize the material against failure [10].

A dramatic increase of the material strength after HPT can be mainly attributed to the formation of the homogeneous UFG microstructure that provides a significant strengthening according to the Hall-Petch law [2]. Segregations of solute atoms induced by HPT should also provide some additional strengthening [8]. It can be outlined that these segregations play a key role not only in the formation of the UFG microstructure during HPT as was suggested in [8], but also in the deformation behavior of the UFG Al6061 alloy. Indeed, its deformation behavior at room temperature (Fig. 2) is very different to that reported earlier for UFG pure Al by Miyamoto et al. (see Fig. 1 in [11]). These authors demonstrated that the UFG pure Al tested at 298 K at strain rate of $1.6\times10^{-3}\,s^{-1}$ has a viscous nature: the material is homogeneously deformed to high strains up to ~0.15–0.2 without strain hardening [11]. A similar effect was also observed in pure nanocrystalline (NC) Cu [12]. In both works, the authors explained the observed effect by the predominance of grain boundary diffusion-like mechanisms during plastic deformation of the UFG Al and NC Cu at room temperature [11,12]. Unlike pure Al and pure Cu, the HPT processed Al6061 alloy is a super saturated solid solution containing massive segregations of solute atoms along grain boundaries, as was experimentally demonstrated earlier (see Fig. 3 in [8]). These segregations located along grain boundaries could significantly reduce the self-diffusion of the Al atoms along grain boundaries [13] suppressing activation of grain boundary diffusion mechanisms during plastic deformation at room temperature.

There is a body of experimental research on the deformation behavior of pure metals at cryogenic temperatures [10,11,14]. Ultra-high yield strength at 77 K was observed in NC Ni (1237 MPa) and NC Co (1711 MPa) [14]. It was demonstrated that the ratio $\sigma_y^{77K}/\sigma_y^{298K}$ is significantly larger for the NC pure metals than for their CG counterparts. For instance, for the NC Ni this ratio was found to be 1.47, whereas for the CG Ni it was 1.20 [14]. This effect was related to the activity of the grain boundary dislocation nucleation as the thermally activated deformation mechanism in NC grains. However, the UFG Al6061 alloy shows the opposite behavior: the ratio $\sigma_y^{77K}/\sigma_y^{298K}$ is larger for the CG material than for the UFG one (Table 1). This observation can be rationalized as follows. A temperature drop down to 77 K could induce local thermal residual stresses in the material due to the difference in thermal expansion coefficient between the Al matrix and areas with the massive segregations of solute atoms. As well known, the yield strength of the UFG metallic materials is determined by the stress required for the emission of dislocations at grain boundaries [15]. In the UFG Al6061 tested at liquid nitrogen temperature, dislocations could be generated at a lower applied stress compared to that in the UFG pure metal due to the local thermal residual stresses already induced at grain boundaries due to the temperature drop.

4. Conclusions

HPT processing can be successfully applied for the fabrication of the UFG Al6061 alloy with a grain size of 100–200 nm. The UFG Al6061 alloy shows higher strength at both 298 K and 77 K. A decrease of the testing temperature results in improved strength of both the CG and the UFG material, increased strain hardening coefficient, and enhanced elongation to failure. However, the deformation behavior of the UFG Al6061 alloy is very different to that of the UFG and NC pure metals. Unlike in pure metals, the ratio $\sigma_y^{77K}/\sigma_y^{298K}$ is larger for the CG material (1.47) than for the UFG one (1.23). These effects could be related to the presence of segregations of solute atoms along grain boundaries.

References

[1] Polmear IJ. Light alloys—metallurgy of the light metals. 3rd ed. London: Arnold; 1995.
[2] Valiev RZ, Islamgaliev RK, Alexandrov IV. Bulk nanostructured materials from severe plastic deformation. Prog Mater Sci 2000;45:103–89.
[3] Morris DG, Gutierrez-Urrutia I, Munoz-Morris MA. Analysis of the strengthening mechanisms in a severely plastically-deformed Al–Mg–Si alloy with submicron grain size. J Mater Sci 2007;42:1439–43.
[4] Sabirov I, Barnett MR, Estrin Y, Hodgson PD. The effect of strain rate on the deformation mechanisms and the strain rate sensitivity of an ultra-fine-grained Al alloy. Scr Mater 2009;61:181–4.
[5] Troeger LP, Starke EA. Microstructural and mechanical characterization of a superplastic 6xxx aluminum alloy. Mater Sci Eng A 2000;277:102–13.
[6] Kashyap BP, Hodgson PD, Estrin Y, Timokhina I, Barnett MR, Sabirov I. Plastic flow properties and microstructural evolution in an ultrafine-grained Al–Mg–Si alloy at elevated temperatures. Metall Mater Trans A 2009;40:3294–303.
[7] Murayama M, Hono K. Pre-precipitate clusters and precipitation processes in Al–Mg–Si alloys. Acta Mater 1999;47:1537–48.
[8] Nurislamova GB, Sauvage X, Murashkin M, Islamgaliev R, Valiev RZ. Nanostructure and related mechanical properties of an Al–Mg–Si alloy processed by severe plastic deformation. Phil Mag Lett 2008;88:459–66.
[9] Dieter GE. Mechanical metallurgy. Boston: McGraw-Hill; 1986.
[10] Wang YM, Ma E, Valiev RZ, Zhu YT. Tough nanostructured metals at cryogenic temperatures. Adv Mater 2004;16:328–31.
[11] Miyamoto H, Ota K, Mimaki T. Viscous nature of deformation of ultrafine aluminum processed by equal-channel angular pressing. Scr Mater 2006;54:1721–5.
[12] Champion Y, Langlois C, Guerin-Mailly S, Langlois P, Bonnentien JL, Hytch MJ. Near-perfect elastoplasticity in pure nanocrystalline copper. Sci 2003;300:310–1.
[13] Du N, Qi Y, Krajewski PE, Bower AF. The effect of solute atoms on aluminum grain boundary sliding at elevated temperature. Metall Mater Trans A 2010;42:651–9.
[14] Wang YM, Ma E. On the origin of ultra cryogenic strength on nanocrystalline metals. Appl Phys Lett 2004;85:2750–2.
[15] Valiev RZ, Enikeev, Murashkin MY, Kazykhanov VU, Sauvage X. On the origin of extremely high strength of ultrafine-grained Al alloy produced by severe plastic deformation. Scr Mater 2010;63:949–52.